Electronic Theses and Dissertations

Theses, Dissertations, and Major Papers

1-1-2006

Surface-enhanced Raman and resonance Raman scattering: Substrate development, interpretation, and single -molecule detection.

Paul J. G. Goulet
University of Windsor

Follow this and additional works at: https://scholar.uwindsor.ca/etd

Recommended Citation

Goulet, Paul J. G., "Surface-enhanced Raman and resonance Raman scattering: Substrate development, interpretation, and single -molecule detection." (2006). *Electronic Theses and Dissertations*. 7228.
https://scholar.uwindsor.ca/etd/7228

SURFACE-ENHANCED RAMAN AND RESONANCE RAMAN SCATTERING: SUBSTRATE DEVELOPMENT, INTERPRETATION, AND SINGLE-MOLECULE DETECTION

BY

PAUL J. G. GOULET

A Dissertation
Submitted to the Faculty of Graduate Studies and Research
through Chemistry and Biochemistry
in Partial Fulfillment of the Requirements for the Degree of Doctor of Philosophy at the
University of Windsor

Windsor, Ontario, Canada
2006

© 2006 Paul J. G. Goulet

Library and
Archives Canada

Published Heritage
Branch

395 Wellington Street
Ottawa ON K1A 0N4
Canada

Bibliothèque et
Archives Canada

Direction du
Patrimoine de l'édition

395, rue Wellington
Ottawa ON K1A 0N4
Canada

Canada

ABSTRACT

In this work, the results of several fundamental and applied studies employing surface-enhanced Raman scattering (SERS) and surface-enhanced resonance Raman scattering (SERRS) are presented.

First, the fabrication, characterization, and application of several new substrates for SERS/SERRS are demonstrated. These SERS/SERRS substrates include mixed Ag/Au evaporated nanoparticle films; self-sustained, Au nanoparticle embedded chitosan films; dendrimer/Ag nanosphere LbL films; dendrimer/Ag nanowire LbL films; and avidin/Ag nanoparticle LbL films. They are characterized using a variety of techniques including: UV-visible surface plasmon absorption spectroscopy, X-ray photoelectron spectroscopy, atomic force microscopy, transmission electron microscopy, and infrared absorption. They are shown to be excellent substrates for SERS/SERRS measurements, demonstrating significant enhancement capability and several other valuable characteristics.

Next, the SERS spectra of the surface complexes of salicylic acid and 1-naphthylamine on Ag are studied. Density functional theory (DFT) calculations and several vibrational spectroscopic techniques are employed to aid in the interpretation of the SERS results. It is concluded that salicylate chemically adsorbs on Ag nanoparticles through its carboxylate group in a tilted, head-on orientation, while 1-NA on Ag forms a coordination complex that is highly sensitive to water solvation.

Finally, single-molecule SERS/SERRS from Langmuir-Blodgett monolayers on nanostructured metal films is discussed. Six molecular systems are studied at the single-molecule level, using three nanostructured metal films, a variety of laser excitation

iii

wavelengths, and single-point and 2D spatial mapping techniques. For the first time, overtones and combinations are observed in the single-molecule spectra of several perylene derivatives; 2D SERRS mapping techniques are used to explore the breakdown of ensemble averaging; single-molecules are distinguished in one-to-one binary mixtures in LB monolayers; and non-resonant single-molecule SERS spectra are detected from LB monolayers on nanostructured metallic films.

iv

For Nicole.

.

ACKNOWLEDGEMENTS

First, I thank my research advisor, friend, and mentor, Ricardo Aroca. He has expanded my world several times over. His support, guidance, patience, and encouragement can never be repaid.

I also thank the many friends that I have been fortunate to work with in the Materials and Surface Science Group: Nik, David, Lalo, Teo, Case, Tibebe, Daniel, Igor, Mat, Salwen, Ben, Shazia, Eduardo, Aldo, Francisco, Ramon, Clavijo, Miguel-Angel, Domingo, Golam, Grace, Marta, and Alicia. I cannot begin to detail the ways in which they have enriched my life.

I also thank all of my friends and family (and adopted families) for their love, support, and understanding in the face of my too frequent inattention.

Finally, I save my biggest thanks for Nicole and Paisley.

TABLE OF CONTENTS

LIST OF TABLES

LIST OF FIGURES

LIST OF ABBREVIATIONS

1-NA: 1-Naphthylamine

2-NAT: 2-Naphthalenethiol

5-AF: 5-(Aminomethyl)Fluorescein

AA: Arachidic Acid

AFM: Atomic Force Microscopy

ATR: Attenuated Total Reflection

Azo PTCD: Bis(benzimidazo)-Perylene

B4F: Biotin-4-Fluorescein

BBIP PTCD: Bis-Benzylimido Perylene

BNPTCD: N,N'-Bis(neopentyl)-3,4,9,10-Perylenebis(dicarboximide)

DFT: Density Functional Theory

EF: Enhancement Factor

FTIR: Fourier Transform Infrared

G1 DAB-Am: DAB-Am-4-Polypropylenimine Tetraamine Dendrimer

G5 DAB-Am: DAB-Am 64-Polypropylenimine Tetrahexacontaamine Dendrimer

IR: Infrared

LB: Langmuir-Blodgett

LbL: Layer-by-Layer

PAH: Polycyclic Aromatic Hydrocarbon

Pentyl PTCD: N-Pentylimidobenzimidazo-Perylene

PBS: Phosphate Buffered Saline

PSS: Polystyrene Sulfonate

PTCD: Perylenetetracarboxylic Diimide

PVP: Poly(vinylpyrrolidone)

R18: Octadecylrhodamine B

R6G: Rhodamine 6G

RAIRS: Reflection Absorption Infrared Spectroscopy

RRS: Resonance Raman Scattering

RS: Raman Scattering

SAL: Salicylic Acid

SalPTCD: *N*-pentyl-5-salicylimidoperylene

SEF: Surface-Enhanced Fluorescence

SEIRA: Surface-Enhanced Infrared Absorption

SEM: Scanning Electron Microscopy

SERRS: Surface-Enhanced Resonance Raman Scattering

SERS: Surface-Enhanced Raman Scattering

TEM: Transmission Electron Microscopy

XPS: X-ray Photoelectron Spectroscopy

Chapter 1

INTRODUCTION

1

1.1 Introduction

The powerful microanalytical techniques of surface-enhance Raman scattering (SERS) and surface-enhanced resonance Raman scattering (SERRS) involve large increases in Raman and resonance Raman scattering cross sections of analyte molecules adsorbed at the surface of nanometric-scale metallic particles that are capable of sustaining radiating localized surface plasmon resonances.[1-4] The study and application of these techniques has seen tremendous growth recently, and there are now almost a thousand scientific publications that discuss them per year. They are being employed widely in the medical, biological, chemical, and physical sciences toward a broad range of problems.[5-7] In particular, their high spatial resolution, high information content, and ultrasensitivity make them especially attractive as analytical techniques. As well, high quality, inexpensive, portable, and user-friendly Raman instruments are now becoming available, making these techniques accessible to many more scientists than ever before.

At this point of remarkable growth, however, there remain several important challenges facing SERS/SERRS. Three of the most critical of these challenges are represented by the primary objectives of this thesis: *(1)* to develop high-quality, specialized substrates that provide high enhancement of signals; *(2)* to provide strategies for the comprehensive vibrational study of molecules adsorbed on metal nanoparticles, by doing fundamental work on the interpretation of the SERS/SERRS spectra of different molecular systems; and finally, *(3)* to develop and improve techniques for ultrasensitive and single-molecule analysis of various molecules. These objectives are reflected in the structure of this thesis, with each being the focus of a major chapter.

2

In Chapter 2, though, a review is given of the most fundamental concepts employed in the work of this thesis. In particular, Raman scattering, resonance Raman scattering, SERS, SERRS,[8] surface-enhanced fluorescence[9] and the Langmuir-Blodgett film fabrication technique are introduced and discussed. In Chapter 3, the details of the experimental and computational work of this thesis are presented in sections on samples, characterization, and computation.

In Chapter 4, the development of high-quality, specialized substrates that provide high enhancement of signals, the first objective of this thesis, is addressed. The results of several studies on the fabrication, characterization, and application of new SERS/SERRS substrates are presented.[10-15] In particular, new SERS/SERRS substrates presented in this chapter include: mixed Ag/Au evaporated nanoparticle films; self-sustained, Au nanoparticle embedded chitosan films; dendrimer/Ag nanosphere LbL films; dendrimer/Ag nanowire LbL films; and avidin/Ag nanoparticle LbL films. These substrates were characterized using a variety of techniques including: UV-visible surface plasmon absorption spectroscopy, X-ray photoelectron spectroscopy, atomic force microscopy, transmission electron microscopy, and infrared absorption. They were demonstrated to be excellent substrates for SERS/SERRS measurements, demonstrating significant enhancement capability and other valuable characteristics including: chemical selectivity, functionality, biocompatibility, broadened and tunable enhancement regions, improved physical properties, incorporation of different metallic nanoparticles, low cost, easy fabrication, and water insolubility.

In Chapter 5, the provision of strategies for the comprehensive vibrational study of molecules adsorbed on metal nanoparticles, the second objective of this thesis, is

3

addressed. In this chapter, the results of studies on the interpretation of the SERS spectra of the surface complexes of salicylic acid and 1-naphthylamine are presented.[16-18] Due to the major structural changes that arise through the formation of the surface complexes of these analytes, the interpretation of their spectra on Ag was of unusual complexity and required the utilization of a variety of spectroscopic techniques, as well as DFT computation, for different related chemical species. Through the use of these techniques, the nature of the surface complexes of these analytes was determined. As well, the origins of many of the effects that confound SERS spectral analysis, and strategies that can be employed to resolve them, are discussed in this chapter.

In Chapter 6, the development and improvement of techniques for ultrasensitive and single-molecule analysis of various molecules, the final objective of this work, is addressed. In this chapter, the results of several studies where the Langmuir-Blodgett approach to single molecule SERS/SERRS detection was employed are presented.[19-23] In this work, 6 molecular systems were studied at the single-molecule level, using three nanostructured metal films, a variety of laser excitation wavelengths, and single-point and 2D spatial mapping techniques. The sections of this chapter discuss the study of overtones and combinations in the single-molecule spectra of perylene derivatives; the use of 2D SERRS mapping techniques to explore the breakdown of ensemble averaging; single-molecule SERRS from one-to-one binary mixtures; and non-resonant single-molecule SERS on nanostructured metallic films.

Finally, in Chapter 7, the conclusions of this thesis are summarized.

4

References

(1)   Aroca, R. *Surface-Enhanced Vibrational Spectroscopy*; John Wiley & Sons, Ltd.: Chichester, UK, 2006.

(2)   Moskovits, M. *Rev. Mod. Phys.* **1985**, *57*, 783-826.

(3)   Otto, A.; Mrozek, I.; Grabhorn, H.; Akemann, W. *J. Phys.-Condens. Matter* **1992**, *4*, 1143-1212.

(4)   Vo-Dinh, T. *TrAC, Trends Anal. Chem.* **1998**, *17*, 557-582.

(5)   Haynes, C. L.; McFarland, A. D.; Van Duyne, R. P. *Anal. Chem. A-Pages* **2005**, *77*, 338A-346A.

(6)   Kneipp, K.; Kneipp, H.; Itzkan, I.; Dasari, R. R.; Feld, M. S. *Curr. Sci.* **1999**, *77*, 915-926.

(7)   *Surface-Enhanced Raman Scattering- Physics and Applications*; Kneipp, K.; Moskovits, M.; Kneipp, H., Eds.; Springer-Verlag: Berlin Heidelberg, 2006; Vol. 103.

(8)   Pieczonka, N. P. W.; Goulet, P. J. G.; Aroca, R. F. Applications of the Enhancement of Resonance Raman Scattering and Fluorescence by Strongly Coupled Metallic Nanostructures. In *Surface-Enhanced Raman Scattering- Physics and Applications*; Kneipp, K., Moskovits, M., Kneipp, H., Eds.; Springer-Verlag: Berlin Heidelberg, 2006; Vol. 103; pp 197-216.

(9)   Goulet, P. J. G.; Aroca, R. F. Surface-enhancement of fluorescence near noble metal nanostructures. In *Topics in Fluorescence Spectroscopy: Radiative Decay Engineering*; Lakowics, J. R., Geddes, C. D., Eds.; Springer Science + Business Media, Inc.: New York, 2005; Vol. 8; pp 223-247.

(10)   Goulet, P. J. G.; Pieczonka, N. P. W.; Aroca, R. F. *Can. J. Anal. Sci. Spect.* **2003**, *48*, 146-152.

(11)   dos Santos Jr., D. S.; Goulet, P. J. G.; Pieczonka, N. P. W.; Oliveira Jr., O. N.; Aroca, R. F. *Langmuir* **2004**, *20*, 10273-10277.

(12)   Goulet, P. J. G.; Dos Santos, D. S., Jr.; Alvarez-Puebla, R. A.; Oliveira, O. N., Jr.; Aroca, R. F. *Langmuir* **2005**, *21*, 5576-5581.

(13)   Aroca, R. F.; Goulet, P. J. G.; Dos Santos, D. S., Jr.; Alvarez-Puebla, R. A.; Oliveira, O. N., Jr. *Anal. Chem.* **2005**, *77*, 378-382.

(14)   Goulet, P. J. G.; Pieczonka, N. P. W.; Aroca, R. F. In *New Approaches in Biomedical Spectroscopy*; Kneipp, K., Aroca, R. F., Kneipp, H., Wentrup-Byrne, E., Eds.; American Chemical Society: Washington, DC, in press.

(15)   Pieczonka, N. P. W.; Goulet, P. J. G.; Aroca, R. F. *J. Am. Chem. Soc.* **2006**, *128*, 12626-12627.

(16)   Goulet, P. J. G.; Aroca, R. F. *Can. J. Chem.* **2004**, *82*, 987-997.

(17)   Goulet, P. J. G.; Alvarez-Puebla, R.; Aroca, R. F. Trace Detection of an Environmental Pollutant by Surface-Enhanced Raman Scattering. In *Applications of Surface-Enhanced Raman Spectroscopy*; Farquharson, S., Ed.; CRC Press, in press.

(18)   Alvarez-Puebla, R. A.; Arceo, E.; Goulet, P. J. G.; Garrido, J. J.; Aroca, R. F. *J. Phys. Chem. B* **2005**, *109*, 3787-3792.

(19)   Goulet, P. J. G.; Pieczonka, N. P. W.; Aroca, R. F. *Anal. Chem.* **2003**, *75*, 1918-1923.

(20)   Goulet, P. J. G.; Pieczonka, N. P. W.; Aroca, R. F. *J. Raman Spectrosc.* **2005**, *36*, 574-580.

(21)   Goulet, P. J. G.; Aroca, R. F. submitted for publication.

(22)   Goulet, P. J. G.; Aroca, R. F. manuscript in preparation.

(23)   Constantino, C., J. L.; Lemma, T.; Antunes Patricia, A.; Goulet, P.; Aroca, R. *Appl. Spectrosc.* **2003**, *57*, 649-654.

Chapter 2

BACKGROUND

2.1 Introduction

In this chapter, a brief overview is given to the most fundamental concepts employed in the work of this thesis. In particular, Raman and resonance Raman scattering are introduced, with particular focus on how they arise and how their intensities are determined. Next, the surface-enhanced versions of these spectroscopies, SERS and SERRS, are discussed. A particular focus is given in this section to the nature of the electromagnetic enhancement mechanism that defines these phenomena. Surface-enhanced fluorescence is then briefly described and distinguished from SERS/SERRS. Finally, the Langmuir-Blodgett thin film fabrication technique is introduced.

2.2 Raman and Resonance Raman Scattering

When light is scattered by molecules it is usually done so elastically, and is referred to as Rayleigh scattering. However, it is also possible for molecules to inelastically scatter ca. 1 in every 10^7 photons. This weak inelastic scattering, now referred to as Raman scattering, was first predicted theoretically by Smekel in 1923,[1] and demonstrated experimentally, using filtered sunlight as a source of monochromatic light, in 1928 by C. V. Raman and K. S. Krishnan.[2] Because of the weakness of this effect, it was very difficult to employ in chemical analysis early on. However, since the advent of lasers and high sensitivity detectors, its use has skyrocketed. Much of this can be attributed to the fact that it provides complementary vibrational information to one of the most widely used analytical techniques, infrared absorption, with the benefit that it can more effectively probe molecules in aqueous environments.

9

In the process of Raman scattering,[3-6] an oscillating electric field of incident light (generally a laser) polarizes the electron cloud of a molecule producing a short-lived virtual state lying between the electronic ground state and the first electronic excited state. This induced dipole can then radiate scattered light. If it does not induce nuclear motion through energy transfer, then the emitted radiation will be Rayleigh scattering and have the same frequency as the incident light. However, if it induces vibrational motion, energy will be transferred either to or from the molecule, and the emitted radiation will be Raman scattering that is shifted in frequency from the incident light. These shifts, known as Raman shifts, are independent of the wavelength of excitation, correspond to the quantized energy differences between the vibrational states of the electronic ground state of the molecular system, and provide information about its normal vibrational modes.

In Figure 2.1, Rayleigh and Raman scattering processes are depicted using a simple energy level diagram. Raman scattering is divided into Stokes and anti-Stokes emission, with the former being shifted to lower energy and the latter being shifted to higher energy. Under normal conditions Stokes-shifted Raman scattering is favored over anti-Stokes, because the population of excited vibrational states is low. This is particularly true for high frequency vibrations. Because of this, Stokes-shifted Raman scattering is more intense and is most often reported. However, with elevated temperatures, where excited vibrational states are more heavily populated, the anti-Stokes/Stokes ratio increases, and this can be useful for determining sample temperatures. Rayleigh scattering, on the other hand, is far more probable than either of these Raman scattering processes, and it is usually necessary to filter it out experimentally. In Figure 2.2, the scattering spectrum of a hypothetical molecule is given

10

showing the general trend in relative intensities for these processes. Stokes and anti-stokes bands mirror each other in terms of Raman shift values, but not in terms of intensity because the population of higher excited vibrational states is of low probability at normal ambient temperatures.

Figure 2.1 Rayleigh and Raman scattering processes.

11
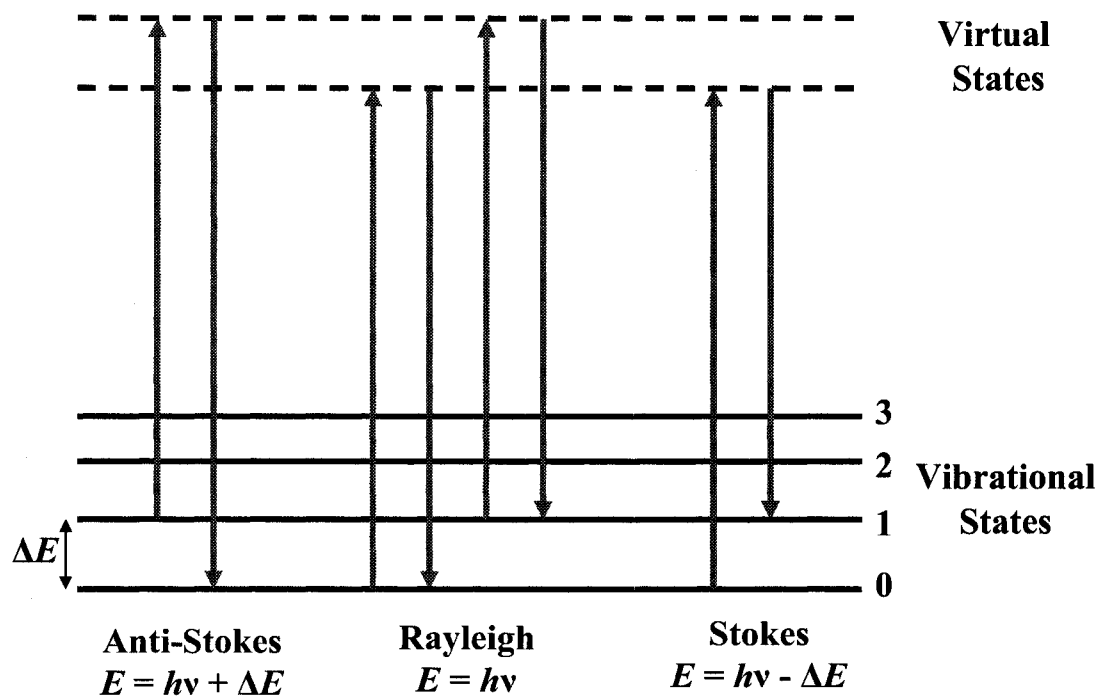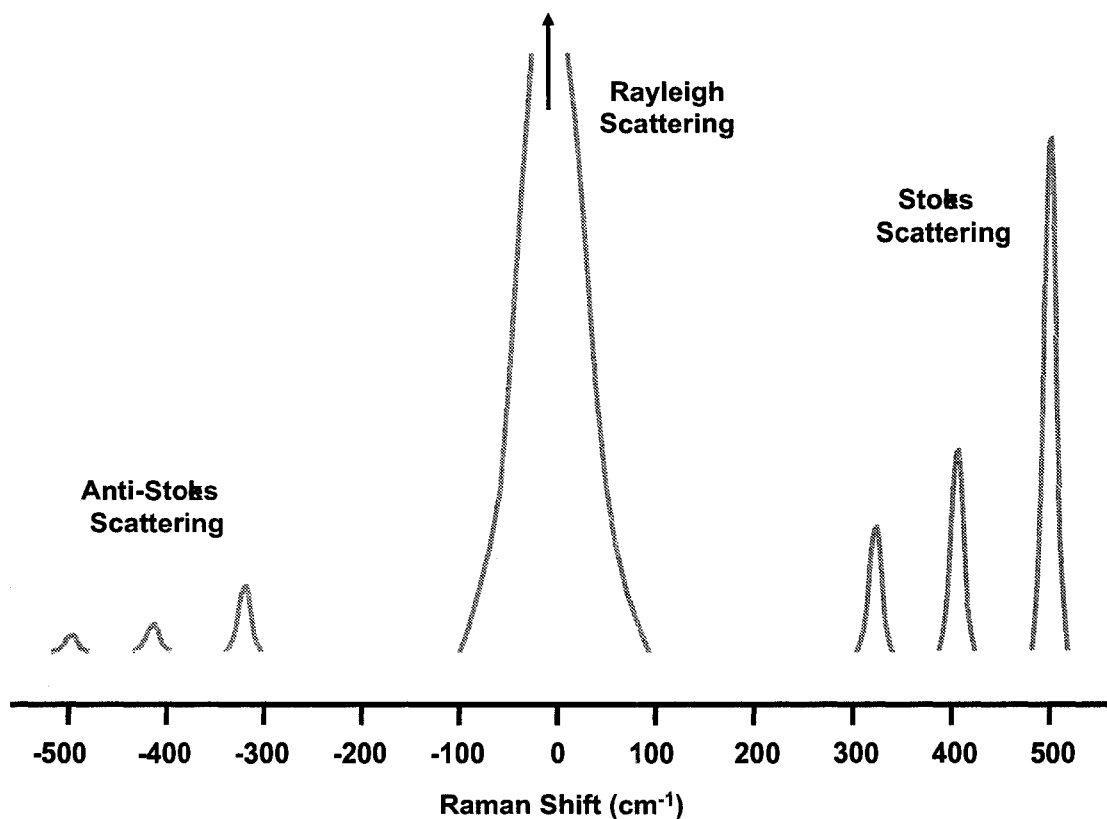
Figure 2.2 Scattering spectrum of a hypothetical molecule.

The strength of the induced dipole in a molecule, P, described above, is given by the expression

$$P = \alpha E$$

where α is polarizability and E is the incident electric field. The polarizability is a tensor that describes the volume and shape of the molecular electronic cloud, and gives information about its ability to be distorted (polarized) in an electric field:

$$\alpha = \begin{bmatrix} \alpha_{xx} & \alpha_{xy} & \alpha_{xz} \\ \alpha_{yx} & \alpha_{yy} & \alpha_{yz} \\ \alpha_{zx} & \alpha_{zy} & \alpha_{zz} \end{bmatrix}$$

12

Each of the components of this tensor can be expressed as a series expansion:[6]

$$\alpha = \alpha_0 + \left(\frac{\partial \alpha}{\partial q}\right)_0 q + \frac{1}{2}\left(\frac{\partial^2 \alpha}{\partial q^2}\right)_0 q^2 + \ldots$$

where α_0 is the value of the polarizability at the equilibrium geometry, and q is the change from equilibrium. The second term in this expression determines whether or not vibrational modes will be observed, and provides us with the fundamental selection rule for linear Raman:

$$\frac{\partial \alpha}{\partial q} \neq 0$$

This indicates that a change in the polarizability must be associated with a vibrational mode for it to be Raman active. This, of course, will be determined by the symmetry of the vibration.

The amplitude of the electric field of incident radiation can be described by:

$$E = E_0 \cos(\omega_0 t)$$

where ω_0 is the frequency of the incident laser. By substituting this, and our expression for polarizability, into our expression for induced dipole moment, ignoring higher order terms, we yield:

$$P = \alpha_0 E_0 \cos(\omega_0 t) + \left(\frac{\partial \alpha}{\partial q}\right)_0 q_0 \cos(\omega t) E_0 \cos(\omega_0 t) \ldots$$

where ω_0 is the frequency of the incident light and ω is the vibrational frequency of the molecule. This can then be re-expressed in the more convenient form:

13

$$P = \alpha_0 E_0 \cos(\omega_0 t) + \frac{1}{2}\alpha' q_0 E_0 \cos(\omega_0 - \omega)t + \frac{1}{2}\alpha' q_0 E_0 \cos(\omega_0 + \omega)t ...$$

The first term corresponds with Rayleigh scattering, while the latter two correspond to Stokes and anti-Stokes Raman scattering, respectively. It can be seen from this expression that both Rayleigh and first order Raman scattering processes are linear with laser intensity. However, in addition to laser intensity, Raman intensity will also be determined by the wavelength of the source. In ranges where the molecule does not have electronic absorptions, the intensity of Raman scattering increases with the fourth power of the source frequency. In cases where the molecule is absorbing at the excitation wavelength, however, resonance Raman scattering occurs.

Resonance Raman scattering (RRS)[7-9] spectra are recorded when laser excitation falls within the envelope of an electronic transition of a molecular system. Under these conditions, Raman intensities associated with the most symmetric vibrational modes of a molecular chromophore can be enhanced by a factor of up to 10^6, leading to great increases in the sensitivity of this technique over non-resonant Raman scattering as well as simplified spectra with fewer observable modes. RRS is most commonly applied to dye molecules using visible lasers,[10,11] but with UV lasers becoming more widely available, it is now more widely employed in the study of many large biological systems that have high energy electronic transitions.[12-14]

The process of resonance Raman scattering is shown in a simple energy level diagram in Figure 2.3. As can be seen in this figure, excitation is no longer into a virtual state but is directly into one of the excited states of the molecule. As a result of this, the intensities of RRS lines are determined by the properties of the excited state. In

14

particular, the coupling of the vibrational modes of a molecule to its electronic transition strongly depends on a dimensionless displacement between the ground and excited electronic potential energy surfaces along a normal coordinate. The most common case of RRS occurs when a component of the normal coordinate of a vibration is in the same direction that the molecule expands (polarizes) during an electronic excitation, leading to increases in polarizability and therefore to increases in induced dipole moment as well. This is the case for the large dye molecules that are employed in RRS measurements in this thesis. In fact, the ring stretching modes of extended pi systems benefit particularly from this form of RRS enhancement, referred to as Franck-Condon enhancement. The ring breathing modes of these molecules are along the same normal coordinates as the expansion of the molecule that occurs when π-π* electronic transitions are excited. Consequently, these modes are greatly enhanced, preferentially over the other vibrational modes of the molecule. Finally, overtones and combinations are forbidden in non-resonant Raman scattering, but are allowed transitions in resonance Raman scattering, and can often be easily observed, as will be discussed in Chapter 6.

15
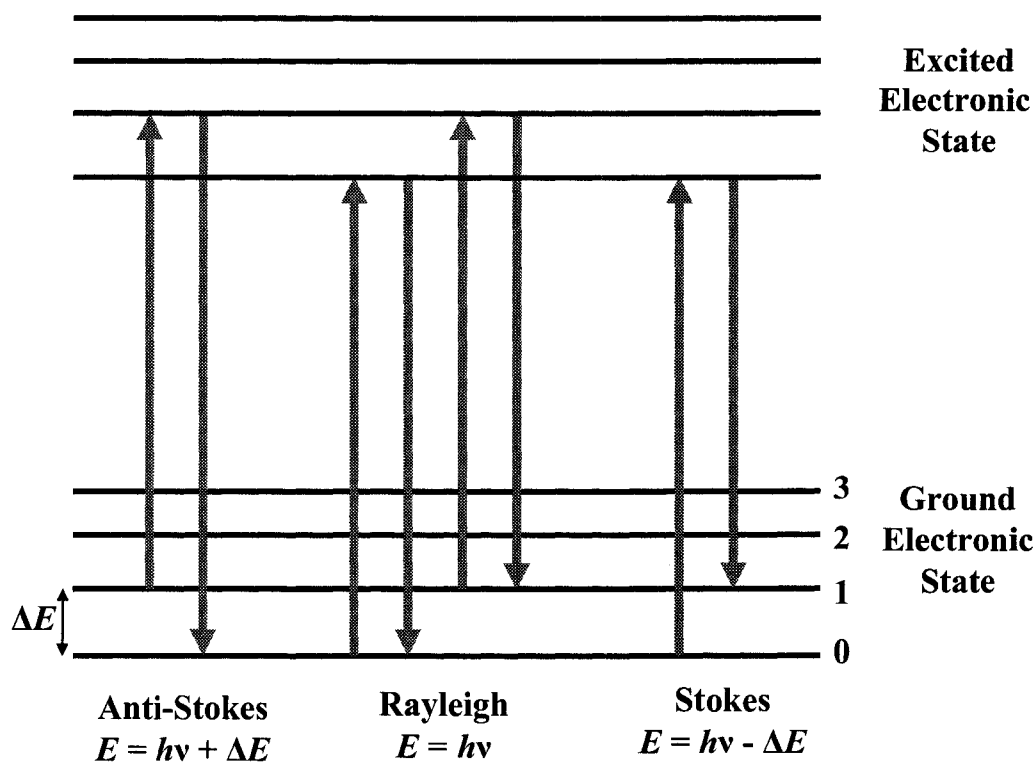
Figure 2.3 Resonance Rayleigh and Raman scattering.

2.3 Surface-Enhanced Raman and Resonance Raman Scattering

The closely related phenomena of surface-enhanced Raman scattering (SERS), and surface-enhanced resonance Raman scattering (SERRS)[5,15-21] have now been established as enormously important micro-analytical techniques due primarily to their high spatial resolution,[22] ultrasensitivity,[23] and high structural information content.[3,24,25] They are largely defined by the increased sensitivity they demonstrate over their relatively weak non-enhanced counterparts, Raman scattering (RS),[3] and resonance Raman scattering (RRS),[7] that have cross section values of only ca. 10^{-29} and 10^{-24} cm^2 per molecule, respectively. This increased sensitivity results from surface-enhancement that occurs when molecules are excited with electromagnetic radiation while at or near

16

the surface of appropriate enhancing metal nanoparticles and their aggregates, due to dramatically strengthened electromagnetic fields resulting from radiating localized surface plasmon resonances of the metal.[18,26-30] Average enhancement factors (EF) for ensemble SERS/SERRS measurements often range between ca. 10^3 and 10^6,[31-34] while those at so called hot spots, areas of very intense and highly localized EM fields,[35-39] have been reported to far exceed this, with some reports of values as high as 10^{14} and 10^{15}.[40-42] The exact magnitude of hot spot enhancement, however, remains a topic of much discussion. [43,44]

The first observation of strongly enhanced Raman signals was reported in 1974 by Fleischmann et al., and was attributed to an increase in the number of scattering molecules due to the increase in the roughness of the Ag electrode where they were measuring pyridine.[45] In 1977, however, it was discovered that this large increase in Raman intensity could not be explained on the basis of surface area increases alone. Jeanmaire and Van Duyne,[46] and Albrecht and Creighton,[47] demonstrated that the observed enhancement was in fact a result of a surface-enhancement process, and the term surface-enhanced Raman scattering, SERS, was coined. This significant scientific discovery led to a flurry of activity in the field of surface spectroscopy, and soon other surface-enhanced photoprocesses were recognized.[28,48]

In the late 1970s and early 1980s, a great deal of important work was done to determine the fundamental mechanisms at work in SERS/SERRS. Nearly all of the important aspects of the basic nature of the phenomenon were explained during this time,[27] although it is quite common for some authors to still write that "the nature of the enhancement in SERS is not well understood". Two basic mechanisms were set forth to

explain the enhancement of Raman and resonance Raman signals and these are referred to as the electromagnetic (EM)[26,49,50] and chemical enhancement[19,51-54] models. The former represents the main, defining feature of SERS/SERRS, while the latter is responsible for much of the complex surface behaviour that is observed and makes these effects very difficult to control.

Chemical enhancement is generally viewed as being able to provide enhancements of no more than ca. 10^2, and arises from several different first layer electronic effects that can alter the normal Raman scattering cross-section. For this mechanism to function there must be a direct interaction that allows electronic coupling of the molecule to the metal surface. These interactions could involve the formation of a new molecule-metal charge transfer electronic transition[51] or a dynamic charge transfer between the metal and the molecule.[19] The nature of the interactions that an adsorbate has with a metal surface can critically change what is observed in SERS/SERRS spectra. However, it is the dominant EM mechanism that ultimately provides the enhancement that makes it possible to observe these changes by providing enhancement factors many orders of magnitude larger.

Electromagnetic enhancement of Raman and resonance Raman scattering is fundamentally driven by the excitation of surface plasmon resonances (also commonly called dipole particle plasmon resonances to stress the importance of the dipolar modes over higher order modes) in metal nanoparticles and nanoaggregates. These resonances involve the collective oscillation of conduction electrons in the metal with the electric field of incident light, and provide the most effective enhancement for particles with diameters much smaller than the wavelength of the visible light used to excite them,

18

generally between 10 and 150 nm.[18] The resonant frequency of nanoparticle surface plasmons is determined by the dielectric constant of the metal, the dielectric constant of the medium, as well as the size, and shape of the particle, and can be tuned through variation of these properties.[55] Generally a simplified model is employed that assumes a spherical particle, and it is found that the resonance condition, and maximum field enhancement, is achieved when the real part of the dielectric function of the metal is equal to -2.[18,56] In the visible region, this condition is best satisfied by three coinage metals: Ag, Au, and Cu, and these metals are, not surprisingly, also by far the most widely used substrates for surface-enhanced spectroscopies.

When incident light is resonant with dipolar surface plasmon modes, they radiate coherently with the exciting field. This has the effect of concentrating enhanced electric fields around the surface of the nanoparticles. These enhanced fields extend beyond the surface of the nanoparticle, and therefore are able to enhance the RS and RRS of molecules not directly adsorbed on the surface. As a result, when molecules are sitting at or near the surface of these particles, their polarization is not induced by the incident field of the laser, but rather by the enhanced field in which they sit. This strengthens their induced dipole moment and therefore enhances their Raman scattering. Secondary enhancements of Raman-scattered fields, which may be slightly different, at the vibrational frequencies of the molecule, then take place according to the same mechanism that enhanced the incident light. In other words, the Raman-scattered fields induce collective oscillations in the nanoparticle at the Raman shifted frequencies and these radiate with huge intensity due to the large cross section of the nanoparticles. The result of this is that, at low Raman shift values, SERS intensities will be enhanced by a factor

19

proportional to the fourth power of the enhancement of the local incident field. Experimentally this is taken advantage of through dipolar coupling of closely spaced nanoparticles, producing even greater fields and therefore larger enhancement of Raman and resonance Raman scattering.

Many different SERS/SERRS substrates have been developed to date, employing a variety of physical and chemical methods, and producing a wide assortment of interesting architectures.[31,57-63] Some of these architectures include those produced by vacuum evaporation of metal,[64,65] electrochemical roughening of metal electrodes,[47,66] and lithographical techniques.[67,68] Essentially all substrates that produce strong enhancement of RS and RRS, involve electromagnetically coupled particles, either as dimers and larger aggregates, or as larger networks of interacting nanoparticles, generally in films. Both of these rely on short interparticle spacing for maximum enhancement. This is achieved at highly localized electromagnetic hot spots that provide the greatest enhancements of RS and RRS. In dimers and small aggregates, hot spots are thought to occur exclusively at the junctions of particles where there is the greatest constructive interference of electric fields.[69,70] In large networks of interacting particles, on the other hand, multi-particle dipole-dipole interactions lead to highly localized, excitation wavelength-dependent surface plasmon normal modes that are not strongly correlated with local particle geometries.[38,39,43] Hot spots of both of these types have now been employed by several groups to demonstrate detection and spectroscopic identification of analytes down to the single molecule level.[23,40-43,53,69-96]

20

2.4 Surface-Enhanced Fluorescence (SEF)

Surface-enhanced fluorescence arises from the electromagnetic interaction that occurs between fluorescent molecules and metal nanoparticles that have appropriate enhancing optical properties,[28,97-100] and has been described as the "weak cousin of the SERS effect",[18] owing to its rather tiny enhancement factors of generally less than ca. 100. The enhancement of SEF is fundamentally held back by its rather long lifetime in a way that RS and RRS are not. SEF can be viewed as a product of three different processes: enhanced emission, enhanced absorption, and radiationless transfer of energy to metallic surfaces, with the former two processes resulting from enhanced EM fields at the surface of plasmon sustaining metal nanoparticles.[101]

It is well known that SERS/SERRS is strengthened when adsorbates are placed directly on metal nanostructures. In surface-enhanced fluorescence (SEF), on the other hand, intensity is expected to exhibit a maximum enhancement at some distance of separation between the molecule and the surface. Energy transfer to the metal can take place during the finite lifetime of the excitation, and it is thus common to observe a reduction in luminescence when a fluorophore is placed directly on the surface of a metal (i.e. enhancement factor <1). The latter is explained by a direct energy transfer from the dipole to the planar surface, as shown in the classic work of Chance, Prock, and Silbey.[97] Dipolar energy transfer is proportional to d^3 (where d is the dipole-metal surface separation), and energy is dissipated into the phonon bath. The distance dependence of EM enhancement indicates that it decreases appreciably when d approaches the dimension of the metal particle, and SEF is thus a balance between the two opposing processes of surface-enhancement, and non-radiative energy loss to the metal surface.

21

Electromagnetic enhancement is a much slower decaying function of molecule-surface separation than that of surface quenching, and as a result of this, maximum fluorescence will occur at distances (d) that are intermediate between the maximum quenching ($d=0$) and "no effect" conditions.

2.5 Langmuir-Blodgett Monolayers

Langmuir-Blodgett (LB) films[102,103] are thin films composed of one or more monomolecular layers deposited onto solid substrates, and take their name from Irving Langmuir and Katherine Blodgett who did much of the pioneering work on them in the late 1930s.[104] These films are assembled at gas-liquid interfaces (most commonly the air-water interface) and then transferred by moving solid substrates vertically through them at the monolayer/air interface, as depicted in Figure 2.4. Most commonly LB monolayers are composed of amphiphilic organic molecules that orient themselves at a air-water interface in order to minimize free energy. However, an increasing diversity of materials are now being employed with this powerful thin film fabrication technique.[62,105,106] The LB technique has been widely, and successfully employed in the study of SERS/SERRS due to the high degree of control it offers for sample architectures.[107-111] At the same time, SERS/SERRS are well suited for the characterization of monolayers due to their very high sensitivity.[112,113]
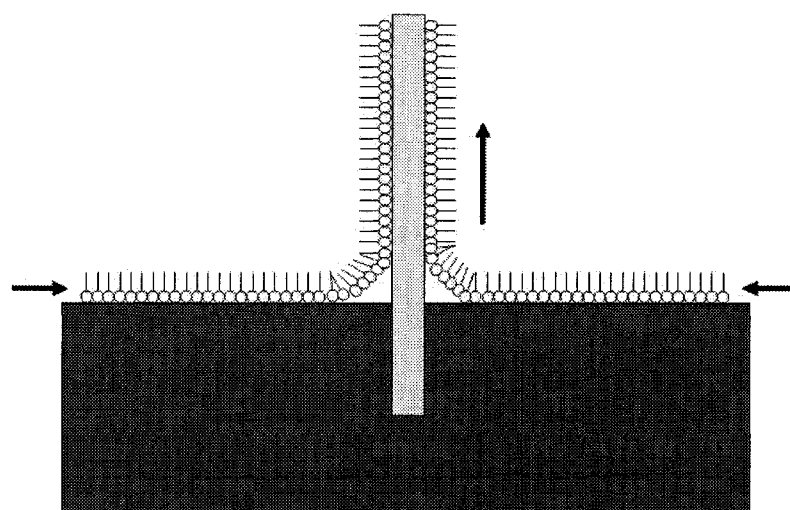
Figure 2.4 Depiction of Langmuir-Blodgett film transfer to solid substrate.

Classic monolayer-forming materials have two distinct ends; a hydrophilic head, and a hydrophobic tail. It is this that leads to molecular orientation on water surfaces. The hydrophilic head will be directed toward the water surface, while the hydrophobic end will be repelled by it. Common examples of such amphiphiles include stearic acid and arachidic acid. When solutions of molecules such as these are made in water-immiscible solvents and spread on a water subphase, they tend to spread out quickly to cover the available area. The solvent then evaporates off, and an oriented monolayer is formed on the surface of the water. Immediately after spreading, the distance between molecules is generally quite large and their interactions are limited. In this state, they can be regarded as forming a two-dimensional expanded phase, and will have very little effect on the surface tension of the subphase.[102] When a film is compressed on the liquid surface, however, it will undergo several phase transformations. These phase

23

transformations are similar in nature to the phase transitions between gases, liquids, and solids, and range from expanded to condensed phase as a function the molecule-molecule interactions on the surface. These transformations are monitored by measuring surface pressure, Π, as a function of the area per molecule in the film. Surface pressure is a measure of the surface tension reduction that occurs when monolayers are deposited onto liquid subphases, and is given by $\Pi = \gamma_0 - \gamma$, where γ_0 is the surface tension of the pure liquid, and γ is the surface tension of the liquid covered with the monolayer. Water is the most commonly used subphase, and has a maximum Π value of 72.8 mN m^{-1} at 20 °C.[102] Plots of surface pressure against molecular area are referred to as isotherms, as they are recorded at constant temperature. They provide a wealth of information about the behaviour of monolayer films, and are the basis for the determination of transfer conditions.[103]

In expanded phase, molecules in films exert very little force upon one another, and so surface pressure remains relatively low. As the film is compressed, the area per molecule drops causing an increase in the interactions between the molecules, and consequently an increase in surface pressure. At this stage, the molecules begin to organize themselves on the subphase. Upon further compression, condensed phases are reached, where molecules are tightly packed and oriented with their hydrophobic ends directed away from the water surface. If the film is compressed further, film collapse will occur and a drop in surface pressure will be observed.

When monolayers are transferred to solid substrates, surface pressure and temperature are monitored and controlled throughout. There are three types of LB film deposition, and the technique employed will depend on the type of molecule and the type

24

of substrate that is being used. The most commonly used vertical deposition is called Y-type deposition, and involves a monolayer being deposited on each traversal of the monolayer/air interface. This vertical type of deposition produces a head to head and tail to tail pattern on the substrate. When monolayers are transferred only on the downstroke, it is referred to as X-type deposition, while transfer on the upstroke only is referred to as Z-type deposition. The success of film transfer is generally monitored by the measurement of transfer ratios, τ. The transfer ratio for a depostion is given by $\tau = A_L/A_S$, where A_L is the decrease in the area occupied by the monolayer on the water surface, and A_S is the coated area of the solid substrate. Transfer ratios that vary significantly from unity indicate poor film homogeneity and transfer.

References

(1)   Smekal, A. *Naturwissenschaften* **1923**, *11*, 873-875.

(2)   Raman, C. V.; Krishnan, K. S. *Nature* **1928**, *121*, 501-502.

(3)   Long, D. A. *The Raman Effect: A Unified Treatment of the Theory of Raman Scattering by Molecules*; John Wiley & Sons, Ltd.: Chichester, UK, 2002.

(4)   McCreery, R. L. *Raman Spectroscopy for Chemical Analysis*; John Wiley & Sons, Ltd.: New York, 2000; Vol. 157.

(5)   Smith, E.; Dent, G. *Modern Raman Spectroscopy: A Practical Approach*; John Wiley & Sons, Ltd.: West Sussex, UK, 2005.

(6)   Aroca, R. F. *Surface-Enhanced Vibrational Spectroscopy*; John Wiley & Sons, Ltd.: Chichester, UK, 2006.

(7)   Shorygin, P. P.; Krushinskij, L. L. *J. Raman Spectrosc.* **1997**, *28*, 383-388.

(8)   Albrecht, M. G. *J. Chem. Phys.* **1961**, *34*, 1476-1484.

(9)   Myers, A. B. *J. Raman Spectrosc.* **1997**, *28*, 389-401.

(10)   Aroca, R. F.; Clavijo, R. E. *Spectrochim. Acta, Part A* **1991**, *47A*, 271-277.

(11)   Vosgroene, T.; Meixner, A. J. *ChemPhysChem* **2005**, *6*, 154-163.

(12)   Lednev, I. K.; Karnoup, A. S.; Sparrow, M. C.; Asher, S. A. *J. Am. Chem. Soc.* **1999**, *121*, 4076-4077.

(13)   Lednev, I. K.; Karnoup, A. S.; Sparrow, M. C.; Asher, S. A. *J. Am. Chem. Soc.* **2001**, *123*, 2388-2392.

(14)   Zhao, X.; Wang, D.; Spiro, T. G. *J. Am. Chem. Soc.* **1998**, *120*, 8517-8518.

(15)   Aroca, R. *Surface-Enhanced Vibrational Spectroscopy*; John Wiley & Sons Ltd: West Sussex, 2006.

(16)   *Surface-Enhanced Raman Scattering- Physics and Applications*; Kneipp, K.; Moskovits, M.; Kneipp, H., Eds.; Springer-Verlag: Berlin Heidelberg, 2006; Vol. 103.

(17)   *Surface Enhanced Raman Scattering*; Chang, R. K.; Furtak, T. E., Eds.; Plenum Press: New York, 1982.

(18)   Moskovits, M. *Rev. Mod. Phys.* **1985**, *57*, 783-826.

(19)   Otto, A.; Mrozek, I.; Grabhorn, H.; Akemann, W. *J. Phys.-Condens. Matter* **1992**, *4*, 1143-1212.

(20)   Vo-Dinh, T. *TrAC, Trends Anal. Chem.* **1998**, *17*, 557-582.

(21)   Metiu, H. *Prog. Surf. Sci.* **1984**, *17*, 153-320.

(22)   Deckert, V.; Zeisel, D.; Zenobi, R.; Vo-Dinh, T. *Anal. Chem.* **1998**, *70*, 2646-2650.

(23)   Kneipp, K.; Kneipp, H.; Itzkan, I.; Dasari, R. R.; Feld, M. S. *Chem. Rev.* **1999**, *99*, 2957-2976.

(24)   Aroca, R.; Rodriguez-Llorente, S. *J. Mol. Struct., Theochem* **1997**, *408-409*, 17-22.

(25)   Goulet, P. J. G.; Aroca, R. F. *Can. J. Chem.* **2004**, *82*, 987-997.

(26)   Schatz, G. C.; Van Duyne, R. P. Electromagnetic mechanism of surface-enhanced spectroscopy. In *Handbook of Vibrational Spectroscopy*; Chalmers, J. M., Griffiths, P. R., Eds.; John Wiley & Sons, Ltd.: Chichester, UK, 2002; Vol. 1; pp 759-774.

(27)   Moskovits, M. *J. Raman Spectrosc.* **2005**, *36*, 485-496.

(28)   Weitz, D. A.; Garoff, S.; Gersten, J. I.; Nitzan, A. *J. Chem. Phys.* **1983**, *78*, 5324-5338.

(29)   Sanchez-Gil, J. A.; Garcia-Ramos, J. V.; Mendez, E. R. *Optics Express [online computer file]* **2002**, *10*, 879-886.

(30)   Etchegoin, P.; Cohen, L. F.; Hartigan, H.; Brown, R. J. C.; Milton, M. J. T.; Gallop, J. C. *Chem. Phys. Lett.* **2004**, *383*, 577-583.

(31)   Pieczonka, N. P. W.; Goulet, P. J. G.; Aroca, R. F. *J. Am. Chem. Soc.* **2006**, *128*, 12626-12627.

(32)   Aroca, R. F.; Goulet, P. J. G.; Dos Santos, D. S., Jr.; Alvarez-Puebla, R. A.; Oliveira, O. N., Jr. *Anal. Chem.* **2005**, *77*, 378-382.

(33)   Alvarez-Puebla, R. A.; Arceo, E.; Goulet, P. J. G.; Garrido, J. J.; Aroca, R. F. *J. Phys. Chem. B* **2005**, *109*, 3787-3792.

(34)   dos Santos Jr., D. S.; Goulet, P. J. G.; Pieczonka, N. P. W.; Oliveira Jr., O. N.; Aroca, R. F. *Langmuir* **2004**, *20*, 10273-10277.

(35)   Shalaev, V. M. *Phys. Rep.* **1996**, *272*, 61-137.

(36)   Poliakov, E. Y.; Shalaev, V. M.; Markel, V. A.; Botet, R. *Opt. Lett.* **1996**, *21*, 1628-1630.

(37)   Zhang, P.; Haslett, T. L.; Douketis, C.; Moskovits, M. *Phys. Rev. B* **1998**, *57*, 15513-15518.

(38)   Stockman, M. I. *Phys. Rev. E* **1997**, *56*, 6494-6507.

(39)   Gresillon, S.; Aigouy, L.; Boccara, A. C.; Rivoal, J. C.; Quelin, X.; Desmarest, C.; Gadenne, P.; Shubin, V. A.; Sarychev, A. K.; Shalaev, V. M. *Phys. Rev. Lett.* **1999**, *82*, 4520-4523.

(40)   Kneipp, K.; Wang, Y.; Kneipp, H.; T. Perelman, L. T.; Itzkan, I. *Phys. Rev. Lett.* **1997**, *78*, 1667-1670.

(41)   Nie, S.; Emory, S. R. *Science* **1997**, *275*, 1102-1106.

(42)   Kneipp, K.; Kneipp, H.; Kartha, V. B.; Manoharan, R.; Deinum, G.; Itzkan, I.; Dasari, R. R.; Feld, M. S. *Phys. Rev. E* **1998**, *57*, R6281-R6284.

(43)   Moskovits, M.; Tay, L.-L.; Yang, J.; Haslett, T. SERS and the single molecule. In *Optical Properties of Nanostructured Random Media*; Shalaev, V. M., Ed.; Springer-Verlag: Berlin Heidelberg, 2002; Vol. 82; pp 215-226.

(44)   Otto, A. *J. Raman Spectrosc.* **2006**, *37*, 937-947.

(45)   Fleischmann, M.; Hendra, P. J.; McQuillan, A. J. *Chem. Phys. Lett.* **1974**, *26*, 163-166.

(46)   Jeanmaire, D. L.; Van Duyne, R. P. *Electroanal. Chem.* **1977**, *84*, 1-20.

(47)   Albrecht, M. G.; Creighton, J. A. *J. Am. Chem. Soc.* **1977**, *99*, 5215-5217.

(48)   Nitzan, A.; Brus, L. E. *Journal of Chemical Physics* **1981**, *75*, 2205-2214.

(49)   Moskovits, M. *J. Chem. Phys.* **1978**, *69*, 4159-4161.

(50)   Etchegoin, P.; Cohen, L. F.; Hartigan, H.; Brown, R. J. C.; Milton, M. J. T.; Gallop, J. C. *J. Chem. Phys.* **2003**, *119*, 5281-5289.

(51)   Kambhampati, P.; Child, C. M.; Foster, M. C.; Campion, A. *J. Chem. Phys.* **1998**, *108*, 5013-5026.

(52)   Otto, A. *Indian J. Phys. B* **2003**, *77B*, 63-73.

(53)   Otto, A. *Phys. Stat. Sol. (a)* **2001**, *188*, 1455-1470.

(54)   Otto, A. *J. Ram. Spectrosc.* **2005**, *36*, 497–509.

(55)   Kelly, K. L.; Coronado, E.; Zhao, L. L.; Schatz, G. C. *J. Phys. Chem. B* **2003**, *107*, 668-677.

(56)   Kerker, M.; Wang, D. S.; Chew, H. *App. Opt.* **1980**, *19*, 4159-4173.

(57)   Wu, Y.; Livneh, T.; Zhang, Y. X.; Cheng, G.; Wang, J.; Tang, J.; Moskovits, M.; Stucky, G. D. *Nano Lett.* **2004**, *4*, 2337-2342.

(58)   Green, M.; Liu, F. M. *J. Phys. Chem. B* **2003**, *107*, 13015-13021.

(59)   Chan, S.; Kwon, S.; Koo, T.-W.; Lee, L. P.; Berlin, A. A. *Adv. Mat.* **2003**, *15*, 1595-1598.

(60)   Bjerneld, E. J.; Svedberg, F.; Kaell, M. *Nano Lett.* **2003**, *3*, 593-596.

(61)   Freeman, R. G.; Grabar, K. C.; Allison, K. J.; Bright, R. M.; Davis, J. A.; Guthrie, A. P.; Hommer, M. B.; Jackson, M. A.; Smith, P. C.; et al. *Science* **1995**, *267*, 1629-1631.

(62)   Tao, A.; Kim, F.; Hess, C.; Goldberger, J.; He, R.; Sun, Y.; Xia, Y.; Yang, P. *Nano Lett.* **2003**, *3*, 1229-1233.

(63)   Brolo, A.; Arctander, E.; Gordon, R.; Leathem, B.; Kavanagh, K. L. *Nano Lett.* **2004**, *4*, 2015-2018.

(64)   Semin, D. J.; Rowlen, K. L. *Anal. Chem.* **1994**, *66*, 4324-4331.

(65)   Schlegel, V. L.; Cotton, T. M. *Anal. Chem.* **1991**, *63*, 241-247.

(66)   Ren, B.; Lin, X.-F.; Yang, Z.-L.; Liu, G.-K.; Aroca, R. F.; Mao, B. W.; Tian, Z. Q. *J. Am. Chem. Soc.* **2003**, *125*, 9598-9599.

(67)   Liao, P. F.; Bergman, J. G.; Chemla, D. S.; Wokaun, A.; Melngailis, J.; Hawryluk, A. M.; Economou, N. P. *Chem. Phys. Lett.* **1981**, *82*, 355-359.

(68)   Haynes, C. L.; McFarland, A. D.; Smith, M. T.; Hulteen, J. C.; Van Duyne, R. P. *J. Phys. Chem. B.* **2002**, *106*, 1898-1902.

(69)   Michaels, A. M.; Jiang, J.; Brus, L. *J. Phys. Chem. B* **2000**, *104*, 11965-11971.

(70)   Le Ru, E. C.; Meyer, M.; Etchegoin, P. *J. Phys. Chem. B* **2006**, *110*, 1944-1948.

(71)   Michaels, A. M.; Nirmal, M.; Brus, L. E. *J. Am. Chem. Soc.* **1999**, *121*, 9932-9939.

(72)   Otto, A. *J. Raman Spectrosc.* **2002**, *33*, 593-598.

(73)   Meixner, A. J.; Vosgrone, T.; Sackrow, M. *J. Lumin.* **2001**, *94&95*, 147-152.

(74)   Maruyama, Y.; Ishikawa, M.; Futamata, M. *Chem. Lett.* **2001**, 834-835.

(75)   Krug, J. T., II; Wang, G. D.; Emory, S. R.; Nie, S. *J. Am. Chem. Soc.* **1999**, *121*, 9208-9214.

(76)   Mandal, M.; Kundu, S.; Ghosh, S. K.; Jana, N. R.; Panigrahi, M.; Pal, T. *Curr. Sci.* **2004**, *86*, 556-559.

(77)   Bizzarri, A. R.; Cannistraro, S. *Appl. Spectrosc.* **2002**, *56*, 1531-1537.

(78)   Bizzarri, A. R.; Cannistraro, S. *Chem. Phys.* **2003**, *290*, 297-306.

(79)   Bjerneld, E. J.; Foeldes-Papp, Z.; Kaell, M.; Rigler, R. *J. Phys. Chem. B* **2002**, *106*, 1213-1218.

(80)   Bosnick, K. A.; Jiang, J.; Brus, L. E. *J. Phys. Chem. B* **2002**, *106*, 8096-8099.

(81)   Constantino, C. J. L.; Lemma, T.; Antunes, P. A.; Aroca, R. *Anal. Chem.* **2001**, *73*, 3674-3678.

(82)   Constantino, C. J. L.; Lemma, T.; Antunes, P. A.; Aroca, R. *Spectrochim. Acta, Part A* **2002**, *58A*, 403-409.

(83)   Constantino, C., J. L.; Lemma, T.; Antunes Patricia, A.; Goulet, P.; Aroca, R. *Appl. Spectrosc.* **2003**, *57*, 649-654.

(84)   Eggeling, C.; Schaffer, J.; Seidel, C. A. M.; Korte, J.; Brehm, G.; Schneider, S.; Schrof, W. *J. Phys. Chem. A* **2001**, *105*, 3673-3679.

(85)   Etchegoin, P.; Liem, H.; Maher, R. C.; Cohen, L. F.; Brown, R. J. C.; Hartigan, H.; Milton, M. J. T.; Gallop, J. C. *Chem. Phys. Lett.* **2002**, *366*, 115-121.

(86)   Futamata, M.; Maruyama, Y.; Ishikawa, M. *J. Phys. Chem. B* **2004**, *108*, 13119-13127.

(87)   Futamata, M.; Maruyama, Y.; Ishikawa, M. *Vib. Spectrosc.* **2004**, *35*, 121-129.

(88)   Goulet, P. J. G.; Pieczonka, N. P. W.; Aroca, R. F. *Anal. Chem.* **2003**, *75*, 1918-1923.

(89)   Goulet, P. J. G.; Pieczonka, N. P. W.; Aroca, R. F. *Can. J. Anal. Sci. Spect.* **2003**, *48*, 146-152.

(90)   Goulet, P. J. G.; Pieczonka, N. P. W.; Aroca, R. F. *J. Raman Spectrosc.* **2005**, *36*, 574-580.

(91)   Ishikawa, M.; Maruyama, Y.; Ye, J. Y.; Futamata, M. *J. Lumin.* **2002**, *98*, 81-89.

(92)   Itoh, T.; Hashimoto, K.; Ikehata, A.; Ozaki, Y. *Chem. Phys. Lett.* **2004**, *389*, 225-229.

31

(93)   Kneipp, K. *Single Molecules* **2001**, *2*, 291-292.

(94)   Kneipp, K.; Kneipp, H.; Dasari, R. R.; Feld, M. S. *Indian J. Phys. B* **2003**, *77B*, 39-47.

(95)   Kneipp, K.; Kneipp, H.; Deinum, G.; Itzkan, I.; Dasari, R. R.; Feld, M. S. *Appl. Spectrosc.* **1998**, *52*, 175-178.

(96)   Lemma, T.; Aroca, R. F. *J. Raman Spectrosc.* **2002**, *33*, 197-201.

(97)   Chance, R. R.; Prock, A.; Silbey, R. *Adv. Chem. Phys.* **1978**, *37*, 1-65.

(98)   *Radiative Decay Engineering*; Lakowicz, J. R.; Geddes, C. D., Eds.; Springer: New York, 2005; Vol. 8.

(99)   Lakowicz, J. R.; Geddes, C. D.; Gryczynski, I.; Malicka, J.; Gryczynski, Z.; Aslan, K.; Lukomska, J.; Matveeva, E.; Zhang, J.; Badugu, R.; Huang, J. *Journal of Fluorescence* **2004**, *14*, 425-441.

(100)   Wokaun, A.; Lutz, H.-P.; King, A. P.; Wild, U. P.; Ernst, R. R. *J. Chem. Phys.* **1983**, *79*, 509-513.

(101)   Goulet, P. J. G.; Aroca, R. F. Surface-enhancement of fluorescence near noble metal nanostructures. In *Topics in Fluorescence Spectroscopy: Radiative Decay Engineering*; Lakowics, J. R., Geddes, C. D., Eds.; Springer Science + Business Media, Inc.: New York, 2005; Vol. 8; pp 223-247.

(102)   Petty, M. C. *Langmuir-Blodgett Films. An Introduction*; Cambridge University Press: Cambridge, 1996.

(103)   *Langmuir-Blodgett Films*; Roberts, G., Ed.; Plenum Press: New York, 1990.

(104)   Blodgett, K. B. *J. Am. Chem. Soc.* **1935**, *57*, 1007-1022.

(105)   Kumaki, J.; Hashimoto, T. *J. Am. Chem. Soc.* **1998**, *120*, 423-424.

(106)   Kim, F.; Kwan, S.; Akana, J.; Yang, P. *J. Am. Chem. Soc.* **2001**, *123*, 4360-4361.

(107)   Aroca, R.; Battisti, D. *Langmuir* **1990**, *6*, 250-254.

(108)   Aroca, R.; Guhathakurta-Ghosh, U. *J. Am. Chem. Soc.* **1989**, *111*, 7681-7683.

(109)   Uphaus, R. A.; Cotton, T. M.; Mobius, D. *Thin Solid Films* **1985**, *132*, 173-184.

(110)   Chen, Y. J.; Carter, G. M.; Tripathy, S. K. *Solid State Comm.* **1985**, *54*, 19-22.

(111)   Aroca, R.; Jennings, C.; Kovacs, G. J.; Loutfy, R. O.; Vincett, P. S. *J. Phys. Chem.* **1985**, *898*, 4051-4054.

(112)   Aroca, R.; Johnson, E.; Maiti, A. K. *Appl. Spectrosc.* **1995**, *49*, 466-471.

(113)   Aroca, R. F.; Constantino, C. J. L. *Langmuir* **2000**, *16*, 5425-5429.

33

Chapter 3

EXPERIMENTAL AND COMPUTATIONAL DETAILS

34

In this chapter, divided into three main sections on samples, characterization, and computation, the details of the experimental and computational work of this thesis are introduced.

3.1 Samples

3.1.1 Reagents

Unless otherwise noted, all reagents were obtained from Sigma-Aldrich and used without further purification. These include: hydrochlorauric acid, rhodamine 6G (R6G), trisodium citrate, silver nitrate, DAB-Am-4 polypropylenimine tetraamine dendrimer (G1 Dab-Am), DAB-Am-64 polypropylenimine tetrahexacontaamine dendrimer (G5 Dab-Am), polystyrene sulfonate (PSS), 2-naphthalenethiol (2-NAT), poly(vinylpyrrolidone) (PVP) (monomer-based calculation MW= 55 000) , arachidic acid (AA), ultrapure Ag shot, ultrapure Au shot, avidin (from egg white), 3-amino-propyltriethoxysilane, fluorescein, biotin 3-sulfo-N-hydroxysuccinimide ester, salicylic acid (SAL), sodium salicylate, potassium bromide, and 1-naphthylamine (1-NA).

Biotin-4-fluorescein (B4F), 5-(aminomethyl)fluorescein (5-AF), and octadecylrhodamine B (R18), on the other hand, were obtained from Molecular Probes, and used without further purification. Chitosan, obtained from shrimp chitin (an N-acetylglucosamine polymer), was provided by Cyrbe do Brasil Corporation. It had an average molecular weight of 500 000 g/mol, as determined by viscometry, and a 75% degree of deacetylation, as obtained from ^{1}H NMR measurements.[1] The perylene derivatives used in this work, bis(benzylimido)-perylene (BBIP PTCD), n-pentylimidobenzimidazo-perylene (pentyl PTCD), bis(benzimidazo)-perylene (azo PTCD), n-pentyl-5-salicylimido perylene (salPTCD), and N,N'-bis(neopentyl)-3,4,9,10-

35

perylenebis(dicarboximide) (BNPTCD) were synthesized and purified at the Xerox Research Centre of Canada, and used as provided.

3.1.2 Evaporated Metal Films

In this work, nanostructured Ag and mixed Ag/Au films, as well as Ag mirror films, were produced on clean, pre-heated glass substrates by vacuum evaporation. These metal films were prepared at pressures of 10^{-6} to 10^{-7} Torr (1 Torr = 133.322 Pa) using a Balzers BSV 080 glow discharge evaporation unit, where mass thickness was monitored with an XTC Inficon quartz crystal oscillator. All depositions were carried out at evaporation rates of ca. 0.5 Å/s. Nanostructured metal films, with appropriate nanoparticle size distributions for surface-enhanced spectroscopy, were prepared with mass thickness values of 10 nm or less, while Ag mirror films for reflection absorption infrared spectroscopy (RAIRS) were prepared with a mass thickness of 100 nm. All Ag films of 6, 9, and 10 nm mass thickness were deposited onto substrates at 200 °C, except the 10 nm Ag films utilized for single-molecule bi-analyte studies of salPTCD and R18 (Chapter 6), which were deposited onto substrates at 150 °C. Mixed 10 nm Ag/Au nanostuctured films, were prepared by two separate evaporation procedures. First, Ag films of 5 nm mass thickness were deposited onto glass microscope slides at a temperature of 200 °C. After the slides cooled slowly (1-2 h) to room temperature, the vacuum was broken and the evaporation source was changed. The chamber was then returned to high vacuum and 5 nm films of Au were deposited on top of the Ag at 200 °C. In all cases, substrates were maintained at elevated temperature for 1 h following film deposition. The vacuum evaporation system utilized in this work is shown in Figure 3.1.

36
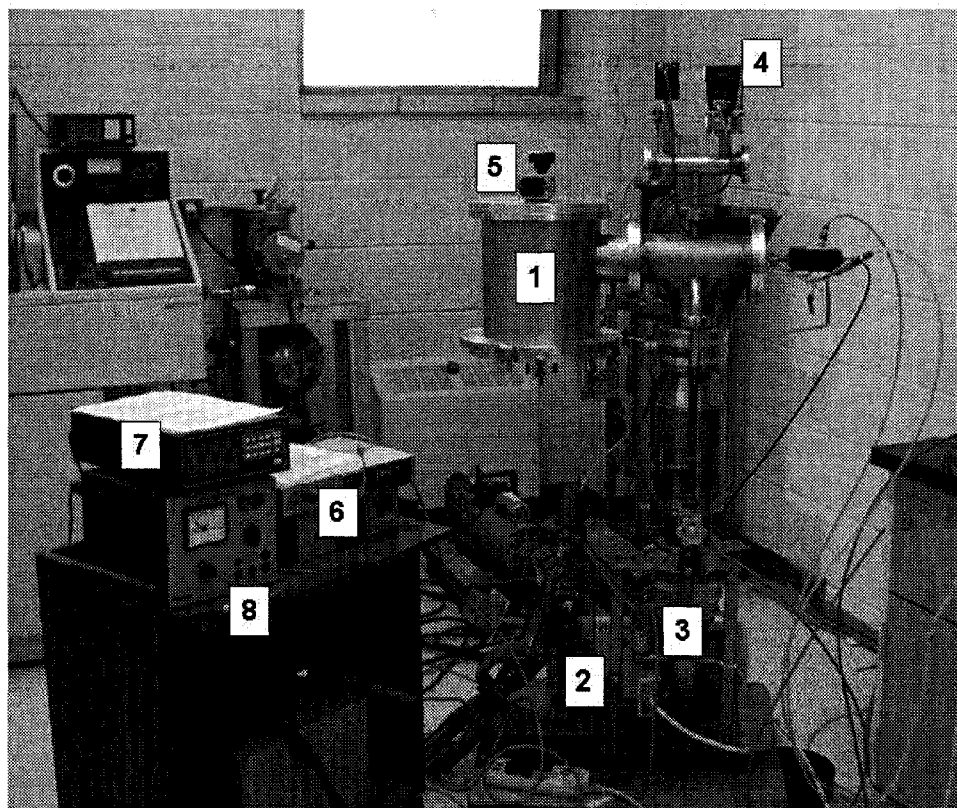
Figure 3.1 Vacuum evaporation system. System includes: **1.** evaporation chamber; **2.** mechanical vacuum pump; **3.** diffusion pump; **4.** pressure gauge; **5.** heater; **6.** pressure monitor and temperature monitor/controller; **7.** quartz crystal oscillator monitor; and **8.** evaporation controller.

3.1.3 Colloidal Solutions of Silver

In this work, colloidal solutions of silver nanoparticles were produced for use as substrates for SERS/SERRS. They were used in the fabrication of layer-by-layer film substrates, or simply as solutions, and were produced according to the common citrate reduction method of Lee and Meisel.[2] Briefly, 90 mg of $AgNO_3$ was dissolved into 500 mL of water, and the solution was brought to a slow boil under reflux. Then, 10 mL of a

37

1% solution of trisodium citrate was added, and the solution was left to boil for the next hour under constant stirring before the heat was removed and the solution was allowed to slowly come to room temperature.

In the fabrication of dendrimer/Ag nanosphere LbL films (Chapter 4), colloidal Ag solutions were utilized as produced, while in the fabrication of avidin/Ag nanoparticle films (Chapter 4), they were diluted by a factor of 2. In work on 1-naphtylamine (Chapter 5), Ag colloidal solutions were diluted by a factor of 2 for SERS measurements to reduce their particle concentration and the effect of aggregation. As well, aliquots of 50 mL were adjusted to target pH values, ranging between 2 and 9, by additions of 2 M solutions of NaOH or HNO_3. For zeta potential measurements, colloidal solutions were diluted by a factor of 10.

3.1.4 Langmuir-Blodgett Monolayers

In this work, mixed Langmuir-Blodgett monolayers of arachidic acid (AA) doped with dye molecules were deposited, at a variety of concentrations, onto several substrates, including: glass, nanostructured Ag films (6 and 10 nm), nanostructured Ag/Au films (10 nm), and Ag nanowire LbL films. These monolayers were prepared at the air-water interface of the Lauda Langmuir film balance shown in Figure 3.2. The subphase employed in their preparation was pure water (18.2 MΩ cm) maintained at a constant temperature of 15 °C, and containing small amounts of $CdCl_2$ (2.5 $\times$ 10^{-4} M). Solid substrates were immersed into this subphase using a Lauda Film Lift FL-1 electronically controlled dipping device. The mixed solutions of AA and the dyes were then spread, and 5-10 minutes was allowed for solvent evaporation. Film compression was then begun with a single barrier moving at 3.5 cm/min. Corresponding with the condensed

38

phase of the Langmuir film, a constant surface pressure setting of 25 mN/m was employed. The Langmuir film was transferred to a solid support, maintaining constant surface pressure and using the Lauda Film Lift FL-1 (3 mm/min), after allowing a complete stabilization of the monolayer on the subphase. All film depositions gave transfer ratios near unity, and were performed by Z-deposition.
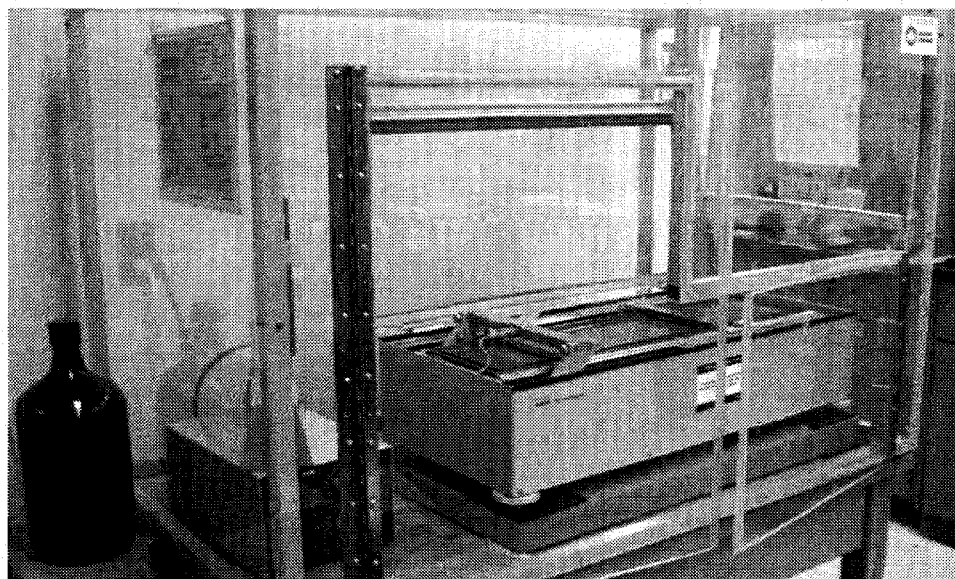
Figure 3.2 Lauda Langmuir film balance.

The spreading solutions used for Langmuir-Blodgett film preparation were composed of dye molecules and arachidic acid, a fatty acid that forms well characterized and stable LB films. All solutions were prepared using spectrophotometric grade dichloromethane as the solvent. However, due to limited solubility, it was necessary to add minimal quantities of spectrophotometric grade trifluoroacetic acid (TFA) to initial stock solutions (10^{-4} M) of all PTCD derivatives in order to fully dissolve their powders.

Also, the tiny concentration of dye molecules within many of these spreading solutions necessitated extremely clean glassware.

In work where AA monolayers embedded with BBIP PTCD were deposited onto 10 nm mixed Ag/Au nanostuctured films and glass (Chapter 4), as well as work where monolayers of AA and BBIP PTCD, pentyl PTCD, or azo PTCD were deposited onto 6 nm Ag nanostructured films and glass (Chapter 6), solutions were prepared so as to achieve, on average, 2×10^6, 100, 10, and 1 dye molecule(s) per square micron, the probing area of the Raman microscope. In experiments where AA-BNPTCD monolayers were deposited onto Ag and mixed Ag/Au nanoparticle films (Chapter 6), concentrated films (10:1 AA:BNPTCD) and single-molecule films (1 BNPTCD molecule/μm^2) were prepared. In experiments where AA-salPTCD monolayers were deposited onto glass or 6 nm Ag nanoparticle films (Chapter 6), spreading solutions were prepared with AA:salPTCD concentration ratios of 10:1, 10^2:1, 10^3:1, 10^4:1, and 10^5:1, and were ultimately diluted down so as to achieve, on average, a single salPTCD molecule per square micron of surface area. Arachidic acid monolayers containing salPTCD were also deposited onto Ag nanowire/G5 Dab-Am dendrimer LbL substrates at an AA:salPTCD concentration ratio of 10:1 (Chapter 4). Finally, in work where arachidic acid Langmuir-Blodgett monolayers containing R18, salPTCD, and one-to-one binary mixtures of the two, were deposited onto 10 nm Ag nanostructured films (Chapter 6), spreading solutions were prepared so as to achieve 4×10^4, 10^3, 10^2, 10, or 1 molecule(s) of either dye (R18 or salPTCD), or of each dye (for binary mixtures), within the 1 μm^2 scattering area being probed.

40

3.1.5 Gold Nanoparticle Embedded, Self-Sustained Chitosan Films[a]

In this work, self-sustained, Au nanoparticle embedded chitosan films were fabricated for use as substrates for SERS/SERRS. The purification of chitosan was carried out by dissolving it twice in a 1% aqueous acetic acid solution, filtering it, precipitating it using a 1% aqueous sodium hydroxide solution, and finally, washing it extensively with deionized water until neutral pH was reached. To prepare Au nanoparticle solutions, a 1% chitosan solution in 1% aqueous acetic acid was mixed in a one-to-one ratio with a 0.0625% solution of $HAuCl_4$ in a round-bottom flask equipped with a reflux condenser. The solutions were then heated to a temperature of 85 °C, and this was maintained for 5 h under constant stirring. To prepare thin films from these solutions, they were allowed to cool under ambient conditions then measured volumes were cast onto clean glass substrates where they were left to dry for 24 h. Thin, self-sustained, stable, and flexible nanocomposite films were produced by neutralizing these films with a 1% aqueous solution of NaOH, rinsing them with deionized water until neutral pH was reached, then removing them from the glass substrates. For SERS test measurements, Au nanoparticle embedded chitosan films were dipped into rhodamine 6G (R6G) solutions with concentrations ranging between 10^{-4} and 10^{-6} M.

---

[a] All Au nanoparticle embedded chitosan films were prepared by D. S. dos Santos, Jr. with direction and feedback, based on characterization and application, from P. J. G. Goulet and N. P. W. Pieczonka.

41

3.1.6 Dendrimer/Ag Nanosphere Layer-by-Layer Films[b]

In this work, layer-by-layer films composed of dendrimers and Ag nanoparticles were fabricated for use as substrates for SERS/SERRS. All glassware was thoroughly cleaned using water, aqua regia, then deionized water. Glass microscope slides were cleaned prior to LbL film deposition employing Kern's method.[3] Colloidal silver solutions were obtained by citrate reduction of $AgNO_3$ according to the method proposed by Lee and Meisel[2] and used as synthesized. Solutions of generation 5 DAB-Am-64 polypropylenimine tetrahexacontaamine dendrimer (G5 DAB-Am), 0.045 g/L, generation 1 DAB-Am-4 polypropylenimine tetraamine dendrimer (G1 DAB-Am), 0.100 and 0.045 g/L, and polystyrene sulfonate (PSS), 1.0 g/L, in Milli-Q water (18.2 MΩ cm), were also prepared and used in the fabrication of the LbL multilayer films. All films were prepared by immersing clean glass substrates into dendrimer solutions for 10 minutes, rinsing them with Milli-Q water, drying them with nitrogen gas, and then immersing them into solutions containing silver nanospheres for 2 hours. Upon completion of these steps, the films were rinsed and dried, and could be then be used for the possible deposition of further dendrimer/nanosphere bilayers. The colloidal silver solution was changed after each deposition. In the cases where PSS spacer layers were substituted for Ag nanosphere layers, they were deposited using the same procedures, but with immersion times of only 10 minutes for each layer. All samples for SERS measurements were prepared by casting 30 μL of a 10^{-3} M ethanol solution of 2-naphthalenethiol (2-NAT) onto the LbL film substrates and allowing the solvent to evaporate.

---

[b] All dendrimer/Ag nanosphere films were prepared by D. S. dos Santos, Jr. with direction and feedback, based on characterization and application, from P. J. G. Goulet and R. A. Alvarez-Puebla.

42

3.1.7 Silver Nanowire Layer-by-Layer Films[c]

Silver nanowire syntheses were carried out employing the polyol process according to the method of Sun et al.[4] and Tao et al.[4] All glassware was thoroughly cleaned using water, aqua regia, and then deionized water. In a round-bottom flask, with magnetic stirring and reflux, a 25 mL 0.36 M solution of poly(vinylpyrrolidone) (PVP) was prepared in anhydrous ethylene glycol and heated to 160 °C. A 12 mL 0.12 M solution of silver nitrate in ethylene glycol, at room temperature, was then added dropwise into the hot PVP solution at a rate of 0.625 mL/min. Heating and stirring were kept constant during this step. After the addition of the reactants, the solution was kept stirring for 30 min at the same temperature. The solution was then cooled to room temperature, diluted (10x) with acetone, and then centrifuged three times at 2 krpm for 20 min. The precipitate was dispersed into a volume of ethyl alcohol equivalent to three times the volume of acetone in the preceding step, and sonicated for 4 min. This dispersion was centrifuged (1.7 krpm, for 20 min) twice. The final precipitate was then suspended in 15 mL of ethyl alcohol and sonicated for 10 min before LbL film preparation. Glass microscope slides were cleaned employing Kern's method[3] before LbL deposition. To prepare the LbL films, substrates were immersed into a 0.1 g/L aqueous solution of G5 DAB-Am dendrimer, for 10 min, followed by rinsing with deionized water, drying with nitrogen gas, immersion in a Ag nanowire solution for 3 h, and finally drying with nitrogen gas.

For most SERS/SERRS measurements, 10 μL drops (with 8 mm diameters when dry) of dilute rhodamine 6G (R6G), and 2-naphthalenethiol (2-NAT) solutions, of

---

[c] All dendrimer/Ag nanowire films were prepared by D. S. dos Santos, Jr. with direction and feedback, based on characterization and application, from P. J. G. Goulet and R. A. Alvarez-Puebla.

43

varying concentrations, were cast onto the Ag nanowire/G5 DAB-Am dendrimer LbL substrates. However, 10:1 mixed monolayers of arachidic acid and n-pentyl-5-salicylimidoperylene (salPTCD) were also transferred to the LbL substrates using the Langmuir-Blodgett technique, for detection of the enhanced Raman signals of the dye.

3.1.8 Avidin/Ag Nanoparticle Layer-by-Layer Films

In this work, LbL films composed of the glycoprotein avidin and colloidal Ag nanoparticles were produced for use as chemically selective substrates for SERS/SERRS. Colloidal Ag solutions were prepared by citrate reduction of $AgNO_3$,[2] and diluted by a factor of 2 before use. All avidin, R6G, fluorescein, B4F, 5-AF, and biotin solutions were prepared in 10 mM phosphate buffered saline (PBS) at pH 7.5. The in situ biotinylation of 5-AF was carried out by mixing it with biotin 3-sulfo-N-hydroxysuccinimide ester in a 1:1 molar ratio in PBS solution (pH 7.5) at room temperature, to produce a solution 10^{-4} M in each. The reaction was allowed 30 min to reach completion.

Prior to film fabrication, all glass microscope slides were cleaned and silanized. They were washed in detergent and deionized water, immersed in 20% H_2SO_4, rinsed again in deionized water, and dried. Next, they were immersed into pure acetone for 5 min, immersed into a 2% acetone solution of 3-amino-propyltriethoxysilane for 5 min, and then rinsed thoroughly with water and dried. All LbL films were prepared by immersing these clean, silanized slides into colloidal Ag solution for 30 min, rinsing them with water, drying them with air, then immersing them into a 50 μg/mL avidin solution in PBS for 30 min. Upon removal, these films were again rinsed and dried, then

44

re-immersed into colloidal Ag solution. Through these alternating deposition steps, films were built up until they were composed of up to 14 bilayers.

All SERS/SERRS measurements of R6G were recorded from dried 5 μL drops of 10^{-5} M solution (with ~ 5 mm diameters when dry) cast onto avidin/Ag nanoparticle LbL substrates. All other SERRS spectra were recorded from these films after immersion for 30 min into fluorescein, 5-AF, B4F, and biotinylated 5-AF solutions with concentrations ranging from 10^{-4} to 10^{-7} M. After removal from these solutions, films were thoroughly rinsed with deionized water and dried before measurement.

3.1.9 Salicylate-Silver Complex

The silver salt of salicylate was prepared in this work according to the methods described by Alvarez-Ros et al.[5] Briefly, equal volumes of a 0.1 M aqueous solution of sodium salicylate and a 0.1 M aqueous solution of $AgNO_3$ were mixed. After mixing the metal complex was produced as a precipitate. It was then filtered, washed in triplicate with distilled water, and dried at 80°C before storage in a dessicator.

3.1.10 1-Naphthylamine-Silver Complex

For comparison with SERS spectra, a silver-1-NA coordination complex was produced in this work by mixing 10 mL of a 0.1 M 1-NA ethanolic solution with 5 mL of a 0.1 M $AgNO_3$ aqueous solution, or by adding excess solid $AgNO_3$ to a 0.1 M 1-NA solution in $CHCl_3$ and agitating. To gain information about amino proton interactions, both 1-NA and its silver complex, were studied by ^1H NMR (Bruker DPX 300 MHz) using $CDCl_3$ as a solvent.

3.2 Characterization

3.2.1 UV-visible Absorption

In this work, all UV-visible absorption spectra were collected using a Cary 50 UV-visible spectrometer, including those of evaporated metallic nanostructured films, colloidal metal nanoparticle solutions, nanocomposite films, LbL films, and molecular solutions. This instrument is shown in Figure 3.3.
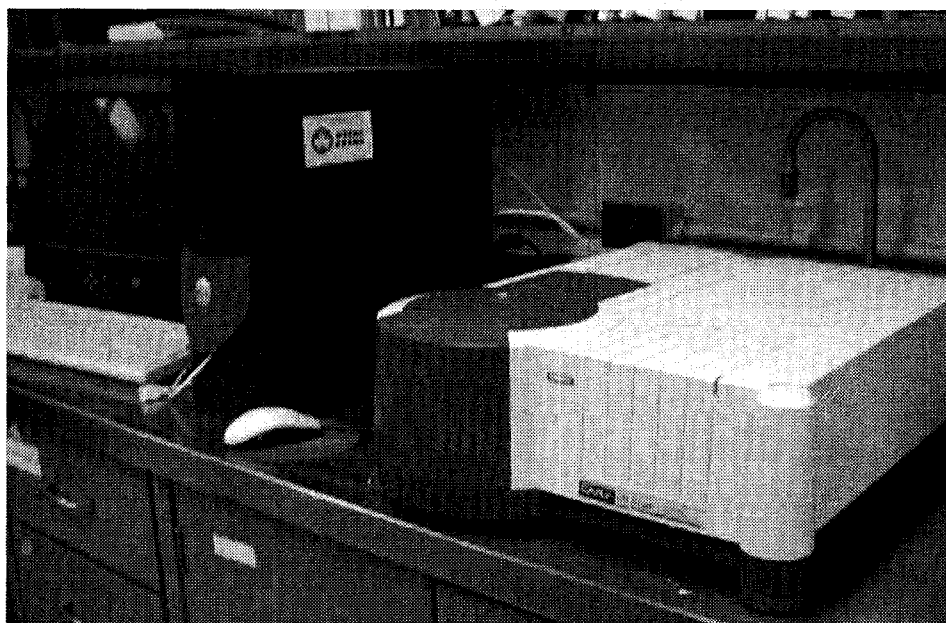
Figure 3.3 Cary 50 UV-visible spectrometer.

3.2.2 Atomic Force Microscopy (AFM)

All atomic force microscopy (AFM) measurements were performed using a Digital Instruments NanoScope IV operating in tapping mode with a n+-silicon tip (NSC 14 model, Ultrasharp) at a resonant frequency of ca. 300 kHz, and this instrument is shown in Figure 3.4. Images were collected with high resolution (256 or 512 lines per

46

scan) at scan rates of 0.5 to 1.0 Hz. Topographical, error, and phase images were all used for analysis of the surface morphology of the films, and data were collected under ambient conditions. Each scan was duplicated to ensure that any features observed were reproducible.
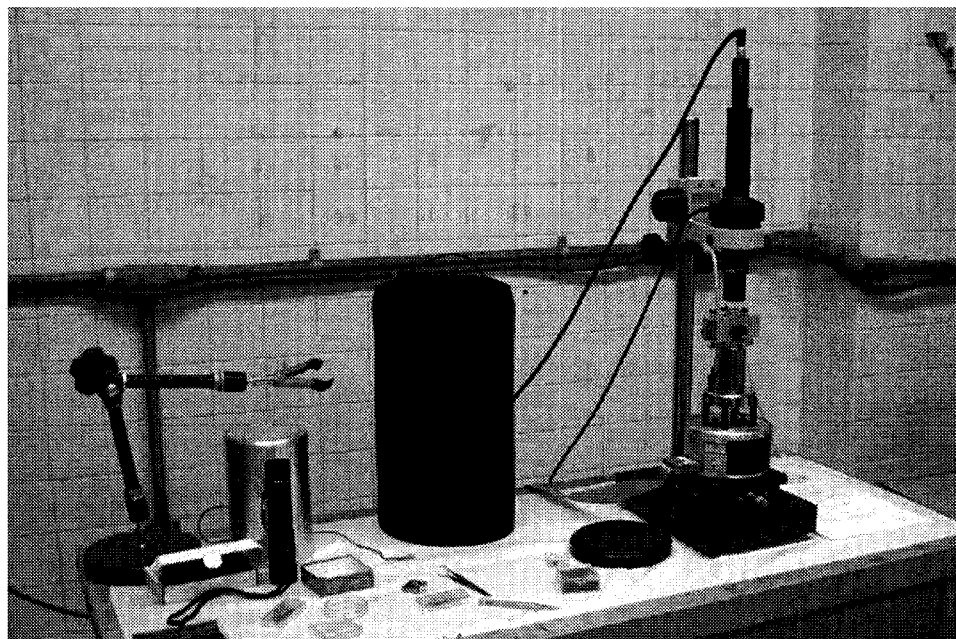
Figure 3.4 Digital Instruments NanoScope IV.

3.2.3 Transmission Electron Microscopy (TEM)[d]

All transmission electron microscopy (TEM) images were obtained employing a Philips CM20 scanning transmission electron microscope operating with a 120kV accelerating voltage.

---

[d] All transmission electron microscopy (TEM) samples were sent out for analysis at McMaster University in Hamilton, Ontario.

3.2.4 X-ray Photoelectron Spectroscopy (XPS)[e]

All x-ray photoelectron spectroscopy (XPS) samples were analysed using a Kratos Axis Ultra X-ray photoelectron spectrometer with a take off angle of 90°, a probe depth of 10 nm, and a sample area of 160 × 700 microns.

3.2.5 Infrared Absorption (IR)

All infrared absorption measurements were recorded with a Bruker Equinox 55 Fourier transform infrared (FTIR) spectrometer, equipped with a microscope, and employing a nitrogen-cooled mercury cadmium telluride (MCT) detector. This instrument is shown in Figure 3.5. All spectra were recorded with 4 cm^{-1} resolution. In work on nanocomposites of chitosan and Au nanoparticles, spectra were recorded directly from self-sustained films in transmission mode. In work on the adsorption of salicylate on Ag, attenuated total reflection (ATR) IR spectra of pure salicylic acid were obtained directly from the powder using an ATR accessory from Pike Technologies. IR spectra of silver salicylate were recorded from the powder dispersed in KBr pellets. SEIRA measurements were collected in transmission mode from a Ge substrate coated with a vacuum evaporated 10 nm Ag nanostructured film dipped into 10^{-3} and 10^{-4} M solutions of salicylic acid in spectrophotometric grade acetone. The slides were allowed to remain several minutes in the salicylic acid solution before removal and drying. RAIRS spectra were collected from a thin salicylic acid film on a 100 nm mass thickness Ag mirror with the Harrick Auto Seagull variable-angle reflectance accessory. Measurements were made with p-polarized light at an angle of incidence of 80° to the surface normal.

---

[e] All x-ray photoelectron spectroscopy (XPS) samples were sent out for analysis at Surface Science Western in London, Ontario.

48
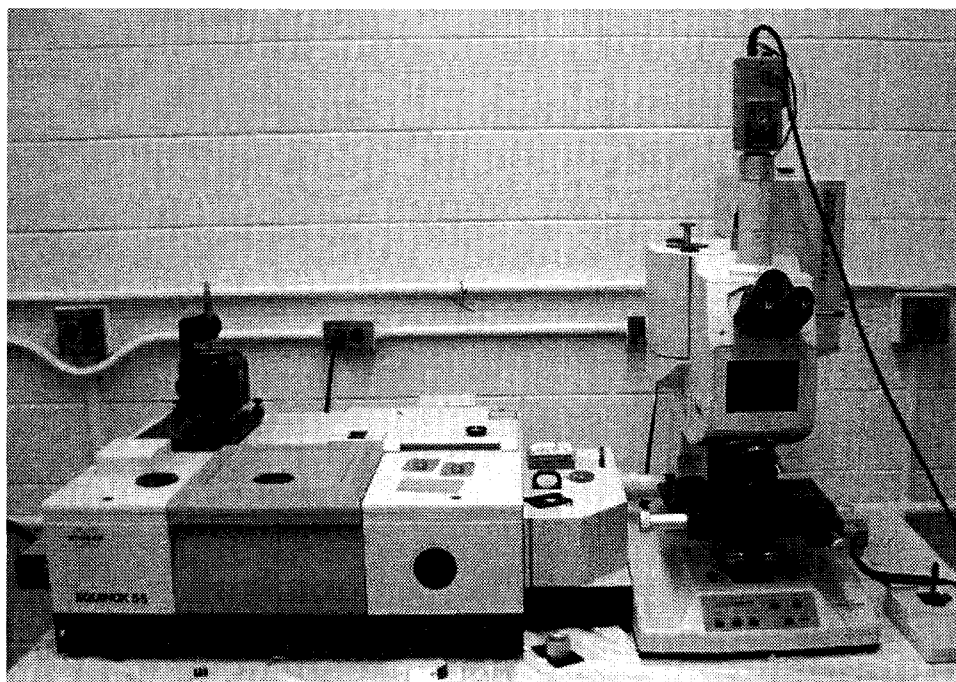
Figure 3.5 Bruker Equinox 55 Fourier transform infrared (FTIR) spectrometer.

3.2.6 Raman Microscopy

In this work, all Raman scattering experiments were conducted employing micro-Raman Renishaw 2000 and InVia systems, and these are shown in Figures 3.6 and 3.7, respectively. These instruments are equipped with Peltier cooled CCD detectors (-70°C), Leica microscopes, 1200 and 1800 g/mm gratings, and a computer controlled 3-axis encoded (XYZ) motorized stage, with a minimum step of 0.1 μm. Laser excitation lines at 442, 488, 514, 633, and 785 nm, ranging through the visible to the infrared region of the electromagnetic spectrum, were used to record Raman measurements. Single point, spatial mapping, and solution measurements were all recorded using a backscattering geometry with 4 cm^{-1} spectral resolution. All single point and mapping spectra excited with visible and infrared radiation were recorded using a 50x objective, with a numerical

49

aperture of 0.75, providing a scattering area of ca. 1 μm^2, except the SERS measurements of 2-NAT on dendrimer/Ag nanoparticle LbL films, which were recorded using a 785 nm laser directed through a 5x objective, and focused to an area of ca. 10 μm^2. For SERS/SERRS measurements, particularly at the low concentrations, laser powers were kept extremely low (typically < 20 μW) at the sample to prevent damage to the highly photoreactive metal surfaces employed. For solution and powder measurements, however, laser powers of up to ca. 5 mW were often employed without photoinduced sample changes being observed. All solution spectra were recorded using a microscope mounted macro-sampling kit that redirects the objective by 90°, allowing upright vials to be illuminated from the side. This attachment is shown in Figure 3.8. All SERRS mapping experiments were carried out using the rastering of a computer controlled XYZ motorized stage, with a step of 1 μm, where a single 1 s accumulation was recorded at each spot. This strategy served to facilitate the fast and easy collection of large amounts of data, while also minimizing sample laser exposure times, and thus sample photodegradation, allowing slightly increased laser powers to be used.

50
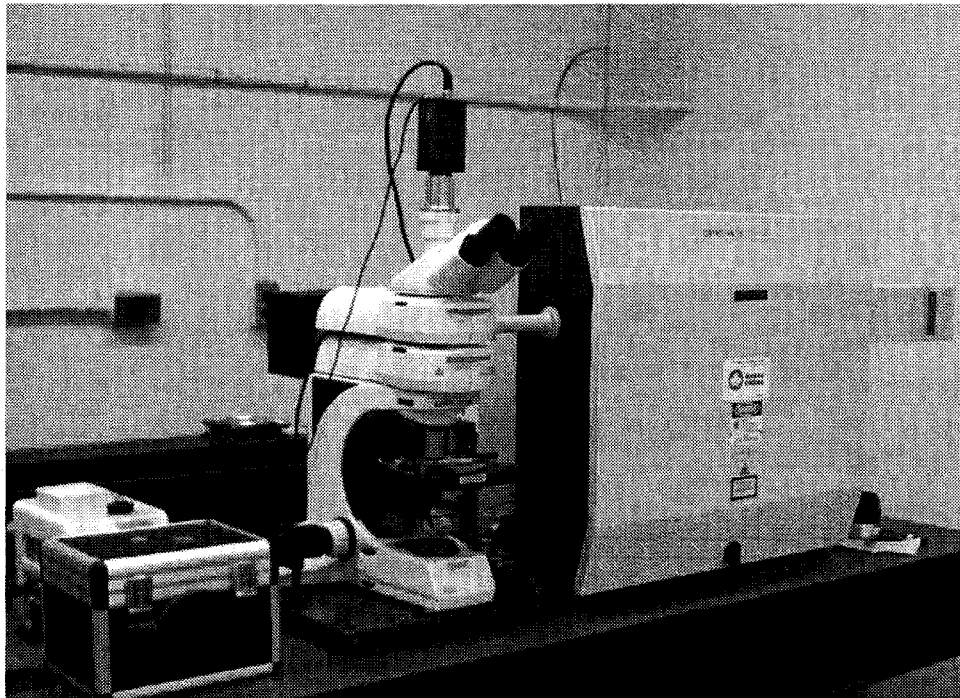
Figure 3.6 Renishaw 2000 micro-Raman system.
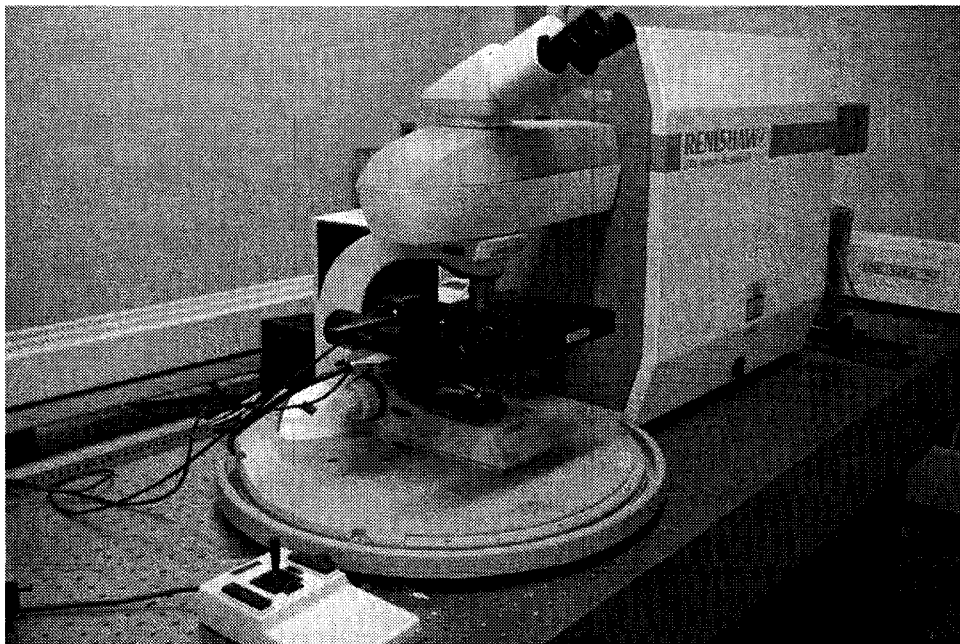
Figure 3.7 Renishaw InVia micro-Raman system.

51

Figure 3.8 Renishaw 90° macro-sampling attachment and sample holder.

3.2.7 Fluorescence Spectroscopy

As with all the Raman measurements of this work, all fluorescence and surface-enhanced fluorescence (SEF) spectra were recorded using the Renishaw 2000 and InVia systems. Measurements from monolayers deposited onto solid glass (fluorescence) and metal nanoparticle films (SEF) were recorded using a 50x objective, while all solution spectra were acquired employing a macro-sampling objective focusing the laser into solutions within quartz cuvettes. Laser powers were kept low for SEF measurements to prevent sample damage, and for high concentration solution measurements to prevent detector saturation.

3.2.8 Photon Correlation Spectroscopy[f]

Zeta potential values were determined by injecting 10 mL aliquots of 10× diluted colloidal metal suspensions into a Malvern Zetasizer HS3000 photon correlation

---

[f] All photon correlation spectroscopy reported here was carried out by R. A. Alvarez-Puebla at the Universidad Publica de Navarra in Pamplona, Spain.

52

spectrometer with an applied voltage of 100 V, and a 5-cm quartz cell.[6] To ensure reproducibility, 2 sub-samples were studied, and three measurements were co-added for each.

3.2.9 Scanning Electron Microscopy (SEM)[g]

All scanning election microscopy (SEM) was performed using a Hitachi S-4500 Field Emission Scanning Electron Microscope.

3.3 Computation

3.3.1 Salicylic Acid and Silver-Salicylate Complexes

All reported calculations of salicylic acid and silver-salicylate complexes were performed using the Gaussian 98 suite of programs[7] and employed Becke's three-parameter functional[8] including the correlational functional of Lee, Yang, and Parr[9] (B3LYP). To calculate an optimized structure and vibrational spectra for salicylic acid, the 6-311+G(d,p) basis set was employed using tight convergence criteria. This basis set was deemed to be a reasonable compromise between accuracy and computational expense for this molecule. The optimized structures and vibrational spectra of the two Ag–salicylate complexes were computed using the Lanl2DZ basis set[10,11], also employing tight convergence criteria. GaussView for Windows was used to view all computed results, and an in-house program was used to artificially apply a 5 cm^{-1} bandwidth to all peaks in the presented calculated Raman and IR spectra. Raman frequencies were not scaled, as scaling factors are not available for the basis sets used in this study. It is expected, however, that an appropriate scaling factor for the 6-311+G(d,p) basis set would be close to unity for the B3LYP functional. As a general rule, neglecting scaling

---

[g] All scanning election microscopy (SEM) samples were sent out for analysis at Surface Science Western in London, Ontario.

results in an overestimation of harmonic frequencies,[12] and so, this must be considered when reviewing the results for the two calculated silver complexes. In calculations of the Ag1 complex, the molecule was fixed in the x–y plane to simplify the application of surface selection rules in the spectral interpretation.

3.3.2 1-Naphthylamine

An optimized structure and Raman spectrum for 1-NA were calculated using density functional theory (DFT) methods at the B3LYP 6–311G(d,p) level of theory[8,9] utilizing the Gaussian '03 suite of programs[13] and tight convergence criteria.

References

(1)   Signini, R.; Campana, S. P. *Polym. Bull.* **1999**, *42*, 159-166.

(2)   Lee, P. C.; Meisel, D. *J. Phys. Chem.* **1982**, *86*, 3391-3395.

(3)   Kern, W. *Semicond. Int.* **1984**, *94*, 94-98.

(4)   Sun, Y. G.; Gates, B.; Mayers, B.; Xia, Y. N. *Nano Letters* **2002**, *2*, 165-168.

(5)   Alvarez-Ros, M. C.; Sanchez-Cortes, S.; García-Ramos, J. V. *Spectrochim. Acta, Part A* **2000**, *56A*, 2471-2477.

(6)   Alvarez-Puebla, R. A.; Arceo, E.; Goulet, P. J. G.; Garrido, J. J.; Aroca, R. F. *J. Phys. Chem. B* **2005**, *109*, 3787-3792.

(7)   Frisch, M. J.; Trucks, G. W.; Schlegel, H. B.; Scuseria, G. E.; Robb, M. A.; Cheeseman, J. R.; Zakrzewski, V. G.; Montgomery, J., J. A. ; Stratmann, R. E.; Burant, J. C.; Dapprich, S.; Millam, J. M.; Daniels, A. D.; Kudin, K. N.; Strain, M. C.; Farkas, O.; Tomasi, J.; Barone, V.; Cossi, M.; Cammi, R.; Mennucci, B.; Pomelli, C.; Adamo, C.; Clifford, S.; Ochterski, J.; Petersson, G. A.; Ayala, P. Y.; Cui, Q.; Morokuma, K.;

Malick, D. K.; Rabuck, A. D.; Raghavachari, K.; Foresman, J. B.; Cioslowski, J.; Ortiz, J. V.; Stefanov, B. B.; Liu, G.; Liashenko, A.; Piskorz, P.; Komaromi, I.; Gomperts, R.; Martin, R. L.; Fox, D. J.; Keith, T.; Al-Laham, M. A.; Peng, C. Y.; Nanayakkara, A.; Gonzalez, C.; Challacombe, M.; Gill, P. M. W.; Johnson, B.; Chen, W.; Wong, M. W.; Andres, J. L.; Gonzalez, C.; Head-Gordon, M.; Replogle, E. S.; Pople, J. A. Gaussian 98, Revision A.3; Gaussian Inc.: Pittsburgh, PA, 1998.

(8)   Becke, A. D. *J. Chem. Phys.* **1993**, *98*, 5648-5652.

(9)   Lee, C.; Yang, W.; Parr, R. G. *Phys. Rev. B* **1988**, *37*, 785-789.

(10)   Hay, P. J.; Wadt, W. R. *J. Chem. Phys.* **1985**, *82*, 299-310.

(11)   Dunning, T. H.; Hay, P. J. In *Methods of Electronic Structure Theory*; Schaefer, H. F., Ed.; Plenum Press: New York, 1977; Vol. 2.

(12)   Scott, A. P.; Radom, L. *J. Phys. Chem.* **1996**, *100*, 16502-16513.

(13)   Frisch, M. J.; Trucks, G. W.; Schlegel, H. B.; Scuseria, G. E.; Robb, M. A.; Cheeseman, J. R.; Zakrzewski, V. G.; Montgomery, J. J. A.; Stratmann, R. E.; Burant, J. C.; Dapprich, S.; Millam, J. M.; Daniels, A. D.; Kudin, K. N.; Strain, M. C.; Farkas, O.; Tomasi, J.; Barone, V.; Cossi, M.; Cammi, R.; Mennucci, B.; Pomelli, C.; Adamo, C.; Clifford, S.; Ochterski, J.; Petersson, G. A.; Ayala, P. Y.; Cui, Q.; Morokuma, K.; Malick, D. K.; Rabuck, A. D.; Raghavachari, K.; Foresman, J. B.; Cioslowski, J.; Ortiz, J. V.; Stefanov, B. B.; Liu, G.; Liashenko, A.; Piskorz, P.; Komaromi, I.; Gomperts, R.; Martin, R. L.; Fox, D. J.; Keith, T.; Al-Laham, M. A.; Peng, C. Y.; Nanayakkara, A.; Gonzalez, C.; Challacombe, M.; Gill, P. M. W.; Johnson, B.; Chen, W.; Wong, M. W.; Andres, J. L.; Gonzalez, C.; Head-Gordon, M.; Replogle, E. S.; Pople, J. A. Gaussian 03, Revision A.2; Gaussian, Inc.: Pittsburgh PA, 2003.

Chapter 4

FABRICATION, CHARACTERIZATION, AND APPLICATION OF NEW

SUBSTRATES FOR SURFACE-ENHANCED RAMAN AND RESONANCE

RAMAN SCATTERING

56

4.1 SERS/SERRS Substrate Development

The development of substrates for the enhancement of Raman and resonance Raman signals remains one of the most critical challenges facing SERS/SERRS research today.[1,2] One of the fundamental reasons for this is that these phenomena are intrinsically determined by the interaction between molecular and metallic nanoparticle systems. Because molecular systems are numerous and diverse, substrates for SERS/SERRS may also need to be numerous and diverse for the value of effect to be fully exploited for analytical purposes. Substrates could be designed to be complementary to different classes of molecular analytes so as to mimic the kind of strong complementarity that exists, as an example, in insect/flower systems due to their co-evolution. Furthermore, in addition to the variety that exists in molecular analytes, there is also a large variety of different uses that will be proposed for these techniques, and it is likely that many of these will also require rational design of unique substrates. Indeed, several important drivers are behind the push for new and innovative substrates for SERS/SERRS, and these include: improved enhancement and the manufacture of electromagnetic hot spots for single-molecule detection, chemical selectivity, functionality, biocompatibility and environmental sustainability, broadened and tunable enhancement regions, improved physical properties, incorporation of different metallic nanoparticles, lower cost, easier fabrication, water insolubility, and others. Of course, the pursuit of improved substrates for enhanced spectroscopy is in fact fundamental research in nanoscience, and therefore it also has major implications in a large variety of distant and not-so-distant fields.

In this chapter, the fabrication, characterization, and application as SERS/SERRS substrates, of several new and unique thin films, are discussed. All of this work was

57

carried out with the goal of improved detection of analytes; however, many of the other factors behind the push for new SERS/SERRS substrates were addressed. The new SERS/SERRS substrates developed in this work include: mixed Ag/Au evaporated nanoparticle films; self-sustained, Au nanoparticle embedded chitosan films; dendrimer/Ag nanosphere LbL films; dendrimer/Ag nanowire LbL films; and finally avidin/Ag nanoparticle LbL films. These substrates were characterized using a variety of techniques including: UV-visible surface plasmon absorption spectroscopy, X-ray photoelectron spectroscopy, atomic force microscopy, transmission electron microscopy, and infrared absorption. They were demonstrated to be excellent substrates for SERS/SERRS measurements, demonstrating significant enhancement capability and many other valuable characteristics.

4.2 Mixed Ag/Au Vacuum Evaporated Nanostructured Films[a]

4.2.1 Introduction

As was noted in Section 4.1, the development of nanostructured substrates capable of enhancing Raman and resonance Raman signals of single molecules, to the point of detection, is of great interest, and continues to be pursued widely.[3-5] Central to this work, is the generation of electromagnetic hot spots, areas of highly localized electromagnetic fields, at the laser excitation energies being employed.[6] Clusters of colloidal Ag and Au have now been shown by several groups to be capable of providing enhancement that makes single-molecule SERS/SERRS spectroscopy possible.[7-19] As well, Aroca et al. have demonstrated that single-molecule SERRS can be detected from

---

[a] The work of this section was done in close collaboration with N. P. W. Pieczonka. With the exception of Langmuir-Blodgett film fabrication, all aspects of this work benefited from his valuable contributions.

58

perylene derivatives embedded within Langmuir-Blodgett monolayers deposited onto evaporated, nanostructured Ag films.[20-22]

In this section, the introduction of a new substrate for application toward single-molecule LB SERRS is discussed.[23] This substrate was prepared by evaporating Ag then Au onto glass substrates, at elevated temperatures, to produce mixed Ag/Au nanostructured thin films. It was then characterized by UV-visible surface plasmon absorption spectroscopy, atomic force microscopy, and X-ray photoelectron spectroscopy, and employed as a substrate for SERRS of a perylene molecule, BBIP PTCD, in LB monolayers, down to the single-molecule level. It takes advantage of the enhancing properties of the two most commonly used metals for enhanced spectroscopy, and provides surfaces that are less reactive, and therefore, cleaner spectrally, than pure silver nanostructured films.[24] It also opens a new range of possibilities for tuning the surface plasmon absorption of evaporated metal SERS substrates to make them functional at a wide variety of readily available laser lines. This work was the first where mixed Ag/Au evaporated films were employed for single molecule SERRS detection, and saw the introduction of a new molecule to the short list of molecules for which SM SERRS detection had been demonstrated.

4.2.2 Characterization of Mixed Ag/Au Films

In Figure 4.1, the surface plasmon absorption spectrum of a 10 nm mixed Ag/Au film (5nm Ag + 5 nm Au) is shown. Due to the presence of the Au in the film, its surface plasmon is shifted to lower energy than a pure evaporated Ag film, and shows a broad absorption band with a maximum at ca. 697 nm. The breadth of this band, spanning the entire visible and tailing into the infrared, indicates that the film is composed of a broad

distribution of particle sizes, and shapes. It also suggests that in the film there is a high degree of particle-particle interaction. The large width of this band allows for a wide range of possible excitation frequencies that will fall within the plasmon envelope of the substrate. It also makes it possible to couple a large range of molecular absorptions to the surface plasmon, fulfilling the double resonance condition of SERRS, and increasing the number of potential SERRS active analytes that can be studied.
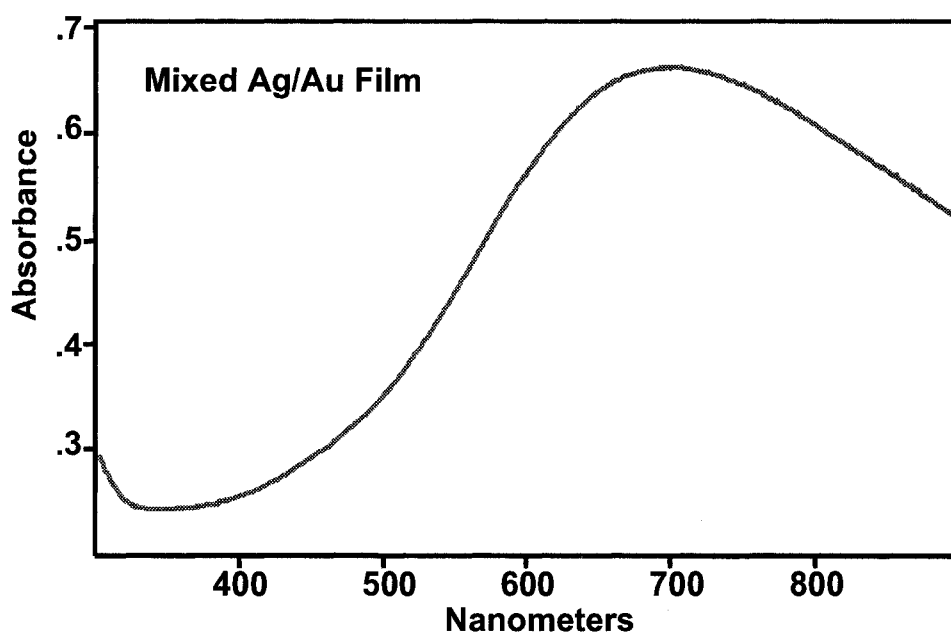
Figure 4.1 Surface plasmon absorption of 10 nm mixed Ag/Au film.

In this work, AFM results were attained to study further the morphology of these 10 nm mixed metal substrates, and a typical height image (2D) is shown in Figure 4.2. A large distribution of particle sizes is revealed in this image, with particles ranging between about 25 and 120 nm in diameter, in agreement with what is expected on the basis of surface plasmon results. Particles in this size range are known to provide strong

enhancement of Raman and resonance Raman signals, and also to sustain so called electromagnetic hot spots when aggregated in evaporated films.[25,26] When XPS measurements were made, results revealed that these mixed Ag/Au films had equal amounts of Ag and Au at their surfaces, indicating a high degree of mixing upon heating of the films at 200 °C.
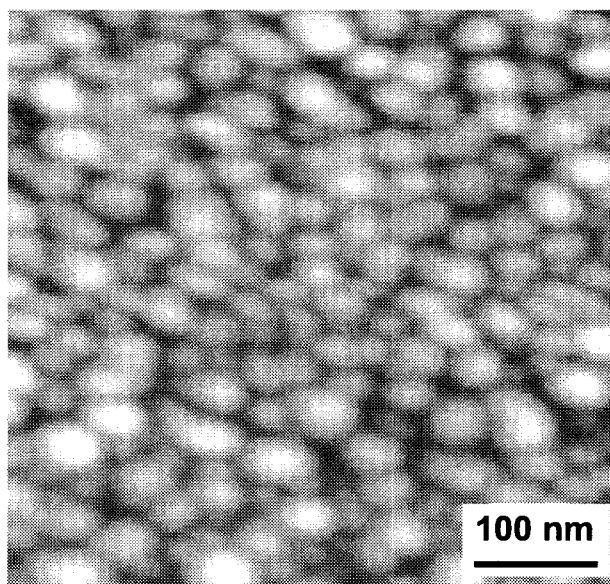
Figure 4.2 AFM image of 10 nm mixed Ag/Au film.

4.2.3 Resonance Raman Scattering of BBIP PTCD

The insets of Figure 4.3 show the molecular structure and solution absorption spectrum (10^{-4} M in dichloromethane) of BBIP PTCD. The absorption of the bright orange dye solution shows strong peaks characteristic of the π-π^* electronic transition of the PTCD chromophore at 543, 495, and 465 nm. The 514.5 nm laser excitation line of the argon ion laser used in this work is in strong resonance with this molecular transition, and so powder results are properly referred to as resonance Raman scattering (RRS) and

61

show resonance enhancement on the order of the molecule's extinction coefficient, ca. 10^4. The RRS spectrum of BBIP PTCD powder is also shown in Figure 4.3. This spectrum is dominated by three fundamental vibrational modes at 1298, 1376, and 1573 cm^{-1} that can be assigned to the ring stretches of the perylene chromophore.[27] It is these three strong peaks that are followed down to the single molecule level in these SERRS studies on mixed Ag/Au film substrates.
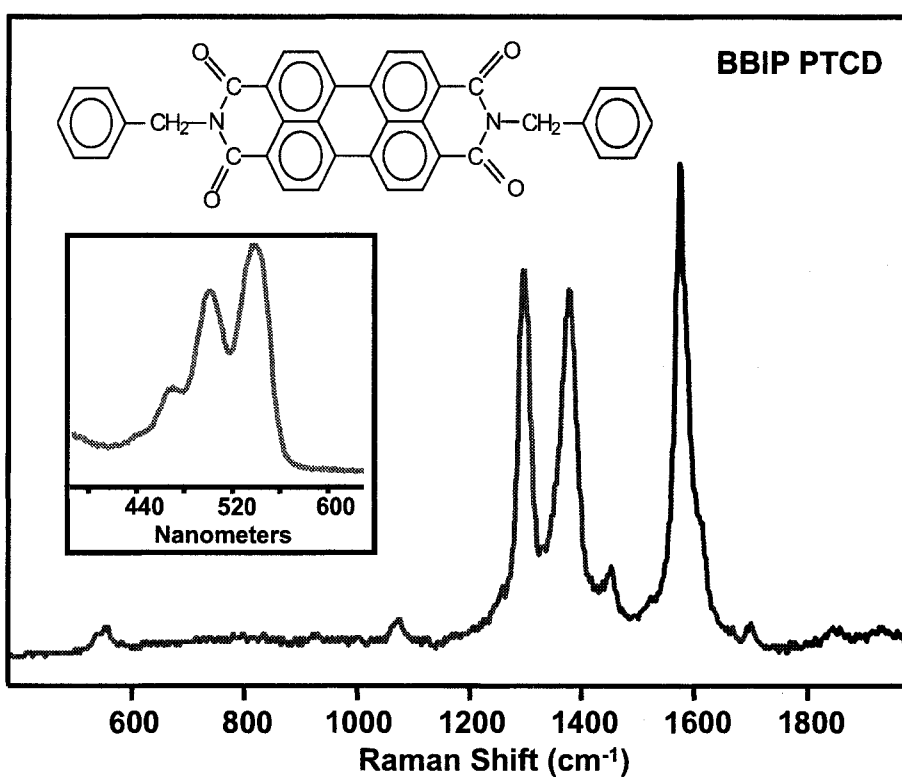
Figure 4.3 BBIP PTCD resonance Raman Scattering. Resonance Raman scattering spectrum of powder BBIP PTCD, with insets showing the molecular structure and solution absorption spectrum (10^{-4} M in dichloromethane) of this molecule.

62

4.2.4 Ensemble LB SERRS and SEF from Mixed Ag/Au Films

As was mentioned, 514.5 nm laser excitation was used throughout this study. Thus, for SERRS measurements, the laser was in resonance with the surface plasmon absorption of the Ag/Au mixed film as well as the electronic transition of the dye system, and the multiplicative effects of both molecular resonance enhancement and surface electromagnetic enhancement were realized. The SERRS spectrum of a concentrated LB monolayer (1:1 molar ratio of BBIP to arachidic acid) deposited onto a mixed Ag/Au film is shown in Figure 4.4. The inset of the figure shows a baselined version of this spectrum, allowing the vibrational SERRS bands to be more easily observed. It can be seen that strong fundamentals, as well as overtones and combinations, are clearly observed, and this will be discussed further in Chapter 6. Simultaneously recorded with the SERRS, is very intense surface-enhanced excimer fluorescence of BBIP PTCD. By comparing the Raman intensities of concentrated LB monolayers on glass, and on mixed Ag/Au films, an average surface enhancement of about 10^4 was estimated for this system. The local enhancements at hot spots for single molecule detection, however, are much larger, and are probably on the order of ca. 10^6-10^7 for this system.

63
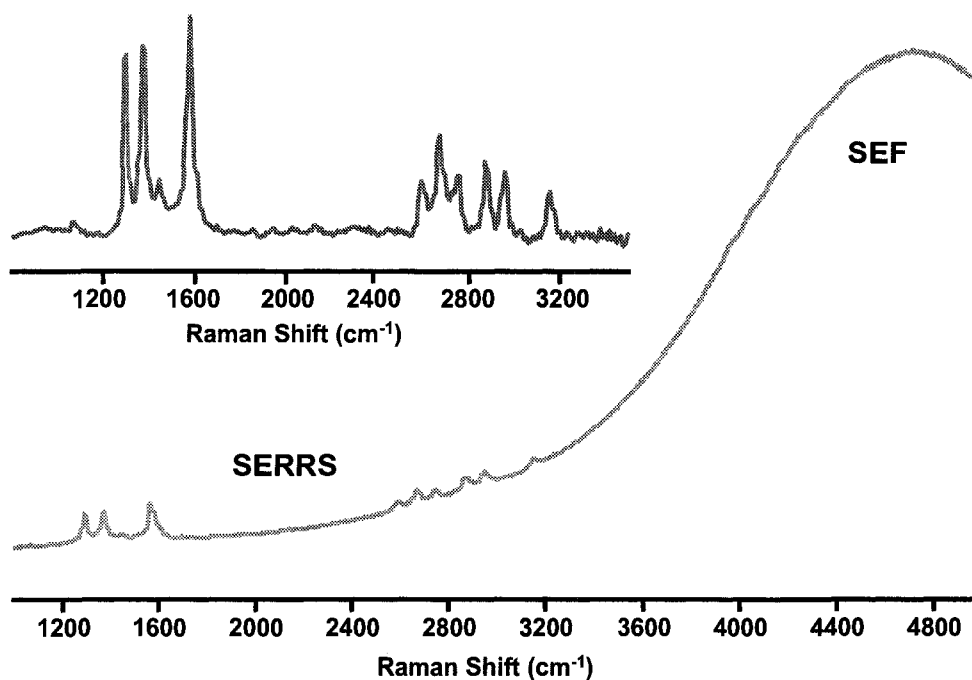
Figure 4.4 Ensemble LB SERRS of BBIP PTCD on mixed Ag/Au film. Average SERRS and excimer SEF of a 10:1 BBIP PTCD:AA LB monolayer deposited onto a 10 nm mixed Ag/Au nanostructured film. Inset shows baselined SERRS spectrum of BBIP PTCD.

4.2.5 Single-Molecule LB SERRS from Mixed Ag/Au Films

In Figure 4.5 the SERRS spectrum of BBIP PTCD, embedded within monolayers of AA deposited onto mixed Ag/Au substrates, including fundamentals and first overtones and combinations, is followed down to the single-molecule level. Spectra recorded from, on average, 2×10^6 molecules, 10 molecules, and finally, a single BBIP PTCD molecule, are shown in Figures 4.5 (a), (b), and (c), respectively. It is likely that the latter two spectra were both recorded from single, isolated monomers, and this will be discussed further in Chapter 6. Single molecule spectra were found to vary from spot-to-

64

spot in all band parameters including Raman shift, bandwidth, band shape, and absolute and relative intensity, signaling the loss of ensemble averaging. Further, excimer fluorescence was not observed at the single molecule level confirming that aggregation does not occur at this concentration level. A number of difficulties were encountered in trying to obtain single molecule BBIP PTCD spectra with good signal to noise ratios in this work. Foremost of these, was the disappearance of signals with even mininum exposure to the laser. This prevented all attempts at high power measurements or accumulation of spectra, and necessitated the use of fresh sampling spots and very low energy densities in order to obtain good signals. These problems eventually led to the use of the 2D spatial mapping techniques discussed in Chapter 6, however, the use of less reactive mixed Ag/Au substrates helped immensely with this problem in this work, as background signals from surface contamination were much lower than on Ag substrates. Silver is known to be highly reactive with its environment,[24] and as the single molecule regime is approached, this becomes an even more important factor. Often contaminant signals compete with those of the analyte, and cause a masking of adsorbate spectra, as well as a diminishing of surface enhancement effects. By coating silver films with gold, the unavoidable reactivity of the resultant mixed metal films can be reduced, while the high Raman enhancements that are attained with silver island films can be maintained. This low reactivity of mixed Ag/Au films facilitates greatly the collection of single molecule spectra.
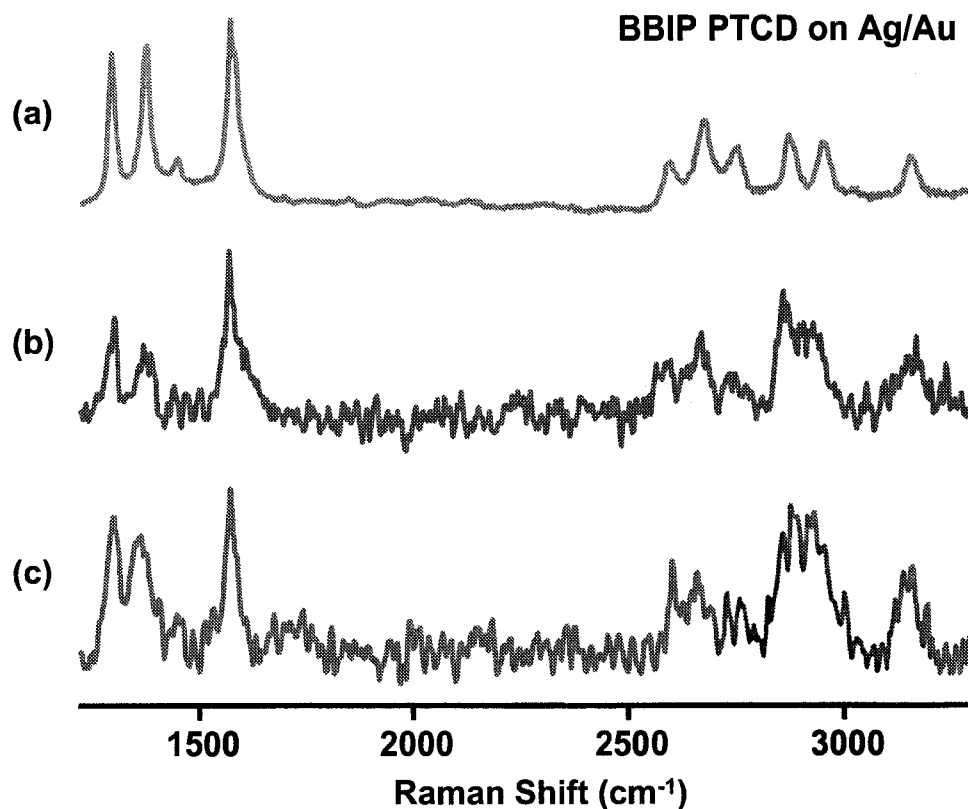
Figure 4.5 Single-Molecule LB SERRS from Mixed Ag/Au Films. SERRS spectra from AA Langmuir-Blodgett monolayers deposited onto mixed Ag/Au nanostructured films having, on average, **(a)** 2×10^6, **(b)** 10, and **(c)** 1 BBIP PTCD molecule(s) per square micron, the scattering area of the Raman microscope.

4.2.6 Conclusions

In this section, the introduction of new mixed Ag/Au nanostructured film substrates for application toward single-molecule LB SERRS was discussed. The substrate was prepared by vacuum evaporation of Ag and Au onto glass substrates, at elevated temperatures, and these mixed metal films were characterized by UV-visible surface plasmon absorption spectroscopy, atomic force microscopy, and X-ray

66

photoelectron spectroscopy. They were employed as substrates for SERRS of a perylene molecule, BBIP PTCD, in LB monolayers, down to the single-molecule level, and demonstrated an advantage of lower reactivity over traditional Ag films. They present promise for future use as substrates for surface-enhanced spectroscopies, including single-molecule SERRS studies.

4.3   Gold Nanoparticle Embedded, Self-Sustained Chitosan Films[b]

4.3.1 Introduction

With massive growth of spectroscopic applications occurring in biological and medical sciences, it is of great interest to develop SERS/SERRS substrates that can employed in the study of sensitive living systems without causing harm. Likewise, reducing the environmental impact of new analytical techniques is increasingly essential. In this section, work toward meeting both of these challenges, through the incorporation of the biopolymer chitosan and Au nanoparticles into thin film SERS/SERRS substrates, is discussed.

Chitosan is the (β-1,4)- linked D-glucosamine derivative of the polysaccharide chitin, the most abundant natural polysaccharide after cellulose, and has been extensively studied for more than 30 years.[28] Its structure is shown in Figure 4.6. It is biocompatible and biodegradable, and an inexpensive, renewable material with many applications in cosmetics, pharmaceuticals, food science, wastewater treatment, biotechnology, and others.[29,30] Analogous to other polysaccharides, chitosan has unique structural and physicochemical characteristics that differ considerably from typical synthetic polymers.

---

[b] This work was done in close collaboration with D. S. dos Santos Jr. and N. P. W. Pieczonka. D. S. d. S. Jr. prepared all films with direction and feedback, based on characterization and application, from P. J. G. Goulet and N. P. W. P.

67

Chitosan's structure is similar to that of cellulose, but it has better processability due to the presence of amino groups (pKa 6.2) in its chains. In fact, its chemistry is largely determined by its amino and hydroxyl groups that act as potential sites for chemical enzyme immobilization, or simply for altering the polymer's functionalty.[31] Also, chitosan is well known as a strong chelating agent for metals and proteins,[32] making it particularly useful in sensor development.[33]
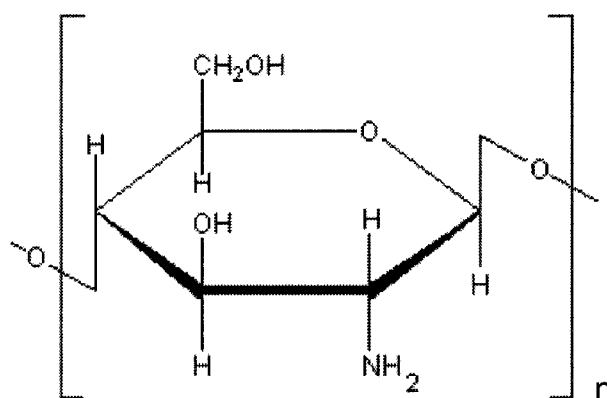
Figure 4.6 Structure of chitosan.

Gold nanoparticles, on the other hand, have found widespread use in fundamental research,[34] as well as in catalytic,[35] biological,[36] and sensing applications.[37-39] They possess excellent biocompatibility, low toxicity, and low reactivity, making them excellent candidates for use within living systems. Moreover, their unique optical properties, which result from surface plasmon resonances in the visible range of the electromagnetic spectrum, make them particularly attractive for optical applications, including the enhancement of Raman and resonance Raman scattering down to the

68

single-molecule level.[10,40] Recently, it was shown that Au nanoparticles can be employed as analytical tools for the investigation of single living cells.[40-42]

Many physical and chemical methods have been employed in the fabrication of gold nanoparticles, producing a wide variety of sizes and shapes.[43-47] Thin solid films containing gold nanostructures have also found wide application.[48-50] Gold is electropositive and can be reduced by various agents such as borohydride, amines, alcohols, and carboxylic acids. The most common methods, however, are based on sodium citrate, sodium borohydride, and ascorbic acid.[34] Typically nanoparticles tend to aggregate during their synthesis, and stabilizers, such as small organic molecules or polymers, must be used. The latter often protect nanoparticles after their formation through steric hindrance, thereby preventing aggregation. Polymers can also offer control over the rate of the reduction process, and thus enable the production of nanoparticles of different shapes and sizes.[51]

In this section, the fabrication, characterization, and application as substrates for SERS/SERRS, of a new class of self-sustained chitosan thin films containing dispersions of gold nanoparticles, is discussed. Gold nanoparticles were generated using acetic acid as a reducing agent in a reaction mediated by the biopolymer chitosan. Self-sustaining films were then formed from the resultant nanocomposite solutions, and characterized by surface plasmon absorption, TEM, and infrared spectroscopy. They were shown to effectively enhance Raman signals of a test analyte, rhodamine 6G, down to trace quantities.

69

4.3.2 Characterization of Chitosan/Au Nanoparticle Films

In this work, gold nanoparticles were produced using acetic acid as a reducing agent, while employing chitosan as a stabilizer and mediator of the reaction. It was found that the properties of the nanoparticles produced could be tuned by varying several experimental parameters, including the relative and absolute concentrations of each of the reactants, temperature, ionic strength, pH, and reaction time. Thin films were prepared from each of these reaction solutions by casting measured volumes of each onto glass substrates and leaving them to dry for 24 hours. To produce self-sustained films, films on glass were then neutralized with a 1% aqueous solution of NaOH, rinsed with deionized water until reaching neutral pH, and removed from the glass substrates. Figure 4.7 shows a variety of these nanocomposite films produced from different reaction conditions, including a stable, flexible, self-sustained film that is held in tweezers. It can be seen that the optical properties of each of these films is slightly different, with their colour ranging from light pink to dark violet. Each was tested for SERS/SERRS activity, which varied widely, and the reaction condition that produced the film with the highest enhancement levels (method given in Chapter 3) was employed for all further studies. It is these films that are discussed throughout this section.
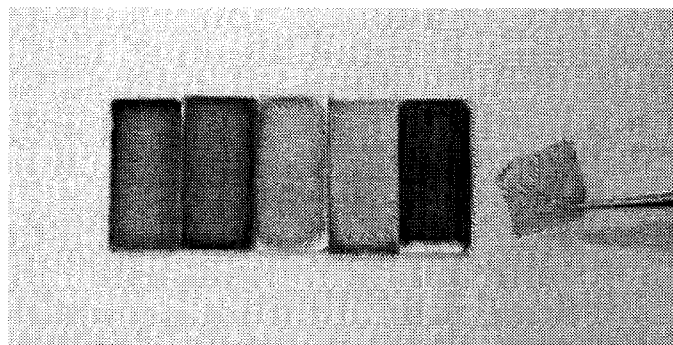
Figure 4.7 Photograph of various Au nanoparticle embedded chitosan films.

Surface plasmon absorption, which has proven very sensitive for measuring differences in metallic nanoparticle size, shape, and spatial distribution,[52,53] was employed in the study of all nanoparticle solutions and resulting nanocomposite films in this work. The production of Au nanoparticles in solution is illustrated in Figure 4.8, where the increase in the extinction of the 539 nm surface plasmon band with reaction time can be attributed to the formation and increasing population of Au nanoparticles. Visually, this process can be observed as a change in the colour of the solution from yellow to dark pink as the reaction proceeds. In the inset of this figure, the surface plasmon absorption of the corresponding nanocomposite film is shown. This spectrum reveals a shift in the absorption maximum to 555 nm for the film from 539 nm for the solution. This redshift results from increased aggregation of the Au nanoparticles, and an increased refractive index of the media surrounding the metallic nanoparticles, in the films.[54]

71
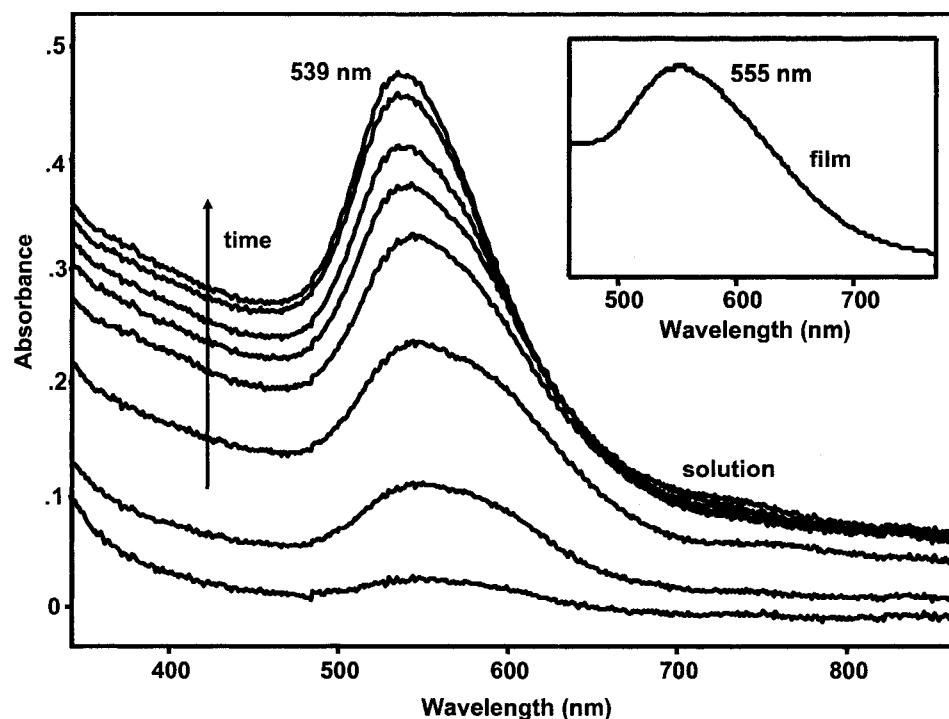
Figure 4.8   Surface plasmon absorption of chitosan/Au nanoparticle mixtures.
Shown, is the growth of surface plasmon absorption with reaction time indicating the production of Au nanoparticles. Inset shows surface plasmon absorption spectrum of a dry Au nanoparticle embedded chitosan film.

In Figure 4.9, TEM results obtained from self-sustained chitosan/Au nanoparticle films are shown. Aggregates of Au nanoparticles with diameters ranging from ca. 10-20 nm are found to be dispersed throughout the nanocomposite films, in agreement with what would be expected on the basis of UV-visible absorption results. It is known that aggregates of this size produce strong enhancement of Raman signals.[55] Higher magnification images shown in Figure 4.9(b) reveal that these nanoparticles are multifaceted, and often triangular. Also, electron diffraction results, shown in Figure

72

4.9(c), have rather sharp spots with diffuse rings, indicating some crystallinity of the particles even at these small sizes.
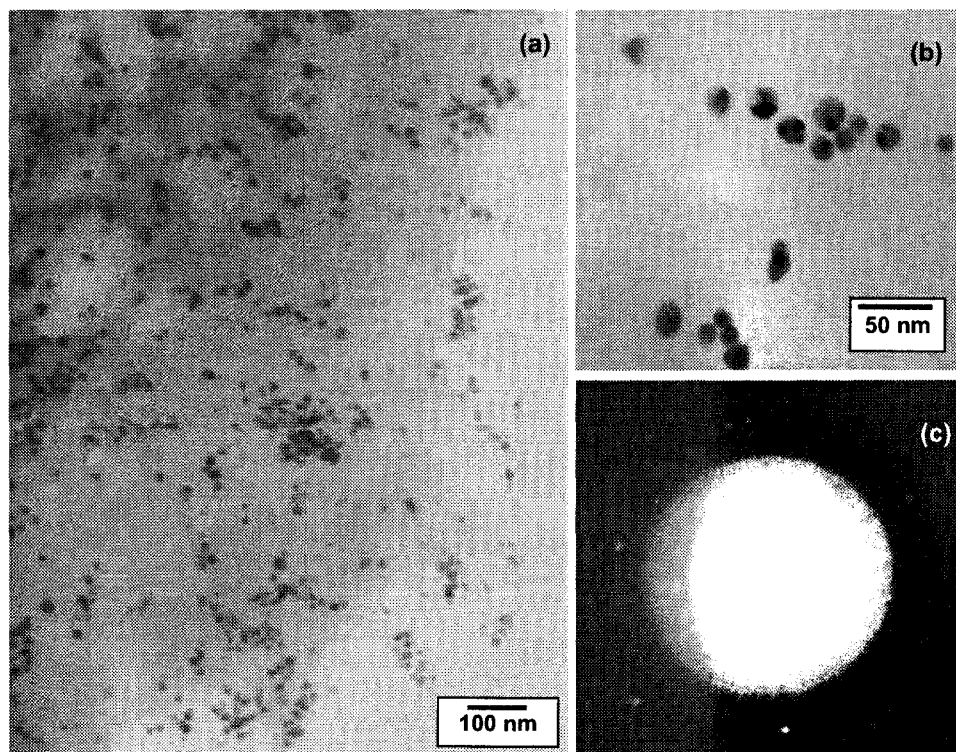
Figure 4.9 TEM images and electron diffraction of chitosan/Au nanoparticle films.

In this work, infrared absorption measurements were also made to characterize both pure and Au nanoparticle embedded chitosan films, and the results are shown in Figure 4.10. While there is little difference between the spectra of these samples, it is clear that there is a shifting of the amide (II) + NH_2 bending mode,[56] from 1569 to 1593 cm^{-1}, upon inclusion of Au nanoparticles. This spectral shift indicates an interaction between the amine groups of chitosan and the Au nanoparticles.

73
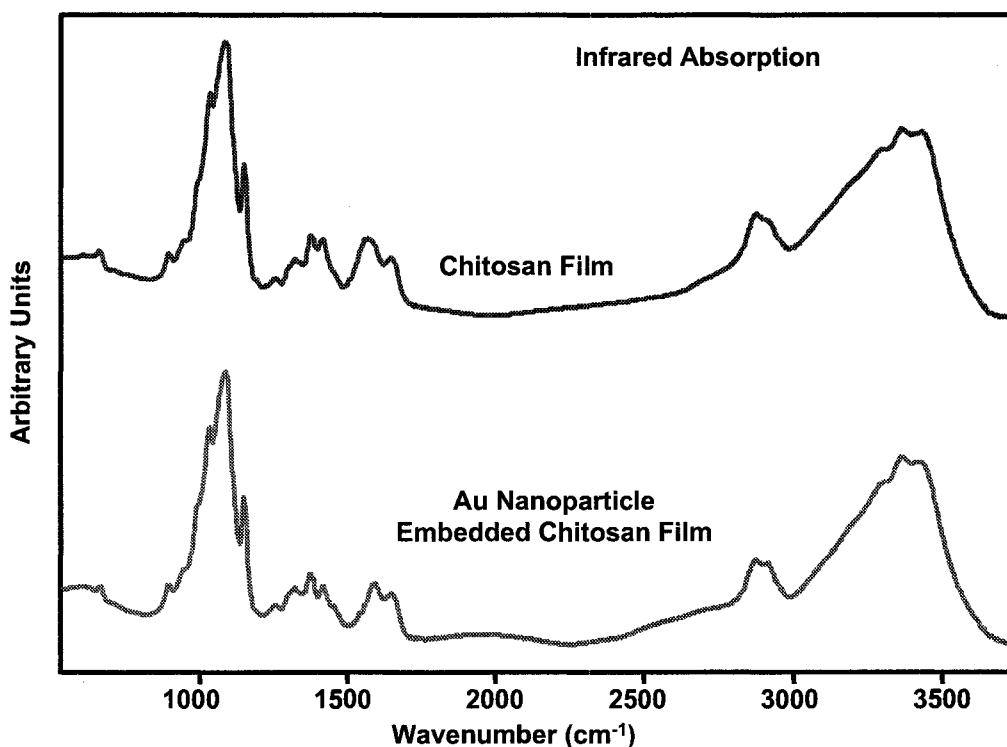
Figure 4.10 IR absorption of pure and Au nanoparticle embedded chitosan films.

4.3.3 SERS from Chitosan/Au Nanoparticle Films

Finally, it was demonstrated that these nanocomposite films are capable of large surface-enhancement of Raman signals, and this is shown in Figure 4.11. Both pure and Au nanoparticle embedded chitosan films were dipped into rhodamine 6G solutions having concentrations ranging from 10^{-4} to 10^{-6} M. The pure chitosan films showed strong fluorescence and extremely weak Raman peaks resulting from R6G, as is shown in Figure 4.11(a). In the case of the Au-chitosan nanocomposite films, however, this strong fluorescence was quenched by the nanoparticles, and, at the same time, the Raman bands were enhanced greatly (Figure 4.11(b)). SERS of R6G was easily detected from films

dipped into solutions with concentrations as low as 10^{-6} M, providing trace detection with full molecular vibrational information.
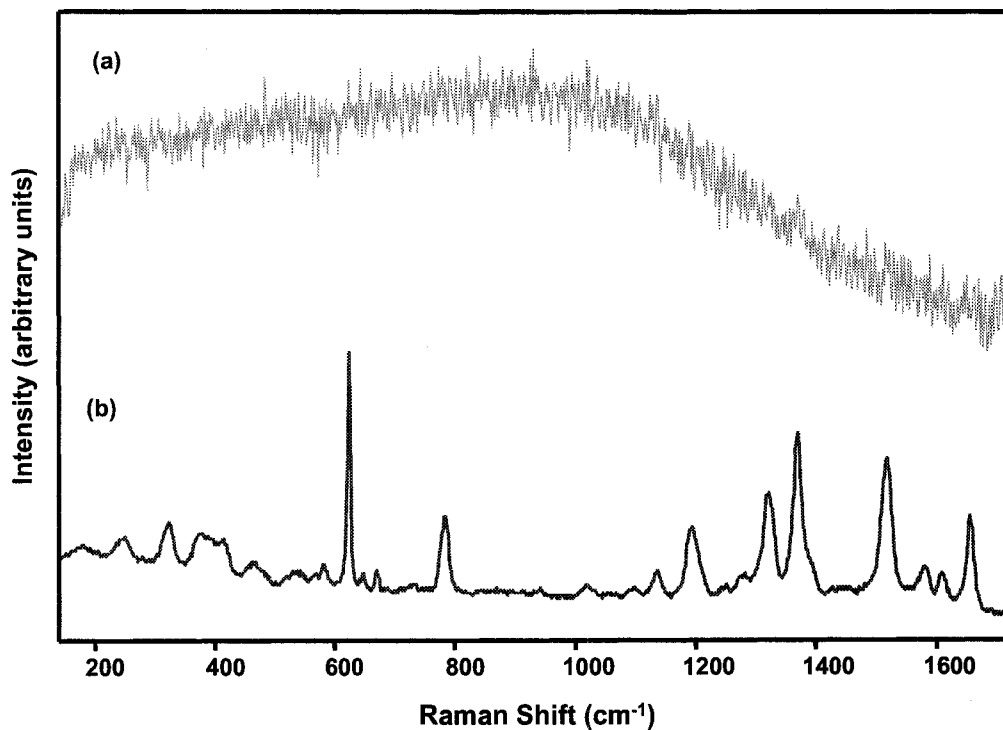
Figure 4.11 SERS from Chitosan/Au Nanoparticle Films. (a) Raman spectrum obtained from pure chitosan film dipped into a 10^{-4} M R6G solution. (b) SERS spectrum obtained from a Au nanoparticle embedded chitosan film dipped into a 10^{-4} M R6G solution.

4.3.4 Conclusions

In this work, gold nanoparticles were generated through the reaction of tetrachloroauric(III) acid, acetic acid, and chitosan. Gold-chitosan nanocomposite films were produced from the reaction solutions, and characterized by UV-visible surface plasmon absorption, transmission electron microscopy, and infrared absorption. It was

75

shown that these films could be employed as substrates for trace analysis using surface-enhanced Raman scattering.

4.4 Dendrimer/Ag Nanosphere Layer-by-Layer Films[c]

4.4.1 Introduction

Substrates for SERS have been fabricated using a variety of physical and chemical methods, producing a wide assortment of interesting architectures.[57-61] Some of these architectures include those produced by vacuum evaporation of metal,[62-64] electrochemical roughening of metal electrodes[65,66] and lithographic techniques.[67,68] However, the use of these techniques tends to be somewhat limited because they require expensive, specialized equipment or specialized techniques. Chemically reduced colloidal metal solutions, on the other hand, are quite easy to prepare, and have now become the most widely used SERS substrates.[69,70]

Despite the exceptional utility that colloidal solutions have shown as SERS substrates, there are some drawbacks to their use. First and foremost, they can become very unstable and collapse with the introduction of analyte molecules, due to a reduction in the repulsive forces between particles. In addition, when working in solution, fairly strong adsorption of molecules onto particles, producing short interaction distances, is required for large enhancement, but this may not exist for all combinations of interest. Finally, when casting these solutions onto solid surfaces, there is very little control over the resulting inter-particle spacing. It is known, however, that this spacing critically determines the optical properties of the aggregates produced, including the large

---

[c] This work was done in close collaboration with D. S. dos Santos Jr. and R. A Alvarez-Puebla. D. S. d. S. Jr. prepared all films with direction and feedback, based on characterization and application, from P. J. G. Goulet and R. A A.-P.

76

electromagnetic fields that define SERS. One simple method for SERS substrate fabrication that seems to address all of these issues is the layer-by-layer (LbL) technique.

The layer-by-layer technique was pioneered by Decher,[71] and involves the electrostatic assembly of alternating positively and negatively charged layers. It is an extremely versatile method for nano-dimension film fabrication, and this can be seen in the large variety of materials that have been employed in LbL films.[72] These supramolecular architectures may be tailored for specific applications, including those in biology, optics, and electronics.[73,74] Included in the materials that are particularly well suited for use in LbL films are dendrimers.[75] These are macromolecules composed of a core (generation zero) and a hyper branched structure that extends in a highly organized fashion out to the terminal groups. In contrast to conventional polymers, dendrimers have precisely controlled structures, molecular weights, and chemical functionalities. They have recently been employed as stabilizers in the synthesis of metallic nanoparticles of gold and silver, using reducing agents such as sodium borohydride and citrate.[76-78] In some cases, dendrimers have been applied directly as reducing agents for the production of metallic nanoparticles.[79]

Several groups have incorporated metallic nanoparticles into LbL thin films,[80-82] and examined the use of these films as substrates for SERS measurements.[83] In the work discussed in this section, the exceptional characteristics of dendrimers, and the powerful optical properties of colloidal Ag nanospheres, are utilized to produce unique SERS substrates using the LbL self-assembly technique.[84] Films are prepared by successive alternating immersions in solutions of dendrimer and colloidal Ag particles and characterized by surface plasmon absorption and atomic force microscopy. They are

77

shown to provide excellent enhancement of the Raman scattering of 2-naphthalenethiol. The optical properties of several different possible architectures are studied as a function of the size (generation) and concentration of the dendrimer used, as well as the number of layers produced. Ag nanoparticles are shown to be effectively immobilized and stabilized by the dendrimers, with increased control over their spacing and aggregation. Finally, the possibility of collecting SERS from architectures with intervening layers between metal nanoparticles and the surface is demonstrated.

4.4.2 Characterization of Dendrimer/Ag Nanosphere LbL Films

Layer-by-layer film depositions, as well as the properties of films produced by this technique, are known to depend critically upon the various experimental parameters employed. Among the most important of these are the chemistry, size, and concentration of the species involved, and the number of deposition steps performed. In this work, an attempt has been made to systematically study these variables for LbL films produced from colloidal Ag and DAB-Am dendrimer (amine-terminated) solutions. In Figure 4.12, the growth of films is monitored using UV-visible absorption spectroscopy for generation 5 (G5 DAB-Am) and generation 1 (G1 DAB-Am) dendrimer/Ag multilayers. The surface plasmon absorption spectra for LbL films produced using a 0.045 g/L G5 DAB-Am dendrimer solution as the source of the cationic species are shown in Figure 4.12(a), while the spectra for films produced using 0.100 g/L and 0.045 g/L solutions of G1 DAB-Am dendrimer are shown in Figures 4.12 (b) and (c), respectively.

78
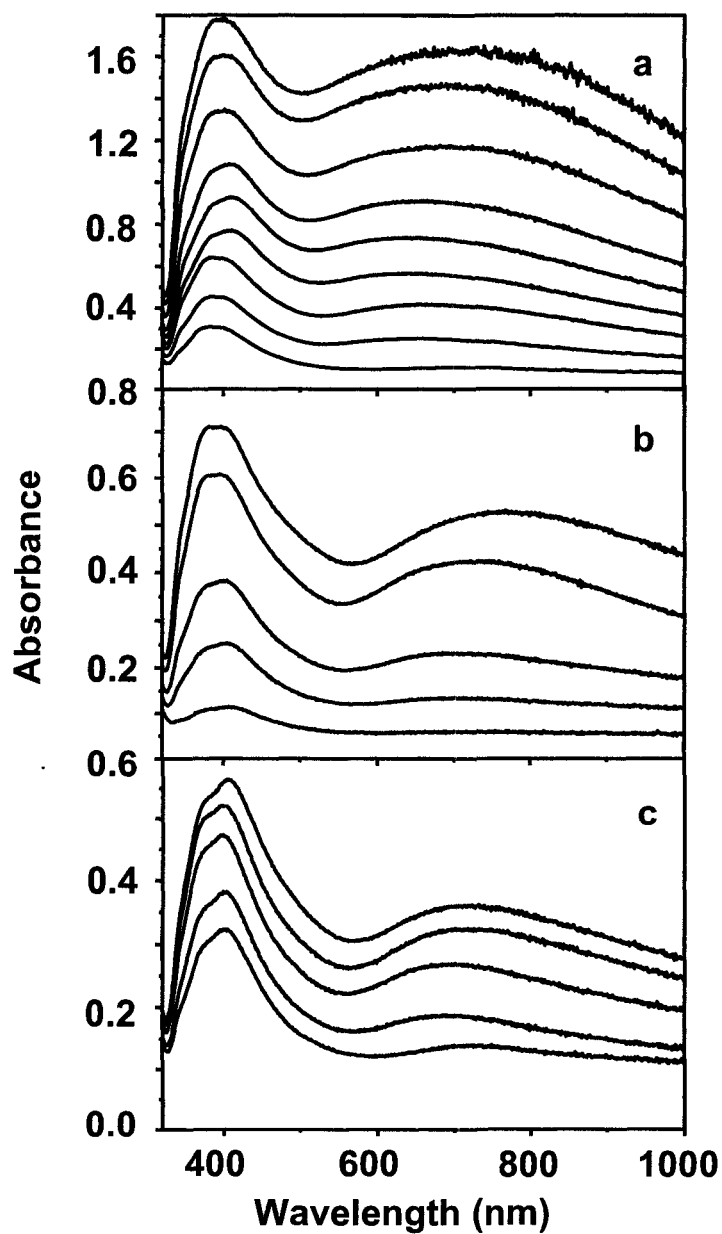
Figure 4.12 UV-visible absorption of dendrimer/Ag nanosphere LbL films. Surface plasmon absorption spectra of layer-by-layer films showing increasing extinction with increasing number of bilayers for films produced with a Ag colloid solution and (a) G5 DAB-Am dendrimer solution (1.0 g/L) (up to 9 bilayers), (b) G1 DAB-Am dendrimer solution (2.4 g/L) (up to 5 bilayers), and (c) G1 DAB-Am dendrimer solution (1.0 g/L) (up to 5 bilayers).

79

There are several traits that appear to be common to all three sets of experiments. First, the overall shape of the absorption spectra is similar for all films, displaying a broad maximum at ca. 390 nm, and a second broad feature at ca. 700 nm. The former can be attributed to the absorption of single isolated Ag particles with a mean diameter of ca. 20 nm. The latter feature, on the other hand, is the result of the absorption due to coupling particles, whether as dimers or higher order aggregates. Second, in all three cases, the extinction of the films grows with the addition of each bilayer, indicating that, within these limits, adsorption of the nanoparticles is a favored process over desorption. Finally, in all three sets of spectra, a general trend towards growth in the relative intensity of the longer wavelength band is observed with increasing number of bilayers, before stabilizing after ca. 3 bilayers have been deposited. This can be interpreted as an increase in the number of electromagnetically coupling nanoparticles relative to single isolated ones, and ultimately to the uneven distribution of material in the initial bilayers.

By comparing the corresponding data of Figures 4.12 (a) and (c), it can be seen that higher Ag adsorption occurs with the generation 5 dendrimer than with the generation 1 dendrimer (with equal concentrations of 0.045 g/L), as revealed by higher surface plasmon absorption. This suggests, as expected, that there are a larger number of available amino groups for binding Ag nanoparticles on the surface of the generation 5 dendrimer films than on the generation 1 films. This also holds when the concentration of the generation 1 dendrimer is increased to 0.100 g/L, as in Figure 4.12(b). Moreover, a comparison of the spectra in Figures 4.12 (b) and (c) reveals that the higher concentration of generation 1 dendrimer leads to increased adsorption of silver nanoparticles, and thus higher absorption. It was also found that the adsorption of Ag

nanoparticles on the dendrimer layers continued to increase up to 20 hrs., indicating that film growth is not governed by strong electrostatic interactions alone, and that other driving forces such as van der Waals or hydrogen bond interactions may also play an important role.[85]

The surface morphologies of the LbL films produced in this work were analyzed by AFM imaging. The results obtained for films prepared using a G5 DAB-Am solution with a concentration of 0.045 g/L and a Ag colloidal solution are shown in Figure 4.13. These images are of films produced with 1 to 6 bilayers, and correspond to the lower 6 absorption spectra of Figure 4.12(a). Based on the analysis of these images, the mean diameter of the silver nanoparticles was found to be ca. 20 nm. With the deposition of a single bilayer, the vast majority of nanoparticles are observed as single isolated particles or as dimers, with the surface being covered quite incompletely, as shown in Figure 4.13(a). This effect is commonly observed for LbL films and is the result of the non-uniform coverage of the glass substrate by the first dendrimer layer. As the number of bilayers deposited is increased up to 6, as shown in Figures 4.13(b-f), however, surface coverage becomes more complete, forming continuous interacting networks of nanoparticles with occasional larger aggregates. The RMS roughness values of the films also seem to support the idea that after the first few bilayers have been deposited, the depositions become more consistent and the surface morphology changes little with each additional bilayer. The first bilayer has an RMS roughness value of ca. 20 nm, and this is fairly consistent with the mean particle size. As more layers are added to the film, the roughness of the surface increases up to approximately 60 nm in the third layer, after which it remains relatively constant with increasing numbers of bilayers.
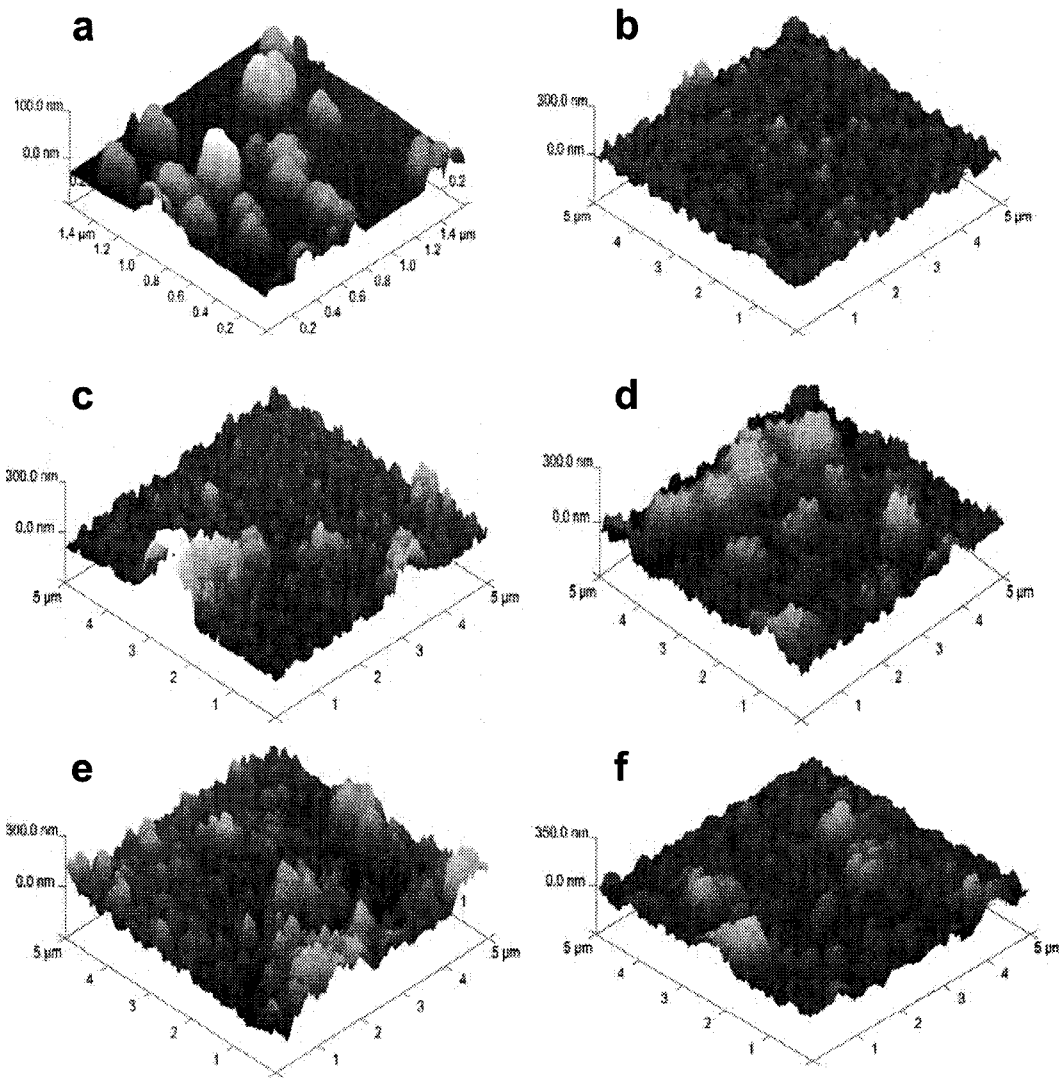
Figure 4.13 AFM images of dendrimer/Ag nanosphere LbL films. AFM images recorded from G5 DAB-Am/Ag nanoparticle LbL films (1.0 g/L) demonstrating the effect of increasing numbers of bilayers on film morphology and RMS roughness. (a) 1 bilayer (RMS= 20.2 nm), (b) 2 bilayers (RMS= 40.2 nm), (c) 3 bilayers (RMS= 55.3 nm), (d) 4 bilayers (RMS= 63.1 nm), (e) 5 bilayers (RMS= 67.0 nm), and (f) 6 bilayers (RMS= 62.9 nm).

4.4.3 SERS from Dendrimer/Ag Nanosphere LbL Films

In Figure 4.14, the effect of the number of bilayers of G5 dendrimers and Ag nanoparticles, on the SERS intensity of 2-naphthalenethiol (2-NAT) cast onto LbL film substrates, is examined. As a reference for the SERS spectra reported here, the normal Raman scattering spectrum of 2-NAT powder is shown in Figure 4.14(a). This spectrum, along with the SERS spectra of this molecule, has been reported previously.[86] The SERS spectra of 2-NAT cast onto LbL films of 1 to 6 bilayers are shown in Figures 4.14(b-g), and were all recorded under the same experimental conditions using a 785 nm diode laser. The SERS spectra recorded from all the substrates show the same basic features, with nearly no variation in the relative intensities, frequencies, or bandwidths of the observed bands. However, there is an important trend revealed in the observed average absolute intensities of the spectra, and this is illustrated by the values in brackets for each of the SERS spectra in Figure 4.14, which indicate the intensity of the 1382 cm^{-1} band of 2-NAT in kilocounts. It can be seen that average enhancement increases proceeding from 1 to 3 G5 DAB-Am/Ag bilayers before stabilizing. This trend can be attributed to increased surface coverage, surface area, and aggregation (more structures resonant at 785 nm) with increasing numbers of bilayers, and agrees well with the trends observed for surface plasmon absorption and AFM measurements.
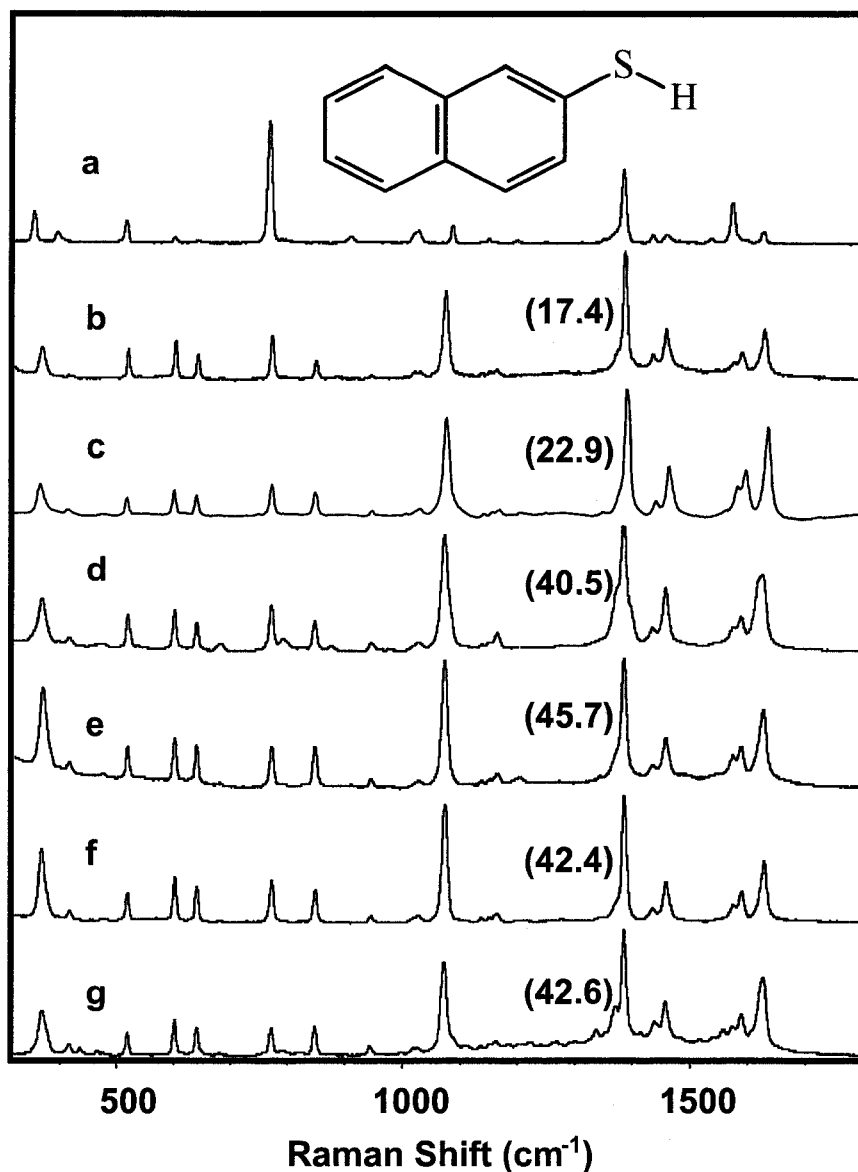
Figure 4.14 SERS from G5 DAB-Am/Ag nanoparticle LbL films. (a) Normal Raman scattering spectrum of 2-NAT powder. Also shown are SERS spectra recorded from 2-NAT cast onto LbL films, fabricated from Ag nanospheres and G5 DAB-Am dendrimer, and composed of (b) 1, (c) 2, (d) 3, (e) 4, (f) 5, and (g) 6 bilayers. The number in brackets for each of the SERS spectra indicates the average intensity of the 1382 cm^{-1} band of 2-NAT in kilocounts, where all spectra were recorded using the same experimental conditions. Inset shows structure of 2-NAT.

84

Strong SERS enhancement can also be observed from 2-NAT cast onto LbL film substrates prepared using G1 DAB-Am and Ag nanoparticle solutions, as shown in Figure 4.15. In this figure, the effect of the concentration of the cationic dendrimer species on the average enhancement of the SERS signals collected from the substrates is explored. In agreement with the surface plasmon absorption results presented for these film sets, the average enhancement of the Raman scattering signals is significantly higher for the films prepared with the higher dendrimer concentration (a-e). This is likely due to higher concentrations of nanostructures resonant at 785 nm, and also possibly to increases in electromagnetic fields surrounding the nanostructures due to higher particle-particle coupling in these films. In addition, these substrate sets show similar behavior to those prepared using the generation 5 dendrimer (Figure 4.14), as enhancement grows initially when bilayers are added, then stabilizes.

85
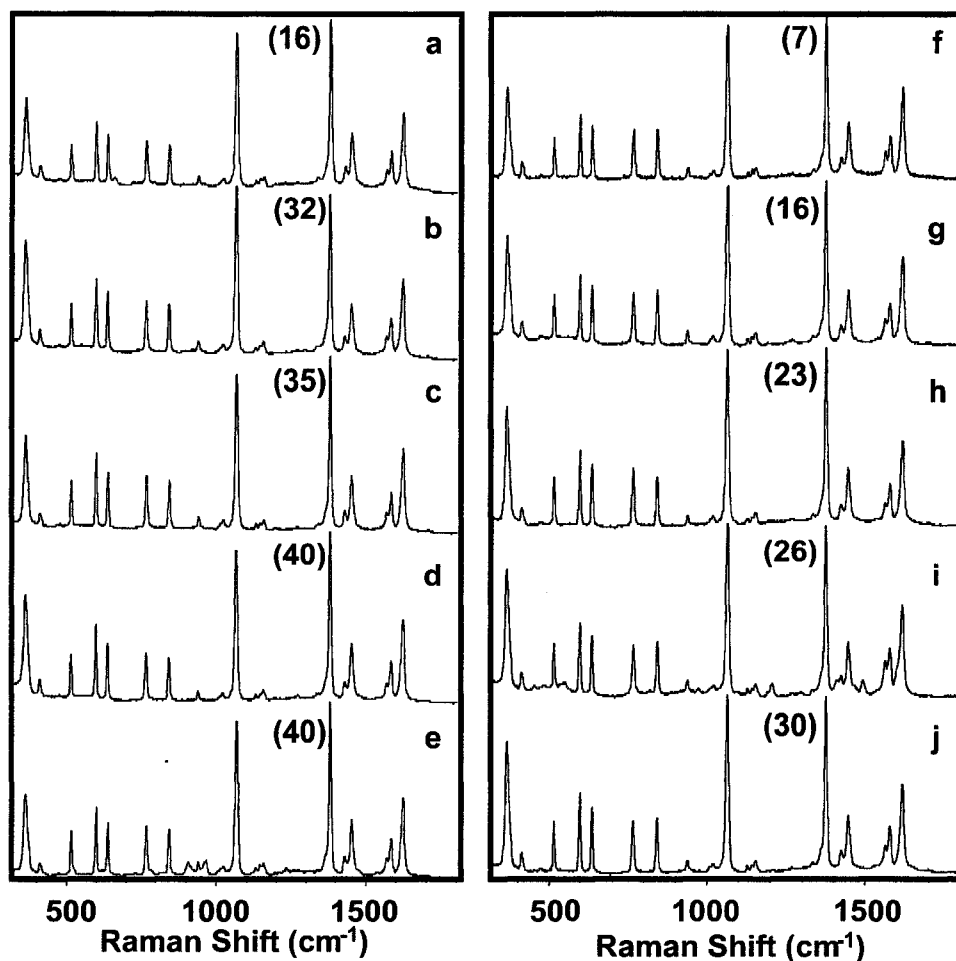
Figure 4.15 SERS from G1 DAB-Am/Ag nanoparticle LbL films. Comparison of SERS spectra of 2-NAT as a function of the concentration of G1 DAB-Am dendrimer used to produce the LbL substrates, and the number of bilayers they are composed of. All spectra on the left (a-e) were produced from a 0.100 g/L G1 DAB-Am solution, and are composed of (a) 1, (b) 2, (c) 3, (d) 4, and (e) 5 bilayers. All spectra on the right (f-j), however, were produced from a 0.045 g/L G1 DAB-Am solution, and are composed of (f) 1, (g) 2, (h) 3, (i) 4, and (j) 5 bilayers. The number in brackets for each of the spectra indicates the average intensity of the 1382 cm^{-1} band of 2-NAT in kilocounts, where all spectra were recorded using identical experimental conditions.

86

In all of the SERS experiments described above, enhancement was observed for the Raman scattering signals of analytes deposited directly onto Ag nanoparticle layers. To demonstrate that it is possible to develop sensors with external layers that are chemically selective for specific analytes, without significantly decreasing the enhancement afforded by SERS, experiments were performed with architectures having intervening layers between the metal nanoparticles and the film's surface. These architectures were prepared by substituting outer Ag nanoparticle layers with the polymer polystyrene sulfonate (PSS), as shown in Figure 4.16. Films were prepared from colloidal Ag, 0.045 g/L G5 DAB-Am dendrimer, and 1.0 g/L PSS solutions, and SERS spectra were recorded from solutions of 2-NAT cast onto them and evaporated. The value in brackets for each of the spectra indicates the average intensity of the 1382 cm^{-1} band of 2-NAT in kilocounts, where all spectra were recorded using the same experimental conditions. Although there are decreases in average SERS intensities with increasing number of intervening layers, electromagnetic enhancement is still strong, even with 2 complete layers between the metallic nanoparticles and the surface.
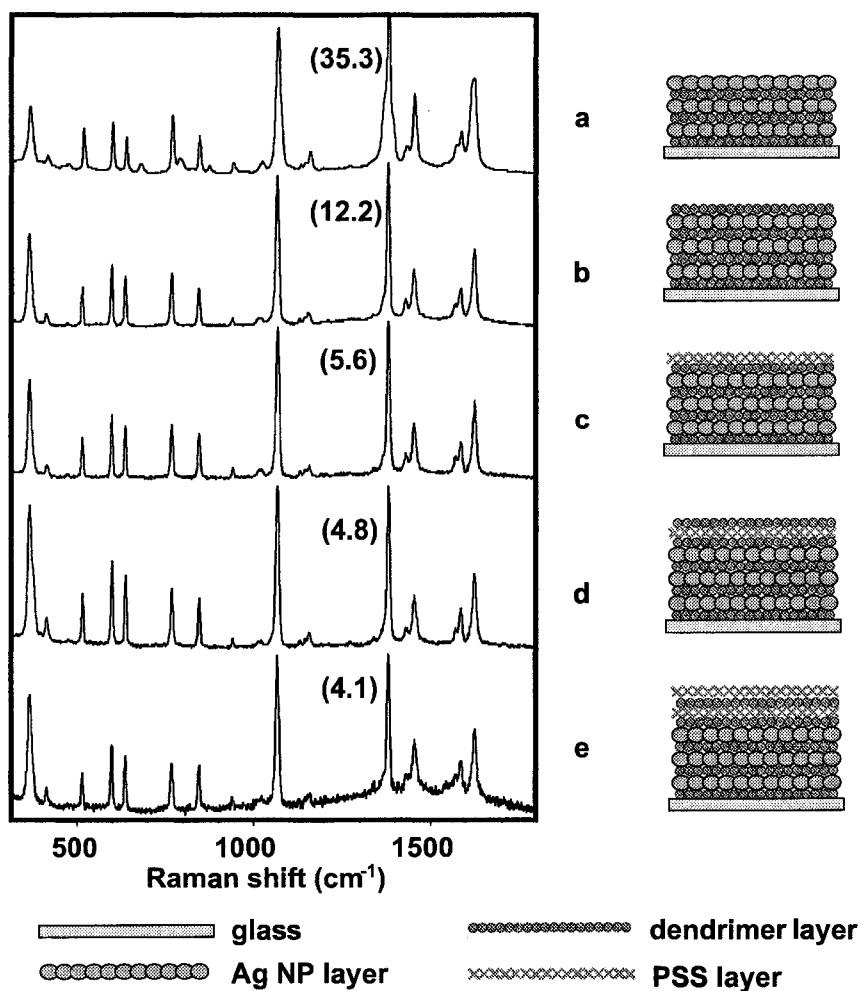
Figure 4.16 SERS from LbL films with intervening layers. Spectra from LbL substrates demonstrating the effect on intensity of introducing intervening layers between the Ag nanospheres and the surface of the films. The value in brackets for each of the spectra indicates the average intensity of the 1382 cm^{-1} band of 2-NAT in kilocounts, where all spectra were recorded using the same experimental conditions. The architectures are as shown in the legend.

88

4.4.4 Conclusions

In this work, the layer-by-layer technique was successfully employed in the production of unique substrates for measurements of surface-enhanced Raman scattering. The exceptional characteristics of dendrimers, along with the powerful optical properties of colloidal Ag nanospheres, were utilized to produce a variety of different film architectures, and these were studied by surface plasmon absorption, AFM, and SERS measurements. It was shown that the optical properties of these different substrate architectures are strongly influenced by the generation and concentration of the dendrimers used, as well as the number of layers produced. These LbL films were shown to have some particular benefits over many commonly used substrates for SERS, and were able to provide excellent enhancement of the Raman scattering of 2-naphthalenethiol. Finally, the collection of SERS from architectures with intervening layers between the metal nanoparticles and the surface of the films was demonstrated, showing potential for application in the development of chemically specific SERS sensors.

4.5 Dendrimer/Ag Nanowire Layer-by-Layer Films[d]

4.5.1 Introduction

In this section, the development of a new substrate for SERS/SERRS, that once again employs the layer-by-layer technique, is discussed. This technique[71] for nano-dimension film fabrication involves the electrostatic assembly of alternating positively and negatively charged layers, and allows for the controlled production of nano-

---

[d] This work was done in close collaboration with D. S. dos Santos Jr. and R. A Alvarez-Puebla. D. S. d. S. Jr. prepared all films with direction and feedback, based on characterization and application, from P. J. G. Goulet. R. A. A.-P. performed measurements not included in this thesis.

89

architectures, and represents a great potential for broadening the possibilities of surface-enhanced experiments.[83] In particular, it allows for the incorporation of a large variety of materials into thin films,[87-89] where, in most cases, their interesting properties are maintained. In this way, the LbL technique allows for the marriage of the properties and function of different materials into useful thin films.

In this section, the fabrication of SERS/SERRS active dendrimer/Ag nanowire layer-by-layer thin solid films is discussed.[90] Ag nanowires were employed in this work, because they are known to produce strong enhancement of Raman and resonance Raman signals, particularly when aligned parallel to one another where electromagnetic coupling can occur.[6,61,91] Briefly, Ag nanowires, approximately 100 nm in diameter, were produced in solution and allowed to self-assemble into a single layer on a single G5 DAB-Am dendrimer layer coating a glass substrate. The Ag nanowires, and the resulting LbL films were characterized using UV-visible surface plasmon absorption, while the films were characterized further by atomic force microscopy (AFM), and applied as substrates for SERS/SERRS. The dendrimer was found to effectively immobilize and control the spacing of the Ag nanowires within the films. Through a series of experiments these films were shown to be excellent substrates for SERS/SERRS measurements, demonstrating significant enhancement, and trace detection capability. A common analyte (R6G) was tested using a variety of excitation energies, and results confirmed effective enhancement of Raman signals throughout the visible range of the electromagnetic spectrum (442 to 785 nm), making possible the observation of both SERS and SERRS. This molecule was cast onto the films from aqueous solution. However, the insolubility of the LbL film substrates was capitalized upon in this work

through the use of the Langmuir-Blodgett technique[92] to introduce analytes onto the Ag nanowire surface for SERRS experiments. This technique allows for highly controlled deposition of single monomolecular layers onto solid supports.

4.5.2 Characterization of Dendrimer/Ag Nanowire LbL Films

Based on the report of Sun et al.,[93] the solution-phase synthesis of uniform nanowires of bicrystalline silver, with diameters of ca. 100 nm and lengths of several microns, was successfully completed. The synthesized nanowires were characterized by their surface plasmon absorption in the visible region of the electromagnetic spectrum, and the results are shown in Figure 4.17(a). The plasmon absorption of the nanowires in solution is distinctly different from the nanowires in the LbL film with the G5 DAB-Am dendrimer (Figure 4.17(b)). The spectrum of the LbL film shows two well-resolved maxima at 358 nm and 396 nm, while a shoulder at 353 nm and a maximum at 383 nm can be seen in the solution phase. A clear redshifting, broadening absorption is evident for the Ag nanowires in the LbL film, and this can be readily explained by changes in the dielectric function of the medium surrounding the particles,[53] as well as by the aggregation (bundling) of the nanowires. The plasmon absorption of the nanowires (elongated cylinders) is distinctly different from that of a distribution of spherical silver particles in colloidal solutions, or metal island films, showing a characteristic strong, blue shifted maximum below 400 nm, as can be seen in Figure 4.17. This band can be assigned of the transverse plasmon absorption mode of the nanowires.[93,94]

91
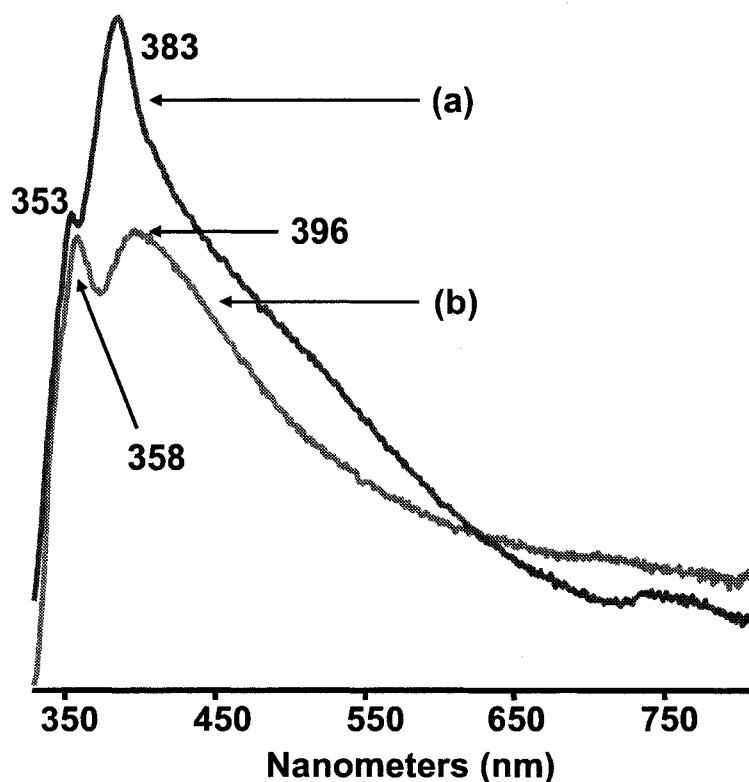
Figure 4.17 Surface plasmon absorption of dendrimer/Ag nanowire film. Extinction spectra of (a) Ag nanowire solution, and (b) G5 DAB-Am/Ag nanowire LbL film.

The morphology of the Ag nanowires in the LbL films is shown in Figure 4.18. Particles are several micrometers in length, bundled together, and have average diameters of approximately 100 nm. Higher magnification images reveal this lengthwise aggregation, and show the structures to be many-sided, rather than smooth cylinders. This confirms previous results that demonstrated pentagonal cross-sections for these wires.[61] Notably, the bundling apparent in these images appears to be directly related to the process of assembling the nanowires onto the dendrimer layer in the LbL film, as it is not observed in images of the wires cast directly onto glass. Also in these images, large irregularly shaped particles can be seen interspersed with the nanowires. AFM phase

92

imaging suggests that these particles are Ag, but their contribution to the surface plasmon absorption spectra, or enhancement of the Raman signals, appears to be minimal, as expected from their large size. In fact, the large size of these particles (200-500 nm) largely precludes their effectiveness as enhancing nanostructures for SERS/SERRS experiments, particularly in the visible region of the electromagnetic spectrum. The AFM images of the LbL water insoluble film, show abundant metal nanostructures on the surface of the film, making it an ideal candidate for SERS/SERRS measurements from cast solutions, as well as from single monolayers transferred from the air-water interface to the probing surface using the LB technique. Moreover, the presence of known contributors to high surface-enhancement of Raman signals, in these films, such as sharp edges and tips, as well as aggregates of particles, is noteworthy.
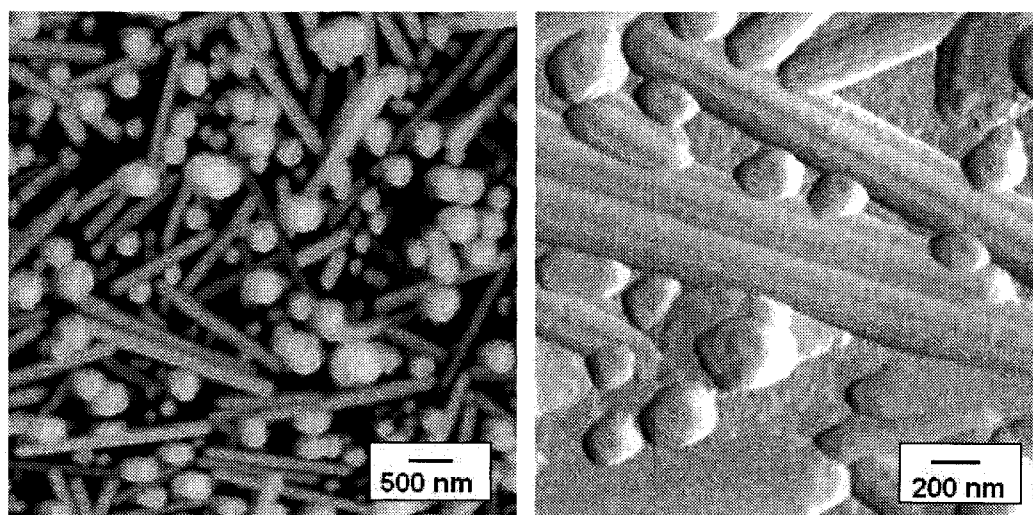
Figure 4.18 AFM images of a G5 DAB-Am/Ag nanowire LbL film.

93

4.5.3 SERS/SERRS from Dendrimer/Ag Nanowire LbL Films

In this work, the ability of G5 DAB-Am/Ag nanowire LbL substrates to produce SERS/SERRS was tested in two ways. First, a known volume (10 μL) of a 10^{-5} M aqueous solution of R6G was cast onto the LbL film, and a section of the surface covered by the solution (ca. 1 μm2) was excited with several laser wavelengths to gather the inelastic scattering. Second, mixed Langmuir-Blodgett monolayers of n-pentyl-5-salicylimido perylene (salPTCD) were deposited onto the LbL films and SERRS experiments were carried out. The SERS/SERRS spectra of R6G are illustrated in Figures 4.19 and 4.20. The insets of Figure 4.19 show the molecular structure of R6G, as well as the absorption and emission spectra of the stock solution of the dye used in the SERS experiments. It can be seen that the 633 and 785 nm laser excitation lines are not in resonance with the observed electronic transitions of the molecule, and therefore these enhanced spectra are referred to as surface-enhanced Raman scattering (SERS). When laser excitation is in electronic resonance with the molecular system, however, the observed enhanced spectra are referred to as surface-enhanced resonance Raman scattering (SERRS). This is the case for this molecular system at 442, 488, and 514 nm laser excitation. Figure 4.19 shows the SERRS spectrum recorded from R6G employing 514.5 nm excitation, on Ag nanowire LbL films. Shown are the fundamentals, in the spectral region up to 1700 cm^{-1}, and also the combinations and overtones, clearly seen in the 1900-3500 cm^{-1} region. This spectrum demonstrates strong enhancement, with signals being detected from attomole quantities. Further, in Figure 4.20, it is shown that all laser excitation lines from the visible, starting at 442 nm, to the near-infrared, at 785 nm, provide strong SERS/SERRS with these LbL substrates. As laser excitation is

94

brought in and out of resonance with the molecular electronic transition, the relative

intensities in the SERS/SERRS spectra vary, and this is a result of the coupling of the

vibrational modes to the electronic transition in the resonant case.
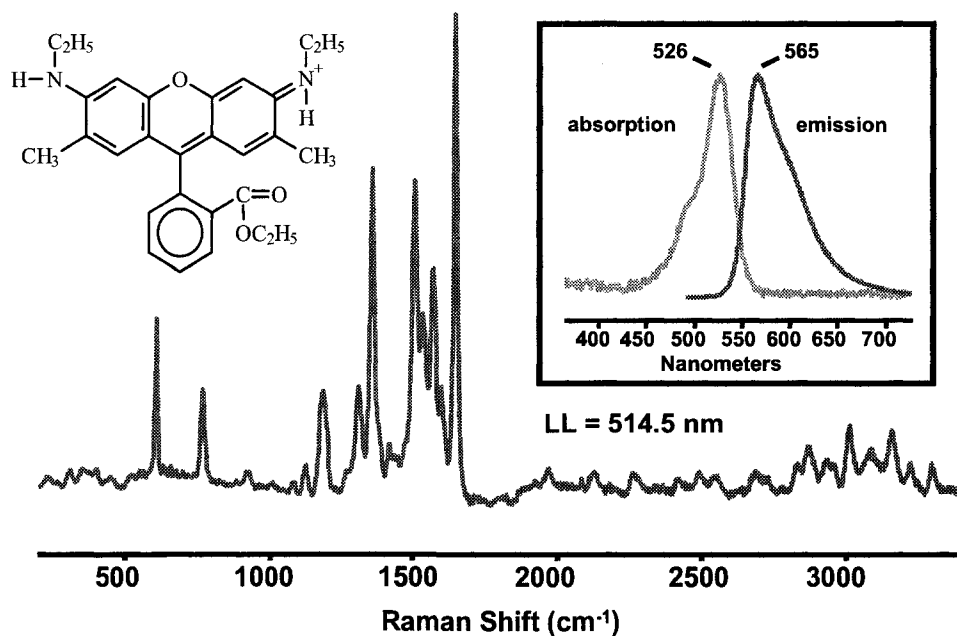
Figure 4.19 SERRS of R6G on G5 DAB-Am/Ag nanowire LbL film. Baselined

SERRS spectrum of R6G recorded using laser excitation at 514 nm, and showing strong

overtone and combination bands. Insets show R6G molecular structure, and absorption

and fluorescence emission of 10^{-5} M R6G solution.
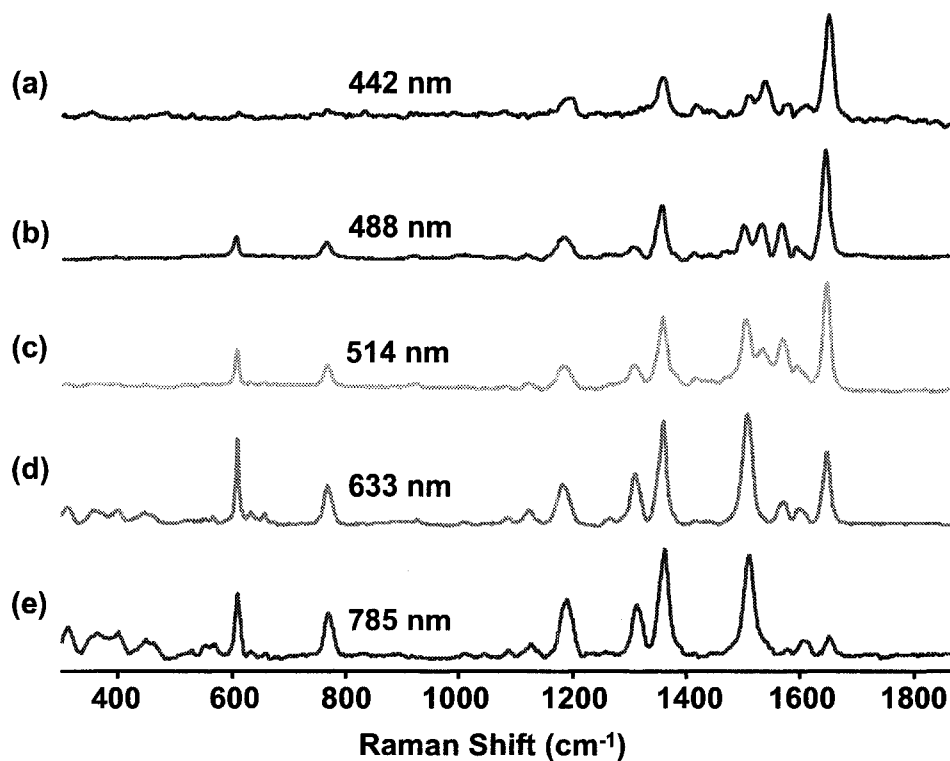
Figure 4.20 Broad enhancement region of G5 DAB-Am/Ag nanowire LbL film. SERS/SERRS spectra of R6G recorded using laser excitation at **(a)** 442, **(b)** 488, **(c)** 514, **(d)** 633, and **(e)** 785 nm.

4.5.4 LB SERS/SERRS from Dendrimer/Ag Nanowire LbL Films

Finally, these LbL films are water insoluble, and therefore offer the possibility for use as substrates for Langmuir-Blodgett SERS/SERRS.[95] Mixed LB monolayers were prepared by spreading a mixed solution containing arachidic acid and salPTCD, in a 10:1 molar ratio, at the air water interface of a Langmuir trough. A single LB monolayer was then transferred by Z-deposition to the LbL substrate. Spectra were recorded using 514.5 and 633 nm laser excitation, and collected from an area of ca. 1 μm^2. They are shown in Figure 4.21, and arise from attomole quantities of the perylene dye. A change in the

96

relative intensities of the vibrational bands with different excitation energies is once again the result of molecular resonance of the dye at 514.5 nm.
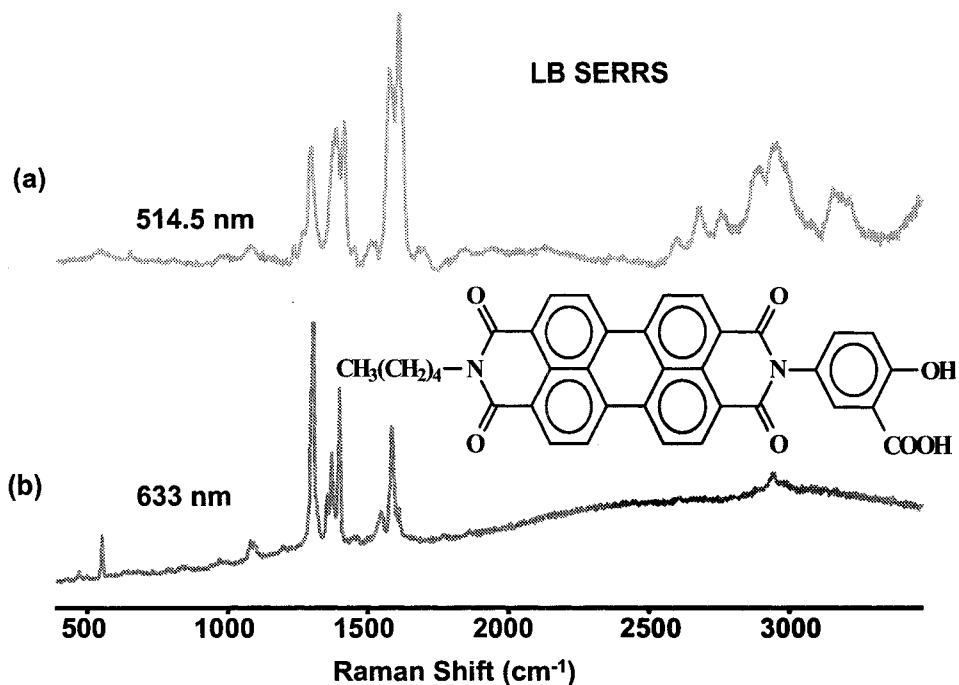
Figure 4.21   LB SERS/SERRS from Dendrimer/Ag Nanowire LbL Films. SERS/SERRS spectra of a 10:1 mixed AA:salPTCD LB monolayer recorded using laser excitation at **(a)** 514, and **(b)** 633 nm. Also shown is the molecular structure of salPTCD.

4.5.5 Conclusions

In this work, a versatile G5 DAB-Am/Ag nanowire LbL substrate for enhanced optical applications was developed and characterized by UV-visible surface plasmon absorption and AFM. It was employed as a substrate for SERS/SERRS measurements from solution-casted and Langmuir-Blodgett samples at a variety of excitation energies,

97

and found to provide excellent enhancement of Raman and resonance Raman signals, down to trace levels.

4.6 Avidin/Ag Nanoparticle Layer-by-Layer Films[e]

4.6.1 Introduction

The design of novel nanostructured SERS/SERRS substrates that provide functionality beyond simple optical amplification is now of great interest.[96] In meeting this challenge, materials exhibiting strong, bio-specific interactions promise to be among the most widely used. These include, among others, enzyme/substrate, antibody/antigen, and DNA strand/complementary strand systems.[37,97-99] Of course, for the functionality of these systems to be effectively coupled with the unique optical properties of metallic nanoparticles, to produce the next generation of SERS/SERRS substrates, they will first have to be incorporated together into well designed nanoarchitectures. One of the best strategies for accomplishing this goal is through the use of the simple and inexpensive layer-by-layer (LbL) technique for thin film fabrication, which has been employed using a wide variety of different materials, including biopolymers,[33] proteins,[100] quantum dots,[101] and metallic nanoparticles.[80]

In the work discussed in this section, the LbL technique is employed to efficiently couple the strong natural biotin-chelating ability of the glycoprotein avidin with the powerful optical enhancing properties of colloidal Ag nanoparticles to produce functional, chemically specific SERS/SERRS substrates.[102,103] These substrates are characterized by surface plasmon absorption spectroscopy, atomic force microscopy, and

---

[e] This work was done in close collaboration with N. P. W. Pieczonka. Most aspects of this work benefited from his valuable contributions.

98

SERRS, as a function of the number of bilayers deposited. They are demonstrated to effectively enhance Raman and resonance Raman scattering signals throughout the entire visible region of the electromagnetic spectrum, and enhancement is shown to be uniform on the surface through the use of 2D SERRS mapping. It is shown that biotinylated species are preferentially adsorbed from solution by these thin films, relative to their non-tagged counterparts, leading to concentration enhancements and improved SERRS detection sensitivities of ca. 10^2 (Figure 4.22). It is also demonstrated that species of interest can be biotinylated in situ in aqueous solution, using existing strategies, and detected with corresponding increases in intensity and sensitivity.

Layer-by-layer film on glass

Avidin   Biotinylated Dye   Ag Nanoparticle
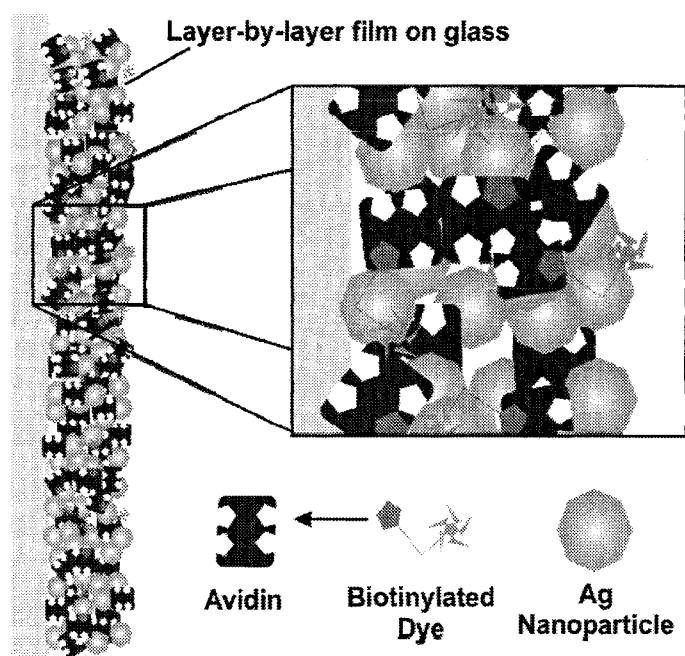
Figure 4.22 Chemically selective adsorption on avidin/Ag nanoparticle LbL films.

99

4.6.2 Characterization of Avidin/Ag Nanoparticle LbL Films

Based on the method of Lee and Meisel,[69] colloidal Ag nanoparticles were prepared in solution through the citrate reduction of $AgNO_3$. The collapse of such colloidal solutions is prevented by the repulsion of negative charges at the surface of different nanoparticles that result from the adsorption of ions and the ionization of surface adsorbates. The extent of the surface charge of colloidal nanoparticles can be monitored through the measurement of the potential across the electrical double layer formed at the particle-liquid interface. This potential is referred to as the zeta potential, ζ, and has recently been measured to be about -50 mV for this colloidal Ag solution at neutral pH.[104] Avidin, on the other hand, is cationic at neutral pH due to its isoelectric point of 10.5.[105] Together, these facts make the effective fabrication of LbL films of these materials, through electrostatic interactions, possible.

After each layer of these avidin/Ag nanoparticle LbL films was deposited, surface plasmon absorption spectra were recorded. In Figure 4.23, these are shown for films with 2, 4, 6, 8, 10, 12, and 14 bilayers. It can be seen that the extinction of these films grows with increasing number of bilayers, confirming effective film building and the advantage of adsorption over desorption under these conditions. These spectra reveal two well resolved high energy bands at ca. 383 and 430 nm that redshift slightly with increasing number of bilayers. These bands can be assigned to quadrupolar and dipolar particle plasmon resonances, respectively, with the quadrupolar mode being due to the presence of larger spherical particles with diameters up to 70 nm.[53] The slight redshifting of these bands can be attributed to changes in the dielectric function of the medium surrounding the particles with film growth. Also observed in these spectra is a very

100

broad feature with a maximum at about 700 nm that increases in relative intensity, and then stabilizes, as the number of bilayers deposited is increased. This band can be assigned to dimers and higher order particle aggregates that are known to increase in number as film growth proceeds. Also shown in Figure 4.23, are digital camera and 50x microscope images of an LbL film made up of 14 bilayers. From these, it can be seen that this film is relatively homogeneous on the macro scale, but becomes less so on the micro scale where Raman measurements are generally made. Large clusters of nanoparticles can be clearly observed in the latter image.
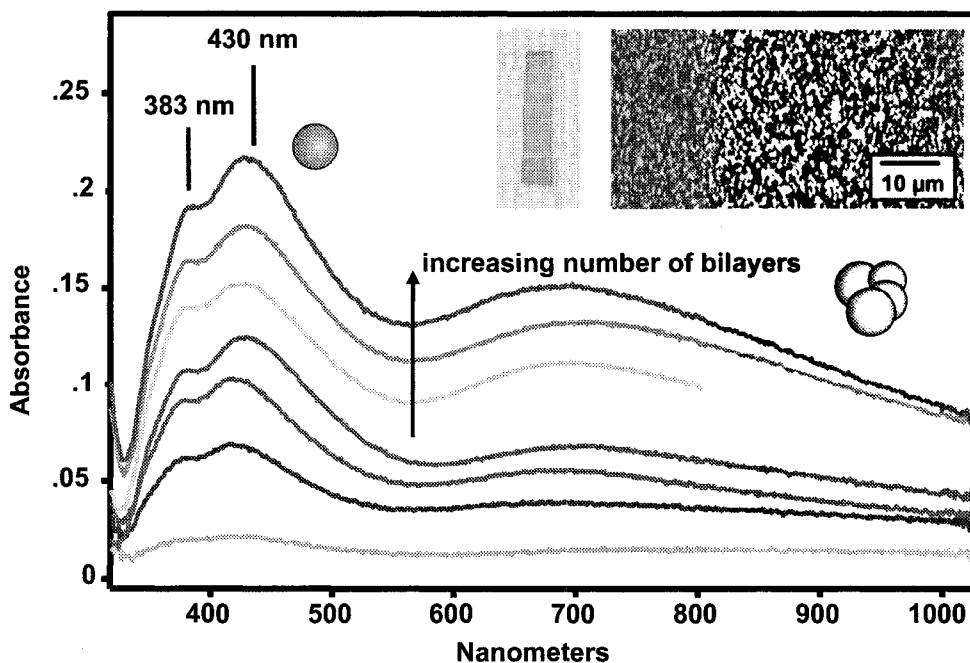
Figure 4.23 Surface plasmon absorption of avidin/Ag nanoparticle LbL films. Increasing extinction of avidin/Ag nanoparticle LbL films with increasing number of bilayers (2, 4, 6, 8, 10, 12, 14). Insets show digital camera image (left) and 50x microscope image (right) of a 14 bilayer film.

To demonstrate the relationship between the optical and physical properties of the avidin/Ag nanoparticle LbL films produced in this work, their surface morphologies were analyzed by AFM imaging. Selected representative topographical images are presented in Figure 4.24 for substrates consisting of 2, 4, 6, 8, 12, and 14 layers. It can be seen that as the number of bilayers deposited is increased, there is a general trend toward greater surface coverage, increased particle-particle interaction, and cluster/aggregate formation, as is expected. This trend is supported by increasing RMS roughness values with film growth, from 7.2 nm for 2 bilayers to 32.6 nm for 14 bilayers. Also, on the basis of the analysis of these images, the diameter of single isolated particles was found to be between ca. 30 and 70 nm, while clusters were generally found to range between ca. 150 and 500 nm. These results are consistent with what is expected on the basis of the surface plasmon results presented for these films, and confirm the presence of interacting nanoparticle clusters that are well known to be the source of the strongest EM enhancements of Raman and resonance Raman scattering.
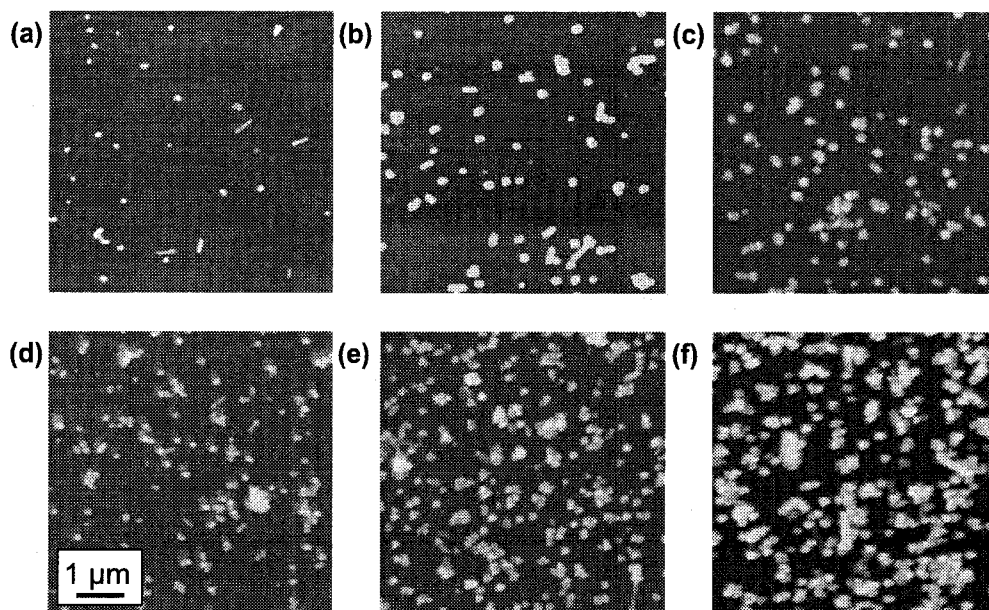
Figure 4.24 AFM images of avidin/Ag nanoparticle LbL films. Tapping mode AFM images recorded from **(a)** 2, **(b)** 4, **(c)** 6, **(d)** 8, **(e)** 12, and **(f)** 14 bilayer films.

4.6.3 SERS/SERRS from Avidin/Ag Nanoparticle LbL Films

In Figure 4.25, the relationship between the number of avidin/Ag nanoparticle bilayers incorporated into these LbL films, and the mean integrated intensity of rhodamine 6G (R6G) SERRS derived from them, is examined. In each case, 5 μL of a 10^{-5} M aqueous solution of the common SERRS dye was cast onto the film, allowed to dry, and then probed with laser excitation at 514.5 nm using identical power, and accumulation time. This laser is in full resonance with the strong electronic transition of the molecular system as well as the surface plasmon resonance of the Ag nanoparticles incorporated into the LbL substrate, fulfilling the double resonance condition of SERRS. To obtain values for mean integrated SERRS intensity, 10 spectra were acquired from different spots on each sample and the 1650 cm^{-1} band of the molecule was fit using

103

appropriate spectroscopic software. The mean of these 10 values was then determined and plotted in Figure 4.25. This plot reveals a general increase in mean integrated SERRS intensity up to ca. 8 bilayers, while from 8 to 14 bilayers, intensity appears to level off. This trend generally agrees well with extinction and AFM results, and can be explained on the basis on increasing surface coverage, and particle-particle interaction with increasing number of bilayers. Based on these results, it was decided that 14 bilayer films would be used for all further application.
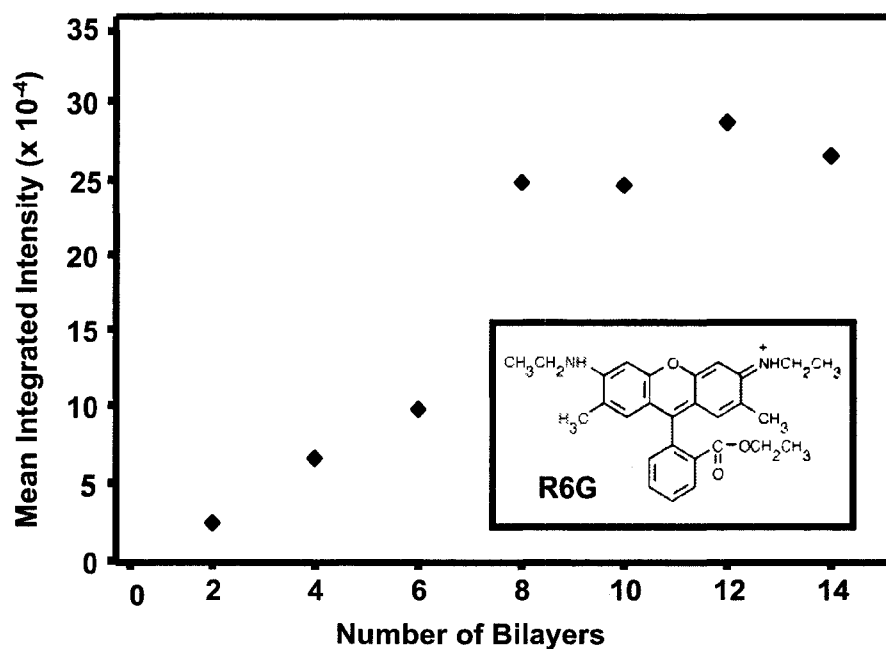
Figure 4.25 SERRS intensity increase with avidin/Ag nanoparticle film growth. Mean integrated SERRS intensity of 1650 cm^{-1} band of R6G as a function of the number of bilayers incorporated into the LbL substrate.

The ability of avidin/Ag nanoparticle LbL films to effectively enhance Raman and resonance Raman scattering signals throughout the visible was explored, and the results are shown in Figure 4.26. Measurements were made from a 5 µL drop of 10^{-5} M R6G cast onto a 14 bilayer film, and recorded with laser excitation at 442, 514.5, 633, and 785 nm. Notably, strong SERS/SERRS was observed from this substrate at all wavelengths, making it highly flexible for application in a variety of different laboratory settings, with diverse chemical systems. At 442 and 514 nm excitation, this molecular system is resonant, at 633 nm it is pre-resonant, and at 785 nm it is effectively non-resonant. Therefore these results are properly referred to as SERRS, pre-SERRS, and SERS, respectively. Differences between these phenomena are revealed through the variation of the relative intensities in the spectra of Figure 4.26 as laser excitation is brought in and out of resonance with the molecular electronic transition.
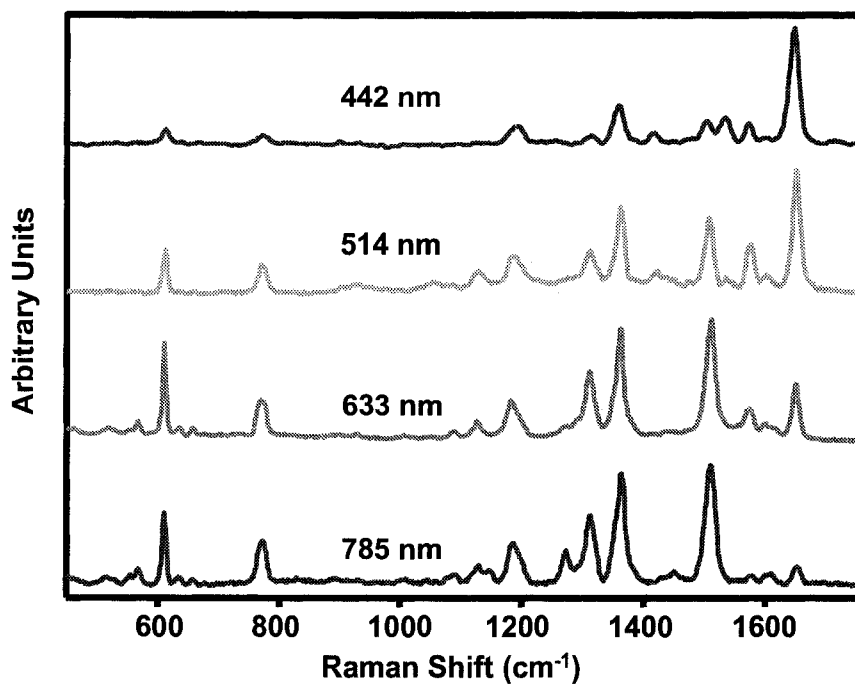
Figure 4.26   Broad enhancement region of avidin/Ag nanoparticle films. SERS/SERRS spectra of R6G, cast onto a 14 bilayer film, and recorded using laser excitation at **(a)** 442, **(b)** 514, **(c)** 633, and **(d)** 785 nm.

4.6.4 Concentration Enhancement Through Chemical Selectivity

The ability of these avidin/Ag nanoparticle LbL films to act as chemically selective SERRS substrates was tested and the results are shown in Figure 4.27. A 14 bilayer avidin/Ag nanoparticle film was immersed into a 10^{-4} M solution of a commercially available, biotinylated fluorescein dye, biotin-4-fluorescein (B4F), for 30 min, while another was immersed into a solution of non-tagged fluorescein, at the same concentration, for the same period of time. Both samples were removed, rinsed with distilled water, and dried before SERRS measurements were made using 514.5 nm laser excitation. The spectra obtained from these samples were found to be essentially the

106

same, however, the biotinylated sample was found to exhibit absolute intensities that were, on average, 10^2 greater than those measured for its non-tagged counterpart. It was also found that the non-tagged fluorescein could not be observed at all spots and was near its detection limit, while biotin-4-fluorescein could be readily observed at all spots with strong intensity. The uniformity of this response is demonstrated in the 2D spatial SERRS mapping results of Figure 4.27(g). Moreover, B4F was found to be detectable from substrates dipped, using identical procedures, into solutions with concentrations as low as 10^{-7} M, while non-tagged fluorescein was undetectable when extracted from solutions with concentrations below 10^{-5} M. In both cases, SERRS spectra result from the same resonant, central chromophore, with an unchanged Raman cross section. Therefore, the 100 fold increase in intensity, and related 100 fold increase in detection sensitivity, associated with biotinylation, can be attributed to a concentration enhancement that arises specifically as a result of the strong, bio-specific interaction between the avidin in the LbL film and the biotin tag.
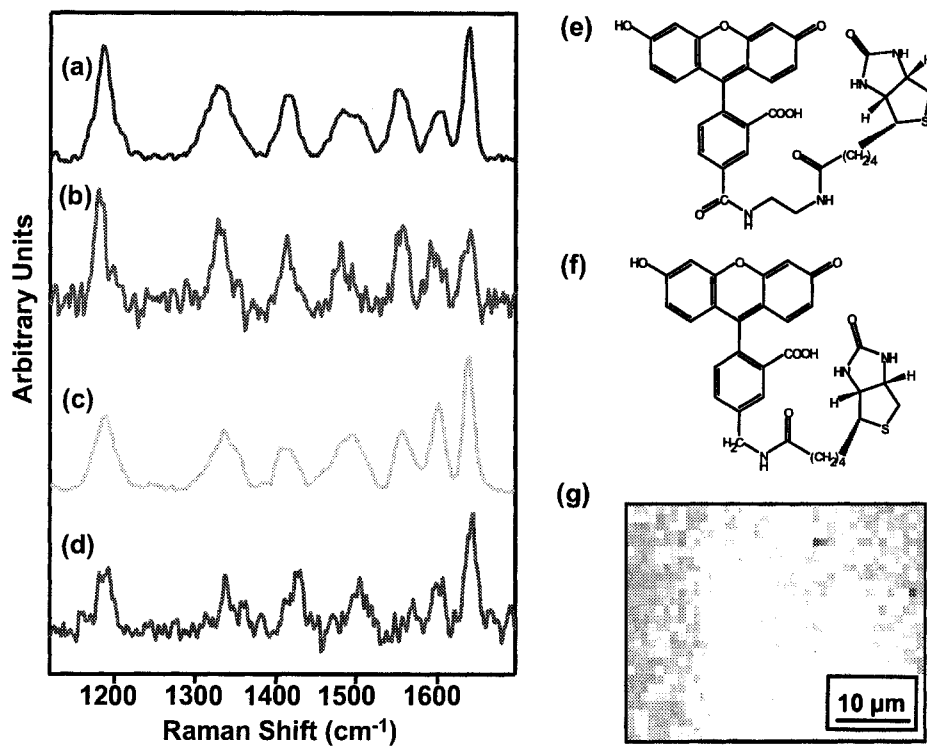
Figure 4.27 Chemical Selective SERRS from avidin/Ag nanoparticle LbL films.

SERRS spectra, recorded using 514.5 nm excitation, from avidin/Ag nanoparticle layer-by-layer film dipped into (a) 10^{-4} and (b) 10^{-7} M B4F, and (c) 10^{-4} and (d) 10^{-7} M biotinylated 5-AF solutions. Shown, in (e) and (f), respectively, are the structures of these biotinylated species. In (g), a 2D spatial map of SERRS intensities for B4F, showing highly uniform response, is shown.

The concentration enhancement and improved detection limits discussed here for pre-synthesized biotinylated species are clearly significant; however, it is also interesting to pursue similar results for analytes biotinylated in situ in aqueous solution. This approach further broadens the possible uses for this substrate, as there are many well-established biotinylation procedures available in the literature. Here, as a proof of

108

concept, a water soluble biotinylation reagent, biotin 3-sulfo-*N*-hydroxysuccinimide ester was reacted in-situ with 5-(aminomethyl)fluorescein (5-AF) in pH 7.5 PBS solution. The two reagents were combined in a 1:1 molar ratio, at room temperature, to produce a solution 10^{-4} M in each. The reaction was allowed 30 min for completion before LbL film substrates were immersed into it, and a solution of non-tagged 5-AF, for 30 min. Upon removal, the films were rinsed and dried, and SERRS spectra were recorded. It was found that in situ biotinylation yielded similar 10^2 improvements in signal intensity as a result of concentration enhancement. Moreover, it was found that biotinylated 5-AF was also detectable down to 10^{-7} M, with a corresponding 10^2 advantage in detection limits over its non-tagged counterpart. Finally, to ensure that observed enhancements were indeed the result of preferential capture of biotinylated species, films were immersed into concentrated solutions of biotin before immersion into solutions of the two biotinylated analytes. In both cases, saturation of the surface with biotin was in fact found to greatly reduce SERRS intensities, thus confirming the importance of biorecognition in this work.

4.6.5 Conclusions

In this section, the fabrication, characterization, and application of avidin/Ag nanoparticle layer-by-layer (LbL) films as chemically selective substrates for SERS/SERRS was discussed. The growth of these nanocomposite films was characterized by surface plasmon absorption, and AFM imaging. They were found to exhibit significant Raman/resonance Raman enhancing capability across a broad spectral window, covering essentially the entire visible region. They were also found to demonstrate strong, bio-specific interactions with two biotinylated species, thus

109

providing chemical selectivity, with increased sensitivity, in substrates for surface-enhanced spectroscopy. Biotinylated dye molecules were shown to be selectively captured by these substrates, and this preferential adsorption yielded an additional concentration enhancement of ca. 10^2, while detection limits were improved by at least 2 orders of magnitude. It is anticipated that this development will promote further the coupling of the unique optical properties of metallic nanoparticles with systems demonstrating strong bio-specific interactions, particularly through the use of the powerful LbL technique.

4.7 Summary

In this chapter, the fabrication, characterization, and application of several unique thin film SERS/SERRS substrates have been discussed. These substrates were prepared using the powerful film fabrication techniques of vacuum evaporation, nanocomposite solution casting, and layer-by-layer deposition using a variety of interesting materials including Ag and Au nanoparticles, chitosan, dendrimers, and the glycoprotein avidin. They were characterized using the techniques of surface plasmon absorption, AFM, TEM, XPS, and IR absorption, then utilized as effective substrates for SERS/SERRS measurements. In addition to demonstrating strong enhancement of Raman and resonance Raman signals, these substrates also showed a variety of other positive characteristics that will help in the development of SERS/SERRS as powerful analytical techniques.

110

References

(1)   Haynes, C. L.; McFarland, A. D.; Van Duyne, R. P. *Anal. Chem. A-Pages* **2005**, *77*, 338A-346A.

(2)   Aroca, R. F.; Alvarez-Puebla, R. A.; Pieczonka, N.; Sanchez-Cortez, S.; Garcia-Ramos, J. V. *Adv. Colloid Interface Sci.* **2005**, *116*, 45-61.

(3)   Moskovits, M.; Jeong, D. H. *Chem. Phys. Lett.* **2004**, *397*, 91-95.

(4)   Zhang, X.; Zhao, J.; Whitney, A. V.; Elam, J. W.; Van Duyne, R. P. *J. Am. Chem. Soc.* **2006**, *128*, 10304-10309.

(5)   Kneipp, K.; Kneipp, H.; Itzkan, I.; Dasari, R. R.; Feld, M. S. *Chem. Rev.* **1999**, *99*, 2957-.

(6)   Lee, S. J.; Morrill, A. R.; Moskovits, M. *J. Am. Chem. Soc.* **2006**, *128*, 2200-2201.

(7)   Kneipp, K.; Wang, Y.; Kneipp, H.; T. Perelman, L. T.; Itzkan, I. *Phys. Rev. Lett.* **1997**, *78*, 1667-1670.

(8)   Nie, S.; Emory, S. R. *Science* **1997**, *275*, 1102-1106.

(9)   Xu, H.; Bjerneld, E. J.; Kall, M.; Borjesson, L. *Phys. Rev. Lett.* **1999**, *83*, 4357-4360.

(10)   Krug, J. T., II; Wang, G. D.; Emory, S. R.; Nie, S. *J. Am. Chem. Soc.* **1999**, *121*, 9208-9214.

(11)   Michaels, A. M.; Nirmal, M.; Brus, L. E. *J. Am. Chem. Soc.* **1999**, *121*, 9932-9939.

(12)   Weiss, A.; Haran, G. *J. Phys. Chem. B* **2001**, *105*, 12348-12354.

(13)   Meixner, A. J.; Vosgrone, T.; Sackrow, M. *J. Lumin.* **2001**, *94&95*, 147-152.

(14)   Eggeling, C.; Schaffer, J.; Seidel, C. A. M.; Korte, J.; Brehm, G.; Schneider, S.; Schrof, W. *J. Phys. Chem. A* **2001**, *105*, 3673-3679.

(15)   Maruyama, Y.; Ishikawa, M.; Futamata, M. *Chem. Lett.* **2001**, 834-835.

(16)   Bizzarri, A. R.; Cannistraro, S. *Appl. Spectrosc.* **2002**, *56*, 1531-1537.

(17)   Etchegoin, P.; Liem, H.; Maher, R. C.; Cohen, L. F.; Brown, R. J. C.; Hartigan, H.; Milton, M. J. T.; Gallop, J. C. *Chem. Phys. Lett.* **2002**, *366*, 115-121.

(18)   Habuchi, S.; Cotlet, M.; Gronheid, R.; Dirix, G.; Michiels, J.; Vanderleyden, J.; De Schryver, F. C.; Hofkens, J. *J. Am. Chem. Soc.* **2003**, *125*, 8446-8447.

(19)   Itoh, T.; Hashimoto, K.; Ikehata, A.; Ozaki, Y. *Chem. Phys. Lett.* **2004**, *389*, 225-229.

(20)   Constantino, C. J. L.; Lemma, T.; Antunes, P. A.; Aroca, R. *Anal. Chem.* **2001**, *73*, 3674-3678.

(21)   Constantino, C. J. L.; Lemma, T.; Antunes, P. A.; Aroca, R. *Spectrochim. Acta, Part A* **2002**, *58A*, 403-409.

(22)   Constantino, C., J. L.; Lemma, T.; Antunes Patricia, A.; Goulet, P.; Aroca, R. *Appl. Spectrosc.* **2003**, *57*, 649-654.

(23)   Goulet, P. J. G.; Pieczonka, N. P. W.; Aroca, R. F. *Can. J. Anal. Sci. Spect.* **2003**, *48*, 146-152.

(24)   Pieczonka, N. P. W.; Aroca, R. F. *ChemPhysChem* **2005**, *6*, 2473-2484.

(25)   Goulet, P. J. G.; Pieczonka, N. P. W.; Aroca, R. F. *Anal. Chem.* **2003**, *75*, 1918-1923.

(26)   Goulet, P. J. G.; Pieczonka, N. P. W.; Aroca, R. F. *J. Raman Spectrosc.* **2005**, *36*, 574-580.

112

(27)   Aroca, R. F.; Clavijo, R. E. *Spectrochim. Acta, Part A* **1991**, *47A*, 271-277.

(28)   Ravi Kumar, M. N. V.; Muzzarelli, R. A. A.; Muzzarelli, C.; Sashiwa, H.; Domb, A. J. *Chem. Rev.* **2004**, *104*, 6017-6084.

(29)   Sandford, P. A. Chitosan: commercial uses and potential applications,. In *Chitin and Chitosan: Sources, Chemistry, Biochemistry, Physical Properties and Applications,*; Skjak, G., Anthonsen, T., Sandford, P., Eds.; Elsevier: New York, 1988; pp 51-69.

(30)   Rabea, E. I.; Badawy, E.-T.; Stevens, C. V.; Smagghe, G.; Steurbaut, W. *Biomacromolecules* **2003**, *4*, 1457-1465.

(31)   Kurita, K. *Prog. Polym. Sci.* **2001**, *26*, 1921-1971.

(32)   Ligler, F. S.; Schauer, C. L.; Chen, M.-S.; Chatterley, M.; Eisemann, K.; Welsh, E. R.; Price, R. R.; Schoen, P. E. *Thin Solid Films* **2003**, *434*, 250-257.

(33)   dos Santos Jr., D. S.; Riul Jr., A.; Malmegrin, R. R.; Fonseca, F. J.; Oliveira Jr., O. N.; Mattoso, L. H. C. *Macromol. Biosc.* **2003**, *3*, 591-595.

(34)   Daniel, M.-C.; Astruc, D. *Chem. Rev.* **2004**, *104*, 293-346.

(35)   Mohr, C.; Hofmeister, H.; Radnik, J.; Claus, P. *J. Am. Chem. Soc.* **2003**, *125*, 1905-1911.

(36)   Hone, D. C.; Walker, P. I.; Evans-Gowing, R.; Fitzgerald, S.; Beeby, A.; Chambrier, I.; Cook, M. J.; Russell, D. A. *Langmuir* **2002**, *18*, 2985-2987.

(37)   Cao, Y. C.; Jin, R.; Mirkin, C. A. *Science* **2002**, *297*, 1536-1540.

(38)   Natan, M. J.; Lyon, L. A. Surface Plasmon Resonnance Biosensing with Colloidal Au Amplification. In *Metal Nanoparticles: Synthesis, Characterization and Applications*; Feldheim, D. L., Colby, A. F., Jr., Eds.; Marcel Dekker: New York, 2002; pp 183-205.

(39)   Rosi, N. L.; Mirkin, C. A. *Chem. Rev.* **2005**, *105*, 1547-1562.

(40)   Kneipp, K.; Kneipp, H.; Kneipp, J. *Acc. Chem. Res.* **2006**, *39*, 443-450.

(41)   Kneipp, K.; Haka, A. S.; Kneipp, H.; Badizadegan, K.; Yoshizawa, N.; Boone, C.; Shafer-Peltier, K. E.; Motz, J. T.; Dasari, R. R.; Feld, M. S. *Appl. Spectrosc.* **2002**, *56*, 150-154.

(42)   Kneipp, J.; Kneipp, H.; McLaughlin, M.; Brown, D.; Kneipp, K. **2006**, *6*, 2225-2231.

(43)   Frens, G. *Nat. Phys. Sci.* **1973**, *241*, 20-22.

(44)   Bunge, S. D.; Boyle, T., J.; Headley, T., J. *Nano Lett.* **2003**, *3*, 901-905.

(45)   Liz-Marzán, L. M. *Mater. Today* **2004**, *7*, 26-31.

(46)   Hassenkam, T.; Norsgaard, K.; Iversen, L.; Kiely, C.; Brust, M.; Bjornholm, T. *Adv. Mater.* **2002**, *14*, 1126-1130.

(47)   Kim, J.-U.; Cha, S.-H.; Shin, K.; Jho, J. Y.; Lee, J.-C. *J. Am. Chem. Soc.* **2005**, *127*, 9962-9963.

(48)   Brust, M.; Stuhr-Hansen, N.; Norgaard, K.; Christensen, J. B.; Nielsen, L. K.; Bjornholm, T. *Nano Lett.* **2001**, *1*, 189-191.

(49)   Suzuki, M.; Niidome, Y.; Kuwahara, Y.; Terasaki, N.; Inoue, K.; Yamada, S. *J. Phys. Chem. B* **2004**, *108*, 11660-11665.

(50)   Tian, S.; Liu, J.; Zhu, T.; Knoll, W. *Chem. Mater.* **2004**, *16*, 4103-4108.

(51)   Toshima, N.; Yonezawa, T. *New J. Chem.* **1998**, *22*, 1179-1201.

(52)   El-Sayed, M. A.; Link, S. *J. Phys. Chem. B* **1999**, *103*, 8410-8426.

(53)   Kelly, K. L.; Coronado, E.; Zhao, L. L.; Schatz, G. C. *J. Phys. Chem. B* **2003**, *107*, 668-677.

(54)   Mulvaney, P. *Langmuir* **1996**, *12*, 788-800.

(55)   Moskovits, M.; Tay, L.-L.; Yang, J.; Haslett, T. SERS and the single molecule. In *Optical Properties of Nanostructured Random Media*; Shalaev, V. M., Ed.; Springer-Verlag: Berlin Heidelberg, 2002; Vol. 82; pp 215-226.

(56)   Brugnerotto, J.; Lizardi, J.; Goycoolea, F. M.; Arguelles-Monal; Desbrieres, J.; Rinaudo, M. *Polymer* **2001**, *42*, 3569-3580.

(57)   Wu, Y.; Livneh, T.; Zhang, Y. X.; Cheng, G.; Wang, J.; Tang, J.; Moskovits, M.; Stucky, G. D. *Nano Lett.* **2004**, *4*, 2337-2342.

(58)   Green, M.; Liu, F. M. *J. Phys. Chem. B* **2003**, *107*, 13015-13021.

(59)   Chan, S.; Kwon, S.; Koo, T.-W.; Lee, L. P.; Berlin, A. A. *Adv. Mat.* **2003**, *15*, 1595-1598.

(60)   Bjerneld, E. J.; Svedberg, F.; Kaell, M. *Nano Lett.* **2003**, *3*, 593-596.

(61)   Tao, A.; Kim, F.; Hess, C.; Goldberger, J.; He, R.; Sun, Y.; Xia, Y.; Yang, P. *Nano Lett.* **2003**, *3*, 1229-1233.

(62)   Brolo, A.; Arctander, E.; Gordon, R.; Leathem, B.; Kavanagh, K. L. *Nano Lett.* **2004**, *4*, 2015-2018.

(63)   Semin, D. J.; Rowlen, K. L. *Anal. Chem.* **1994**, *66*, 4324-4331.

(64)   Schlegel, V. L.; Cotton, T. M. *Anal. Chem.* **1991**, *63*, 241-247.

(65)   Albrecht, M. G.; Creighton, J. A. *J. Am. Chem. Soc.* **1977**, *99*, 5215-5217.

(66)   Ren, B.; Lin, X.-F.; Yang, Z.-L.; Liu, G.-K.; Aroca, R. F.; Mao, B. W.; Tian, Z. Q. *J. Am. Chem. Soc.* **2003**, *125*, 9598-9599.

(67)   Liao, P. F.; Bergman, J. G.; Chemla, D. S.; Wokaun, A.; Melngailis, J.; Hawryluk, A. M.; Economou, N. P. *Chem. Phys. Lett.* **1981**, *82*, 355-359.

(68)   Haynes, C. L.; McFarland, A. D.; Smith, M. T.; Hulteen, J. C.; Van Duyne, R. P. *J. Phys. Chem. B.* **2002**, *106*, 1898-1902.

(69)   Lee, P. C.; Meisel, D. *J. Phys. Chem.* **1982**, *86*, 3391-3395.

(70)   Sanchez-Cortes, S.; Garcia-Ramos, J. V.; Morcillo, G. *J. Coll. Int. Sci.* **1994**, *167*, 428-436.

(71)   Decher, G. *Science* **1997**, *277*, 1232-1237.

(72)   Raposo, M.; Oliveira Jr., O. N. *Braz. J. Phys.* **1998**, *28*, 392-404.

(73)   Zucolotto, V.; Barbosa Neto, N. M.; Rodrigues Jr., J. J.; Constantino, C. J. L.; Zilio, S. C.; Mendonca, C. R.; Aroca, R. F.; Oliveira Jr., O. N. *J. Nanosci. Nanotechnol.* **2004**, *4*, 855-860.

(74)   Liu, H.; Rusling, J. F.; Hu, N. *Langmuir* **2004**, *20*, 10700-10705.

(75)   Tomalia, D. A.; Naylor, A. M.; Goddard, W. A. *Angew. Chem. Int. Ed.* **1990**, *29*, 138-175.

(76)   Esumi, K.; Suzuki, A.; Yamahira, A.; Torigoe, K. *Langmuir* **2000**, *16*, 2604-2608.

(77)   Manna, A.; Imae, T.; Aoi, K.; Okada, M.; Yogo, T. *Chem. Mat.* **2001**, *13*, 1674-1681.

(78)   Musick, M. D.; Keating, C. D.; Lyon, L. A.; Botsko, S. L.; Pena, D. J.; Holliway, W. D.; McEvoy, T. M.; Richardson, J. N.; Natan, M. J. *Chem. Mater.* **2000**, *12*, 2869-2881.

(79)   Esumi, K.; Hosoya, T.; Suzuki, A.; Torigoe, K. *J. Coll. Int. Sci.* **2000**, *226*, 346-352.

(80)   Schneider, G.; Decher, G. *Nano Lett.* **2004**, *4*, 1833-1839.

(81)   Tian, S.; Liu, J.; Zhu, T.; Knoll, W. *Chem. Mater.* **2004**, *16*, 4103-4108.

(82)   Salgueirino-Maceira, V.; Caruso, F.; Liz-Marzan, L. M. *J. Phys. Chem. B* **2003**, *107*, 10990-10994.

(83)   Li, X.; Xu, W.; Zhang, J.; Jia, H.; Yang, B.; Zhao, B.; Li, B.; Ozaki, Y. *Langmuir* **2004**, *20*, 1298-1304.

(84)   Goulet, P. J. G.; Dos Santos, D. S., Jr.; Alvarez-Puebla, R. A.; Oliveira, O. N., Jr.; Aroca, R. F. *Langmuir* **2005**, *21*, 5576-5581.

(85)   Raposo, M.; Pontes, R. S.; Mattoso, L. H. C.; Oliveira Jr., O. N. *Macromolecules* **1997**, *30*, 6095-6101.

(86)   Alvarez-Puebla, R. A.; dos Santos Jr., D. S.; Aroca, R. F. *Analyst* **2004**, *129*, 1251-1256.

(87)   Wang, Y.; Joshi, P. P.; Hobbs, K. L.; Johnson, M. B.; Schmidtke, D. W. *Langmuir* **2006**, *22*, 9776-9783.

(88)   Recksiedler, C. L.; Deore, B. A.; Freund, M. S. *Langmuir* **2006**, *22*, 2811-2815.

(89)   dos Santos, D. S., Jr.; Cardoso, M. R.; Leite, F. L.; Aroca, R. F.; Mattoso, L. H. C.; Oliveira, O. N., Jr.; Mendonca, C. R. *Langmuir* **2006**, *22*, 6177-6180.

(90)   Aroca, R. F.; Goulet, P. J. G.; Dos Santos, D. S., Jr.; Alvarez-Puebla, R. A.; Oliveira, O. N., Jr. *Anal. Chem.* **2005**, *77*, 378-382.

(91)   Jeong, D. H.; Zhang, Y. X.; Moskovits, M. *J. Phys. Chem. B* **2004**, *108*, 12724-12728.

(92)   Petty, M. C. *Langmuir-Blodgett Films. An Introduction*; Cambridge University Press: Cambridge, 1996.

(93)   Sun, Y. G.; Gates, B.; Mayers, B.; Xia, Y. N. *Nano Letters* **2002**, *2*, 165-168.

(94)   Papavassilou, G. C. *Prog. Solid State Chem.* **1979**, *12*, 185-271.

117

(95)   Aroca, R.; Jennings, C.; Kovacs, G. J.; Loutfy, R. O.; Vincett, P. S. *J. Phys. Chem.* **1985**, *898*, 4051-4054.

(96)   Rohr, T. E.; Cotton, T. M.; Ni, F.; Tarcha, P. J. *Anal. Biochem.* **1989**, *182*, 388-398.

(97)   Cao, Y. C.; Jin, R.; Nam, J.-M.; Thaxton, C. S.; Mirkin, C. A. *J. Am. Chem. Soc.* **2003**, *125*, 14676-14677.

(98)   Vo-Dinh, T.; Cullum, B. *Fresenius J. Anal. Chem.* **2000**, *3*, 540-551.

(99)   Ni, J.; Lipert, R. J.; Dawson, G. B.; Porter, M. D. *Anal. Chem.* **1999**, *71*, 4903-4908.

(100)   Anzai, J.; Nishimura, M. *J. Chem. Soc. Perk. T 2* **1997**, 1887-1889.

(101)   Zhang, H.; Zhou, Z.; Liu, K.; Wang, R.; Yang, B. *J. Mater. Chem.* **2003**, *13*, 1356-1361.

(102)   Goulet, P. J. G.; Pieczonka, N. P. W.; Aroca, R. F. In *New Approaches in Biomedical Spectroscopy*; Kneipp, K., Aroca, R. F., Kneipp, H., Wentrup-Byrne, E., Eds.; American Chemical Society: Washington, DC, in press.

(103)   Pieczonka, N. P. W.; Goulet, P. J. G.; Aroca, R. F. *J. Am. Chem. Soc.* **2006**, *128*, 12626-12627.

(104)   Alvarez-Puebla, R. A.; Arceo, E.; Goulet, P. J. G.; Garrido, J. J.; Aroca, R. F. *J. Phys. Chem. B* **2005**, *109*, 3787-3792.

(105)   Green, N. M. *Method Enzymol.* **1970**, *18*, 418-424.

Chapter 5

INTERPRETATION OF SURFACE-ENHANCED RAMAN SCATTERING:

TWO CASE STUDIES OF UNUSUAL COMPLEXITY

119

5.1 Interpretation of the SERS of Surface Complexes

The interpretation of SERS spectra is often taken for granted by researchers that are excited by the possibilities afforded by immense signal enhancement. Many are focused on the development of the technique rather than the study of specific molecular systems, and so often use well known analytes where spectral interpretation is not required. This, of course, is quite appropriate and has led to a great deal of knowledge on the nature of the effect. However, it is also essential that fundamental work be done on the interpretation of the spectra of different molecular systems, so that non-specialists will be able to apply the technique widely and effectively. To avoid gross misinterpretation of results, comprehensive, and sometimes complex, vibrational analyses must be performed prior to pursuing more advanced uses for this technique, such as the study of single-molecules.

Surface-enhanced Raman scattering (SERS), and surface-enhanced infrared absorption (SEIRA)[1-3] occur near the surface of metal nanostructures that polarize the electric field of incident light, and consequently, it is necessary to account for the orientation of adsorbates in the interpretation of experimental spectra. A similar situation exists for infrared (reflection absorption infrared spectroscopy, RAIRS[4]) and Raman spectra of molecules adsorbed on reflecting flat metal surfaces. Greenler demonstrated that the light at these surfaces is highly polarized, and at appropriate angles of incidence the p-polarized (parallel to the plane of incidence) component of the electromagnetic wave is three orders of magnitude larger than the s-component.[5] Since the component perpendicular to the surface (P) dominates, we expect to see only those vibrational modes whose polarizability derivatives (Raman), or dipole moment derivatives (IR), align well

120

with the field. This leads to the concept of surface selection rules for preferentially oriented molecules,[6] where vibrational intensities depend upon the contribution of the normal and tangential components of the local electric field near the surface.

Physisorbed molecules show weak interactions with surfaces, and because of this, they often orient randomly and maintain their native symmetry at surfaces. This makes the interpretation of their surface-enhanced vibrational spectra relatively simple, as the molecular selection rules do not change, and a comparison can be made directly with reference Raman scattering and infrared absorption spectra. In the cases of chemical adsorption, surface coordination complex formation, or physical adsorption with preferential orientation, however, a new complexity is introduced that can make the interpretation of spectra very challenging. Chemisorption and coordination complex formation, in particular, involve strong interactions of analytes with surfaces that result in drastic perturbations of the molecule's structure, and therefore lead to striking changes in Raman and infrared spectra. These radical changes are particularly likely for small molecules where interactions through one functional group can often have major influence on the rest of the molecule. The formation of new surface species can thus be a very complicating factor in the interpretation of SERS and SEIRA spectra.

Meeting the challenge of interpretation for such systems generally requires a multi-prong approach involving computation of the molecule and the possible surface complex, in addition to measuring various polarized spectra experimentally, and accounting for the effect of the excitation frequency in Raman scattering. Recently, two studies examined the chemical adsorption of different molecules on Ag surfaces using systematic approaches that brought together a variety of techniques.[7,8] In these studies,

121

the authors calculated the optimized geometries and Raman spectra of analyte-Ag complexes using density functional theory (DFT) methods and compared them to experimental SERS spectra, where there was found to be good agreement. DFT methods have recently become very widely used and popular owing to their accuracy and low computational cost. These methods minimize an energy functional rather than handling a wavefunction for each of the electrons in an N-electron system, and because of this simplification they are of much lower computational cost than other correlational techniques. In this chapter, they are employed, along with various spectroscopic techniques, to study the surface complexes of salicylic acid (SAL) and 1-naphthylamine (1-NA) on silver.

5.2 Chemical Adsorption of Salicylate on Silver

5.2.1 Introduction

Salicylic acid is a molecule that is of interest to science for several reasons. Perhaps the most important of these are its applications in cosmetic and pharmaceutical products, including its use in the synthesis of aspirin (acetyl salicylic acid).[9] Several vibrational studies of salicylic acid and its ions have been reported in the literature,[10] including a few that have employed SERS.[9,11-13] These reports show inconsistencies with regard to the question of the adsorption of the molecule on Ag. In one report it is claimed that salicylic acid interacts with the colloidal Ag surface through both its carboxylate and phenolate groups,[9] while in other reports adsorption is concluded to occur only through the carboxylate group,[11,12] or in a "tilted side on orientation", where the C=O stretch was incorrectly assigned.[13] One recently reported SERS spectrum shows

122

large discrepancies with previous work.[11] Much of the confusion that seems to exist in the literature on this topic is likely due to the difficulty of accurately assigning peaks in the SERS spectra of this molecule. This difficulty is primarily due to the complicating factors of preferential orientation and chemisorption, but also to the fact that it has a very crowded Raman spectrum, and shows strong photodegradation at relatively low laser power.

To simplify the assignment of bands in the SERS spectra of this molecule, and shed light on the question of how it chemically adsorbs to Ag, a comprehensive study of this system, involving several experimental and computational methods, was undertaken and is discussed in this section.[14] Surface, surface-enhanced, and normal vibrational spectroscopies, as well as DFT computational methods, were employed. The structure of salicylic acid, and its infrared and Raman spectra, were determined computationally at the B3LYP/6-311+G(d,p) level of theory, and these results were used in the assignment of the vibrational spectra. Surface-enhanced Raman scattering (SERS) spectra from silver nanoparticle films thinly coated with salicylic acid were obtained, and, to discover the nature of the molecule-surface interaction, the optimized geometries and infrared and Raman spectra of two-model salicylate-silver complexes (Ag1 and Ag2) were calculated at the B3LYP/Lanl2DZ level of theory. It was found that good agreement existed between experimentally observed SERS spectra, and the simulated SERS spectra of a complex with the salicylate monoanion bound to a Ag^+ ion through its carboxylate group (Ag1). The carboxylate silver salt of salicylic acid (essentially the Ag1 complex) was also prepared, and its experimental infrared and Raman spectra were recorded for comparison with the surface-enhanced vibrational spectra. These results, along with the

123

application of surface selection rules, suggests that salicylic acid is deprotonated at silver surfaces, interacting through its carboxylate group alone, and is preferentially in a tilted, head-on orientation.

5.2.2 Structures of Salicylic Acid and Silver-Salicylate Complexes

The optimized geometries of salicylic acid, a salicylate monoanion-Ag+ complex (Ag1), and a salicylate bianion-2Ag+ complex (Ag2) are shown in Figure 5.1. Salicylic acid was calculated at the B3LYP/6-311+G(d,p) level of theory, while the two silver complexes were calculated at the B3LYP/Lanl2DZ level of theory. B3LYP employs Becke's three parameter functional[15] and the correlational functional of Lee, Yang, and Parr.[16] It was used for all DFT calculations in this work, because it has been shown to perform very well in the calculation of vibrational spectra. However, the accuracy of the results for the two different Ag complexes may be expected to be lacking due to the limited size of the Lanl2DZ[17,18] basis set that was used, despite its small size, because it is one of the only basis sets available for silver that is also available for second row elements.[7] All three of these structures belong to the C_s point group symmetry, and have 42 vibrational degrees of freedom, or normal vibrational modes. A summary of pertinent structural parameters for the three optimized geometries is presented in Table 5.1, where all bond and angle numbering refers to those numbers assigned in Figure 5.1. Upon close examination of these results, it can be seen that the substitution of Ag atoms for H atoms causes drastic changes in the structural parameters of these molecules. These changes are largely concentrated on the carboxyl and hydroxyl groups of these structures, and have little impact on the aromatic ring parameters, especially at parts distant from the affected groups of the molecule.

124
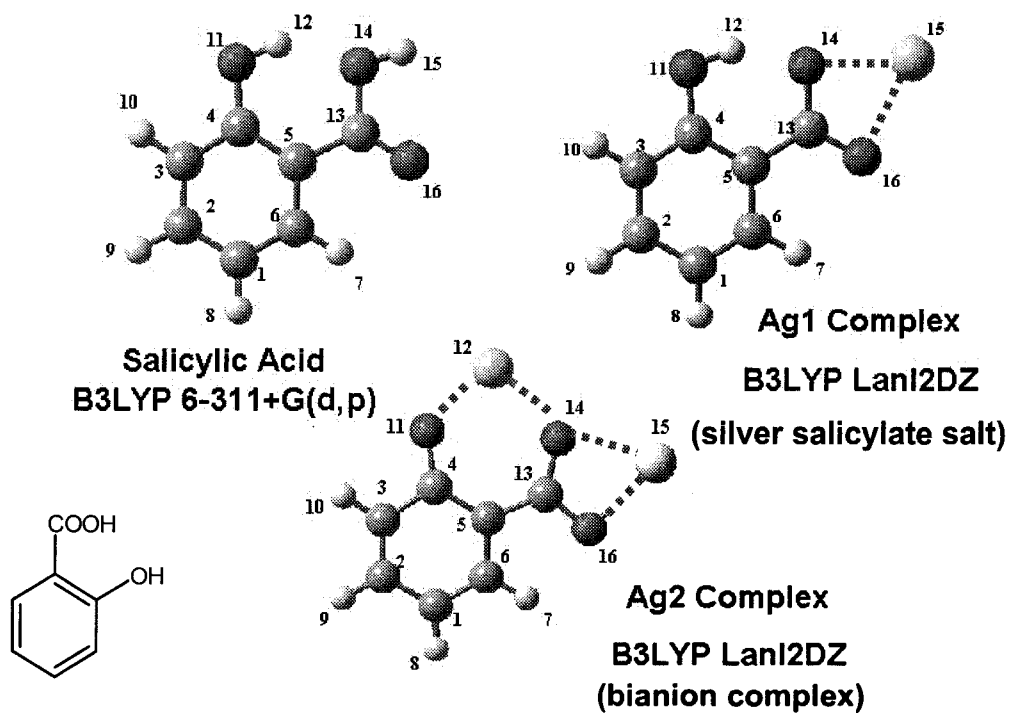
Figure 5.1 Optimized structures of salicylic acid, Ag1, and Ag2. Also shown is the molecular structure of salicylic acid.

Table 5.1. Selected geometrical parameters for salicylic acid, Ag1, and Ag2 complexes.

Bond Lengths (angstroms)			
Bond	**Salicylic Acid**	**Ag1 Complex**	**Ag2 Complex**
1-2	1.400	1.416	1.422
2-3	1.380	1.400	1.380
3-4	1.400	1.410	1.440
4-5	1.410	1.420	1.450
5-6	1.400	1.410	1.430
6-1	1.380	1.400	1.390
6-7	1.080	1.080	1.080
1-8	1.080	1.080	1.080
2-9	1.080	1.080	1.080
3-10	1.080	1.080	1.080
4-11	1.350	1.370	1.330
11-12	0.970	1.000	2.150
5-13	1.470	1.470	1.470
13-14	1.370	1.330	1.330
14-15	0.960	2.310	2.400
13-16	1.200	1.290	1.310

Interatomic Angles (degrees)			
Angle	**Salicylic Acid**	**Ag1 Complex**	**Ag2 Complex**
3-4-11	115.999	118.121	115.450
4-11-12	109.700	108.550	126.490
5-13-14	113.370	118.540	125.590
13-14-15	107.400	91.050	89.580
14-13-16	120.300	119.550	115.630

126

5.2.3 Vibrational Spectra of Salicylic Acid

The experimental Raman and attenuated total reflection (ATR) infrared absorption spectra of bulk salicylic acid powder are directly compared in Figure 5.2 with those calculated at the B3LYP/6-311+G(d,p) level of theory. To supplement these spectra, Table 5.2 shows the calculated and observed infrared and Raman frequencies, calculated symmetries, infrared intensities, Raman activities, and assignments for the fundamental vibrational modes of salicylic acid. It can be seen from these results that acceptable agreement exists between the calculated and experimentally observed Raman spectra at this level of theory. As well, it should be noted that these spectra also agree very well with results previously reported in the literature.[9,11,13] However, there are some important differences between the two, and they can be explained as being a result of condensed phase effects. The calculated spectrum reported is for a non-interacting, gas phase system, whereas the experimental results presented are for a solid powder. This difference is known to account for very significant changes in relative vibrational intensities, and can produce spectra that appear to be quite dissimilar.[7] This is certainly not surprising, as salicylic acid is known to form both inter- and intramolecular hydrogen bonds in condensed phase. Indeed, this effect is even more pronounced in the infrared absorption spectra where strong hydrogen bonding in the condensed phase clearly leads to differences between the calculated and experimental IR spectra of salicylic acid.

The most striking example of this condensed phase effect is the C=O stretch that is calculated at 1794 cm⁻¹ as a very intense band, but is not observed in the experimental Raman spectrum (Figure 5.2). The disappearance of this band is a result of C=O participation in intermolecular interactions in the condensed phase. It is, however,

observed in the experimental IR spectrum as a broad peak showing a maximum at 1657 cm^{-1}. This is in agreement with the vibrational spectra recorded for salicylic acid in aqueous solution, where the C=O stretching was observed in both the Raman and IR at 1660 cm^{-1}.[10] Dissolving the salicylic acid in organic solvents shows that this IR band wanders to higher wavenumbers, indicating less association via C=O interactions. A pair of bands at 1580 and 1609 cm^{-1} in the IR spectrum are assigned to C=C stretching vibrations of the aromatic ring. In the Raman spectrum, similar bands are seen at 1581 and 1634 cm^{-1}, as confirmed by the literature.[9] The computed spectra clearly show that there are only two ring stretching vibrations in this region, the 1580 and 1609 cm^{-1} bands observed in the IR spectrum. The 1634 cm^{-1} band in the Raman spectrum cannot be assigned to the C=O stretching, since this vibration is clearly observed at 1657 cm^{-1} in the IR spectrum. Therefore, it is concluded that the 1634 cm^{-1} vibration observed in the Raman spectrum is a result of dimers or higher order aggregates formed in the condensed phase.
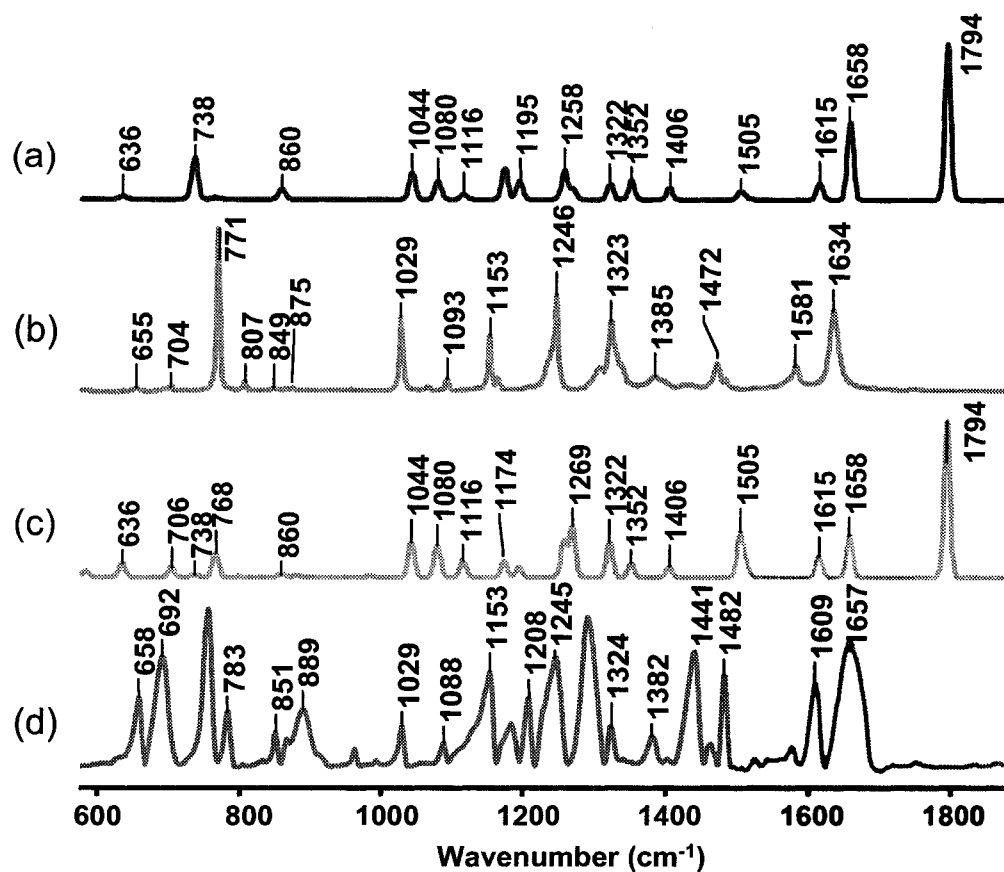
Figure 5.2 Vibrational Spectra of Salicylic Acid. (a) B3LYP/6-311+G(d,p) calculated Raman spectrum, (b) experimental Raman spectrum, (c) B3LYP/6-311+G(d,p) calculated IR absorption spectrum, (d) experimental ATR IR absorption spectrum.

Table 5.2. Calculated and observed infrared and Raman frequencies with corresponding symmetries, infrared intensities (in km/mole), Raman activities (in Å^4/amu), and assignments for the fundamental vibrational modes of salicylic acid.

B3LYP 6-311+G(d,p) Calculation				Experimental		Assignment
cm^{-1}	symmetry	infrared intensity	Raman intensity	infrared cm^{-1}	Raman cm^{-1}	
54	A"	1	0			out of plane COO bend
132	A"	0	2		122	out of plane butterfly
243	A'	3	1		178	out of plane butterfly
254	A'	1	1		257	rocking of COOH group
378	A'	2	3		284	ring stretch
411	A'	8	2			rocking of COOH and OH groups
425	A"	31	1	433	433	out of plane C-H and O-H bends
491	A"	124	3	466	451	out of plane C-H and O-H bends
540	A"	47	0			out of plane C-H and O-H bends
548	A'	7	3	533	533	rocking of COOH and OH groups
565	A'	11	8	567	565	ring stretch
585	A"	16	0			out of plane O-H bends
636	A'	39	2	658	655	ring stretch, COO bend
706	A"	27	0	692	704	out of plane C-H bend
738	A'	6	26	759	771	ring stretch, COO scissor
768	A"	72	1	783		out of plane C-H bend
800	A"	1	0	806	807	out of plane C-H bend
860	A'	9	6	851	849	ring stretch
882	A"	2	0	889	875	out of plane C-H bend
986	A"	2	0	963	961	out of plane C-H bend
1002	A"	0	0	995	995	out of plane C-H bend
1044	A'	103	16	1029	1029	ring stretch, C-O stretch
1080	A'	94	11	1088	1093	C-H bend, C-O stretch
1116	A'	51	3	1153	1153	C-H bend, O-H bend
1174	A'	46	19	1169	1165	C-H bend, O-H bend
1195	A'	27	11	1208	1208	C-H bend, O-H bend
1258	A'	110	18	1245	1246	C-H bend, O-H bend
1269	A'	150	6	1290		C-H bend, O-H bend
1322	A'	102	9	1306	1307	C-O-H bend
1352	A'	42	12	1324	1323	C-H bend, O-H bend, ring stretch
1406	A'	31	7	1382	1385	C-H bend, O-H bend
1505	A'	131	5	1442	1432	ring stretch, O-H bend
1513	A'	33	1	1482	1472	ring stretch, O-H bend
1615	A'	62	10	1580	1581	ring stretch, O-H bend
1658	A'	124	49	1609	1634	ring stretch, O-H bend
1794	A'	471	99	1657		C=O stretch, O-H bend, ring stretch
3172	A'	5	71		3019	C-H stretch
3189	A'	6	88	3062	3059	C-H stretch
3198	A'	4	82		3078	C-H stretch
3205	A'	7	200		3090	C-H stretch
3691	A'	288	100	3235	3239	O-H stretch
3769	A'	88	128		3239	O-H stretch

130

5.2.4 SERS, SEIRA, and RAIRS

A direct comparison of several key Raman spectra for this system is presented in Figure 5.3 for the region below 1700 cm^{-1}. The spectra are supported by Table 5.3, which contains the calculated frequencies, symmetries, Raman activities, IR intensities, and assignments for the fundamental vibrational modes of the Ag1 complex, along with the corresponding experimental frequencies for the silver salicylate salt, SERS, and SEIRA samples. The Raman spectrum of the prepared silver salicylate monoanion salt and the SERS spectrum obtained from 10 nm Ag nanoparticle films coated with thin films of salicylic acid agree well with those previously reported in the literature.[9,11,19] However, they show some differences with one another, because of the effect of hydrogen bonding that occurs for the salt sample, as well the fact that the spectrum of the salt represents a random spatial distribution, whereas the SERS spectrum is primarily derived from an oriented first layer.

131
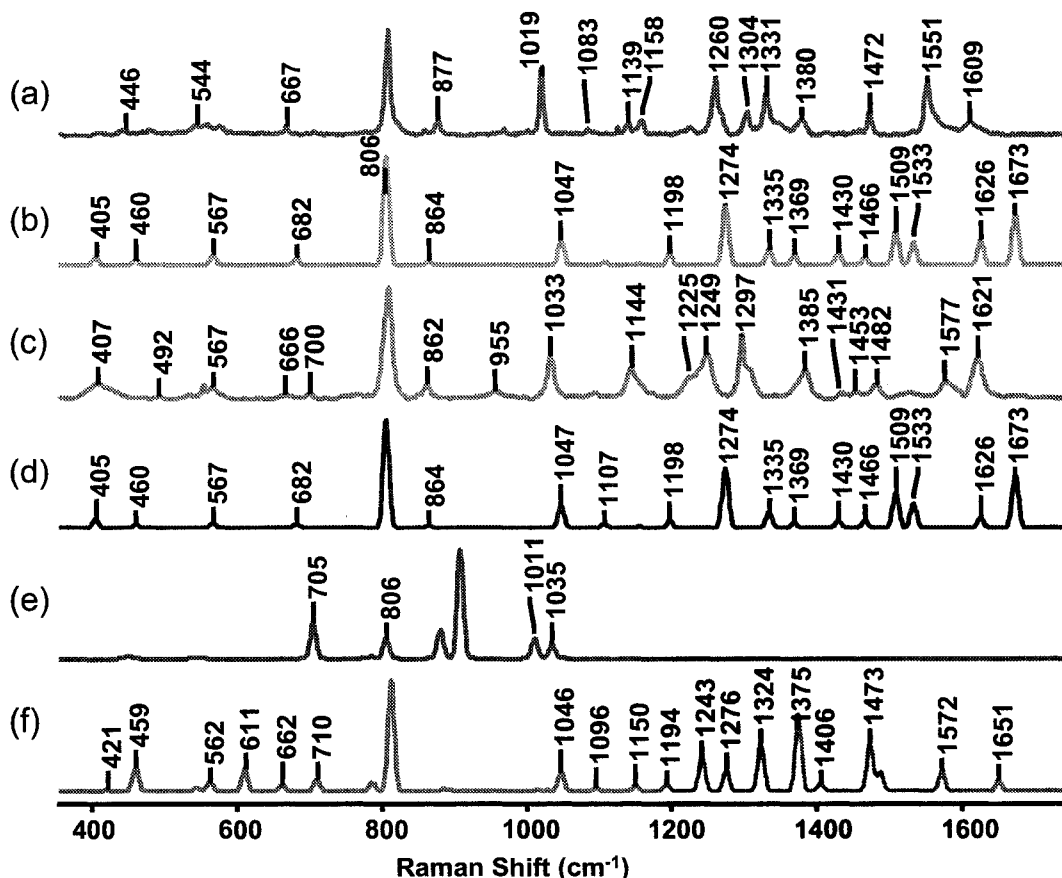
Figure 5.3 SERS spectrum compared with silver salt and computed spectra.
Comparison of **(a)** the Raman spectrum of silver salicylate salt, **(b)** the B3LYP/Lanl2DZ calculated Ag1 Raman spectrum (random orientation), **(c)** the experimental SERS spectrum, **(d)** the B3LYP/Lanl2DZ calculated Raman spectrum for the Ag1 complex with head-on orientation (only xx and xy polarizability derivative components used to calculate Raman activity), **(e)** the B3LYP/Lanl2DZ calculated Raman spectrum for the Ag1 complex with face-on orientation (only xz and yz polarizability derivative components used to calculate Raman activity), and **(f)** the B3LYP/Lanl2DZ calculated Ag2 Raman spectrum (random orientation).

132

Table 5.3. Calculated frequencies, symmetries, Raman activities (in $\text{Å}^4/\text{amu}$), infrared intensities (in km/mole), and assignments for the fundamental vibrational modes of the Ag1 complex. Also shown are the corresponding experimental Raman and infrared frequencies for the Ag salt, SERS, and SEIRA samples.

B3LYP/Lanl2DZ Calculation				Experimental cm⁻¹				assignment
cm⁻¹	Symm.	Raman Int.	Infrared Int.	Ag salt Raman	Ag salt IR	SERS	SEIRA	
68	A"	2	10					Ring wagging
87	A'	0	3					Ring rocking
109	A"	1	1					COO twisting
178	A"	2	2					Ring twisting
186	A'	12	11	204		broad		COO-Ag symmetric stretch
262	A"	2	1	276				COO-ring butterfly
289	A'	0	3			broad		COO-Ag antisymm. stretch
405	A'	8	25			407		C-OH rocking
450	A"	0	0					ring twisting
460	A'	5	13			492		ring stretch, Ag-O stretch
538	A'	1	5					C-C-O deformation
545	A"	0	11					ring twisting
567	A'	10	6	575		567		ring stretch
682	A'	7	29	669	670	700		ring stretch, COO scissor
705	A"	0	13		708			C-H bend
785	A"	0	30		780			C-H bend, O-H bend
806	A'	99	9	809	809	809		ring stretch, COO scissor
806	A'	0	84				757	out of plane C-H bend
864	A'	4	7	859	860	862	852	ring stretch
879	A"	0	152	877	881		888	O-H bend
908	A"	1	0					C-H bend, O-H bend
1011	A"	0	3					out of plane C-H bend
1035	A"	0	0					out of plane C-H bend
1047	A'	23	23	1019	1021	1033	1033	C-H bending, ring stretch
1107	A'	3	4	1083	1086	1093	1089	C-H bend, COO stretch
1156	A'	2	33	1139	1141	1144	1159	C-H bend, COO stretch
1198	A'	11	14	1224		1225		C-H bend
1269	A'	1	54		1213		1210	C-H bend, O-H bend
1274	A'	54	72	1260	1261	1249	1248	C-O stretch + C-H bend
1335	A'	14	275	1304	1302	1297	1307	COO stretch + O-H bending
1369	A'	10	126	1380	1382	1385	1382	ring stretch
1430	A'	11	106			1431		ring stretch, O-H bend, COO stretch
1466	A'	7	197		1454	1453	1447	ring stretch, O-H bend, COO stretch
1509	A'	30	174	1472	1481	1482	1458	ring stretch, C-H bend
1533	A'	20	26			1524	1484	ring stretch, O-H bend, COO stretch
1626	A'	23	82	1551	1555	1577	1612	ring stretch, O-H bend
1673	A'	46	114	1609	1588	1621	1655	ring stretch, O-H bend
3162	A'	207	434		broad	2927	broad	O-H stretch
3198	A'	49	3					C-H stretch
3217	A'	95	13			3022		C-H stretch
3236	A'	27	12					C-H stretch
3243	A'	228	20	3058	3062	3064		C-H stretch

133

When the obtained SERS results are compared with the Raman spectrum of the powder salicylic acid, it becomes immediately clear that the molecule has been altered due to the formation of a surface complex. In the low wavenumber region of the SERS spectrum, very strong Ag-O bonds are detected. These bands appear to be strengthened relative to the usual Ag-O peaks that are nearly always found in the spectra of Ag nanoparticle films (resulting from an ever-present silver oxide layer). The presence of these strengthened Ag-O stretching bands provides strong evidence for the formation of a surface complex. Further strength is provided to this hypothesis by several key spectral changes in the SERS relative to the Raman spectra of salicylic acid. Among these changes, are shifts in vibrations resulting from both the carboxyl and hydroxyl groups of the molecule. For example, a clear upshift of the ring stretching + COO scissoring from 771 to 809 cm^{-1} takes place (attributed to deprotonation producing the monoanion), while downshifts in several bands with considerable phenolic O-H contribution, in particular, those found at 451 and 3239 cm^{-1} in the Raman (seen at 407 and 2927 cm^{-1} in the SERS) are observed upon adsorption of the molecule on Ag. Shifts in bands associated with the carboxylate group suggest that adsorption is occurring through it, while the presence of several downshifted O-H related modes indicates that the molecule is not reacting with the metal through its hydroxyl group, but rather is experiencing drastic changes in the strength of its hydrogen bonds as a result of the adsorption. This is made particularly clear by the unmistakable presence of the O-H stretching band (2927 cm^{-1}) that has shifted below the C-H stretches in the SERS spectrum, as shown in Figure 5.4 (and predicted by theoretical results). Moreover, several other bands involving contributions

134

from the O-H group are clear in the SERS spectrum (Table 5.3). These bands provide direct evidence that salicylic acid is not chemically adsorbed through its hydroxyl group.
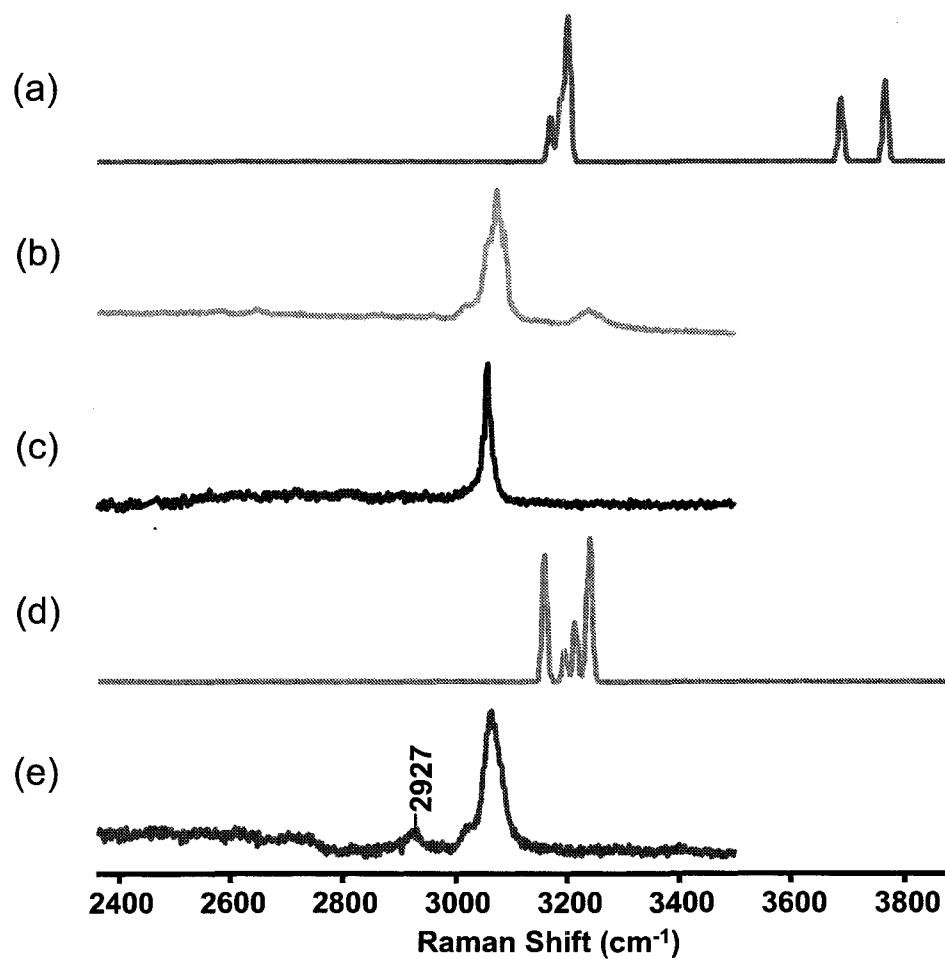
Figure 5.4 Downshifted O-H stretch in SERS spectrum. Comparison of spectra above 2400 cm^{-1} for **(a)** B3LYP/6-311+G(d,p) calculated salicylic acid, **(b)** salicylic acid powder (experimental), **(c)** silver salicylate salt (experimental), **(d)** B3LYP/Lanl2DZ calculated Ag1 complex, and **(e)** SERS (experimental).

135

As mentioned earlier, the structure and vibrational (IR and Raman) spectra of two different Ag-salicylate complexes, Ag1 and Ag2, have been calculated at the B3LYP/Lanl2DZ level of theory in order to determine if one would agree strongly with experimentally observed SERS spectra, and therefore clarify how the chemisorption of this molecule occurs on Ag. The Raman results derived from these calculations are shown in Figure 5.3, where the calculated spectra of these two complexes (Ag1 and Ag2) are compared to the experimentally observed silver salicylate salt, and SERS spectra. Tables 5.3, and 5.4, that show the calculated frequencies, symmetries, Raman activities, infrared intensities, and assignments for the fundamental vibrational modes of Ag1 and Ag2, respectively, support these spectra.

It can be seen in Figure 5.3, that both model complexes seem to approximate the SERS spectrum of the surface species to some extent. However, there are some very clear signs that allow us to eliminate one of these possibilities. The calculated Raman spectrum of Ag2, as expected, does not account for the presence of O-H vibrational bands in the experimental SERS spectrum, as the Ag1 complex does. The O-H stretching (2927 cm^{-1}), in particular, in the SERS spectrum confirms that the phenolate has not been formed. As shown in Figure 5.4, this band demonstrates nearly identical band shape, and relative intensity, to the O-H stretching band in the experimental Raman spectrum of salicylic acid. As well, it cannot be reasonably assigned to a combination band, as there aren't any two fundamentals in the SERS spectrum whose frequencies can be summed to arrive close to 2927 cm^{-1}. Thus, given this quite clear assignment, we can conclude with a great deal of certainty that the Ag2 complex does not represent the chemical adsorption of salicylic acid on Ag.

136

Table 5.4. Calculated frequencies, symmetries, Raman activities (in Å⁴/amu), infrared intensities (in km/mole), and assignments for the fundamental vibrational modes of the Ag2 complex.

Frequency cm⁻¹	symmetry	Raman Intensity	Infrared Intensity	assignment
32	A"	1	6	C-C torsion
66	A'	1	1	Ring rocking
66	A'	1	11	Ring wagging
94	A"	1	2	COO twisting
126	A'	6	19	Ag-O stretch
139	A"	6	2	out of plane C-C torsion
173	A'	23	5	Ring rocking
232	A'	40	22	Ag-O stretching (both Ag atoms)
252	A"	24	2	Ring wagging
332	A'	11	6	Ring rocking
421	A'	3	9	Ag-O stretch
452	A"	1	0	C-H bend
460	A'	33	4	Ag-O stretching, ring stretch
545	A"	6	11	C-H bend
563	A'	13	29	ring stretch
611	A'	31	3	ring stretch
662	A'	10	25	ring stretch., COO scissoring
710	A"	17	21	C-H bend
786	A"	13	58	C-H bend
802	A"	1	26	C-H bend
813	A'	152	2	COO scissor, ring stretch
884	A'	4	19	Ring stretch, COO stretch, C-O stretch
894	A"	2	5	C-H bend
1015	A"	3	3	C-H bend
1029	A"	2	0	C-H bend
1047	A'	26	26	ring stretch
1096	A'	5	15	Ring stretch, COO stretch
1150	A'	8	76	C-H bend,
1194	A'	11	25	C-H bend
1243	A'	48	173	C-H bend, COO stretch, C-O stretch
1276	A'	31	89	C-H bend
1324	A'	67	202	C-H bend , COO stretch
1375	A'	106	264	COO stretch, ring stretch
1406	A'	12	176	COO stretch, ring stretch
1473	A'	66	203	Ring stretch, C-O stretch, C-H bend
1487	A'	27	223	Ring stretch, C-H bend
1572	A'	28	93	Ring stretch, C-H bend
1651	A'	15	117	Ring stretch, C-H bend
3183	A'	87	15	C-H stretch
3210	A'	123	21	C-H stretch
3228	A'	110	27	C-H stretch
3243	A'	89	21	C-H stretch

137

The calculated Raman spectrum of the Ag1 complex, on the other hand, shows good agreement with the experimental SERS spectrum, especially considering the previously discussed complications created by condensed-phase and field polarization effects. Not only does the Ag1 complex calculation account for the presence of the O-H bands in the SERS spectrum, but it also predicts successfully the shifting of these bands. As shown in Table 5.3, the Ag1 complex has its O-H stretching mode shifted below the C-H stretches, as was also observed in the experimental SERS spectra. In light of this theoretical result, there can be little doubt about the assignment of the O-H stretch in the experimental SERS spectrum. Moreover, the Ag1 complex shows generally good agreement with the entire experimental spectrum in terms of band frequencies and relative intensities. Thus, based on the results presented here, it can be concluded that the chemical adsorption of this analyte on Ag occurs only through its carboxylate group. In fact, the calculated Raman spectrum of the Ag1 complex approximates the experimental SERS spectrum far better than it does the silver salicylate salt Raman spectrum. This may seem unexpected, but it simply demonstrates the importance of intermolecular interactions in this system. The prepared salt complex experiences strong hydrogen bonding, while the salicylate ions at the surface of the Ag nanoparticles are much more isolated from one another. For example, the Raman spectrum of the silver salicylate salt does not have an apparent O-H stretching band, as the Ag1 and SERS spectra do.

In a previous study,[7] molecular orientation at the surface was determined by applying SERS surface selection rules to an adsorbate by orienting the calculated surface complex, and then plotting a simulated SERS spectrum by only including those modes of symmetry with polarizability derivative tensor components parallel to the

138

electromagnetic field at the surface. In this way, the surface selection rules were accounted for by the theoretical methods, and good agreement between the calculated and experimental results was obtained. To produce simulated spectra that account for surface selection rules, Raman activities of each mode, using only the polarizability derivative tensor components that align with the electromagnetic field at the surface, must be calculated. The Ag1 complex, having C_s symmetry, shows modes of only two symmetry species, A' and A". Further, there are two general test cases for orientation: the molecule standing (head-on), or lying flat on the surface (face-on). In calculations of the Ag1 complex, the molecular plane was fixed in the x-y plane. Consequently, for the case of the molecule lying flat on the surface, the x-y plane of the molecular system is parallel with the tangential components of the field, and we can calculate the Raman activity of each mode using only the xz, and yz components of the polarizability derivative tensor. This effectively means that we are plotting only the A", or out-of-plane modes for the molecule. If, however, the molecule is standing head-on to the surface, then the perpendicular component of the polarized surface field will be parallel to the plane of the molecular system, and the Raman activity of each mode can be calculated using only the xx, and xy components of the polarizability derivative tensor (assuming the molecule is standing with its x-axis parallel to the surface normal). In this way, we are accounting for all in-plane vibrations that have polarizability derivative components parallel with the surface electromagnetic field. Polarizability derivative tensor components are readily obtained from quantum chemical calculations, and Raman activities can be calculated from the invariants of the derived polarizability tensor.[20]

The two cases mentioned above have been tested in this work, and the results are shown in Figure 5.3. Upon close examination it can be seen that the spectrum representing head-on orientation, as expected, is clearly in closer agreement with the experimental SERS than the spectrum representing face-on orientation. This is clear evidence suggesting that the molecule is not lying flat on the surface. However, it appears that experimental SERS results are likely best approximated by the Ag1 spectrum (average of spatial directions), and from this we can conclude that the molecule is slightly tilted at the surface.

To obtain corroborating evidence about the orientation of salicylate chemically adsorbed at silver surfaces, reflection absorption infrared spectroscopy (RAIRS), and surface-enhanced infrared absorption (SEIRA) measurements were made and used in conjunction with theoretical results for the Ag1 complex. These results are shown in Figure 5.5, which also includes the infrared absorption spectrum of silver salicylate dispersed in a KBr pellet. It can be seen that the RAIRS and SEIRA results show agreement with one another and with results for salicylic acid powder (Figure 5.1), while the silver salt spectrum is quite dissimilar. This can be explained as being the result of strong intermolecular attractions that salicylic acid and the salt complex both exhibit, as confirmed by the observation of several broad infrared bands (more than average full width at half maximum) in the spectra. Due to very modest enhancements in the infrared (SEIRA, and RAIRS), and thus a weak first layer effect, even moderate surface concentrations bring about the spectrum of the bulk material. This is in contrast with what is observed in SERS measurements where first layer effects are dominant.

140
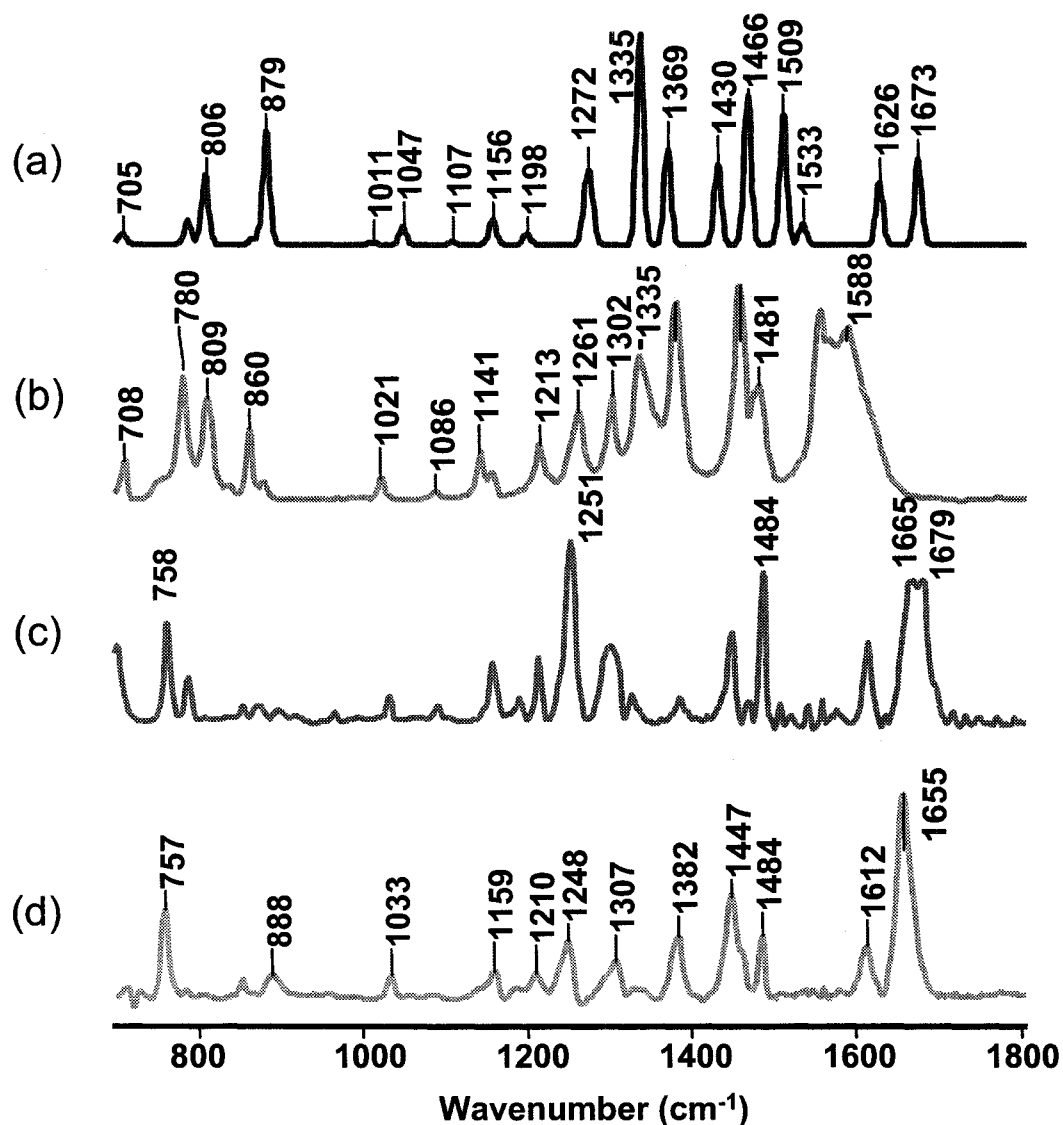
Figure 5.5 IR, RAIRS, and SEIRA results. Comparison of **(a)** B3LYP/Lanl2DZ calculated IR spectrum for the Ag1 complex, **(b)** IR absorption spectrum of silver salicylate salt (KBr pellet), **(c)** reflection–absorption IR spectrum (RAIRS), and **(d)** surface-enhanced IR absorption spectrum.

However, by following the relative intensities of two bands in the SEIRA spectrum, the strong in-plane vibration at 1655 cm^{-1}, characteristic of the carboxylate

moiety, and the out-of-plane C-H bending vibration observed at 757 cm^{-1}, it is possible to gain more information about molecular orientation. Assuming a predominant perpendicular polarization at the silver nanostructures, the intensity ratio for the two bands (I_{1655}/I_{757}) can be used as an indicator of the molecular orientation of the adsorbate near or at the surface. The reference ratio for a random distribution in this case is the spectrum of the salicylic acid powder. The ratio will show a maximum for a head-on orientation, and a minimum for flat or face-on orientation. It can be seen that the ratio increases in the SEIRA spectra, confirming a preferential orientation in favor of the head-on model for the adsorbate. Since the relative intensity of the 757 cm^{-1} mode is diminished, but it is still clearly observed, it can be concluded that on average, the molecule demonstrates a predominantly tilted, head-on orientation at the surface.

5.2.5 Conclusion

In the work discussed in this section, density functional theory (DFT) methods were employed to investigate the nature of the chemical adsorption of salicylate on silver surfaces. The structure of salicylic acid, along with its infrared and Raman spectra, was determined at the B3LYP/6-311+G(d,p) level of theory. These results were then used in the assignment of vibrational spectra, and generally showed good agreement with those obtained experimentally, accounting, of course, for condensed phase effects. Surface-enhanced Raman scattering (SERS) spectra were obtained from silver nanoparticle films thinly coated with salicylic acid, and showed good agreement with results previously reported in the literature for colloidal solutions. In order to determine the nature of the chemisorption that this molecule shows on Ag surfaces, the optimized geometries and Raman spectra of two model salicylate-silver complexes (Ag1 and Ag2) were calculated

142

at the B3LYP/Lanl2DZ level of theory. As well, experimental vibrational spectra were obtained for a silver salicylate salt for comparison with SERS results. It was found that experimentally observed SERS spectra, and simulated SERS spectra of a salicylate complex chemisorbed through its carboxylate group (Ag1) show good agreement with one another. Thus, it is concluded that salicylate chemically adsorbs only through its carboxylate group. Evidence for a tilted, head-on orientation of the salicylate complex on the surface was obtained from calculations of simulated SERS spectra that account for polarization, as well as from comparisons of reference powder results with SEIRA, and RAIRS spectra.

5.3 SERS of the Environmental Pollutant 1-Naphthylamine[a]

5.3.1 Introduction

SERS has been steadily establishing itself as an important tool for environmental analysis.[21,22] With the wide variety of molecular systems that are found as pollutants in air, water, and soil, it is likely that numerous unique SERS analytical protocols will continue to be developed to study these systems at low concentrations in the environment. However, because of the broad scope of materials to be considered, the fundamental nature of SERS, and the relative novelty of environmental applications of this technique, there are still many challenges to be faced by researchers in the development of reliable protocols for the analysis of individual molecules of environmental relevance.

---

[a] This work was done in collaboration with R. A. Alvarez-Puebla who recorded some Raman spectra and performed all of the zeta potential measurements shown here.

The first challenge in implementing SERS toward an environmental application is the selection of an appropriate enhancing substrate for the analyte of interest. Fortunately, to date, countless unique SERS substrates have been developed with a wide variety of physical and chemical characteristics.[2,23] These substrates have generally involved the incorporation of nanostructures of Ag, Au, or Cu, as these metals provide the largest electromagnetic enhancements of Raman signals due to their strong dipolar particle plasmon resonances in the visible range of the electromagnetic spectrum.[24-26] Once a nanostructure is found to be suitable for a given analyte, one of the techniques commonly used in separation science may need to be employed in conjunction with SERS.[27] A SERS protocol can then be further refined by tuning the variables that influence intensities. For example, sensitivity can be optimized by improving adsorption and electromagnetic enhancement conditions or by controlling the influence of different experimental variables such as irradiation time and energy density at the sample to avoid the thermal and photolytic effects inherent in SERS.[28,29] The ideal protocol will provide reproducibility and a considerable linear region, for quantitative analysis, in the signal intensity vs. concentration graph. However, the qualitative identification of trace amounts, on its own, has significant potential for application of SERS toward the analysis of environmental pollutants.

Establishing the conditions that optimize SERS as an analytical technique is, indeed, the fundamental issue for the development of practical environmental applications of this spectroscopy. The reported work on environmental analysis clearly reveals the efforts of several different groups on the road to SERS analytical protocols for several pollutants. For instance, De Jesus et al.[30] developed an analytical protocol that

144

uses Ag-polydimethylsiloxane nanocomposites in combination with a sample translation technique for the qualitative and quantitative analysis of naphthalene, phenol, and benzoic acid derivatives in water. This approach provided improved reproducibility and sensitivity by minimizing the thermal and photolytic effects that commonly hinder SERS measurements. Vo-Dinh[31] reviewed the use of silver-coated microstructured substrates as sensors in environmental analysis. Zhang et al.[32] developed a rapid detection protocol suitable for the analysis of anthrax spores using a low-cost, battery-powered, portable Raman spectrometer. He et al.[33] developed an approach for detecting the components of capillary electrophoresis eluent by interfacing it with a SERS measuring system. Three different substrates were utilized, and the method developed was applied successfully for the identification of chlorophenols in a mixture.

Polycyclic aromatic hydrocarbons (PAHs) form a class of widespread environmental contaminants that are found in diesel emissions, gas fuel, and airborne particulate.[34] Several different SERS substrates have been proposed for the analysis of these pollutants, including silver and silver-gold nanoparticle films, which were used under specifically controlled conditions to prevent active photochemistry.[35] Moreover, Leyton et al.[36] were able to detect trace quantities of PAHs deposited onto a calix[4]arene-functionalized Ag colloidal surface.

In the work discussed in this section, the SERS of the important environmental contaminant, and PAH, 1-naphthylamine (1-NA) was studied.[37] 1-NA is widely used in both industry and research as an intermediate in the synthesis of a wide range of organic compounds. In industry, it is most commonly used in the production of chemicals used for controlling weeds, manufacturing dyestuffs, manufacturing rubber, and toning prints

145

made with cerium salts.[38] It is commonly released into the environment in the waste streams and effluents of these industries, as well as those of coal tar, coal gasification, and shale oil facilities, and is widely recognized as a dangerous component of both first- and second-hand tobacco smoke.[39] It is a suspected human carcinogen,[40,41] and is listed as such by the Occupational Safety & Health Administration (OSHA) of the U.S. Department of Labor. It has been demonstrated to have a strongly negative impact in the environment, is toxic to aquatic organisms, and has been shown to cause cancers in animals.[42] Importantly, it has been demonstrated that leaching of 1-NA into groundwater is possible.[43]

In this work, experimental and DFT-calculated Raman scattering spectra for 1-NA were obtained and assigned. SERS spectra were recorded from colloidal Ag nanoparticles in solution. Enhancement was monitored as a function of the pH of the colloidal metal solution used, and conditions were optimized accordingly. Dramatic spectral changes were observed when the free molecule was placed at the surface of silver nanostructures, making the spectral interpretation of SERS spectra particularly challenging, as is common with small aromatic amines.[44,45] Through spectral comparison with the Raman and SERS spectra of a synthesized coordination complex of silver and 1-NA, it was shown that SERS obtained from aqueous colloidal solutions were the result of the formation, and water solvation, of a coordination complex of two 1-NA molecules and a Ag^+ ion.

5.3.2 Raman Spectrum of 1-Naphthylamine

1-NA is a molecule with C_1 symmetry and 54 normal modes, where 21 are stretching modes and 33 are angle and dihedral angle deformations. B3LYP 6-311G(d,p)

146

calculated and experimental Raman spectra for 1-NA are shown in Figure 5.6. Table 5.5 provides assignment of the key observed and calculated fundamental vibrational modes. Calculated spectra were frequency scaled at 0.9723, and, given that the experimental spectra are of the solid state, it can be said that there is good agreement between the two. In the Raman spectrum, the ring stretching modes (C=C stretching) dominate, with characteristic frequencies observed at 1575 (strong and typical for mono-substituted naphthalenes), 1454, and 1376 cm^{-1}.[46] A strong band is also observed at 710 cm^{-1}, that corresponds to a breathing mode of the two rings. In the Raman spectrum, the C-H stretching and bending modes are observed with medium relative intensity. The locally symmetric C-H stretching is seen at 3061 cm^{-1}, and two characteristic C-H bending modes are recorded at 1089 and 1028 cm^{-1}. The Raman intensity of vibrations involving the NH_2 moiety are rather small compared with those of the ring modes, and consequently, they do not produce characteristic Raman intensities for facile analytical identification.
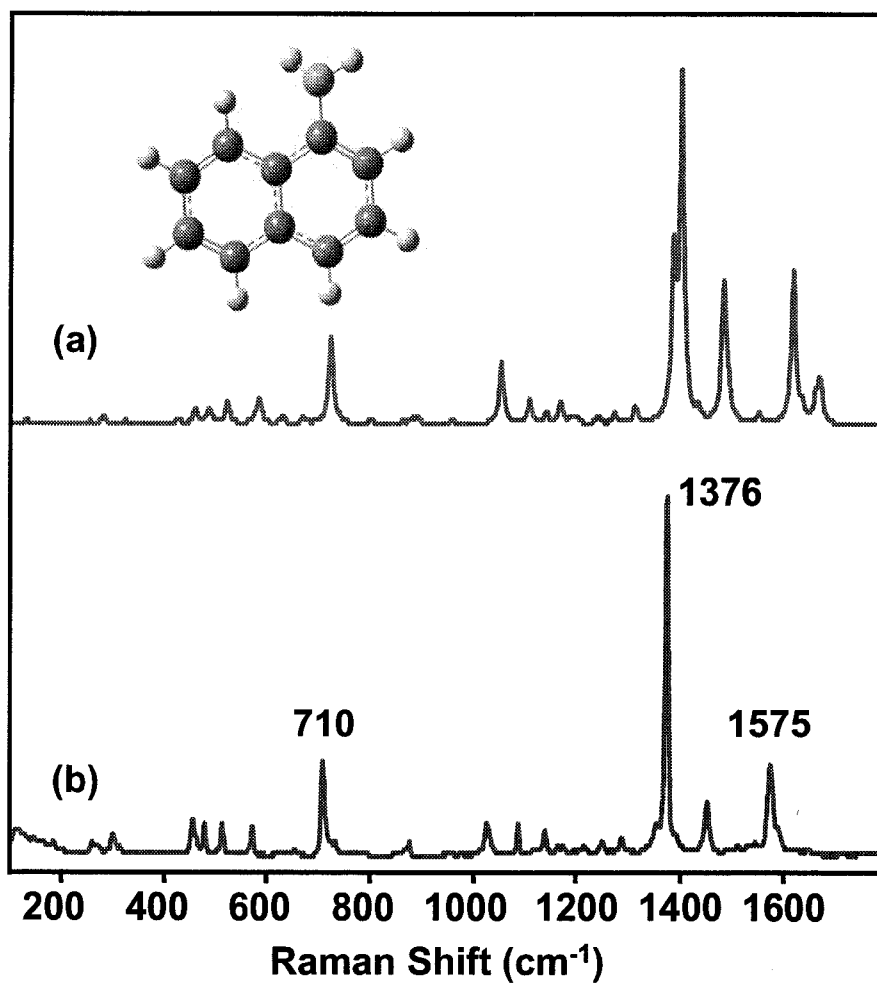
Figure 5.6   Raman Spectrum of 1-Naphthylamine.   (a) B3LYP 6-311G(d,p) calculated, and **(b)** experimental Raman spectra for 1-naphthylamine.   Experimental results were recorded from 1-NA powder.   Inset shows the optimized molecular structure of 1-NA.

Table 5.5. Some observed and calculated (B3LYP 6-311G(d,p)) fundamental Raman modes of 1-naphthylamine and its silver complex.[a]

Calculated[b] cm^{-1}	Raman Int.	Assignment	Raman powder	Silver complex
1574	56	Ring stretching	1575	1575,1567
1443	51	Ring stretching	1454	1462,1454
1364	124	v(C=C) & v(C-N)	1376	1377
1349	57	v(C=C) & β(C-N-H)	1357	1364
1278	6	β(C-C-H) & v(C=C)	1290	1265
1240	3	β(C-C-H) & v(C=C)	1252	1250
1208	2	β(C-C-H) & v(C=C)	1220	1220, 1204
1156	2	β(C-C-H)	1166	1169
1136	8	β(C-C-H)	1141	1142
1078	9	β(C-C-H)	1089	1084
1024	22	β(C-N-H) & β(C-C-H)	1028	1033
839	1	β(C-C-H)	878	866
703	32	Ring breathing	710	747, 707
569	10	β(C-C-C)	573	623, 572
508	8	β(C-C-C)	514	518
474	6	β(C-C-C)	479	493
446	5	β(C-C-C)	456	454
315	1	NH$_2$ rocking	303	341

[a] v: stretching; β: bending
[b] Calculated fundamental vibrations scaled at 0.9723

5.3.3 Effect of pH on SERS Enhancement

To obtain SERS spectra of 1-NA, silver colloids and evaporated Ag nanoparticle films were tested. Casting ethanol solutions of 1-NA directly onto silver films did not yield strong, reproducible results due to active photochemistry at the surface. The results obtained from Ag colloidal solutions, however, provided more consistent results. Surface plasmon absorption results for silver colloidal solutions are shown in Figure 5.7(a), while an SEM image of this dried colloid solution is shown in Figure 5.7(d). The size and shape of the Ag nanoparticles is variable, as is expected given the broad absorption of the plasmon bands, but the solutions are predominantly made up of spherical colloids with an average size of about 30-50 nm.
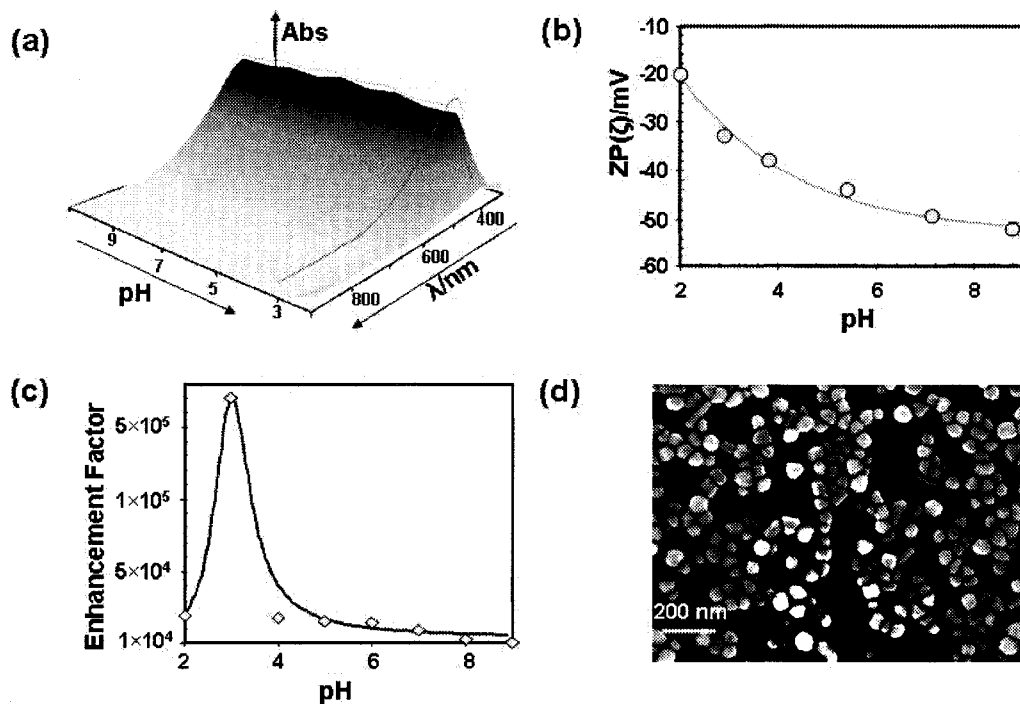
Figure 5.7 Effect of pH on SERS Enhancement. Variation as a function of pH of **(a)** surface plasmon absorption, **(b)** zeta potential of silver colloids, and **(c)** SERS enhancement factor for 1-NA. SEM image of cast silver colloidal solution is shown in **(d)**.

Once an average SERS spectrum was obtained reproducibly, the surface charge of the nanoparticles was varied through changes in pH to optimize the average SERS signal.[28] The variation with pH of the surface plasmon absorption, zeta potential (ζ), and 1-NA SERS enhancement factor are shown in Figure 5.7. As shown in Figure 5.7(a), variation between pH values of 3 and 9 appears primarily to modify the surface charge of the silver citrate colloids, as the surface plasmon absorption maximum remains constant at 442 nm in this range. The colloidal silver solutions are relatively stable within this

150

range, although subtle changes can be observed in the overall surface plasmon absorption spectrum at differing pH values, suggesting some minor changes in the particle distribution. At pH values lower than 3, the intensity of the plasmon decreases dramatically due to particle aggregation. The ζ values in Figure 5.7(b) show an increase from -52 mV at pH 9 to -19 mV at pH 2. The latter value is above the stability limit for a colloidal suspension (-20 to -25 mV), and so particles tend to aggregate and precipitate out of solution. The optimization of the SERS signal is presented in Figure 5.7(c). SERS enhancement factors for 1-NA were calculated by direct comparison with the Raman spectrum of a 0.1 M solution in ethanol. It was found that maximum SERS intensities were realized at pH 3. This is primarily attributed to optimized surface adsorption/complexation, but it is likely that electromagnetic enhancement effects are also playing a role. Particle aggregation will be increased at pH 3, leading to increases in the number of aggregates resonant at 633 nm excitation, where experiments were performed. This is, in fact, confirmed by subtle increases in surface plasmon absorption at this wavelength, and it is well established that nanoparticle aggregates provide the greatest electromagnetic enhancement of Raman signals.[47]

5.3.4 SERS of 1-Naphthylamine

In Figure 5.8, the Raman spectrum of 1-NA powder is compared with its SERS spectrum in colloidal Ag solution with a final concentration of 10^{-5} M (10 μL of a 10^{-3} M 1-NA solution was added to 1 mL of colloidal solution). The SERS spectrum is reproducible under different laser powers, suggesting that the analyte is not undergoing photoreactions initiated by the laser excitation. It also, notably, matches the spectrum recorded previously in an incomplete study by Volkan et al.[22] However, it displays many

151

significant differences from the 1-NA powder spectrum. In particular, it is a much more crowded spectrum, showing many more bands. Typically in SERS experiments, the first logical approach would be to try to explain these differences in terms of the effects of chemisorption, including symmetry change and preferential orientation of chemisorbed species. Similarly, the appearance of many new bands is often the result of photodissociation or photochemistry at the metal interface.[48] However, the strong naphthalene characteristic band at 1376 cm^{-1} is present in all spectra, confirming that the aromatic ring is still participating in the scattering process. Moreover, there is no evidence of the formation of the characteristic Ag-N bond that is generally observed in the 200 cm^{-1} region for chemisorption. In fact, a surface complex of one 1-NA molecule attached to silver, with a specific orientation, is expected to actually reduce the number of observed Raman bands.[24]
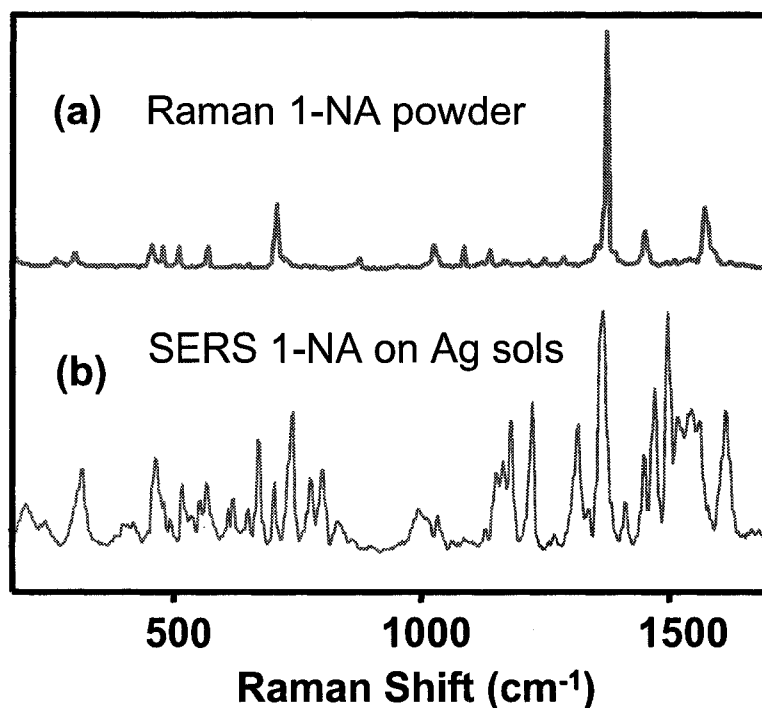
Figure 5.8 SERS of 1-naphthylamine. (a) Raman scattering spectrum of solid 1-NA.
(b) SERS spectrum of 1-NA in silver citrate colloidal solution.

5.3.5 Raman and SERS of the Ag Complex of 1-Naphthylamine

The alternative to a monomolecular complex as the SERS active system, was a very stable silver coordination complex of the $Ag(1-NA)_2^+$ type. This soluble, coloured complex was produced in both ethanol/water and chloroform solutions by reaction of 1-NA with $AgNO_3$, and is shown in Figure 5.9 ($[Ag(1-NA)_2NO_3]$). It was also produced in $CDCl_3$ for analysis by ^1H NMR.[b] The integrated ^1H NMR spectrum showed that the 1-NA was indeed part of the complex and that the NH_2 group remained intact, thus confirming the formation of a coordination complex with a silver ion. The soluble complex in $CDCl_3$ was then cast and dried on a glass slide, and the Raman spectrum was

---

[b] All ^1H NMR measurements were made by M. Fuerth at the University of Windsor in Windsor, Ontario.

153

recorded. This result is shown in Figure 5.10(a), and selected bands are assigned in Table 5.5. The same solution was also used to cast the complex onto a silver nanoparticle film to record its SERS spectrum, and the results are shown in Figure 5.10(b). Notably, the Raman and the SERS spectra are very similar and they can be obtained reproducibly from spot to spot on the cast films. Similar experiments were then carried out using the solution of the complex dissolved in ethanol/water. The SERS spectrum of the complex obtained from this solvent mixture cast onto a silver nanoparticle film is shown in Figure 5.10(c), and is essentially the same as the SERS spectrum of 1-NA on silver colloids. This spectrum also changes in a similar manner to the SERS of 1-NA in Ag colloidal solution. It appears that the solvation of this complex plays an important role in shaping the SERS spectrum recorded under different conditions. In particular, its labile behaviour can be attributed to water solvation. A water free environment, such as the one obtained in $CDCl_3$, leads to a more stable complex with reproducible spectra. To confirm this hypothesis, the $[Ag(1-NA)_2]NO_3$ complex formed in $CDCl_3$ was added directly to a colloidal silver solution for SERS measurement. The SERS spectrum obtained is shown in Figure 5.11 in comparison with the SERS obtained when an ethanolic solution of 1-NA is added to the silver colloid. It is quite evident that the two spectra are in good agreement, and this confirms that the solvated $[Ag(1-NA)_2]NO_3$ complex in aqueous medium is, in fact, the active SERS species being observed in 1-NA SERS measurements in colloidal nanoparticle solutions.

Figure 5.9 Silver coordination complex [Ag(1-NA)₂]NO₃.
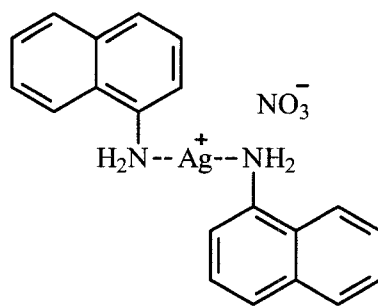
$$\text{Figure 5.9 Silver coordination complex } [\text{Ag}(1\text{-NA})_2]\text{NO}_3.$$
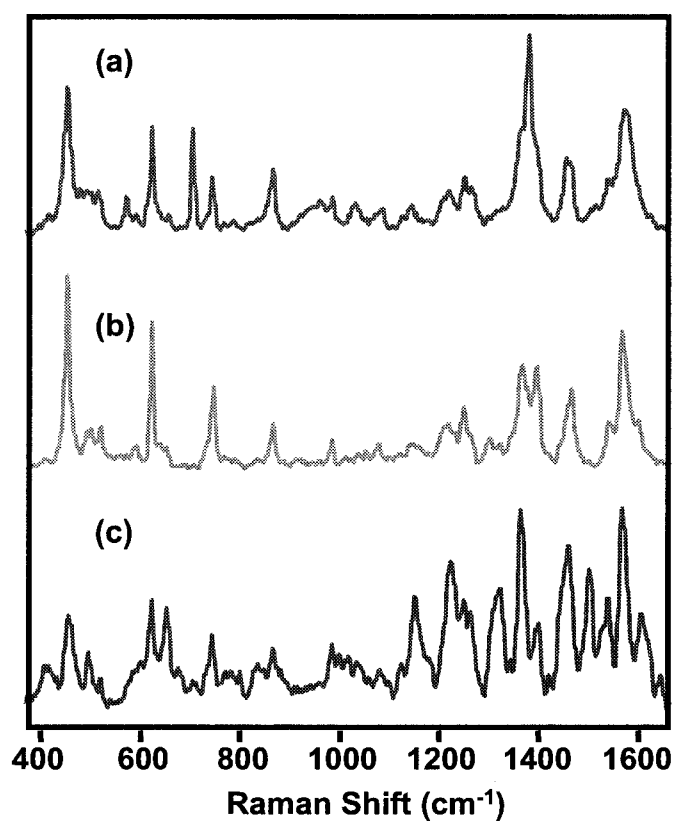
Figure 5.10 Raman and SERS of Ag Coordination Complex. (a) Raman spectrum of Ag coordination complex [Ag(1-NA)₂]NO₃ cast from CDCl₃ onto glass. (b) SERS spectrum of [Ag(1-NA)₂]NO₃ cast from CDCl₃ onto a Ag nanoparticle film. (c) SERS spectrum of [Ag(1-NA)₂]NO₃ cast from ethanol/water onto a silver nanoparticle film.

155
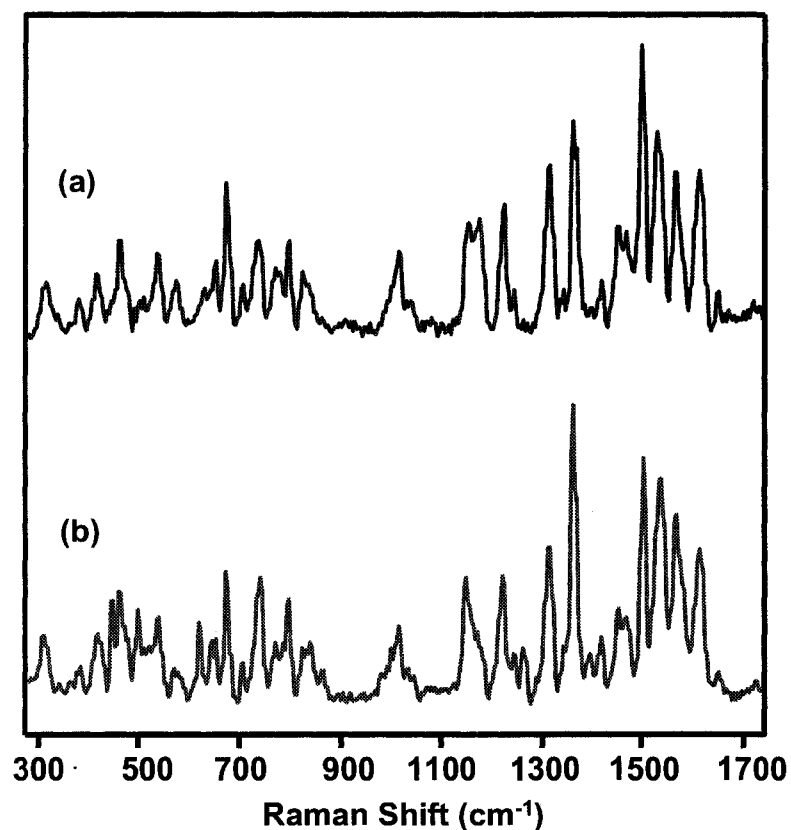
Figure 5.11 SERS of (a) [Ag(1-NA)₂]NO₃ and (b) 1-NA in colloidal Ag solution.

5.3.6 Conclusion

In the work discussed in this section, surface-enhanced Raman scattering (SERS) was employed to detect the important environmental pollutant, and suspected human carcinogen, 1-naphthylamine (1-NA) from colloidal Ag solutions. SERS enhancement conditions were optimized through the variation of pH, a fundamental determinant for solution SERS experiments. Dramatic spectral differences between the free molecule and the SERS obtained from aqueous colloidal solutions were demonstrated to be the result of the formation, and water solvation, of a coordination complex of two 1-NA molecules with the Ag^+ ions present at Ag nanoparticle surfaces.

156

5.4 Summary

In this chapter, the multifaceted approach required for the interpretation of the SERS spectra of the surface complexes of salicylic acid and 1-naphthylamine was discussed. These examples illustrated two distinct cases that are representative of two classes of adsorption in SERS experiments. Due to the major structural changes that arise through the formation of the surface complexes of these analytes, the interpretation of their spectra on Ag was of unusual complexity and required the utilization of a variety of spectroscopic techniques, and DFT computation, for different related chemical species. Through the implementation of these techniques it was determined that salicylate chemically adsorbs on Ag nanoparticles through its carboxylate group in a tilted, head-on orientation, while 1-NA on Ag forms a coordination complex that is highly sensitive to water solvation. Further, the discussion presented in this chapter demonstrates the importance of detailed fundamental vibrational studies, such as these, in the development of SERS/SERRS as analytical techniques for trace spectral analysis.

References

(1)   Aroca, R. F.; Ross, D.; Domingo, C. *Appl. Spectrosc.* **2004**, *58*, 324-338.

(2)   Aroca, R. *Surface-Enhanced Vibrational Spectroscopy*; John Wiley & Sons Ltd: West Sussex, 2006.

(3)   Osawa, M. *Bull. Chem. Soc. Jpn.* **1997**, *70*, 2861-2880.

(4)   Hoffmann, F. M. *Surf. Sci. Rep.* **1983**, *3*, 107-192.

(5)   Greenler, R. G. *J. Chem. Phys.* **1966**, *44*, 310-315.

(6)   Moskovits, M. *J. Chem. Phys.* **1982**, *77*, 4408-4416.

157

(7)   Aroca, R. F.; Clavijo, R. E.; Halls, M. D.; Schlegel, H. B. *J. Phys. Chem. A* **2000**, *104*, 9500-9505.

(8)   Cardini, G.; Muniz-Miranda, M. *J. Phys. Chem. B* **2002**, *106*, 6875-6880.

(9)   Alvarez-Ros, M. C.; Sanchez-Cortes, S.; García-Ramos, J. V. *Spectrochim. Acta, Part A* **2000**, *56A*, 2471-2477.

(10)   Humbert, B.; Alnot, M.; Quiles, F. *Spectrochim. Acta A Mol. Biomol. Spectrosc.* **1998**, *54*, 465-476.

(11)   Wang, Y.; Li, Y.-S.; Zhang, Z.; An, D. *Spectrochim. Acta, Part A* **2003**, *59A*, 589-594.

(12)   Sanchez-Cortes, S.; Garcia-Ramos, J. V. *J. Colloid Interface Sci.* **2000**, *231*, 98-106.

(13)   Philip, D.; John, A.; Panicker, C. Y.; Varghese, H. T. *Spectrochim. Acta A Mol. Biomol. Spectrosc.* **2001**, *57*, 1561-1566.

(14)   Goulet, P. J. G.; Aroca, R. F. *Can. J. Chem.* **2004**, *82*, 987-997.

(15)   Becke, A. D. *J. Chem. Phys.* **1993**, *98*, 5648-5652.

(16)   Lee, C.; Yang, W.; Parr, R. G. *Phys. Rev. B* **1988**, *37*, 785-789.

(17)   Hay, P. J.; Wadt, W. R. *J. Chem. Phys.* **1985**, *82*, 299-310.

(18)   Dunning, T. H.; Hay, P. J. In *Methods of Electronic Structure Theory*; Schaefer, H. F., Ed.; Plenum Press: New York, 1977; Vol. 2.

(19)   Sanchez-Cortes, S.; Garcia-Ramos, J. V.; Morcillo, G. *J. Coll. Int. Sci.* **1994**, *167*, 428-436.

(20)   Long, D. A. *The Raman Effect: A Unified Treatment of the Theory of Raman Scattering by Molecules*; John Wiley & Sons, Ltd.: Chichester, UK, 2002.

(21)   de Jesus, M. A.; Giesfeldt, K. S.; Sepaniak, M. J. *Appl. Spectrosc.* **2004**, *58*, 1157-1164.

(22)   Volkan, M.; Stokes, D. L.; Vo-Dinh, T. *Appl. Spectrosc.* **2000**, *54*, 1842-1848.

(23)   Aroca, R. F.; Alvarez-Puebla, R. A.; Pieczonka, N.; Sanchez-Cortez, S.; Garcia-Ramos, J. V. *Adv. Colloid Interface Sci.* **2005**, *116*, 45-61.

(24)   Moskovits, M. *Rev. Mod. Phys.* **1985**, *57*, 783-826.

(25)   Metiu, H. *Prog. Surf. Sci.* **1984**, *17*, 153-320.

(26)   Otto, A.; Mrozek, I.; Grabhorn, H.; Akemann, W. *J. Phys.-Condens. Matter* **1992**, *4*, 1143-1212.

(27)   *Encyclopedia of Separation Science*; Wilson, I. D.; Adlard, E. R.; Cooke, M.; Poole, C. F., Eds.; Academic Press: London, 2000.

(28)   Alvarez-Puebla, R. A.; Arceo, E.; Goulet, P. J. G.; Garrido, J. J.; Aroca, R. F. *J. Phys. Chem. B* **2005**, *109*, 3787-3792.

(29)   Pieczonka, N. P. W.; Aroca, R. F. *ChemPhysChem* **2005**, *6*, 2473-2484.

(30)   de Jesus, M. A.; Giesfeldt, K. S.; Sepaniak, M. J. *J. Ram. Spectrosc.* **2004**, *35*, 895-904.

(31)   Vo-Dinh, T. *Sens. Actuators B Chem.* **1995**, *B29*, 183-189.

(32)   Zhang, X.; Young, M. A.; Lyandres, O.; Van Duyne, R. P. *J. Am. Chem. Soc.* **2005**, *127*, 4484-4489.

(33)   He, L.; Natan, M. J.; Keating, C. D. *Anal. Chem.* **2000**, *72*, 5348-5355.

(34)   Harvey, R. G. *Polycyclic Aromatic Hydrocarbons*; John Wiley & Sons, Inc.: New York, 1997.

(35)   Carrasco-Flores, E. A.; Clavijo, R. E.; Campos-Vallette, M. M.; Aroca, R. F. *Appl. Spectrosc.* **2004**, *58*, 555-561.

(36)   Leyton, P.; Sanchez-Cortes, S.; García-Ramos, J. V.; Domingo, C.; Campos-Vallette, M. M.; Saitz, C.; Clavijo, R. E. *J. Phys. Chem. B* **2004**, *108*, 17484 -17490.

(37)   Goulet, P. J. G.; Alvarez-Puebla, R.; Aroca, R. F. Trace Detection of an Environmental Pollutant by Surface-Enhanced Raman Scattering. In *Applications of Surface-Enhanced Raman Spectroscopy*; Farquharson, S., Ed.; CRC Press, in press.

(38)   Novoszad, M.; Gerzabek, M. H.; Haberhauer, G.; Jakusch, M.; Lischka, H.; Tunega, D.; Kirchmann, H. *Chemosphere* **2005**, *59*, 639–647.

(39)   Patrianakos, C.; Hoffmann, D. *J. Anal. Chem.* **1979**, *3*, 150-154.

(40)   Boyko, R. W.; Cartwright, R. A.; Glashan, R. W. *J. Occup. Med.* **1985**, *27*, 799-803.

(41)   Mattioni, B. E.; Kauffman, G. W.; Jurs, P. C.; Custer, L. L.; Durham, S. K.; Pearl, G. M. *J. Chem. Inf. Comp. Sci.* **2003**, *43*, 949-963.

(42)   Fent, K.; Hunn, J. *Mar. Environ. Res.* **1996**, *42*, 377-382.

(43)   Riediker, S.; Suter, M. J.-F.; Giger, W. *Water Res.* **2000**, *34*, 2069-2079.

(44)   Rudolf, H. *J. Electroanal. Chem.* **1988**, *250*, 143-157.

(45)   Palys, B. J.; Bukowska, J.; Jackowska, K. *J. Electroanal. Chem.* **1997**, *428*, 19-24.

(46)   Lin-Vien, D.; Colthup, N. B.; Fateley, W. G.; Grasselli, J. G. *The Handbook of Infrared and Raman Characteristic Frequencies of Organic Molecules*; Academic Press: New York, 1991.

(47)   Moskovits, M. *J. Raman Spectrosc.* **2005**, *36*, 485-496.

160

(48)   Franchy, R. *Rep. Prog. Phys.* **1998**, *61*, 691-753.

Chapter 6

SINGLE-MOLECULE SERS/SERRS FROM LANGMUIR-BLODGETT

MONOLAYERS ON NANOSTRUCTURED METALLIC FILMS

162

6.1 Single-Molecule SERS/SERRS from Langmuir-Blodgett Monolayers

SERS/SERRS have tremendous potential for application in a wide variety of fields including biology,[1,2] medicine,[3,4] pharmacy,[5] sensing,[6,7] and nanoparticle and thin film characterization.[8,9] However, perhaps the most significant applications of SERS/SERRS are those in trace analysis.[10] The well-known first reports of single molecule spectroscopy employing these techniques were published nearly a decade ago.[11,12] These pioneering studies demonstrated that the ultimate limit of molecular analysis could be reached using high information content vibrational spectroscopies, and served to kick-start renewed interest into SERS/SERRS, and more generally into surface-enhanced phenomena. Since then, many practitioners have focused on the study of single molecules for the unique insights provided when SERS/SERRS detection is pushed to the ultimate limits of chemical analysis.[1,2,13-23] The first papers on single molecule SERS/SERRS, and the vast majority of others that have followed, have employed Ag and Au colloidal aggregates as enhancing substrates.[24] These systems have served as good models, and a great deal has been learned from them about the ultra-low concentration regime, as well as the optical properties of metal nanoparticles and their aggregates.[25-27]

Concurrent with these experiments, a parallel approach for single molecule SERS/SERRS spectroscopy employing thin film techniques was pioneered by Aroca et al..[16,28-30] This method involves the spatial resolution of single target dye molecules embedded and isolated in Langmuir-Blodgett (LB) fatty acid monolayers deposited onto vacuum evaporated, enhancing metallic nanostructured films, as is depicted in Figure 6.1. This approach offers the benefit of an increased degree of control over sample

163

architectures,[31] and provides, for comparison, a different system for studying the many unique complexities that are encountered when the single molecule regime is approached.

Discussed in this chapter are the results of several studies where the Langmuir-Blodgett approach to single molecule SERS/SERRS detection was employed. In this work, 6 molecular systems were studied at the single-molecule level, using three different nanostructured metal films, a variety of laser excitation wavelengths, and single-point and 2D spatial mapping techniques. The sections of this chapter discuss, in turn, the study of overtones and combinations in the single-molecule spectra of perylene derivatives; the use of 2D SERRS mapping techniques to explore the breakdown of ensemble averaging; single-molecule SERRS from one-to-one binary mixtures; and non-resonant single-molecule SERS on nanostructured metallic films.
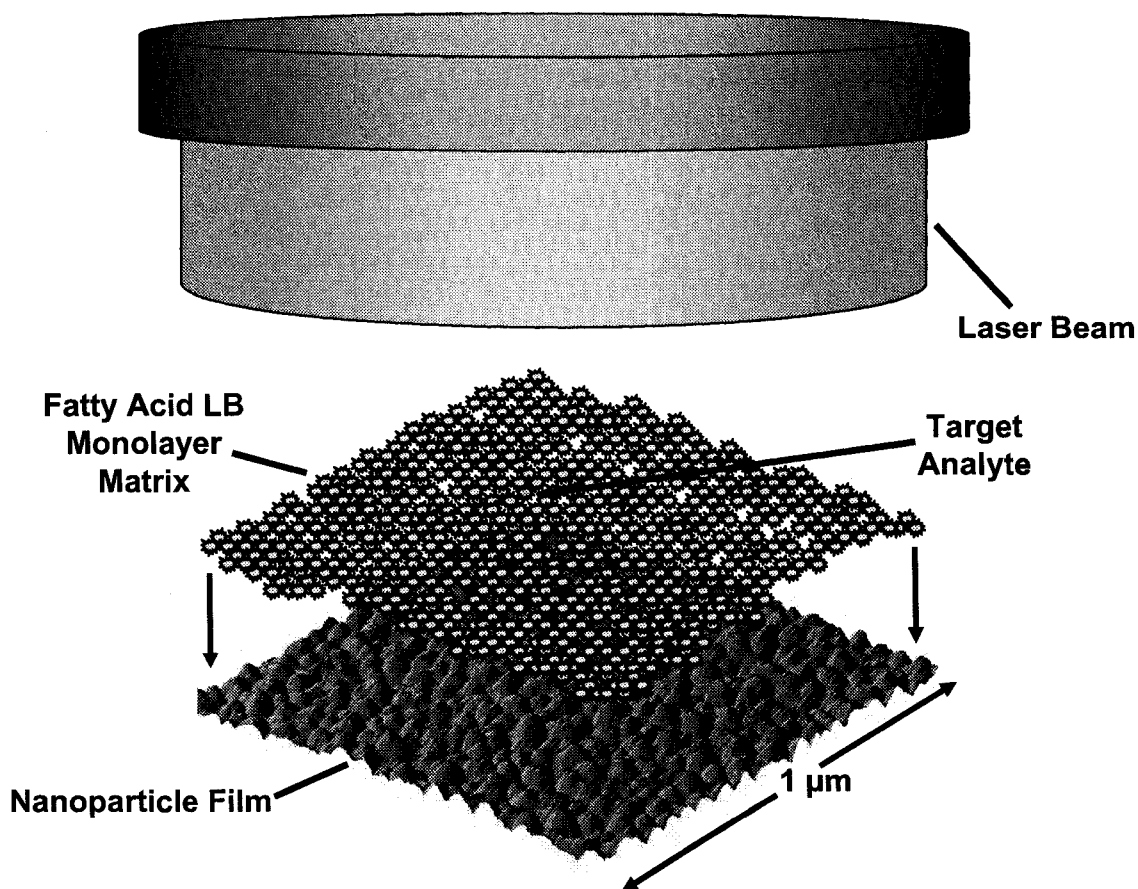
Figure 6.1 Depiction of Single-Molecule Langmuir-Blodgett SERRS.

6.2 Overtones and Combinations in the Single-Molecule SERRS of Perylenes[a]

6.2.1 Introduction

Overtone and combination bands in Raman spectra result from anharmonic behaviour of oscillators that leads to relaxation of the selection rule ($\Delta v = \pm 1$). In general, these bands are of extremely low intensity in non-resonant Raman scattering spectra and are not observed. However, in resonance Raman scattering (RRS) experiments, where laser excitation is resonant with an electronic transition of the

---

[a] The work of this section was done in close collaboration with N. P. W. Pieczonka. With the exception of Langmuir-Blodgett film fabrication, all aspects of this work benefited from his valuable contributions.

molecule, these modes can often be much stronger and be of similar intensity to the fundamentals.[32-35] The intensities of bands in RRS are determined primarily by the properties of the excited electronic state,[36] and it is found that the relative strengths of different modes is highly dependent on excitation wavelength.[32] This plays a large role in whether or not overtones and combinations are observed with high relative intensity. Also, all vibrational modes observed in Raman scattering (RS) are not intensified equally by resonance. Rather, only those modes associated with the electronic transition involved tend to be observed with high intensity. As a result, overtones and combinations of these coupled modes are also those that are observed with greatest intensity.

The molecules that have been most heavily studied in single-molecule SERRS work, in particular rhodamine 6G, do not show extremely high relative intensity of overtone and combination bands at the most commonly employed laser excitation wavelengths. These bands tend to be less than 10% as intense as the fundamentals (see Figure 4.19), and consequently their observation has not been reported for single-molecule experiments where signal-to-noise ratios are often poor. However, many perylene materials have very strong overtones and combinations under green excitation at 514.5 nm.[37] These molecules have also been shown to be detectable at ultralow concentration,[16,28] and so they are excellent candidates for studies into the possibility of detecting these modes at the single-molecule level.

In the work discussed in this section,[34,38] the SERRS spectra of three different perylene derivatives (BBIP PTCD, pentyl PTCD, and azo PTCD) were studied at the single-molecule level. These molecules are shown in Figure 6.2, and were embedded, and diluted within LB monolayers of arachidic acid, deposited onto nanostructured films

166

of Ag, then spatially resolved using a Raman microscope. It was found that overtones and combinations of three characteristic ring stretching vibrations of the chromophore could be distinguished from single-molecule SERRS spectra of each of these derivatives, indicating that they are amplified with similar enhancement factors to fundamental vibrations.

BBIP PTCD
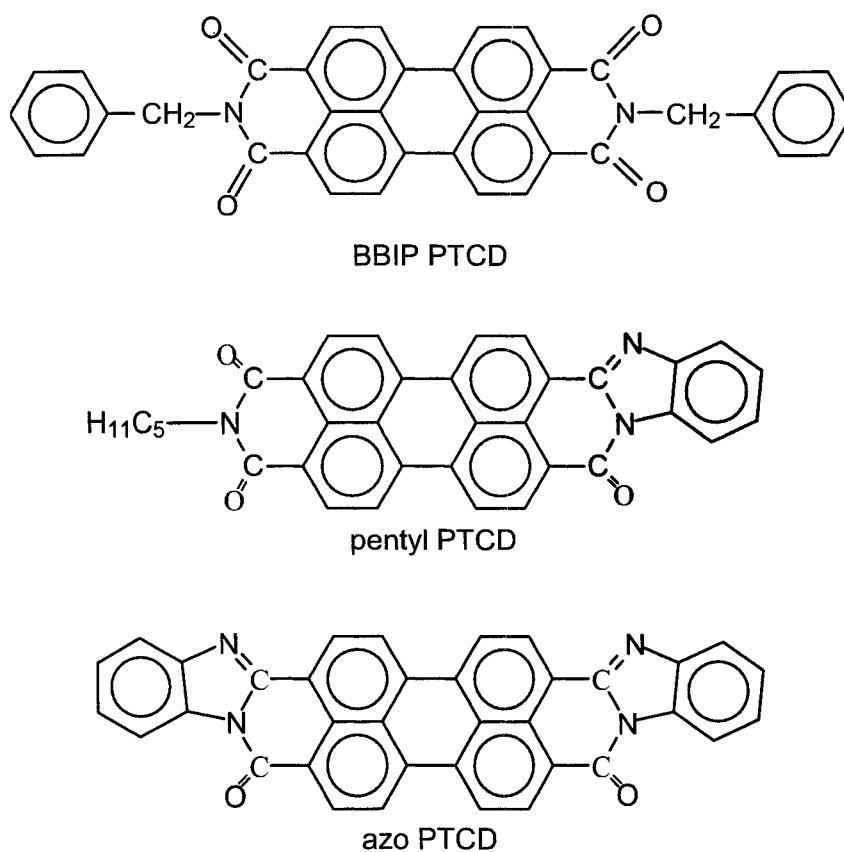
pentyl PTCD

azo PTCD

Figure 6.2 Molecular structures of BBIP PTCD, pentyl PTCD, and azo PTCD.

6.2.2 Characterization of Nanostructured Ag Film Substrate

The surface plasmon absorption spectrum of the 6 nm mass thickness, evaporated Ag nanostructured films used in this work is shown in Figure 6.3(a). It shows a broad

167

extinction covering the entire visible range of the electromagnetic spectrum, with a maximum centered at 491 nm, indicating a large distribution of particle sizes and local particle arrangements. This maximum is centered near the laser excitation wavelength of 514.5 nm used in this work. The atomic force microscopy (AFM) image of this film is shown in Figure 6.3(b). This image reveals an inhomogeneous surface with a broad distribution of particles ranging between ca. 20 and 100 nm in diameter, in agreement with what is expected based on the surface plasmon absorption results. It was recorded from a 1 μm^2 area, which is approximately the area probed in all of the micro-Raman measurements reported in this chapter. The particles in this film form a large electromagnetically interacting network due to their small interparticle spacing. Each particle behaves as an oscillating dipole that can couple with others, and multi-particle dipole-dipole interactions lead to highly localized, excitation wavelength-dependent surface plasmon normal modes.[26,39,40] When excited with radiation, these normal modes produce so called hot spots, highly localized (nanometer scale) areas of intense electromagnetic fields where the highest enhancement of Raman and resonance Raman signals occur. When performing high concentration, ensemble measurements, information about this localization is lost. However, in single-molecule experiments this feature proves highly important. Notably, the allowed, normal mode resonances in these films can be induced by a wide range of excitation wavelengths, and this makes them particularly attractive for work with fixed laser excitation.
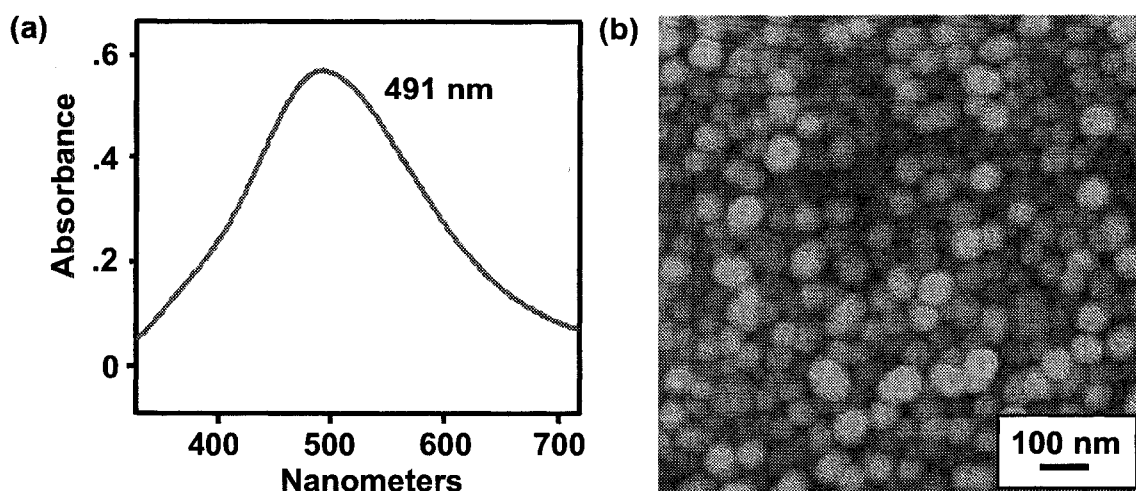
Figure 6.3 Surface plasmon absorption and AFM image of 6 nm Ag film.

6.2.3 Electronic Absorption

In Figure 6.4, the absorption spectra of 10^{-6} M solutions of BBIP PTCD, pentyl PTCD, and azo PTCD in dichloromethane are shown. It can be seen that the 514.5 nm laser excitation used for all of the Raman measurements of this work also falls within the absorption envelope of each of these molecules. Therefore, all of these measurements will benefit from resonance enhancement, and be termed resonance Raman scattering (RRS). In the case of measurements made on Ag nanostructured films, the double resonance condition of SERRS will be fulfilled and both the molecular resonance and surface enhancement mechanisms will be active. The peaks of the absorption spectra of these molecules are characteristic of the π-π^* electronic transition of the perylene chromophore.[41] BBIP PTCD has its 0-0 transition at 539 nm with vibronic structure at 501 and 471 nm. The corresponding bands for pentyl PTCD are at 581, 544, and 512 nm, while for azo PTCD they are at 611, 563, and 522 nm. These strong redshifts result from

169

the extension of the conjugated system through the addition of azo groups in pentyl PTCD and azo PTCD. Each of these molecules was found to have a molar extinction coefficient of ca. 10^3 mole^{-1}m^2, and a corresponding absorption cross section of ca. 10^{-17} cm^2 per molecule, at their respective 0-0 transitions.
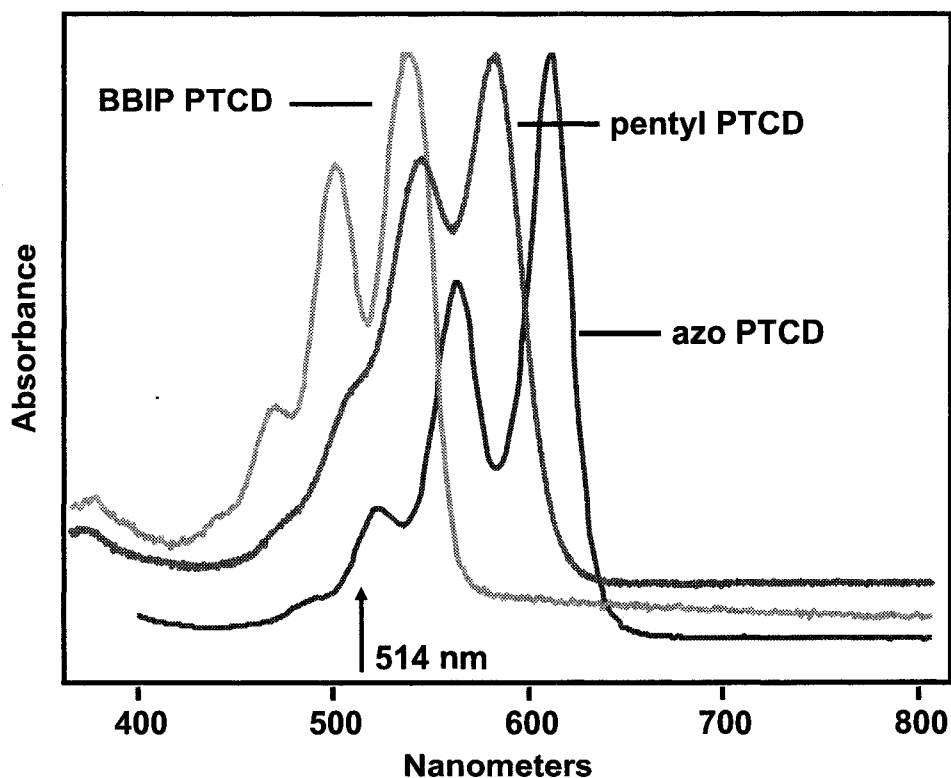
Figure 6.4 Solution absorption of BBIP PTCD, pentyl PTCD, and azo PTCD.

6.2.4 Ensemble SERRS

In this work, the SERRS spectra of BBIP PTCD, pentyl PTCD, and azo PTCD were recorded from mixed arachidic acid/perylene LB monolayers, deposited onto 6 nm mass thickness Ag nanoparticle films, having concentrations of 2×10^6 (1:1 AA:BBIP PTCD ratio), 10, and 1 dye molecule(s) per square micron of surface area, corresponding

170

to the scattering area of the Raman microscope. The most concentrated films for each of these molecules have very similar SERRS spectra. In Figure 6.5, the SERRS spectrum of the concentrated monolayer of BBIP PTCD is shown as an example. The inset of this figure shows a baselined SERRS spectrum of BBIP PTCD where the vibrational bands can be seen more easily, including the fundamentals and first and second sets of overtones and combinations. The SERRS spectra of these molecules are dominated by 3 fundamental ring stretching modes at 1298 (a), 1378 (b), and 1575 cm^{-1} (c), as well as the first overtones and combinations of these bands at 2593 ($2a$), 2672 ($a+b$), 2752 ($2b$), 2874 ($a+c$), 2947 ($b+c$), and 3152 ($2c$) (note: a, b, and c designate the fundamental modes). This progression of overtones and combinations is somewhat unique due to its high relative intensity. Further, for highly concentrated monolayers such as this, it is possible to calculate directly average enhancement factors through comparison with signals from the same monolayer on a non-enhancing substrate such as glass. It is found that average enhancement factors of ca. 10^4 are calculated for each of these molecules on the Ag nanostructured films employed here. Of course, this does not represent the magnitude of enhancement at electromagnetic hot spots, which will be above this average.

In these high concentration SERRS experiments, two important observations were made. First, the RRS and SERRS spectra show no major spectral differences. This indicates that these molecules do not interact strongly with the metal nanostructures, as is expected, and that their interaction with the metal can be viewed as physisorption. Second, with major implications for ultralow concentration measurements, the SERRS signals from these molecules show strong decay with laser exposure, as revealed by time

series measurements. With this decay comes the growth of bands that can be assigned to amorphous carbon, as is well known in SERS/SERRS measurements.[42] This suggests that strong photodegradation/photoreaction occurs on the surface of the metal nanoparticles. As a result, it is necessary to employ very low laser power densities, particularly at low concentrations, to avoid doing irreversible damage to the sample.
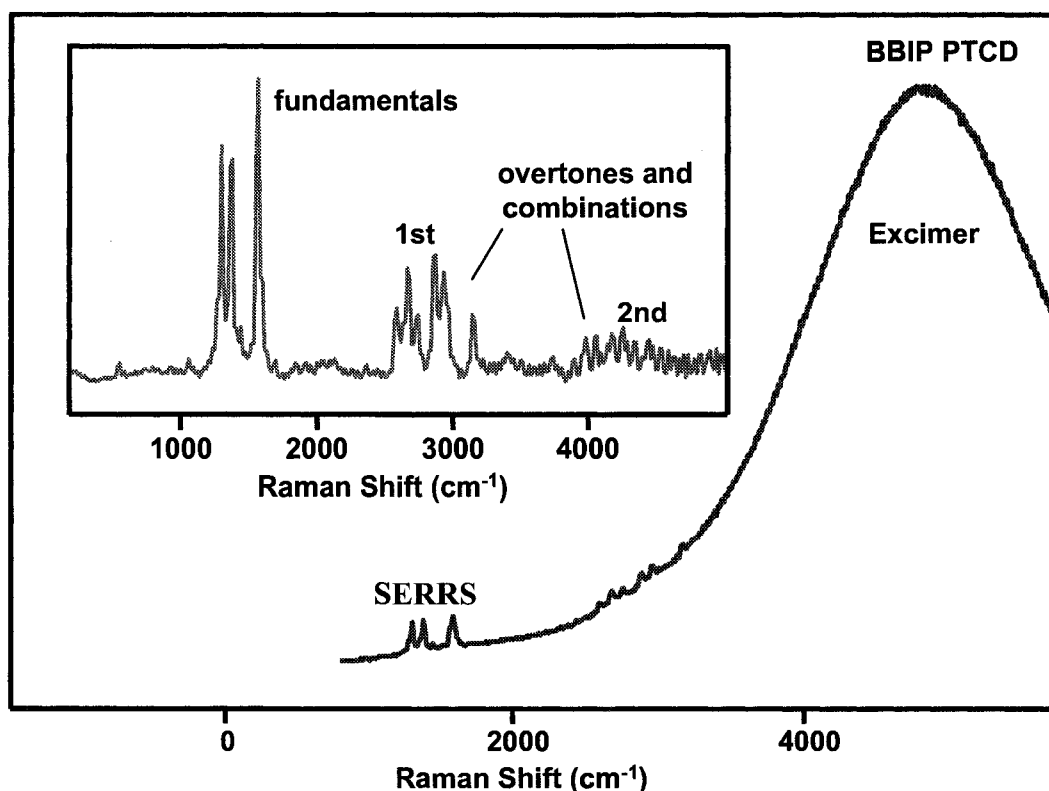

Figure 6.5 Ensemble SERRS of perylene LB monolayers on Ag films. SERRS and SEF recorded with 514.5 nm excitation from a 1:1 AA:BBIP PTCD mixed LB monolayer deposited onto a 6 nm Ag nanostructured Ag film. Inset shows baselined SERRS.

Finally, it can be seen in Figure 6.5 that in highly concentrated monolayers these molecules also exhibit very strong surface-enhanced excimer fluorescence that is of much greater intensity than the SERRS. This excimer fluorescence arises as a result of the high packing of these molecules, and is the emission of excited state dimers that form when excited state molecules dimerize with ground state molecules. It is commonly observed for perylene molecules due to their strong tendency toward pi stacking. On Ag nanostructured films, surface-enhancement of this excimer fluorescence occurs with enhancement factors generally ranging between 10 and 20.

6.2.5 Single-Molecule SERRS

In Figures 6.6, 6.7, and 6.8, respectively, the SERRS spectra of BBIP PTCD, pentyl PTCD, and azo PTCD, recorded from LB monolayers at three concentrations (2×10^6, 10, and 1 dye molecule(s) per square micron) on nanostructured Ag films, are shown. In all cases, strong spectral degradation is observed as the concentration is decreased to the single-molecule level. However, weak fundamentals, overtones, and combinations can still be observed with low signal-to noise ratio. This preservation of the high relative intensities of the overtone and combination bands indicates that their enhancement is very similar to the enhancement of fundamentals. It can be also seen that at ultralow concentrations of the dye, the SERS from the C-H stretching modes of arachidic acid become apparent between 2800 and 3000 cm^{-1}, preventing the observation of some of the overtone and combination bands. These C-H bands are not observed in the concentrated films as their intensity is dwarfed by the very intense SERRS of the dye molecules.

173
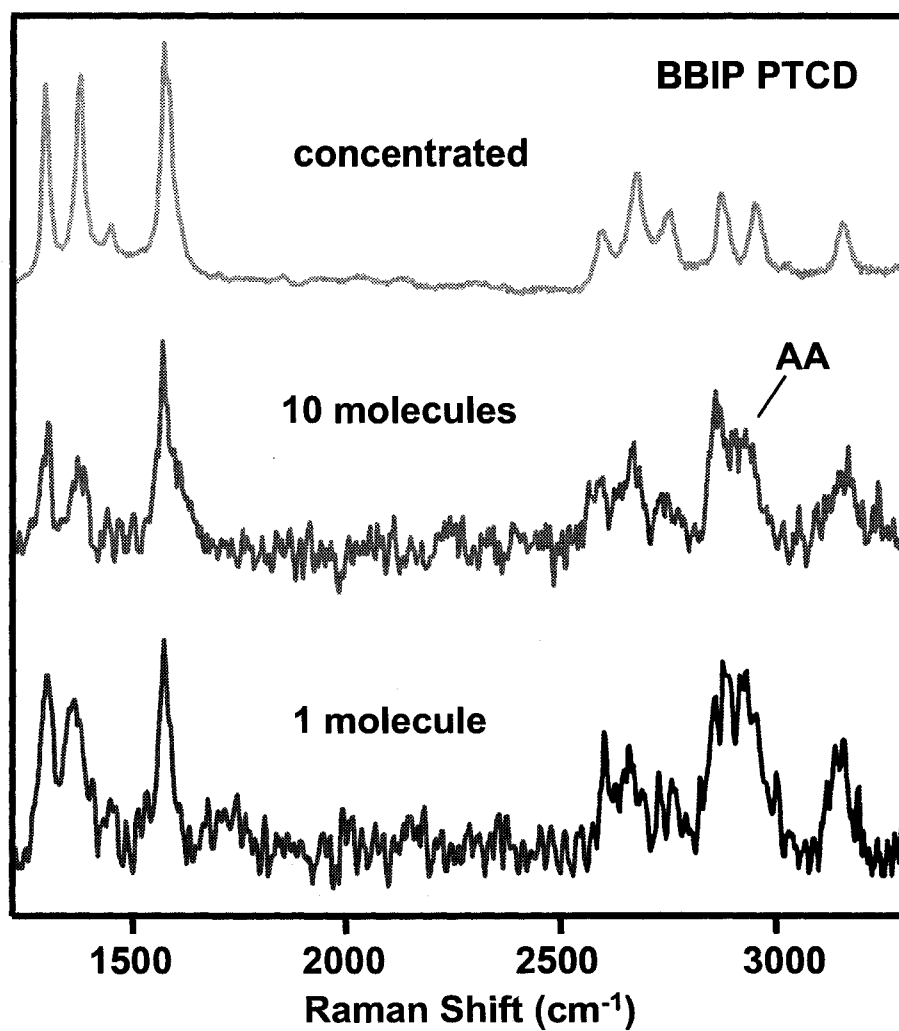
Figure 6.6 BBIP PTCD single-molecule LB SERRS on Ag. SERRS spectra of BBIP

PTCD recorded with 514.5 nm laser excitation from LB monolayers with 2×10^6, 10, and

1 dye molecule(s) per square micron on nanostructured Ag films.

174
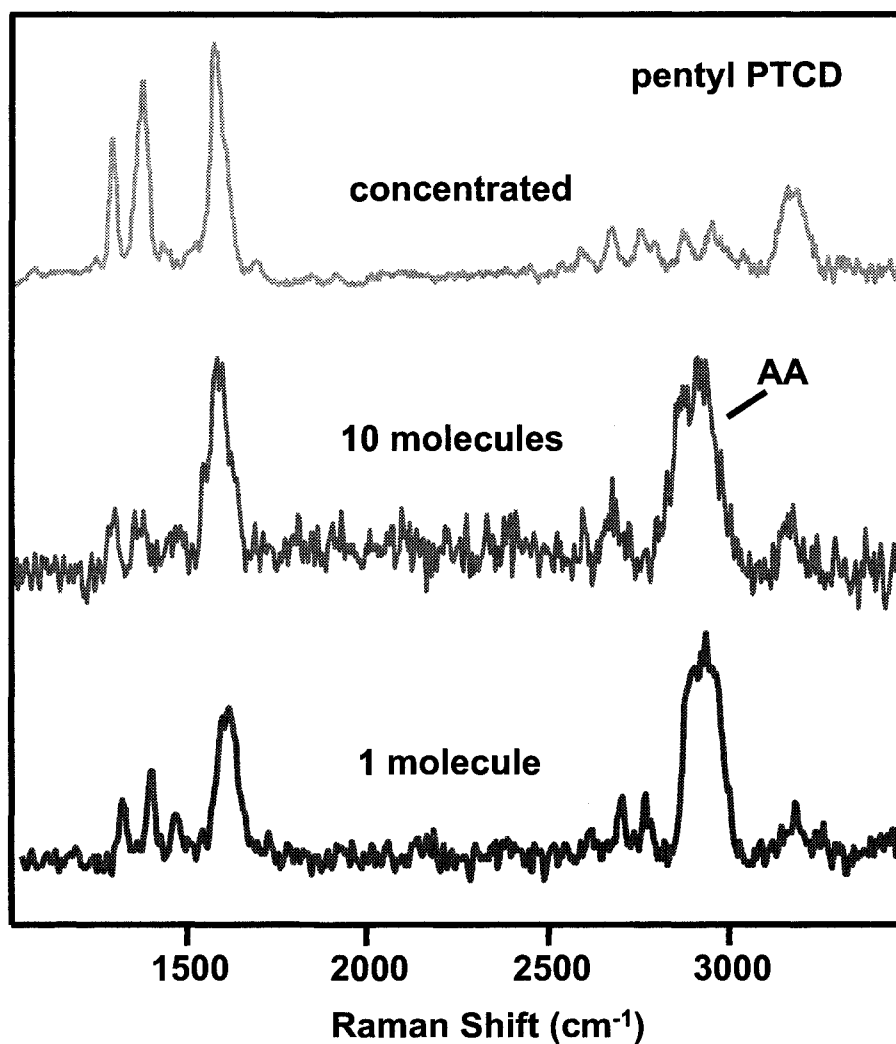
Figure 6.7 Pentyl PTCD single-molecule LB SERRS on Ag. SERRS spectra of pentyl PTCD recorded with 514.5 nm laser excitation from LB monolayers with 2×10^6, 10, and 1 dye molecule(s) per square micron on nanostructured Ag films.
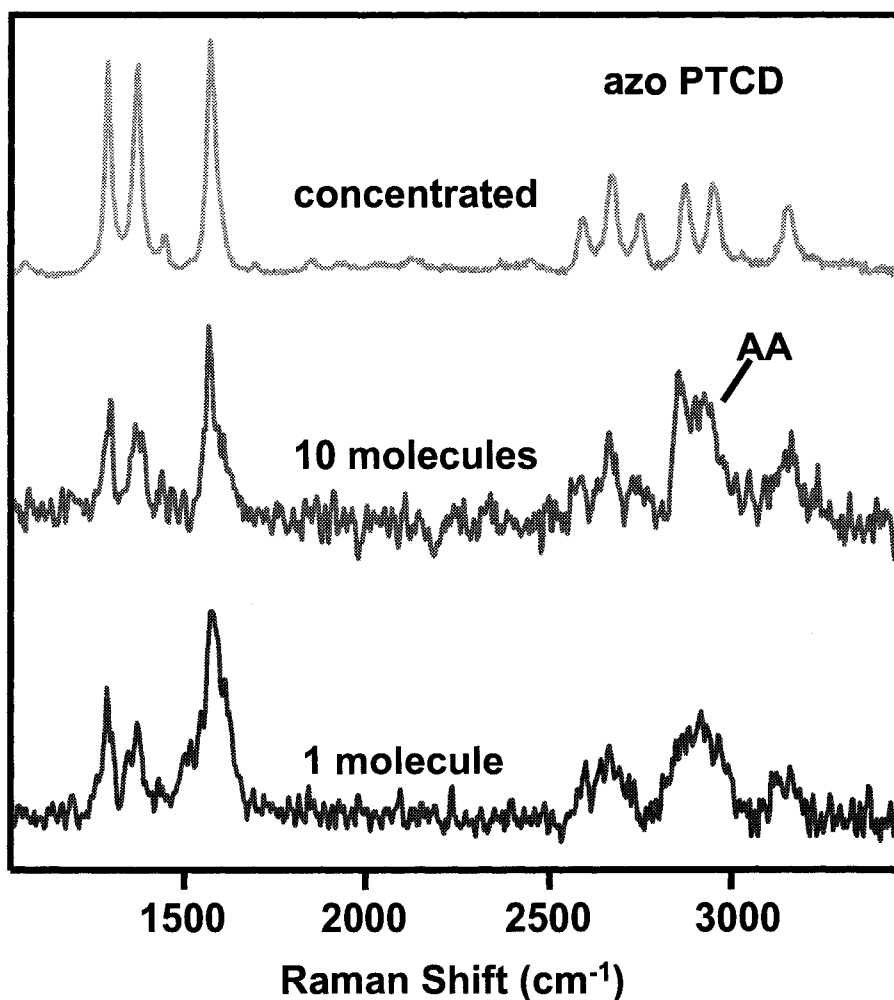
Figure 6.8 Azo PTCD single-molecule LB SERRS on Ag. SERRS spectra of azo

PTCD recorded with 514.5 nm laser excitation from LB monolayers with 2×10^6, 10, and

1 dye molecule(s) per square micron on nanostructured Ag films.

In the monolayers produced in this work there are ca. 4 million molecular sites

per μm^2, which is the scattering area of the microscope, and also the area of the AFM

image in Figure 6.3. Of these only 10 or 1 molecule(s) is a PTCD derivative for the

lower 2 cases in Figures 6.6, 6.7, and 6.8. These molecules are only detected when they

176

sit in areas of highly localized and very intense electromagnetic fields on the Ag film. These areas are commonly referred to as hot spots, and are thought to be no more than a few nanometers across. Because of this, it is highly rare for PTCD molecules to be found in these areas, and it is necessary to record a very large number of spectra before detecting a perylene molecule. Whether the monolayer contains 10 molecules or 1 molecule, this problem remains. Further, at both concentrations, the spectral properties that seem to define single-molecule SERRS spectroscopy are observed. Therefore, it is expected that even when up to 10 molecules on average occupy the field of view, signals are only derived from single-molecules sitting in electromagnetic hot spots. This expectation is confirmed by 2D SERRS mapping results that are discussed in the next two sections of this chapter.

All of the results presented in this section, however, were recorded using single point Raman acquisition strategies. This necessitated a very time consuming 'hunt' for single-molecule signals. These signals, in almost all cases, were found to disappear immediately after being first recorded. This prevented collection of important dynamics data and the accumulation of signals over time, and can be attributed to slight movements of the molecule, including tumbling, as well as a variety of possible photoprocesses that could occur at the surface, such as photodesorption and photodegradation. The latter is supported by results of this work that showed strong signal decay for these molecules at higher concentrations. Also noteworthy in the results of Figures 6.6, 6.7, and 6.8, is the strong degree to which the low concentration spectra vary from one another from spot to spot. This spectral variation is observed for all band parameters including Raman shift,

bandwidth, band shape, and absolute and relative intensity, and is the result of the loss of ensemble averaging.

6.2.6 Conclusion

In the work discussed in this section, the SERRS of three PTCD derivatives was studied down to the single-molecule level. These molecules were embedded in arachidic acid Langmuir-Blodgett monolayers deposited onto nanostructured, evaporated Ag films at concentrations such that single, isolated dye molecules were in the scattering area of the microscope at any given time. When these molecules were located in rare electromagnetic hot spots on the nanostructured surface, their detection was possible. It was found that it was possible to detect weak overtones and combinations of three characteristic fundamental ring stretching modes from all three of the PTCD derivatives measured, demonstrating that these modes can be enhanced by the same mechanism that fundamentals are. Also, many of unique features of single-molecule SERRS spectroscopy were explored in this section, and these include: (1) rarity of detection, (2) very fast signal loss, and (3) spectral variation due to loss of ensemble averaging.

6.3 Mapping Single-Molecule SERRS from Langmuir-Blodgett Monolayers

6.3.1 Introduction

In place of single-point Raman acquisition strategies,[43] 2D spatial SERRS mapping was employed in the single-molecule work discussed in this section.[44] This involved the rastering of a computer-controlled 3-axis encoded (XYZ) motorized stage, with a step of 1 μm, where a single 1 s accumulation was recorded at each spot. This strategy served to facilitate the fast and easy collection of large amounts of data, while

178

also minimizing sample laser exposure time, and thus sample photodegradation, allowing slightly increased laser power to be used. This effectively addressed many of the difficulties encountered using single-point acquisition, but it also presented the possibility of tackling several important and outstanding problems in single-molecule LB SERRS work. Among these, were questions regarding the nature of the breakdown of ensemble averaging as the single-molecule regime is approached; the density of hot spots on nanostructured Ag films; and the distribution of dye molecules within mixed AA:PTCD LB monolayers. To attempt to answer these questions, the perylene derivative n-pentyl-5-salicylimido perylene (salPTCD) was employed, and is shown in Figure 6.9. This molecule was dispersed into mixed fatty acid LB monolayers deposited onto nanostructured Ag films, and by variation of the ratio of the two components in the films, the effects of dye concentration, on both SERRS spectra and LB monolayer architecture, were explored down to the single molecule level.
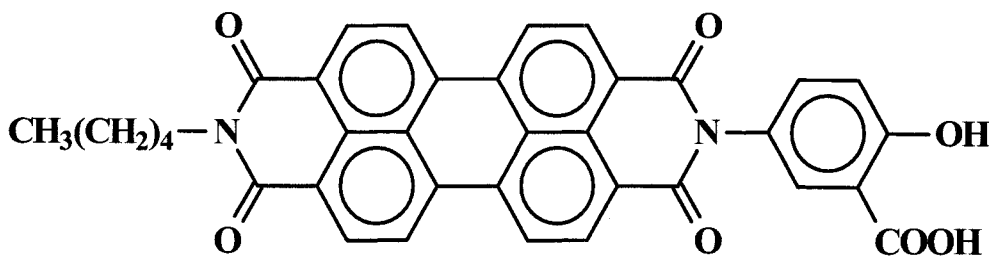
Figure 6.9 Molecular structure of salPTCD.

6.3.2 Absorption and Fluorescence

In this work, 6 nm mass thickness evaporated, nanostructured films of Ag were employed as enhancing substrates for LB SERRS measurements, and the characterization

179

of these films is given in section 6.2.2. In Figure 6.10, on the other hand, the 10^{-5} M

solution absorption of salPTCD in dichloromethane is shown. This molecule is strongly

resonant with the 514.5 nm laser excitation employed in this work, with bands centered at

528, 491, and 459 nm, which can be assigned to the vibronic structure of the π-π*

transition of the PTCD chromophore. Moreover, this molecule, like the three discussed

in the previous section, fulfills the double resonance condition of SERRS and therefore

has its Raman signals enhanced by both molecular electronic resonance and surface

electromagnetic enhancement mechanisms.
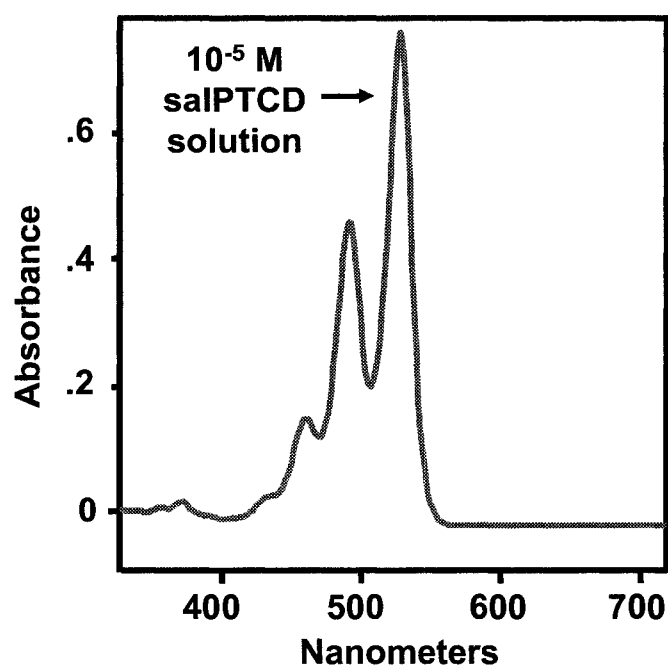
Figure 6.10 Solution absorption of salPTCD.

Fluorescence spectra of salPTCD solutions in dichloromethane are shown in Figure 6.11, with concentrations ranging between 10^{-4} and 10^{-10} M. At higher concentrations, excimer emission from aggregates appears to be the major contributor to the spectra, but as concentrations are decreased, monomer emission takes over. This continuous blue-shifting of the spectra proceeds with dilution, until, at concentrations below ca. 10^{-7} M, monomer emission becomes dominant, indicating that the aggregation of salPTCD molecules is no longer significant. (Between 10^{-8} and 10^{-10} M, on top of the fluorescence of the dye, the Raman scattering of the dichloromethane solvent molecules, and the Rayleigh line at 514 nm, can also be observed.) Similar results are also seen for the mixed AA-salPTCD spreading solutions used to prepare low concentration LB monolayers, including those used in this work to prepare films with less than ca. 100 target molecules in the scattering area of the Raman microscope. Excimer fluorescence is also not observed in the spectra recorded from these LB films. Thus, aggregates of salPTCD are not present in the solutions used to prepare ultra-low concentration mixed LB samples, or in the monolayers themselves, as is corroborated by previously reported work on another PTCD derivative.[45] From this, it can be concluded that single molecule salPTCD spectra recorded from LB monolayers on enhancing nanoparticle substrates are in fact being collected from single isolated monomers, rather than from dimers or higher order aggregates.

181
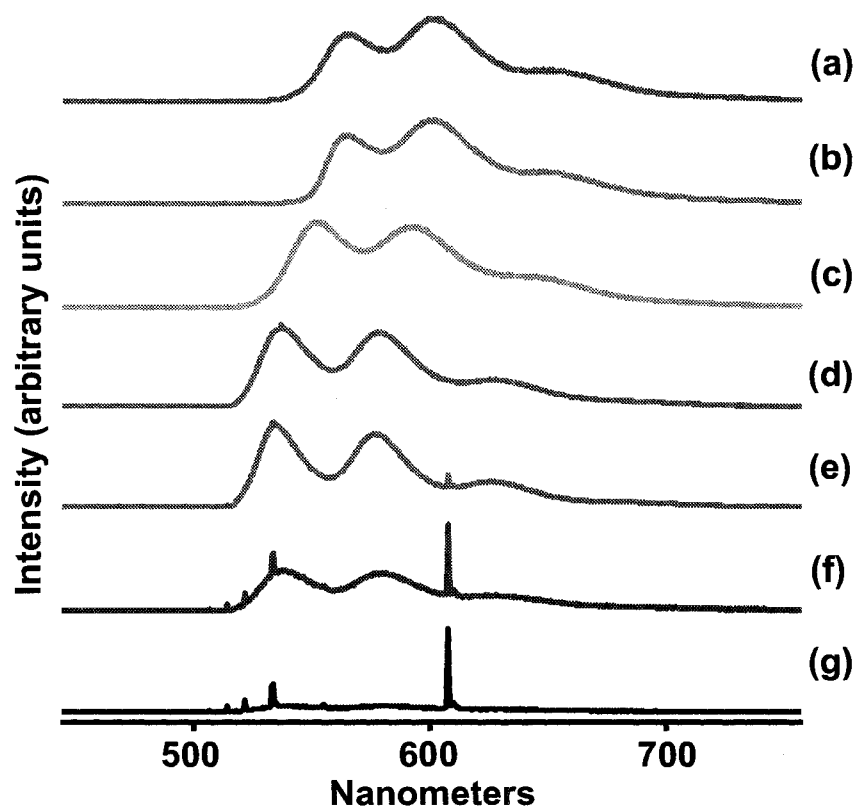
Figure 6.11   Solution fluorescence of salPTCD with decreasing concentration.

Fluorescence spectra of solutions (dichloromethane as solvent) with concentrations of **(a)**

10^{-4} M, **(b)** 10^{-5} M, **(c)** 10^{-6} M, **(d)** 10^{-7} M, **(e)** 10^{-8} M, **(f)** 10^{-9} M, **(g)** 10^{-10} M.

6.3.3 RRS and SERRS from Langmuir-Blodgett Monolayers

In Figure 6.12, the resonance Raman scattering (RRS) spectrum of a single 10:1

AA:salPTCD monolayer deposited onto glass is compared with the SERRS spectrum of a

single 10:1 AA:salPTCD monolayer deposited onto an evaporated 6 nm Ag nanoparticle

film.   Both Raman and excimer fluorescence peaks can be clearly observed, with the

narrow vibrational bands sitting atop, and to lower Stokes shift from (using the 514 nm

excitation) the broad emission band of the excimer fluorescence.   The resonance Raman

182

scattering is enhanced to a much greater extent than the excimer fluorescence in the presence of Ag nanostructures, as is expected. Because the same monolayer was deposited onto the Ag nanoparticle and glass substrates, average surface enhancement factors can be estimated directly for resonance Raman scattering and excimer fluorescence bands, simply by comparing the intensities from measurements made on each substrate under the same experimental conditions. It is found that, at this concentration level, the average enhancement factor due to surface-enhancement for resonance Raman scattering (SERRS) is approximately 10^3-10^4, while the average enhancement factor for excimer fluorescence (surface-enhanced fluorescence, SEF) is about 15. Also, as discussed in the previous section, fundamentals and a strong overtone and combination progression can be observed in the SERRS spectra of several perylene dye derivatives, and these modes can all be assigned to the central perylene chromophore. In this case, as shown in Figure 2, the strongest fundamental bands (below 1600 cm^{-1}) can be seen in the RRS spectrum along with very weak first overtones and combinations (2500-3200 cm^{-1}). In the SERRS spectrum, on the other hand, strong first and second (3800-4800 cm^{-1}) overtones and combinations can be easily observed along with the fundamentals, due to the additional intensity provided by surface-enhancement.
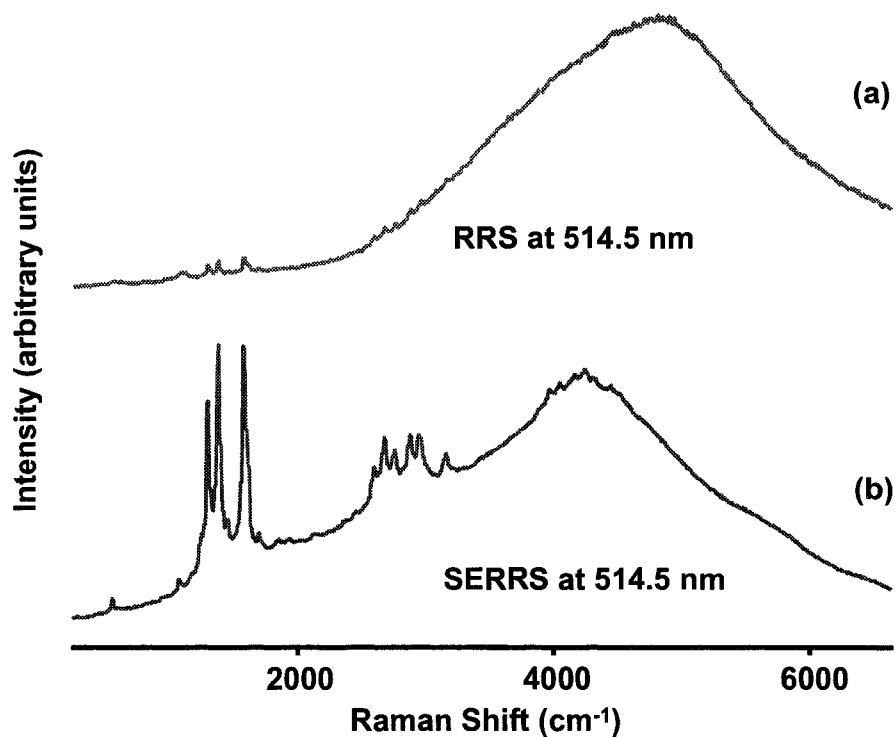
Figure 6.12 RRS and SERRS compared for salPTCD. (a) Resonance Raman scattering (RRS) spectrum of a single 10:1 AA:salPTCD monolayer deposited onto glass. **(b)** Surface-enhanced resonance Raman scattering (SERRS) spectrum of a single 10:1 AA:salPTCD monolayer deposited onto an evaporated 6 nm Ag film.

6.3.4 Mapping SERRS Down to the Single-Molecule Level

Figure 6.13 shows 2D SERRS mapping images recorded from mixed LB monolayers deposited onto 6 nm nanostructured Ag films, having various concentrations of perylene dye. For all images, the intensity of the strong 1300 cm^{-1} fundamental mode of salPTCD has been mapped as a function of x-y area components, and each pixel corresponds to a single recorded spectrum. In Figure 6.13(a), a 10:1 AA:salPTCD LB monolayer on a Ag nanoparticle film has been mapped. Essentially, strong SERRS

184

signals are detected at all spots on this sample, but there are domains present in the monolayer where slight signal differences are observed, and the origin of these areas can be attributed to the aggregation of PTCD dye molecules that is known to be possible at these concentration levels in mixed LB films.
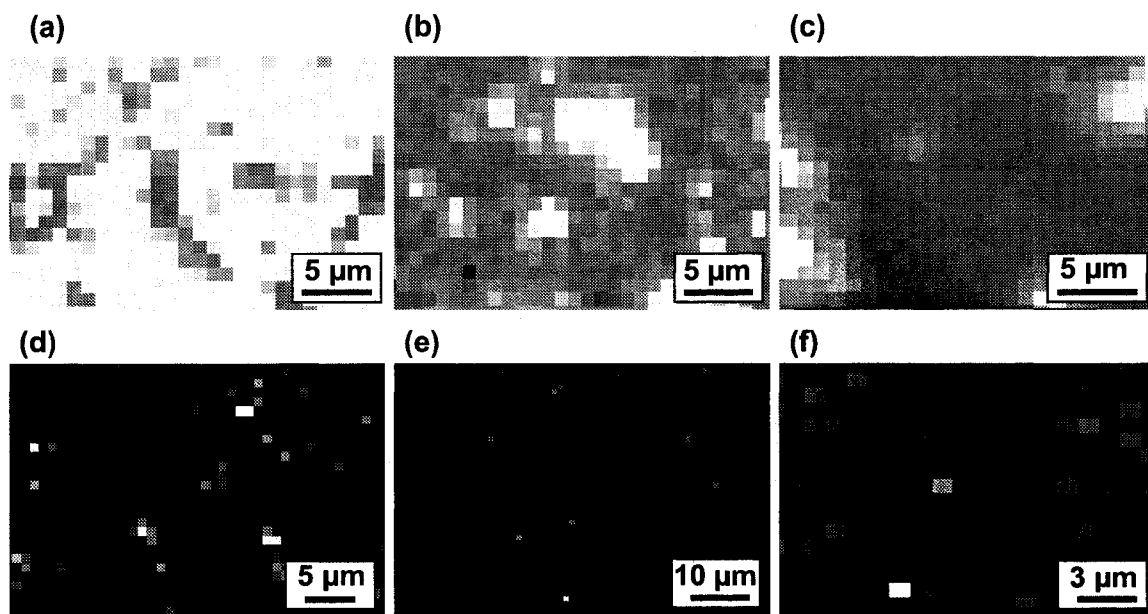
Figure 6.13 Mapping of SERRS Down to the Single-Molecule Level. SERRS mapping images recorded from mixed LB monolayers deposited onto 6 nm Ag films. The concentrations of the monolayers are: **(a)** 10:1 AA:salPTCD, **(b)** 10^2:1 AA:salPTCD, **(c)** 10^3:1 AA:salPTCD, **(d)** 10^4:1 AA:salPTCD, **(e)** 10^5:1 AA:salPTCD, and **(f)** 1 salPTCD molecule/μm^2. (Colour scale is not consistent for different images- see text for discussion.)

As the concentration of salPTCD in these monolayers is decreased by factors of 10 and 100, in Figures 6.13(b) and (c), respectively, this domain formation is clearly seen

in the SERRS mapping images. For the first of these images, strong signals can still be observed at most locations, but definite signal differences between bright and dark regions begin to develop. In Figure 6.13(c), corresponding to a concentration of 10^3:1 AA:salPTCD, the phenomenon of domain formation becomes even stronger, and SERRS signals are not detected, or are detected very weakly, at all darker areas, while signals in the brighter regions are reduced compared to signals of bright spots on images of more highly concentrated films. Importantly, based on AFM imaging, it is highly unlikely that these domains of increased signals, which are on the order of many square microns, are the result of variation in the enhancing substrate, as the 6 nm Ag nanoparticle films used are effectively homogeneous at this length scale. The fact that this variation is a result of dye aggregation in the LB monolayer becomes increasingly clear as we continue to decrease concentration, where a new phenomenon begins to be apparent.

Figures 6.13(d-f) show individual pixels of relatively high intensity where the SERRS spectra of salPTCD can be weakly detected. In Figures 6.13(e) and (f), in particular, these signals (hot pixels) are completely isolated from one another and very rare indeed (0.2 % of spots in 6.13(e), and 0.3 % of spots in 6.13(f)). We can interpret this result as an indication that, at these concentration levels, average surface-enhancement is insufficient for molecular detection, and all signals are detected from local electromagnetic hot spots. As there are only, on average, 40 and 1 dye molecule(s), respectively, out of a possible 4 million molecular sites in a single Raman scattering area (1 pixel), for each of these films, it is clear that, at these ultra-low concentrations, the rarity of coincidence between electromagnetic hot spots on Ag island films, and single isolated monomers in LB monolayers, is a key consideration. Indeed, it appears that even

186

with as many 40 molecules within the relatively large scattering area of the Raman microscope, we are in fact generally detecting spectra from only a single molecule. And, considering that the average single molecule mapping experiment shows that less than ca. 0.5 % of spots are hot, it can be concluded that these hot spots are fairly highly localized on the nano-scale, and correspond to relatively few molecular sites. Further, these hot spots are wavelength and polarization dependent and will be found in different locations if these factors are changed. Moreover, it is at concentrations between 10^3:1 and 10^5:1 AA: salPTCD where the breakdown of ensemble averaging is observed for these samples, as can be seen more clearly in the spectra of Figure 6.14. For mapping measurements recorded for monolayers below these concentrations, the percentage of total spots that are "hot" tends to show significant fluctuation from map to map, and this is a result of the fact that relatively few spectra (1000-2000) are collected for each.

Figure 6.14, shows typical salPTCD SERRS spectra recorded at each concentration level in the mapping measurements of Figure 6.13. The spectra found in Figures 6.14(a-c) show some minor differences with one another, which are likely the result of differences in the aggregation, or photodegradation of the molecules. However, at each of these concentration levels, the spectra observed from spot to spot are fairly stable in terms of preserving their average bandwidths, frequencies, and relative intensities (showing some absolute intensity changes as mentioned above). This is due to the large ensemble averaging represented by these measurements. Nevertheless, when the 10^3:1 AA:salPTCD concentration level is reached, this stability appears to deteriorate strongly leading to variation in all of these band parameters from spot to spot, and this variation becomes much more pronounced as the single molecule level is reached in

187

Figures 6.14(e) and (f). Figure 6.15 shows a comparison of four different single molecule salPTCD SERRS spectra. Quick inspection of these results reveals clearly significant variations, from spot to spot, in the Raman shifts, bandwidths, band shapes, and relative and absolute intensities of the three fundamental bands shown. This is typical of the unique behaviour that is commonly observed as single molecule detection limits are approached using SERRS, and reveals the breakdown of ensemble averaging, as well as the wide variety of different local environments found at the heart of electromagnetic hot spots on nanostructured Ag films.
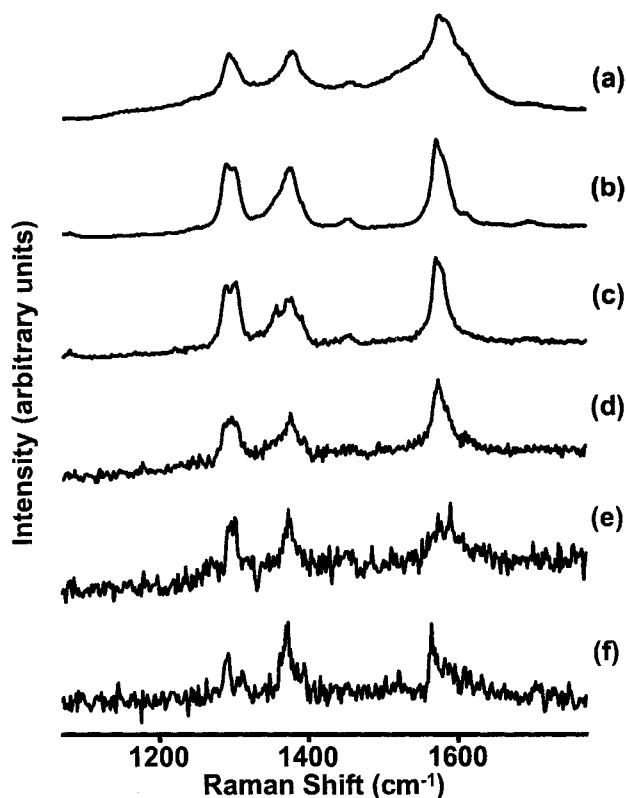
Figure 6.14 SalPTCD SERRS at various concentrations. SalPTCD SERRS spectra recorded in mapping measurements at monolayer concentrations of: **(a)** 10:1, **(b)** 10^2:1, **(c)** 10^3:1, **(d)** 10^4:1, and **(e)** 10^5:1 AA: salPTCD, and **(f)** 1 salPTCD molecule/μm^2.

188
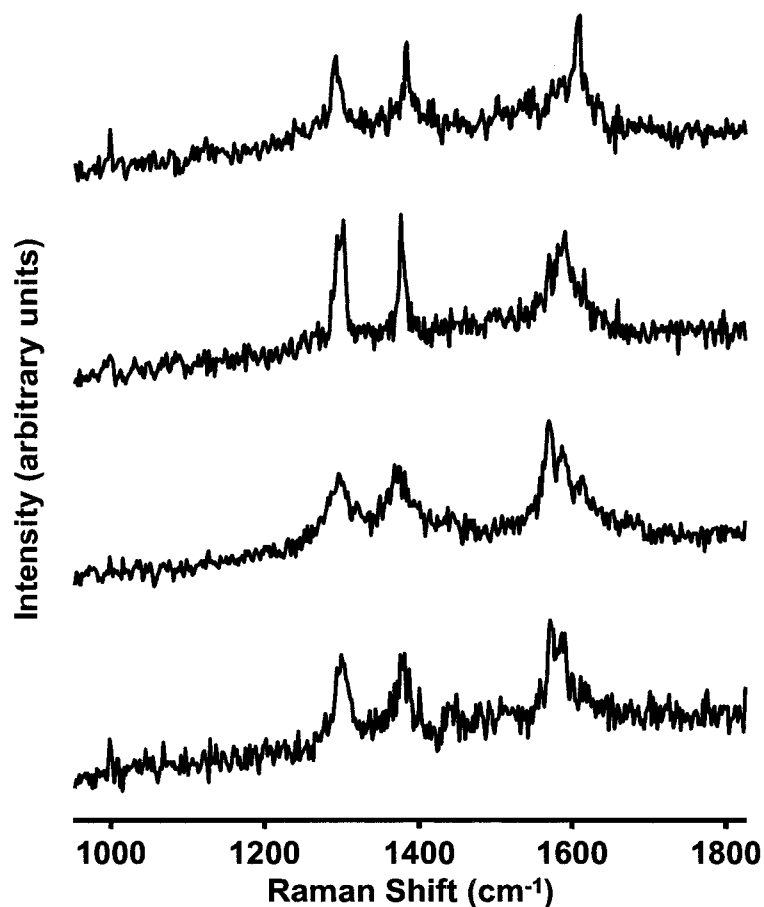
Figure 6.15 Single-molecule spectral variation. A comparison of four different single-molecule salPTCD SERRS spectra.

6.3.6 Conclusion

In the work discussed in this section, mapping of Raman micro-spectroscopy was shown to be a uniquely successful technique for the study of both systematically doped single dye-fatty acid monolayers and single molecules using SERRS. By variation of the ratio of the two components in mixed dye-fatty acid Langmuir-Blodgett (LB) films, 2D SERRS mapping measurements were employed to study the effect of dye concentration on SERRS spectral properties and monolayer architectures, down to the single molecule

189

level. It was shown that the rarity of coincidence between hot spots and single isolated molecules is a key consideration in ultrasensitive SERRS measurements of LB monolayers on nanostructured metallic films.

6.4 SERRS from One-to-One Binary Mixtures in Langmuir-Blodgett Monolayers

6.4.1 Introduction

Recently, Le Ru et al.[46] proposed a method "to pin down unambiguous proof for single-molecule sensitivity in surface enhanced Raman spectroscopy (SERS)". The authors of this report simultaneously employed two target analyte molecules in a single sample to support claims of the single (or few)-molecule nature of the signals they recorded. These experiments differed from previous single-molecule SERS/SERRS work in that the scattering volume contained a relatively large number of molecules of each of the species, rather than employing high dilution, as is usually done. Likewise, Van Duyne et al.[47] have subsequently employed a similar bi-analyte approach in conjunction with isotope editing,[48] where rhodamine 6G and one of its deuterated forms were employed. In both cases, the authors claim that some of the signals observed correspond to SERS of a single (or few) molecule(s).

In the work of this section, the concept of bi-analyte SERRS is adopted and employed in combination with the architectural control of the Langmuir-Blodgett technique,[31] and the high information content of 2D spatial mapping,[43] toward the distinction of similar chemical species within multi-component samples down to the single-molecule level. Together, these techniques are utilized to simultaneously study the SERRS of n-pentyl-5-salicylimidoperylene (salPTCD) and octadecylrhodamine B (R18),

190

changes in the dye distribution within the monolayer, and the breakdown of ensemble averaging, as dilution proceeds. The dyes are dispersed in mixed LB monolayers of arachidic acid, that readily forms high quality monolayers, at varying concentration levels, down to a single monomer of each within the scattering volume, and this is depicted in Figure 6.16. Single-molecule signals are attributed to the rare spatial coincidence of isolated target analyte molecules and localized electromagnetic hot spots in the nanostructured metal film. The bi-analyte nature of the samples provides strong support for the attribution of spectra to single molecules at high dilution, while the effect of domain formation/aggregation is found to be important at higher concentrations.
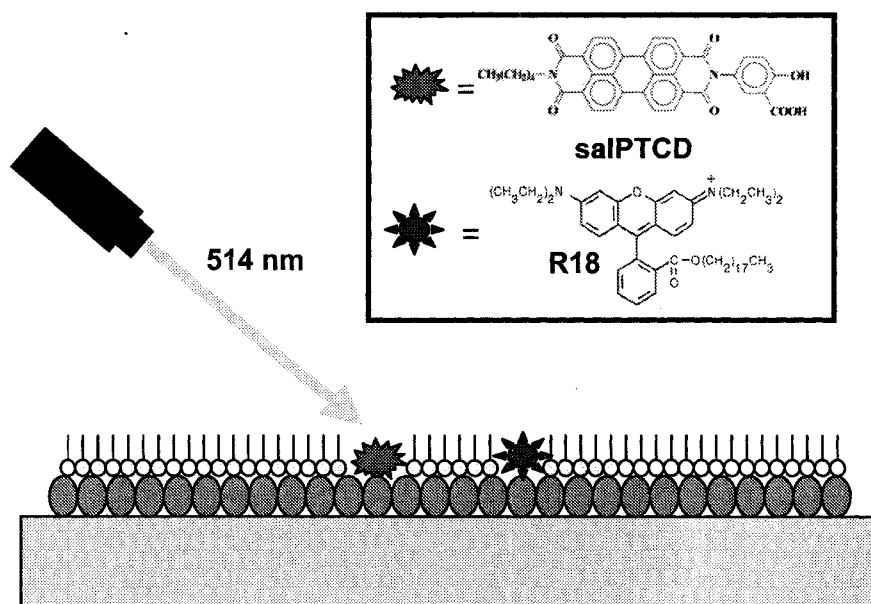

Figure 6.16 Single-molecule bi-analyte Langmuir-Blodgett SERRS.

6.4.2 Absorption Spectroscopy and Atomic Force Microscopy

The absorption spectra of 10^{-5} M solutions of salPTCD and R18 in dichloromethane, and the surface plasmon absorption of a vacuum evaporated 10 nm mass thickness Ag nanoparticle film, are shown in Figure 6.17(a). The spectra of the two dyes reveal absorption maxima resulting from the π-π^* electronic transitions of their respective central chromophores. The 0-0 transition band of salPTCD appears at 528 nm with vibronic structure at 491 and 459 nm, while R18 has peaks at 558, 520, and 491 nm. These dyes have similar molar extinction coefficients (10^3-10^4 mole^{-1}m^2) and highly coincident electronic absorption envelopes, explaining their similar resonance Raman scattering cross section values and making them excellent candidates for fundamental bi-analyte studies of this type. Furthermore, it can be seen that they are also highly resonant with the surface plasmon absorption of the Ag nanoparticle films and the 514.5 nm laser excitation employed in this work, effectively fulfilling the double resonance condition of SERRS, where both electromagnetic and resonance Raman enhancement[49] mechanisms are active. The Ag nanoparticle films have a broad extinction spectrum, covering the entire visible range, with a maximum at 488 nm, indicating a relatively large distribution of particle geometries and particle-particle interactions. The morphology of these 10 nm mass thickness films was studied further by employing atomic force microscopy (AFM), and a typical image is shown in Figure 6.17(b). This image was recorded from a 1 × 1 μm area, which corresponds approximately to the area probed in all of the SERRS measurements of this work. The image demonstrates an inhomogeneous distribution of particles with sizes ranging between ca. 20 and 80 nm, in agreement with surface plasmon absorption results. It has been shown previously that Ag films with similar

192

morphological characteristics demonstrate high average surface enhancement factors of about 10^4, and are capable of providing single-molecule signals from areas of high local SERRS enhancement, commonly known as hot spots.[38,44]
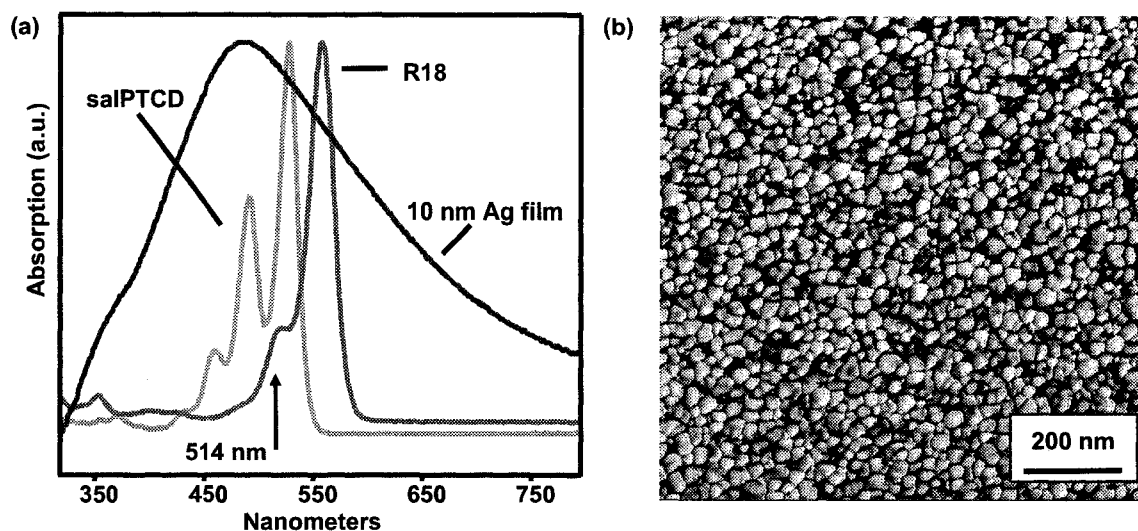
Figure 6.17 Absorption Spectroscopy and Atomic Force Microscopy. (a) Absorption spectra of 10^{-5} M salPTCD and R18 solutions, along with the surface plasmon absorption spectrum of an evaporated 10 nm Ag nanoparticle film. (b) AFM image of 10 nm Ag nanoparticle film.

6.4.3 Ensemble SERRS

To obtain average single-point SERRS spectra for R18 and salPTCD, each was embedded into AA monolayers containing on average 4×10^4 dye molecules/μm^2, then deposited onto Ag nanoparticle films. These films were probed using laser excitation at 514.5 nm, and the results are shown in Figures 6.18, including an expanded view of the most intense region of the spectra in Figure 6.18(c). At this concentration level, the

193

narrow bands of SERRS sit atop broad surface-enhanced fluorescence (SEF)[50,51] for these two resonant dye molecules. Here, however, the SEF is not shown, as the spectra have been baselined to clearly show the vibrational bands.
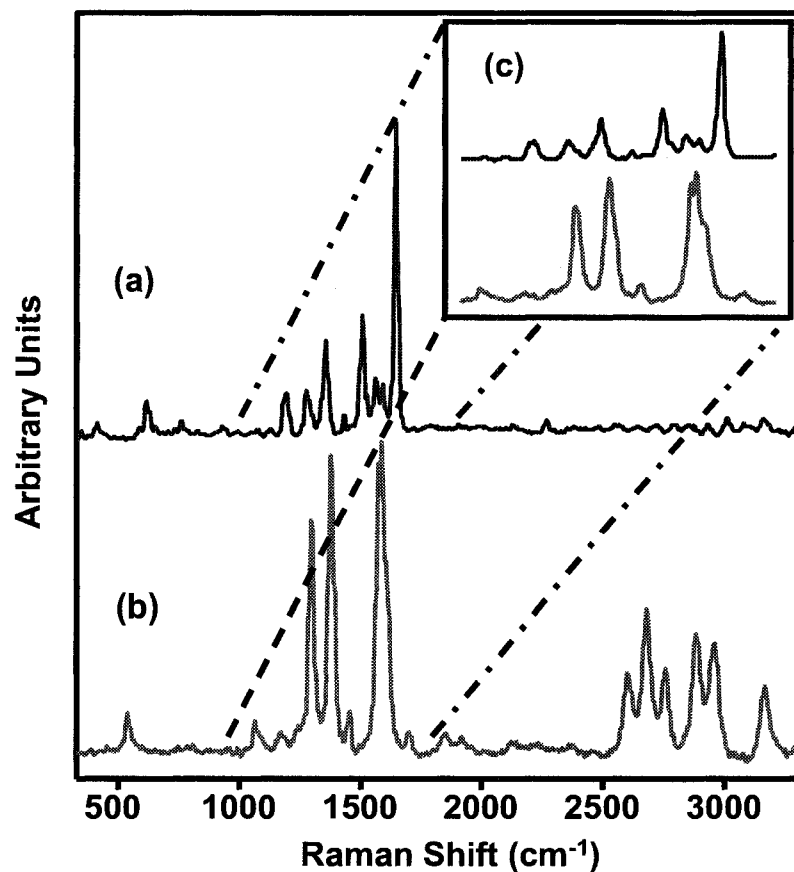
Figure 6.18 Ensemble SERRS of R18 and salPTCD. (a) R18 and (b) salPTCD SERRS spectra of single concentrated (4×10^4 dye molecules/μm^2) monolayers deposited onto 10 nm evaporated Ag nanoparticle films (recorded using 514.5 nm laser excitation). (c) Expanded view of the most intense region of these SERRS spectra.

As can be seen in Figure 6.18, the SERRS spectra of these molecules are significantly different from one another, making them easily distinguishable, as is

194

expected on the basis of their structures. Each is dominated by peaks, falling in the spectral region between 1000 and 1700 cm^{-1}, that have large intensity contributions from the breathing modes of the extended π systems of the central rhodamine and perylene chromophores, as is shown in Figure 6.18(c). Due to the high intensity peaks found in this spectral region, it is used to follow both analytes down to the single molecule regime. In particular, the SERRS spectrum of salPTCD is characterized by strong bands at 1300, 1381, and a complex band centered at 1585 cm^{-1}. The SERRS spectrum of R18, on the other hand, is defined by a strong peak at 1650 cm^{-1}, with weaker bands at 1508, 1360, 1283, and 1198 cm^{-1}. Both molecules show a progression of first overtone and combination bands, which has been previously observed for rhodamine and perylene dyes at this excitation energy.[35,38] However, those of salPTCD (between 2500 and 3200 cm^{-1}) are notably of particularly high relative intensity.

6.4.4 SERRS Mapping of One-to-One Binary Mixtures in LB Monolayers

In Figure 6.19, 2D SERRS intensity maps and selected spectra are shown for arachidic acid Langmuir-Blodgett monolayers containing one-to-one binary mixtures of R18 and salPTCD, at varying concentrations, on Ag nanoparticle films. These were recorded to study the change in the distribution of the two dyes within the single monomolecular layer, and the breakdown of ensemble spectral averaging, which occur as the single-molecule regime is approached. Monolayers were prepared so as to contain, on average, 4×10^4, 10^3, 10^2, 10, or 1 molecule(s) of each dye per square micron, the scattering area of the microscope. For each concentration, the intensity of the R18 band at 1650 cm^{-1} was mapped in blue, while the intensity of the salPTCD band at 1300 cm^{-1}

was mapped in green, with each pixel corresponding to a single recorded spectrum and an area of ca. 1 μm^2 (note: scale is not consistent from map to map).

In Figure 6.19(a), for a monolayer with a concentration of 4×10^4 molecules of each of R18 and salPTCD per μm^2, strong signals are observed for both at essentially all spots on the sample, as revealed by the homogeneous brightness of the maps for both the 1650 cm^{-1} band of R18 and the 1300 cm^{-1} band of salPTCD. Minor differences in the distribution of signals in the two maps can be explained by slight changes in the distribution of the two dyes, while dark areas can be attributed to small film defects or areas of high AA concentration. When spectra are reviewed at all spots, they are found to be rather consistent and correspond well with a one-to-one binary mixture of the two analytes, indicating a high degree of miscibility of the dyes with one another. This is confirmed through the comparison of the spectral result of the 1-to-1 co-addition of pure R18 and salPTCD concentrated SERRS spectra (i) with two typical spectra (ii and iii) taken from the bi-analyte mapping experiment of Figure 6.19(a), showing all three spectra to be quite similar. Notably, this simple comparison is made possible by the fact that R18 and salPTCD have similar SERRS cross section values, as revealed by the similar intensities of the pure average SERRS spectra of each. If this was not the case, the interpretation of results of this type would be greatly complicated.

196
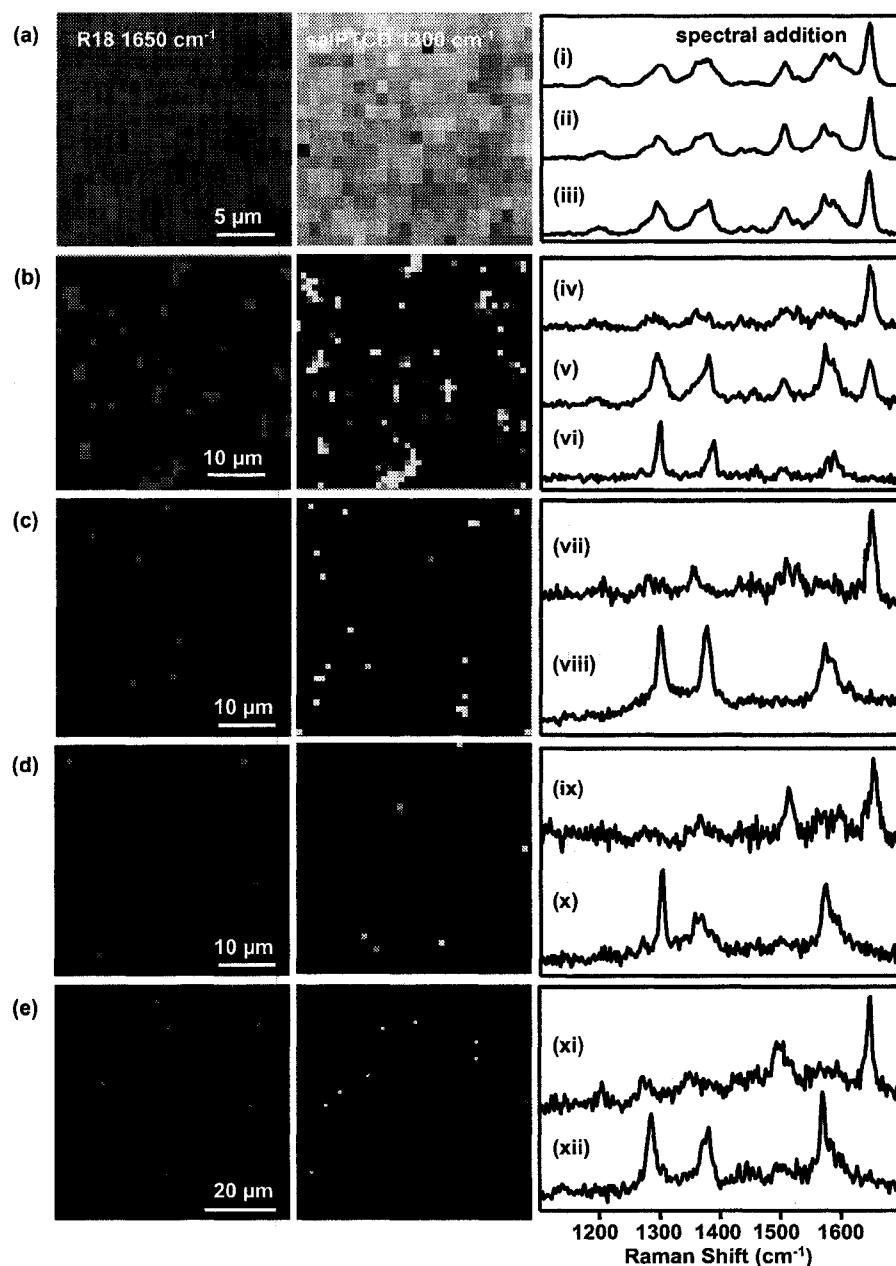
Figure 6.19 SERRS Mapping of 1:1 Mixtures in LB Films. Mapping and selected spectra **(ii-xii)** for AA LB films containing 1:1 R18:salPTCD mixtures at concentrations of **(a)** 4×10^4; **(b)** 10^3; **(c)** 10^2; **(d)** 10; and **(e)** 1 molecule(s) of each dye/μm^2. For each film, the intensity of the R18 band at 1650 cm^{-1} is mapped in blue, the intensity of the salPTCD band at 1300 cm^{-1} is mapped in green, and selected spectra are shown. In **(a)**, **(i)** is the result of the co-addition of pure R18 and salPTCD concentrated SERRS spectra.

197

In Figure 6.19(b), where the concentration of the monolayer on Ag has been reduced to 10^3 molecules of each of R18 and salPTCD per μm^2, domain formation is clearly observed in the SERRS intensity maps. On the basis of the AFM imaging, however, these domains of high and low intensity, of several square microns, cannot rightly be attributed to variations in the enhancing substrate, as it is effectively homogeneous at this length scale. They can however be attributed to variation in the distribution of the dye molecules within the monolayer. The maps of R18 and salPTCD reveal a strong similarity (correspondence of high intensity areas), indicating that the dyes are still highly miscible with one another but have begun to be segregated from the AA matrix. This is quite understandable on the basis of the significant tendency toward pi-pi stacking in these large dye systems where "like attracts like". This is confirmed, for the most part, when spectra are reviewed. At most bright pixels the spectra are found to have some character of each dye, indicating a high degree of mixing, and an example of this is shown in (v). However, at some clusters of pixels, spectra have taken on relatively pure spectral character of either R18 (iv) or salPTCD (vi), indicating the possibility for selective aggregation of molecules with only those of the same identity (i.e. R18 with R18 and salPTCD with salPTCD) at this concentration. Despite the bi-analyte nature of these samples, at high concentrations it is clear that pure domains/aggregates of either dye can form, and so the pure character of these spectra should not be viewed as proof of their single molecule nature.

In Figure 6.19(c), the concentration of the monolayer has been further reduced to 10^2 molecules of each of R18 and salPTCD per μm^2. At this concentration level most domains have broken down, and isolated hot pixels have become dominant. However,

198

some dye aggregates still exist that span several square microns. As well, many of these spectra still show mixed character of R18 and salPTCD, excimer fluorescence, and strong intensities, indicating that they do not arise from single isolated monomers. Spectra (vii) and (viii) are examples where pure spectral character exists, for R18 and salPTCD, respectively; however, (viii) was recorded from a cluster of hot pixels and has definite ensemble spectral characteristics.

Finally, in Figures 6.19(d) and (e), where concentrations have been reduced still further, down to 10 and 1 molecule(s) of each of R18 and salPTCD per μm^2, respectively, only individual, isolated hot pixels are observed. At this dilution, the distribution of the dye in the monolayer is no longer reflected in the mapping results, as all relevant action is occurring on the nanoscale, below the pixel dimension. Rather, the rarity of spatial coincidence between electromagnetic hot spots on the nanostructured Ag film and single isolated monomers in the LB monolayer is a key consideration. This is, of course, expected as the dye molecules occupy only 5.0×10^{-4} and 5.0×10^{-5} % of all molecular sites at these respective concentration levels. Further, all spectra detected at these concentration levels are of pure R18 (ix and xi) or salPTCD (x and xii) character, are of weak intensity, lack excimer fluorescence, and show no signs of ensemble averaging. Together these factors, along with the high dilution, demonstrate that single-molecule spectra are in fact being detected.

6.4.5 Single-Molecule Spectral Variation

Finally, in Figure 6.20, comparisons of several different single-molecule R18 and salPTCD SERRS spectra are shown. These spectra were recorded at different spots from a Langmuir-Blodgett monolayer deposited onto a 10 nm Ag nanoparticle film. It can be

seen that when the single-molecule regime is reached, spectral changes become apparent due to the loss of ensemble averaging. Strong spot-to-spot variation is observed for all band parameters, including Raman shift, bandwidth, band shape, and absolute and relative intensity. This behavior, due to the dynamics and unique environment of the single molecule, is also likely associated with variations in local hot spot properties and different orientations of the molecule with respect to local electromagnetic fields in the nanostructures.

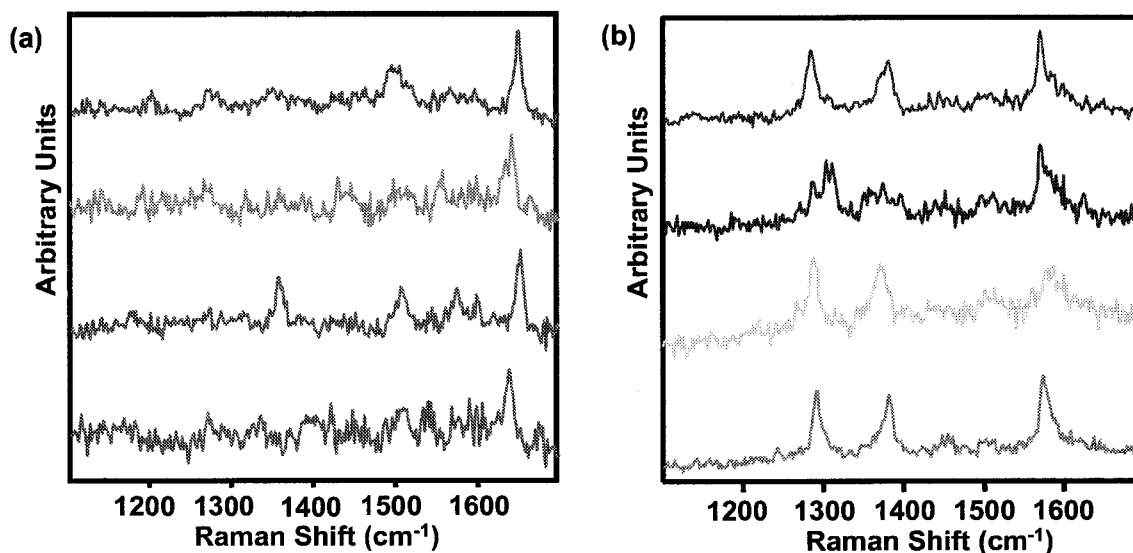**Figure 6.20 Single-Molecule Spectral Variation.** Comparison of single-molecule **(a)** R18 and **(b)** salPTCD SERRS spectra from different spots in a Langmuir-Blodgett monolayer deposited onto a 10 nm Ag nanoparticle film.

6.4.6 Conclusion

In the work of the section, SERRS spectra and 2D spatial intensity maps were recorded from thin Ag nanoparticle films coated with fatty acid Langmuir-Blodgett

200

monolayers containing one-to-one binary mixtures, at varying concentrations, of the dyes R18 and salPTCD. It was demonstrated that similar chemical species within a multi-component sample could be distinguished, down to the single-molecule level, by means of their SERRS fingerprints. These techniques were employed to monitor changes in the distribution of the two dyes within the monolayer, and the breakdown of ensemble spectral averaging, which occurred as the single-molecule regime was approached. It was found that, at high concentrations, there was a high degree of miscibility of the dyes within the monolayer, while, at more intermediate concentrations, domain formation/aggregation was significant. When less than ca. 10 molecules of each dye occupied the 1 μm^2 scattering areas probed by the laser, single, isolated monomers were detected. These signals were attributed to the rare spatial coincidence of isolated target analyte molecules and localized electromagnetic hot spots in the nanostructured metal film.

6.5 Non-Resonant SERS from Single Molecules in Langmuir-Blodgett Monolayers

6.5.1 Introduction

In the work discussed in this section, the Langmuir-Blodgett (LB) approach to single molecule SERRS is employed in the study of the perylene derivative, *N,N'*-Bis(neopentyl)-3,4,9,10-perylenebis(dicarboximide) (BNPTCD), that is shown in Figure 6.21. Single target dye molecules are isolated in a fatty acid monolayer matrix deposited onto an enhancing metallic substrate and spatially resolved with a Raman microscope. Several unique resonance conditions are explored, through variation of the surface-plasmon resonance of the substrate and the laser excitation wavelengths employed, in an

attempt to expand the possibilities for application of this powerful technique. Surface-enhanced Raman scattering (SERS), and surface-enhanced resonance Raman scattering (SERRS) spectra are reported for mixed LB monolayers deposited on Ag and mixed Ag/Au nanoparticle substrates. These spectra are obtained using multiple excitation wavelengths, and single-point and 2D mapping acquisition techniques. For the first time, single molecule SERS (lacking electronic molecular resonance) spectra are reported for LB monolayers deposited on evaporated metal nanoparticle film substrates.
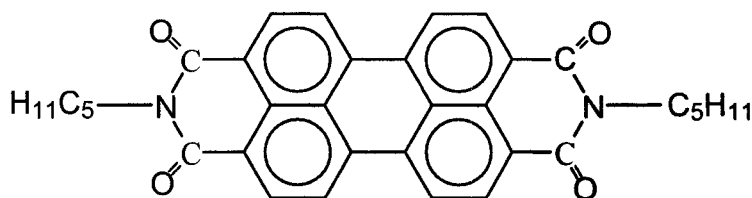
Figure 6.21 Molecular structure of BNPTCD.

6.5.2 Absorption Spectroscopy

In Figure 6.22, the absorption spectrum of a 10^{-5} M solution of BNPTCD is shown with the surface plasmon absorption spectra of a 6 nm Ag nanoparticle film and a 10 nm mixed Ag/Au nanoparticle film. Also shown in this figure, are arrows indicating the wavelength of the lasers employed in the SERS/SERRS studies of this work. The Ag and mixed Ag/Au nanoparticle films used in this work were characterized in sections 6.2.2 and 4.2.2, respectively. The absorption spectrum of BNPTCD shows peaks, as do all the perylene materials used in this work, associated with the π-π* electronic transition of the PTCD chromophore. The 0-0-transition appears at 524 nm with a vibronic

progression at 488 and 456nm. BNPTCD exhibits a large extinction coefficient, and

shows an absorption cross section in dilute solution of ca. 6.63×10^{-17} cm^2/molecule at

524 nm. When excited with laser excitation at 488 and 514.5 nm, this molecule will be

resonant and RRS enhancement will be realized. When it is excited with radiation at 633

and 785 nm it will be non-resonant and yield RS. In the case of highly concentrated

films, however, the absorption of this molecule is redshifted and shows pre-resonance at

633 nm excitation.
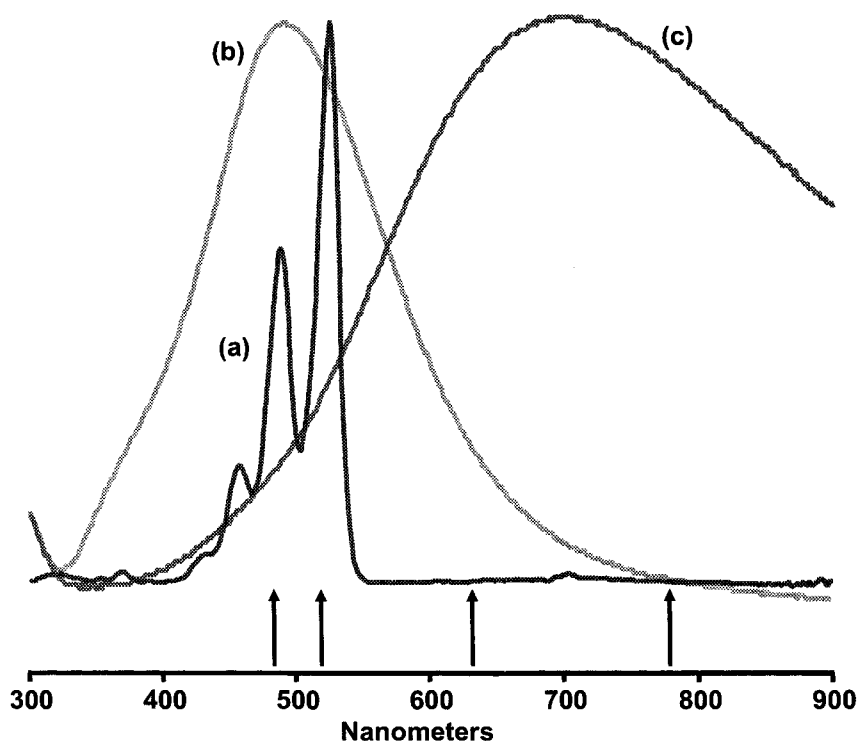
Figure 6.22 Absorption of BNPTCD, and Ag and mixed Ag/Au films. (a) Absorption

spectrum of 10^{-5} M BNPTCD solution, (b) surface plasmon absorption of 6 nm Ag film,

and (c) surface plasmon absorption of mixed Ag/Au film. (Also shown are laser

excitation lines at 488, 514.5, 633, and 785 nm)

6.5.3 Ensemble SERS/SERRS from Ag and Mixed Ag/Au Nanoparticle Films

In Figures 6.23 and 6.24, the SERRS spectra of a concentrated LB monolayer of BNPTCD, recorded at various excitation energies, on Ag and mixed Ag/Au films, respectively, are shown. For the two substrates, the spectra at each wavelength agree well with one another in terms of relative intensities and Raman shift. They also show similar absolute enhancement at each wavelength, with the exception of 488 nm, where the mixed film shows reduced intensities. As excitation wavelength is changed, clear changes are observed in both absolute and relative intensities on both substrates. In particular, those spectra recorded at resonant wavelengths (488 and 514.5 nm) are of greater absolute intensity and have overtones and combinations with greatly increased relative intensities. There are also significant changes in the relative intensities of the fundamentals as excitation is moved into resonance with the molecule's electronic transition. On the other hand, the absence of overtone and combination modes at 633 nm is strong evidence that, at this wavelength, resonance Raman enhancement mechanisms are not functioning, or are functioning very weakly. Furthermore, this lack of resonance Raman enhancement becomes even more important at low concentrations where the absorption of the molecule shifts even further to the blue.
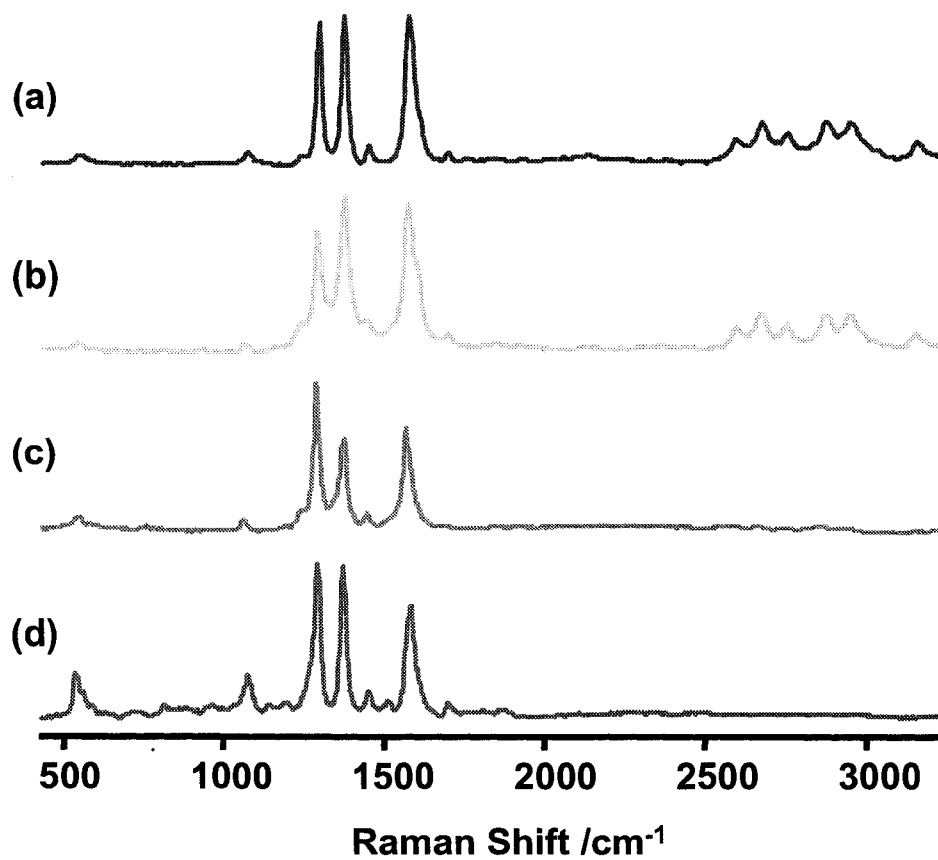
Figure 6.23   Ensemble SERS/SERRS on Ag films. SERS/SERRS spectra recorded from a 10:1 AA:BNPTCD LB monolayer deposited on a 6 nm Ag film at excitation wavelengths of **(a)** 488 nm, **(b)** 514 nm, **(c)** 633 nm, and **(d)** 785 nm.
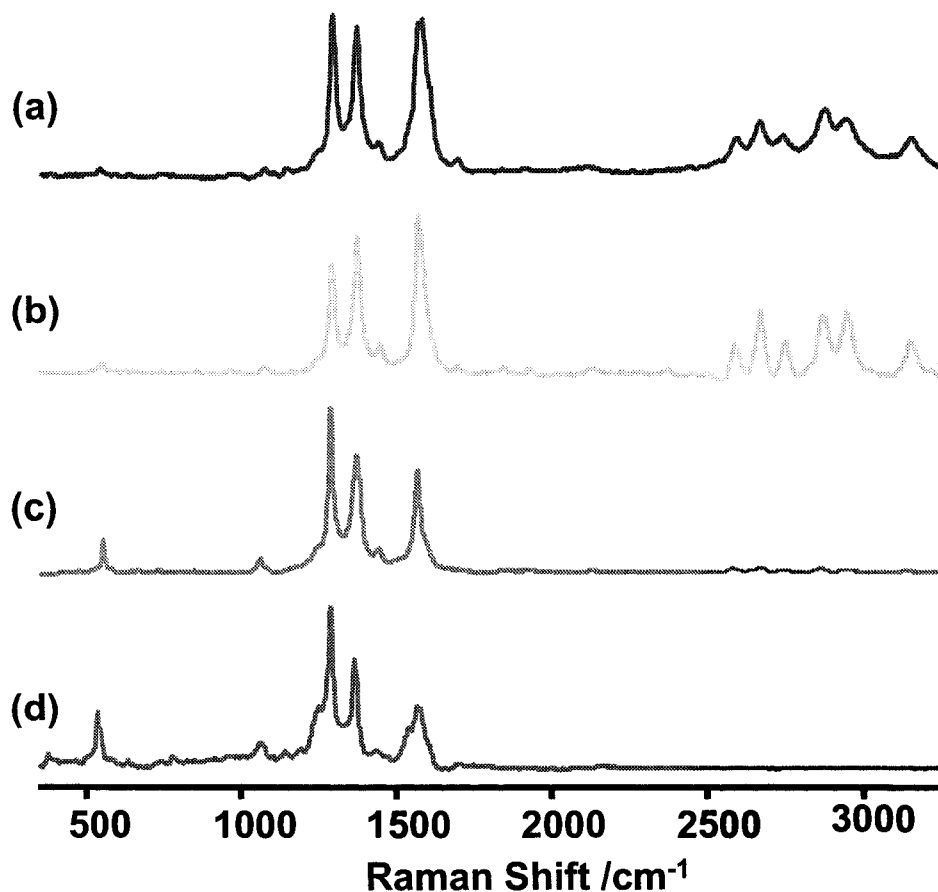
Figure 6.24 Ensemble SERS/SERRS on mixed Ag/Au films. SERS/SERRS spectra recorded from a 10:1 AA:BNPTCD LB monolayer deposited on a 10 nm Ag/Au film at excitation wavelengths of **(a)** 488 nm, **(b)** 514 nm, **(c)** 633 nm, and **(d)** 785 nm.

6.5.4 Single-Molecule SERS/SERRS Mapping with Changing Excitation Energy

Figure 6.25 shows the results of 2D SERRS mapping experiments carried out on AA LB monolayers containing, on average, 1 BNPTCD molecule/μm^2, on Ag and mixed Ag/Au nanostructured films. These experiments were carried out at 488, 514.5, 633, and 785 nm excitation to explore the importance of different resonances. The existence of bright pixels indicates single, isolated BNPTCD molecules sitting in electromagnetic hot

spots on the metal film. It also implies that, at that excitation wavelength, the combination of hot spot surface-enhancement and resonance enhancement are together able to push the signal past the detection threshold. At 785 nm excitation, signals were not detected for either substrate. Resonance Raman enhancement should not function at this wavelength, and so it is clear that surface-enhancement at hot spots is not strong enough on its own to make the detection of BNPTCD molecules possible on either of these substrates. At 488 nm excitation, resonance enhancement is active, yet single-molecules are only detectable on the Ag film. This suggests that the surface-enhancement of hot spots on the mixed film is of lower intensity than on Ag films at this wavelength, as is expected on the basis of its surface plasmon absorption. At 514.5 nm, single-molecules were detected on both substrates. This is expected and is supported by work presented in section 4.2 and the earlier sections of this chapter. Interestingly though, signals from single-molecules were detected at 633 nm on both Ag and mixed Ag/Au nanostructured films. BNPTCD monomers should experience very little resonance enhancement at this wavelength, and this suggests that nearly all enhancement arises from hot spots on the surface of the metal films.

This is the first report of non-resonant single-molecule SERS on films of this type and it raises important questions about the contributions of molecular electronic resonance and EM surface enhancement mechanisms in the case of SERRS where they are interacting and may not be strictly multiplicative. This is particularly true in that very few differences can be distinguished in the spectral and mapping properties of resonant and non-resonant molecules. In both cases, the percentage of total spots that are hot tends to show fluctuations from map to map, and this can be attributed to the fact that

207

relatively few spectra (1000-2000) are collected in most cases. However, the percentage of hot pixels appears to be essentially the same for resonant and non-resonant measurements. Also, under both resonant and non-resonant conditions, strong spectral variation from spot to spot within these maps is observed. These results can be explained if one considers the changes that may occur in the contribution of the 2 enhancement components when they interact at hot spots. In particular, it is possible that under resonant conditions the two enhancement mechanisms could damp each other, due to increased channels for energy transfer. This effect should be reduced under non-resonant conditions and EM hot spot enhancement should dominate.
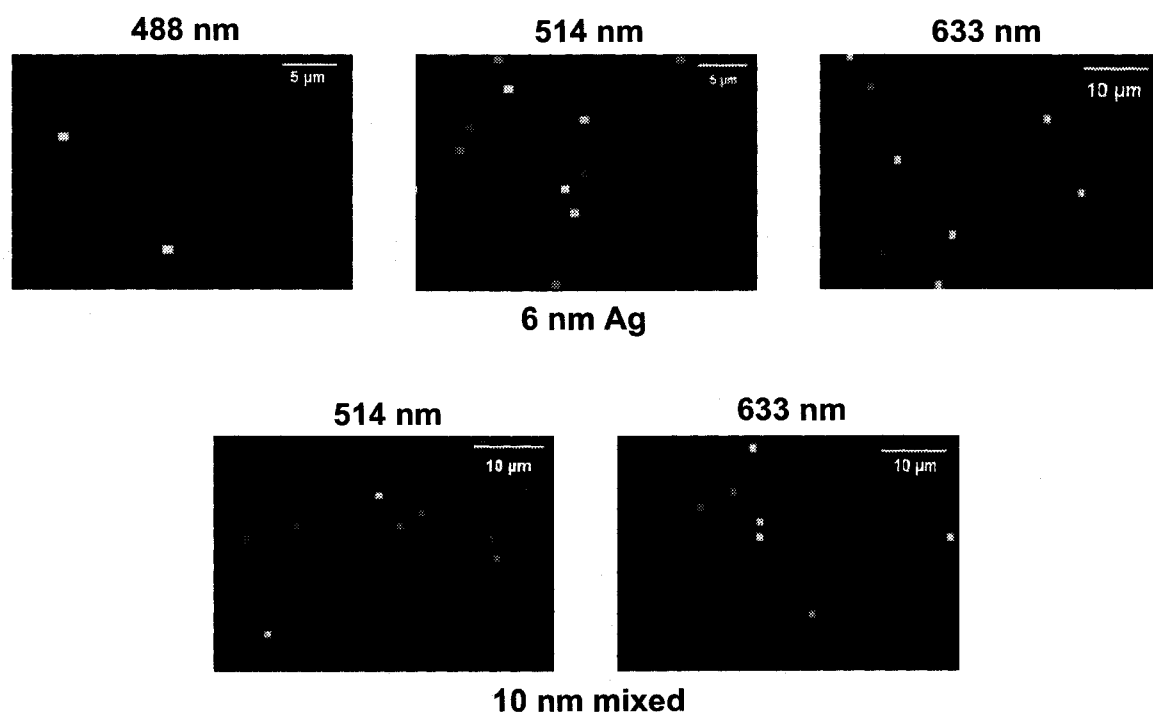
Figure 6.25 Single-molecule SERS/SERRS mapping. Results of 2D SERRS mapping experiments carried out on AA LB monolayers containing, on average, 1 BNPTCD molecule/μm^2, on Ag and mixed Ag/Au nanostructured films..

208

6.5.5 Conclusion

In the work discussed in this section, the effect of different molecular and surface plasmon resonances was explored for SERS/SERRS measurements of BNPTCD on Ag and mixed Ag/Au nanostructured films. For the first time, non-resonant single molecule SERS spectra were reported for LB monolayers deposited on evaporated metal nanoparticle film substrates.

6.6 Summary

In this chapter, the application of the Langmuir-Blodgett approach to single-molecule SERS/SERRS was discussed. Several molecular systems were studied on several nanostructured metallic films, using different laser excitation wavelengths, and single-point and 2D mapping techniques. In particular, this work focused on the study of overtones and combinations in the single-molecule spectra of perylene derivatives; the use of 2D SERRS mapping techniques to explore the breakdown of ensemble averaging; single-molecule SERRS from one-to-one binary mixtures; and non-resonant single-molecule SERS on nanostructured metallic films.

References

(1)   Kneipp, K.; Kneipp, H.; Kartha, V. B.; Manoharan, R.; Deinum, G.; Itzkan, I.; Dasari, R. R.; Feld, M. S. *Phys. Rev. E* **1998**, *57*, R6281-R6284.

(2)   Xu, H.; Bjerneld, E. J.; Kall, M.; Borjesson, L. *Phys. Rev. Lett.* **1999**, *83*, 4357-4360.

(3)   Kneipp, K.; Kneipp, H.; Itzkan, I.; Dasari, R. R.; Feld, M. S. *Curr. Sci.* **1999**, *77*, 915-926.

(4)   Wang, Y.; Li, Y.-S.; Zhang, Z.; An, D. *Spectrochim. Acta, Part A* **2003**, *59A*, 589-594.

(5)   Sepaniak, M. J.; De Jesus, M. A.; Giesfeldt, K. S. *Amer. Pharm.Rev.* **2004**, *7*, 92-97.

(6)   Bello, J. M.; Narayanan, V. A.; Stokes, D. L.; Vo Dinh, T. *Anal. Chem.* **1990**, *62*, 2437-2441.

(7)   Carter, J. C.; Brewer, W. E.; Angel, S. M. *Appl. Spectrosc.* **2000**, *54*, 1876-1881.

(8)   Aroca, R.; Guhathakurta-Ghosh, U. *J. Am. Chem. Soc.* **1989**, *111*, 7681-7683.

(9)   Goulet, P. J. G.; Dos Santos, D. S., Jr.; Alvarez-Puebla, R. A.; Oliveira, O. N., Jr.; Aroca, R. F. *Langmuir* **2005**, *21*, 5576-5581.

(10)   Kneipp, K.; Kneipp, H.; Itzkan, I.; Dasari, R. R.; Feld, M. S. *Chem. Rev.* **1999**, *99*, 2957-2976.

(11)   Kneipp, K.; Wang, Y.; Kneipp, H.; T. Perelman, L. T.; Itzkan, I. *Phys. Rev. Lett.* **1997**, *78*, 1667-1670.

(12)   Nie, S.; Emory, S. R. *Science* **1997**, *275*, 1102-1106.

(13)   Krug, J. T., II; Wang, G. D.; Emory, S. R.; Nie, S. *J. Am. Chem. Soc.* **1999**, *121*, 9208-9214.

(14)   Michaels, A. M.; Nirmal, M.; Brus, L. E. *J. Am. Chem. Soc.* **1999**, *121*, 9932-9939.

(15)   Weiss, A.; Haran, G. *J. Phys. Chem. B* **2001**, *105*, 12348-12354.

(16)   Constantino, C. J. L.; Lemma, T.; Antunes, P. A.; Aroca, R. *Anal. Chem.* **2001**, *73*, 3674-3678.

(17)   Meixner, A. J.; Vosgrone, T.; Sackrow, M. *J. Lumin.* **2001**, *94&95*, 147-152.

(18)   Eggeling, C.; Schaffer, J.; Seidel, C. A. M.; Korte, J.; Brehm, G.; Schneider, S.; Schrof, W. *J. Phys. Chem. A* **2001**, *105*, 3673-3679.

(19)   Maruyama, Y.; Ishikawa, M.; Futamata, M. *Chem. Lett.* **2001**, 834-835.

(20)   Bizzarri, A. R.; Cannistraro, S. *Appl. Spectrosc.* **2002**, *56*, 1531-1537.

(21)   Etchegoin, P.; Liem, H.; Maher, R. C.; Cohen, L. F.; Brown, R. J. C.; Hartigan, H.; Milton, M. J. T.; Gallop, J. C. *Chem. Phys. Lett.* **2002**, *366*, 115-121.

(22)   Habuchi, S.; Cotlet, M.; Gronheid, R.; Dirix, G.; Michiels, J.; Vanderleyden, J.; De Schryver, F. C.; Hofkens, J. *J. Am. Chem. Soc.* **2003**, *125*, 8446-8447.

(23)   Itoh, T.; Hashimoto, K.; Ikehata, A.; Ozaki, Y. *Chem. Phys. Lett.* **2004**, *389*, 225-229.

(24)   Lee, P. C.; Meisel, D. *J. Phys. Chem.* **1982**, *86*, 3391-3395.

(25)   Corni, S.; Tomasi, J. *J. Chem. Phys.* **2002**, *116*, 1156-1164.

(26)   Moskovits, M.; Tay, L.-L.; Yang, J.; Haslett, T. SERS and the single molecule. In *Optical Properties of Nanostructured Random Media*; Shalaev, V. M., Ed.; Springer-Verlag: Berlin Heidelberg, 2002; Vol. 82; pp 215-226.

(27)   Etchegoin, P.; Cohen, L. F.; Hartigan, H.; Brown, R. J. C.; Milton, M. J. T.; Gallop, J. C. *J. Chem. Phys.* **2003**, *119*, 5281-5289.

(28)   Constantino, C. J. L.; Lemma, T.; Antunes, P. A.; Aroca, R. *Spectrochim. Acta, Part A* **2002**, *58A*, 403-409.

211

(29)   Constantino, C., J. L.; Lemma, T.; Antunes Patricia, A.; Goulet, P.; Aroca, R. *Appl. Spectrosc.* **2003**, *57*, 649-654.

(30)   Lemma, T.; Aroca, R. F. *J. Raman Spectrosc.* **2002**, *33*, 197-201.

(31)   Petty, M. C. *Langmuir-Blodgett Films. An Introduction*; Cambridge University Press: Cambridge, 1996.

(32)   Efremov, E. V.; Ariese, F.; Mank, A. J. G.; Gooijer, C. *Anal. Chem.* **2006**, *78*, 3152-3157.

(33)   Hildebrandt, P.; Stockburger, M. *J. Phys. Chem.* **1984**, *88*, 5935-5944.

(34)   Goulet, P. J. G.; Pieczonka, N. P. W.; Aroca, R. F. *Can. J. Anal. Sci. Spect.* **2003**, *48*, 146-152.

(35)   Aroca, R. F.; Goulet, P. J. G.; Dos Santos, D. S., Jr.; Alvarez-Puebla, R. A.; Oliveira, O. N., Jr. *Anal. Chem.* **2005**, *77*, 378-382.

(36)   Michaels, A. M.; Jiang, J.; Brus, L. *J. Phys. Chem. B* **2000**, *104*, 11965-11971.

(37)   Constantino, C. J. L.; Aroca, R. F. *J. Raman Spectrosc.* **2000**, *31*, 887-890.

(38)   Goulet, P. J. G.; Pieczonka, N. P. W.; Aroca, R. F. *Anal. Chem.* **2003**, *75*, 1918-1923.

(39)   Stockman, M. I. *Phys. Rev. E* **1997**, *56*, 6494-6507.

(40)   Gresillon, S.; Aigouy, L.; Boccara, A. C.; Rivoal, J. C.; Quelin, X.; Desmarest, C.; Gadenne, P.; Shubin, V. A.; Sarychev, A. K.; Shalaev, V. M. *Phys. Rev. Lett.* **1999**, *82*, 4520-4523.

(41)   Aroca, R. F.; Clavijo, R. E. *Spectrochim. Acta, Part A* **1991**, *47A*, 271-277.

(42)   Pieczonka, N. P. W.; Aroca, R. F. *ChemPhysChem* **2005**, *6*, 2473-2484.

212

(43) Schlucker, S.; Schaeberle, M. D.; Huffman, S. W.; Levin, I. W. *Anal. Chem.* **2003**, *75*, 4312-4318.

(44) Goulet, P. J. G.; Pieczonka, N. P. W.; Aroca, R. F. *J. Raman Spectrosc.* **2005**, *36*, 574-580.

(45) Akimoto, S.; Ohmori, A.; Yamazaki, I. *J. Phys. Chem. B* **1997**, *101*, 3753-3758.

(46) Le Ru, E. C.; Meyer, M.; Etchegoin, P. *J. Phys. Chem. B* **2006**, *110*, 1944-1948.

(47) Van Duyne, R. P. "Molecular Plasmonics for Surface-Enhanced Sensing and Raman Spectroscopy"; 20th International Conference on Raman Spectroscopy, 2006, Yokohama, Japan.

(48) Zhang, D.; Xie, Y.; Deb, S. K.; Davison, V. J.; Ben-Amotz, D. *Anal. Chem.* **2005**, *77*, 3563-3569.

(49) Shorygin, P. P.; Krushinskij, L. L. *J. Raman Spectrosc.* **1997**, *28*, 383-388.

(50) Goulet, P. J. G.; Aroca, R. F. Surface-enhancement of fluorescence near noble metal nanostructures. In *Topics in Fluorescence Spectroscopy: Radiative Decay Engineering*; Lakowics, J. R., Geddes, C. D., Eds.; Springer Science + Business Media, Inc.: New York, 2005; Vol. 8; pp 223-247.

(51) Geddes, C. D.; Parfenov, A.; Roll, D.; Fang, J.; Lakowicz, J. R. *Langmuir* **2003**, *19*, 6236-6241.

Chapter 7

CONCLUSIONS

7.1 Conclusions

In this work, several studies were carried out that employed surface-enhanced Raman scattering (SERS) and surface-enhanced resonance Raman scattering (SERRS). These studies served to further the development of these techniques toward widespread analytical application, and involved the fabrication, characterization, and application of new substrates for SERS/SERRS; the interpretation of SERS; and the study of single-molecule SERS/SERRS from mixed Langmuir-Blodgett monolayers deposited onto metallic nanoparticle substrates.

The results of the work on the development of new substrates for SERS/SERRS were presented in Chapter 4. In section 4.2, the introduction of new mixed Ag/Au nanostructured film substrates for application toward single-molecule LB SERRS was discussed. The substrate was prepared by vacuum evaporation of Ag and Au onto glass substrates, at elevated temperatures, and these mixed metal films were characterized by UV-visible surface plasmon absorption spectroscopy, atomic force microscopy, and X-ray photoelectron spectroscopy. They were employed as substrates for SERRS of a perylene molecule, BBIP PTCD, in LB monolayers, down to the single-molecule level, and demonstrated an advantage of lower reactivity over traditional Ag films.

In section 4.3, the introduction of a new class of self-sustained chitosan thin films containing dispersions of gold nanoparticles, was discussed. Gold nanoparticles were generated using acetic acid as a reducing agent in a reaction mediated by the biopolymer chitosan. Self-sustaining films were then formed from the resultant nanocomposite solutions, and characterized by surface plasmon absorption, TEM, and infrared

215

spectroscopy. They were shown to effectively enhance Raman signals of a test analyte, rhodamine 6G, down to trace quantities.

In the work discussed in section 4.4, the layer-by-layer technique was successfully employed in the production of unique dendrimer/Ag nanosphere substrates for measurements of surface-enhanced Raman scattering. A variety of different film architectures were produced and these were studied by surface plasmon absorption, AFM, and SERS. It was shown that the optical properties of these different substrate architectures were strongly influenced by the generation and concentration of the dendrimers used, as well as the number of layers produced. These LbL films were found to provide excellent enhancement of the Raman scattering of 2-naphthalenethiol. Finally, the collection of SERS from architectures with intervening layers between the metal nanoparticles and the surface of the films was demonstrated.

In section 4.5, the development and characterization of versatile dendrimer/Ag nanowire LbL film substrates for enhanced optical applications was discussed. These films were employed as substrates for SERS/SERRS measurements from solution-casted and Langmuir-Blodgett samples at a variety of excitation energies, and found to provide excellent enhancement of Raman and resonance Raman signals, down to trace levels.

Finally, in the work discussed in section 4.6, avidin/Ag nanoparticle layer-by-layer (LbL) films were fabricated and employed as chemically selective substrates for SERS/SERRS. The growth of these nanocomposite films was characterized by surface plasmon absorption, and AFM imaging. They were found to exhibit significant enhancement of RS/RRS across a broad spectral window, covering essentially the entire visible region. They were also found to demonstrate strong, bio-specific interactions with

216

two biotinylated species, thus providing chemical selectivity, with increased sensitivity, in substrates for surface-enhanced spectroscopy. Biotinylated dye molecules were shown to be selectively captured by these substrates, and this preferential adsorption yielded an additional concentration enhancement of ca. 10^2, while detection limits were improved by at least 2 orders of magnitude.

Results from the second category of this work, SERS interpretation, were presented in Chapter 5. In the work discussed in section 5.2, density functional theory (DFT) methods were employed to investigate the nature of the chemical adsorption of salicylate on silver surfaces. The structure of salicylic acid, along with its infrared and Raman spectra, was determined at the B3LYP/6-311+G(d,p) level of theory. These results were then used in the assignment of vibrational spectra. Surface-enhanced Raman scattering (SERS) spectra were obtained from silver nanoparticle films thinly coated with salicylic acid. In order to determine the nature of the chemisorption that this molecule has on Ag surfaces, the optimized geometries and Raman spectra of two model salicylate-silver complexes (Ag1 and Ag2) were calculated at the B3LYP/Lanl2DZ level of theory. As well, experimental vibrational spectra were obtained for a silver salicylate salt for comparison with SERS results. It was found that experimentally observed SERS spectra, and simulated SERS spectra of a salicylate complex chemisorbed through its carboxylate group (Ag1) show good agreement with one another. It was concluded that salicylate chemically adsorbs only through its carboxylate group. Evidence for a tilted, head-on orientation of the salicylate complex on the surface was obtained from calculations of simulated SERS spectra that account for polarization, as well as from comparisons of reference powder results with SEIRA, and RAIRS spectra.

In the work presented in Section 5.2, surface-enhanced Raman scattering (SERS) was employed to detect the important environmental pollutant, and suspected human carcinogen, 1-naphthylamine (1-NA) from colloidal Ag solutions. SERS enhancement conditions were optimized through the variation of pH, a fundamental determinant for solution SERS experiments. Dramatic spectral differences between the free molecule and the SERS obtained from aqueous colloidal solutions were demonstrated to be the result of the formation, and water solvation, of a coordination complex of two 1-NA molecules with the Ag^+ ions present at Ag nanoparticle surfaces.

Finally, results on the single-molecule detection of SERS/SERRS from mixed Langmuir-Blodgett monolayers deposited onto metallic nanoparticle substrates were presented in Chapter 6. In the work discussed in section 6.2, the SERRS of three PTCD derivatives was studied down to the single-molecule level. These molecules were embedded in arachidic acid Langmuir-Blodgett monolayers deposited onto nanostructured, evaporated Ag films at concentrations such that single, isolated dye molecules were in the scattering area of the microscope at any given time. When these molecules were located in rare electromagnetic hot spots on the nanostructured surface, their detection was possible. It was found that it was possible to detect weak overtones and combinations of three characteristic fundamental ring stretching modes from all three of the PTCD derivatives measured, demonstrating that these modes can be enhanced by the same mechanism that fundamentals are.

In the work presented in section 6.3, mapping of Raman micro-spectroscopy was shown to be a powerful technique for the study of both systematically doped single dye-fatty acid monolayers and single molecules using SERRS. By variation of the ratio of the

218

two components in mixed dye-fatty acid Langmuir-Blodgett (LB) films, 2D SERRS mapping measurements were employed to study the effect of dye concentration on SERRS spectral properties and monolayer architectures, down to the single molecule level. It was shown that the rarity of coincidence between hot spots and single isolated molecules is a key consideration in ultrasensitive SERRS measurements of LB monolayers on nanostructured metallic films.

In the work discussed in section 6.4, SERRS spectra and 2D spatial intensity maps were recorded from thin Ag nanoparticle films coated with fatty acid Langmuir-Blodgett monolayers containing one-to-one binary mixtures, at varying concentrations, of the dyes R18 and salPTCD. It was demonstrated that similar chemical species within a multi-component sample could be distinguished, down to the single-molecule level, by means of their SERRS fingerprints. These techniques were employed to monitor changes in the distribution of the two dyes within the monolayer, and the breakdown of ensemble spectral averaging, which occurred as the single-molecule regime was approached. It was found that, at high concentrations, there was a high degree of miscibility of the dyes within the monolayer, while, at more intermediate concentrations, domain formation/aggregation was significant. When less than ca. 10 molecules of each dye occupied the 1 μm^2 scattering areas probed by the laser, single, isolated monomers were detected.

Finally, in the work presented in section 6.5, the Langmuir-Blodgett (LB) approach to single molecule SERRS was employed in the study of the perylene derivative BNPTCD. Several unique resonance conditions were explored, through variation of the surface-plasmon resonance of the substrate and the laser excitation wavelengths

219

employed. SERS/SERRS spectra were recorded for mixed LB monolayers deposited onto Ag and mixed Ag/Au nanoparticle substrates using multiple excitation wavelengths, and single-point and 2D mapping acquisition techniques. For the first time, single molecule non-resonant SERS spectra were reported for LB monolayers deposited on evaporated metal nanoparticle film substrates.

7.2 Future Directions

The pursuit of new and innovative substrates will continue to be a priority in SERS/SERRS research for some time to come, and important achievements in this work will go on providing exciting new milestones in the broader field of nanoscience. It is anticipated that the layer-by-layer technique for thin film fabrication, thanks in part to the work presented in this thesis, will take on an especially important role in this regard. Of particular importance will be work focused on the incorporation of materials that demonstrate biospecific interactions, including avidin/biotin, antigen/antibody, and complementary oligonucleotide systems. Single-molecule SERS/SERRS experiments will also continue to take on greater importance as they begin to become practical analytical techniques with ultrasensitivity and high information content. Researchers will likely increasingly focus on the application of these powerful techniques toward problems in the biological, medical, and environmental sciences. To lend further support to the high degree of control already afforded by the Langmuir-Blodgett approach to single-molecule detection, future experiments should be performed under vacuum or inert atmosphere, and at low temperatures.

220

VITA AUCTORIS

Paul Goulet was born in 1978 in Windsor, Ontario, Canada. He received his Ontario Secondary School Diploma in 1997 from Assumption College School, and his Honours Bachelor of Science in chemistry from the University of Windsor in 2001. Since then, he has been working toward a doctorate in chemistry in the Materials and Surface Science Group at the University of Windsor.

221

PUBLICATIONS

1. Overtones and Combinations in Single-Molecule Surface-Enhanced Resonance Raman Scattering, **Goulet, P. J. G.**; Pieczonka, N. P. W.; Aroca, R. F. *Anal. Chem.* **2003**, *75*, 1918-1923.

2. Single Molecule SERRS of Mixed Perylene Langmuir-Blodgett Monolayers on Novel Metal Island Substrates, **Goulet, P. J. G.**; Pieczonka, N. P. W.; Aroca, R. F. *Can. J. Anal. Sci. Spectrosc.* **2003**, *48*, 146-152.

3. Surface-Enhanced Resonance Raman Scattering: Single-Molecule Detection in a Langmuir-Blodgett Monolayer, Constantino, C. J. L.; Lemma, T.; Antunes, P. A.; **Goulet, P.**; Aroca, R. *Appl. Spectrosc.* **2003**, *57*, 649-654.

4. Chemical adsorption of salicylate on silver- A systematic approach to the interpretation of surface-enhanced vibrational spectra, **Goulet, P. J. G.**; Aroca, R. F., *Can. J. Chem.* **2004**, *82*, 987-997.

5. Gold Nanoparticle Embedded, Self-Sustained Chitosan Films as Substrates for Surface-Enhanced Raman Scattering, dos Santos Jr., D. S.; **Goulet, P. J. G.**; Pieczonka, N. P. W.; Oliveira Jr., O. N., Aroca, R. F. *Langmuir* **2004**, *20*, 10273-10277.

6. Retention and induced aggregation of Co(II) on a humic substance: sorption isotherms, infrared absorption, and molecular modeling, Alvarez-Puebla, R. A.; Garrido, J. J.; Valenzuela-Calahorro, C.; **Goulet, P. J. G.** *Surf. Sci.* **2004**, *575*, 136-146.

7. Surface-Enhancement of Fluorescence Near Noble Metal Nanostructures, **Goulet, P. J. G.**; Aroca, R. F. In *Topics in Fluorescence: Radiative Decay Engineering*;

Lakowics, J. R.; Geddes, C. D., Eds.; Springer Science + Business Media, Inc.: New York, **2005**; Vol. 8, 223-247.

8. Silver Nanowire Layer-by-Layer Films as Substrates for Surface-Enhanced Raman Scattering, Aroca, R. F.; **Goulet, P. J. G.**; dos Santos Jr., D. S.; Alvarez-Puebla, R. A.; Oliveira Jr., O. N. *Anal. Chem.* **2005**, *77*, 378-382.

9. Nano-structured Langmuir-Blodgett mixed films of titanyl (IV) phthalocyanine and bis(neopentylimido)perylene- Unique degree of miscibility, Del Cano, T.; **Goulet, P. J. G.**; Pieczonka; N. P. W.; Aroca, R. F.; De Saja, J. A. *Synth. Met.* **2005**, *148*, 31-35.

10. Characterization of the porous structure of different humic fractions, Alvarez-Puebla, R. A.; **Goulet, P. J. G.**; Garrido, J. J.; *Colloids Surf. A* **2005**, *256*, 129-135.

11. Mapping single-molecule SERRS from Langmuir-Blodgett monolayers on nanostructured silver island films, **Goulet, P. J. G.**; Pieczonka, N. P. W.; Aroca, R. F. *J. Raman Spectrosc.* **2005**, *36*, 574-580.

12. Role of Nanoparticle Surface Charge in Surface-Enhanced Raman Scattering, Alvarez-Puebla, R. A.; Arceo, E.; **Goulet, P. J. G.**; Garrido, J. J.; Aroca, R. F. *J. Phys. Chem. B* **2005**, *109*, 3787-3792.

13. Surface-Enhanced Raman Scattering on Dendrimer/Metallic Nanoparticle Layer-by-Layer Film Substrates, **Goulet, P. J. G.**; dos Santos Jr., D. S.; Alvarez-Puebla, R. A., Oliveira Jr., O. N.; Aroca, R. F. *Langmuir* **2005**, *21*, 5576-5581.

14. Applications of the Enhancement of Resonance Raman Scattering and Fluorescence by Strongly Coupled Metallic Nanostructures, Pieczonka, N. P. W.; **Goulet, P. J. G.**; Aroca, R. F. In *Surface-Enhanced Raman Scattering- Physics and Applications,*

Topics in Applied Physics; Kneipp, K.; Moskovits, M.; Kneipp, H., Eds.; Springer-Verlag: Berlin Heidelberg, **2006**; Vol. 103, 197-216.

15. Chemically Selective Sensing through Layer-by-Layer Incorporation of Biorecognition into Thin Film Substrates for Surface-Enhanced Resonance Raman Scattering, Pieczonka, N. P. W.; **Goulet, P. J. G.**; Aroca, R. F. *J. Am. Chem. Soc.* **2006**, *128*, 12626-12627.

16. Trace Detection of an Environmental Pollutant by Surface-Enhanced Raman Scattering, **Goulet, P. J. G.**; Alvarez-Puebla, R.; Aroca, R. F. In *Applications of Surface-Enhanced Raman Spectroscopy*: Farquharson, S., Ed.; CRC Press, **In press.**

17. Protein/Nanoparticle Layer-by-Layer Films as Substrates for Surface-Enhanced Resonance Raman Scattering, **Goulet, P. J. G.**; Pieczonka, N. P. W.; Aroca, R. F. In *ACS Symposium Series Book on New Approaches in Biomedical Spectroscopy*; Kneipp, K.; Aroca, R. F.; Kneipp, H.; Wentrup-Byrne, E., Eds.; ACS Publications, **In press.**

18. Distinguishing Individual Vibrational Fingerprints: Single-Molecule Surface-Enhanced Raman Scattering (SERRS) from One-to-One Binary Mixtures in Langmuir-Blodgett Monolayers, **Goulet, P. J. G.**; Aroca, R. F., **manuscript submitted for publication.**

CONFERENCES

1. Infrared and Raman Spectroscopy of Polypropylenimine Amine (DAB-Am) Dendrimers, **Goulet, P.**; Aroca, R. *29th Annual Southwestern Ontario Undergraduate Student Chemistry Conference*, Toronto, Canada **2001**.

2. Vibrational Spectroscopy of Polypropylenimine Amine (DAB-Am) Dendrimers, **Goulet, P.**; Aroca, R.; Tomalia, D. *84th CSC Conference and Exhibition*, Montreal, Canada, **2001**.

3. Single Molecule SERRS of Mixed Perylene Langmuir-Blodgett Monolayers, Pieczonka, N.; **Goulet, P.**; Aroca, R. *Proceedings of the Fourth Biennial International Conference on Monitoring and Measurement of the Environment*, Toronto, Canada, **2002**; p 539.

4. Single Molecule SERRS of Mixed Perylene Langmuir-Blodgett Monolayers on Novel Metal Island Substrates, Pieczonka, N.; **Goulet, P.**; Aroca, R. *XVIIIth International Conference on Raman Spectroscopy*, Budapest, Hungary, **2002**; p 341-342.

5. Surface Enhanced Resonance Raman Scattering. Properties and Applications, **Goulet, P.**; Lemma, T.; Pieczonka, N.; Aroca, R. *XVIIIth International Conference on Raman Spectroscopy*, Budapest, Hungary, **2002**; p 37-40.

6. A Theoretical Approach to the Study of the Chemical Adsorption of Salicylic Acid on Silver, **Goulet, P. J. G.**; Aroca, R. F. *49th International Conference on Analytical Sciences and Spectroscopy*, Ottawa, Canada, **2003**; p 31.

7. Single Molecule SERRS: Fundamentals, Overtones, and Combinations, **Goulet, P.**; Pieczonka, N.; Aroca, R. *39th IUPAC Congress and 86th Conference of the Canadian Society for Chemistry*, Ottawa, Canada, **2003**.

8. Raman Microscopy and Imaging. Application to Monolayers and Single Molecule Detection, **Goulet, P.**; Pieczonka, N.; Aroca, R. *Microscopy and Microanalysis 2003*, San Antonio, Texas, USA, **2003**; p 1080-1081.

9. Nanostructures for Surface-Enhanced Raman Scattering and Single Molecule Detection, Aroca, R. F.; dos Santos Jr., D. S.; **Goulet, P. J. G.** *IX European Conference on Organised Films*; University of Valladolid: Valladolid, Spain, **2004**, p. 47.

10. Langmuir-Blodgett Mixed Films of Titanyl (IV) Pthalocyanine and Bis(Neopentylimido) Perylene. Unique Degree of Miscibility, Del Cano, T.; **Goulet, P. J. G.**; Pieczonka, N. P. W.; Aroca, R. F.; DeSaja, J. A. *IX European Conference on Organised Films*; University of Valladolid: Valladolid, Spain, **2004**, p. 152.

11. Resonant and Pre-Resonant Surface-Enhanced Raman Scattering of Single Molecules, **Goulet, P. J. G.**; Del Cano, T.; De Saja, J. A.; Aroca, R. F. *IX European Conference on Organised Films*; University of Valladolid: Valladolid, Spain, **2004**, p. 55.

12. The Application of Self-Sustained Nanoparticle Embedded Biopolymer Films for Surface-Enhanced Raman Scattering, Pieczonka, N. P. W.; dos Santos Jr., D. S.; **Goulet, P. J. G.**; Oliveira Jr., O. N.; Aroca, R. F. *IX European Conference on Organised Films*; University of Valladolid: Valladolid, Spain, **2004**, p. 45.

226

13. Nanostructures for Surface-Enhanced Raman Scattering and Single Molecule Detection, Aroca, R. F.; Pieczonka, N. P. W.; dos Santos Jr., D. S.; **Goulet, P. J. G.** *87th Conference of the Canadian Society for Chemistry*; Canadian Society for Chemistry: London, Canada, **2004**.

14. Electromagnetic Hot Spots in the Detection and Chemical Identification of Single Molecules, **Goulet, P. J. G.**; Aroca, R. F. *87th Conference of the Canadian Society for Chemistry*; Canadian Society for Chemistry: London, Canada, **2004**.

15. Raman Microscopy and Imaging Applications to Nanostructures and Single Molecule Detection, **Goulet, P. J. G.**; Pieczonka, N. P. W.; Aroca, R. F. *31st FACSS Conference*: Portland, USA, **2004**; Final Program of Abstracts, p. 200.

16. Protein/Nanoparticle Layer-by-Layer Films as Chemically Selective SERS Substrates, **Goulet, P. J. G.**; Pieczonka, N. P. W.; Alvarez-Puebla, R. A.; Aroca, R. F., *Pacifichem 2005*: Honolulu, Hawaii, USA, **2005**, Book of Abstracts, p. 8-Tech.

17. Avidin/Ag Nanoparticle Layer-by-Layer Films as Substrates for Surface-Enhanced Resonance Raman Scattering, **Goulet, P. J. G.**; Pieczonka, N. P. W.; Aroca, R. F., *2006 Ontario Nano Symposium*: Waterloo, Canada, **2006**.

18. Single Molecule Detection with Langmuir-Blodgett and Layer-By-Layer Films, **Goulet, P. J. G.**; dos Santos Jr., D. S.; Aroca, R. F., *Tsukuba Satellite Symposium on Single Molecule and Tip-Enhanced Raman Scattering*: Tsukuba, Japan, **2006**, p. 22-25.

19. Mixed Langmuir-Blodgett Monolayers: Highly Controlled Architectures for the Study of Single Molecule SERS/SERRS, **Goulet, P. J. G.**; Aroca, R. F., *Tsukuba*

Satellite Symposium on Single Molecule and Tip-Enhanced Raman Scattering: Tsukuba, Japan, **2006**, p. 90-91.

20. Mixed Langmuir-Blodgett Monolayers: Highly Controlled Architectures for the Study of Single Molecule SERS/SERRS, **Goulet, P. J. G.**; Aroca, R. F., *20th International Conference on Raman Spectroscopy*: Yokohama, Japan, **2006**, p. 391.

21. Single Molecule SERRS in Langmuir-Blodgett Monolayers, **Goulet, P. J. G.**; Pieczonka, N. P. W.; Aroca, R. F, *1st International Symposium on Surface-Enhanced Raman Scattering, SERS 2006*: Nishinomiya, Japan, **2006**, p. 28.

22. Mixed Langmuir-Blodgett Monolayers: Highly Controlled Architectures for the Study of Single Molecule SERS/SERRS, **Goulet, P. J. G.**; Aroca, R. F, *1st International Symposium on Surface-Enhanced Raman Scattering, SERS 2006*: Nishinomiya, Japan, **2006**, missing from abstract book.